

University of Strathclyde

Department of Pure and Applied Chemistry

Antibody-conjugated Nanoparticles for SERS-based Lateral Flow Immunoassay

Pietro Gancitano

A thesis submitted to the Department of Pure and Applied Chemistry, University of
Strathclyde, in fulfilment of the requirements for degree of Doctor of Philosophy

2018

This thesis is the result of the author's original research. It has been composed by the author and has not been previously submitted for examination which has led to the award of a degree.

The copyright of this thesis belongs to the author under the terms of the United Kingdom Copyright Acts as qualified by University of Strathclyde Regulation 3.50. Due acknowledgement must always be made of the use of any material contained in, or derived from, this thesis.

Signed:

Date:

This thesis is dedicated to the memory of my dad Vito. He always encouraged me to pursue knowledge.

Acknowledgements

Firstly I would like to thank my supervisors Professor Duncan Graham and Professor Karen Faulds for all their patience, understanding and guidance throughout my PhD. I greatly appreciate the opportunity they have given me in coming to Scotland for taking part of the Centre for Molecular Nanometrology as postgraduate student.

I am very grateful to BBI Solution for funding my PhD, providing materials, equipment and precious information that helped me carry out the project. In particular, thanks go to Stephen Carmichael, Darren Rowles and Steven Lamont who were involved in various parts of my project.

I would like to thank all the postdocs in the group. Without their assistance it would have been much harder to achieve some of the research goals. In particular, thanks go to Dr Lee Barrett and Dr Samuel Mabbott for helpful tips and suggestions.

Also, I owe a thank-you to every single PhD student who I have met over the last three and half years, for making every day in the lab an enjoyable experience. Special thanks go to Julie, Chris, Jon, Sian, Alex, Sureyya, Danny and Kirsty for their help and support during every day routine at the office.

I would like to thank my family that without their help I could not accomplished this studies. Despite the hard time we were facing for the unexpected loss of my dad they have been very supportive and understanding. A big thank-you to my mum.

Finally, thanks to Kate for supporting me during the last part of my postgraduate study and most important for her patience during the writing of this thesis.

Abstract

The success to obtain a sensitive analytical tool such as a nanosensor, starts from its design and fabrication. The investigation of the chemistry behind metallic nanostructures and antibody interactions was a fundamental part of the research described in this thesis. In addition, the development of surface enhanced Raman scattering (SERS) based lateral flow immunoassays (LFIA) for the highly sensitive detection of specific antigens was carried out.

Gold nanoparticles (AuNPs) were used in the development of a universal method for histidine tagged antibodies conjugation. To achieve this, AuNPs were functionalised with a linker that contained a thiol group, which has affinity to the gold surface and a nitrilotriacetic acid (NTA) metal ion complex, which is known to have an affinity towards histidine. A fragment antigen-binding (Fab) antibody that contains 7-histidine residues was conjugated to the functionalised AuNPs in a rapid and straightforward manner. Different metal ions were investigated at various concentrations. Results demonstrated that the antibody uptake was controlled by metal ion concentration and that nickel (II) gave the stronger antibody binding. The Fab conjugated NTA-Ni AuNPs were also evaluated for use in SERS-based LFIA, showing high stability and compatibility compared to passive adsorption conjugates.

A sandwich-like format SERS-based LFIA for the detection of C-reactive protein (CRP) was developed. Results demonstrated that, by using a Raman reporter molecule (RRM) that was in resonance with the excitation laser, a 25-fold improvement in sensitivity was achieved, compared to visual detection. A competitive format SERS-based LFIA was also developed, showing the possibility of detecting a wider range of CRP concentrations, compared to the sandwich format.

Anisotropic nanoparticles such as gold nanostars (AuNSs) were used for the detection of human chorionic gonadotropin (hCG) by LFIA. AuNSs were conjugated to anti-hCG antibodies and labelled with RRM in order to allow a SERS detection. AuNSs showed better assay performance than spherical nanoparticles, either in SERS and visual detection. AuNSs morphology and shape consented the generation of "hot spots" and the possibility to allocate antibodies in an orientated manner on the AuNSs surface, which resulted in highly sensitive signal response. The optimisation of the SERS labelled AuNSs-antibody conjugates along with the choice of an appropriate RRM led to the detection in the picogram range of hCG concentration in a pseudo-biological matrix.

Abbreviations

a.u.	Arbitrary Unit
Ab	Antibody
AgNP	Silver Nanoparticle
AP	Absorbent Pad
AuNP	Gold Nanoparticle
AuNS	Gold Nanostar
BNP	Brain Natriuretic Peptide
BPE	1,2-Bis(4-Pyridyl)Ethylene
CD	Constant Domain
CL	Control Line
CP	Conjugate Pad
CT-PEG	Carboxy-PEG ₁₂ -Thiol
DLS	Dynamic Light Scattering
DMSO	Dimethyl Sulfoxide
DPI	Dots per Inch
EDC	1-Ethyl-3-(3dimethylaminopropyl) Carbodiimide
Eqv	Equivalent
Fab	Fragment Antigen-binding
FBS	Foetal Bovine Serum
Fc	Crystallisable Fragment
FSH	Follicle-Stimulating Hormone
hCG	Human Chorionic Gonadotropin
HEPES	4-(2-Hydroxyethyl)-1-Piperazine Ethane Sulfonic Acid
His-tag	Histidine-Tagged
IDA	Iminodiacetic Acid
Ig	Immunoglobulin
IMAC	Immobilised Metal Ion Affinity Chromatography
KDa	Kilo Dalton
LF	Lateral Flow
LFIA	Lateral Flow Immunoassay

LOD	Limit Of Detection
LSPR	Local Surface Plasmon Resonance
MAb	Monoclonal Antibody
MBA	4-Mercaptobenzoic Acid
MES	2-(N-Morpholino) Ethane Sulfonic Acid
MGITC	Malachite Green Isothiocyanate
Min	Minutes
MNNP	Metal Non-Spherical Nanoparticle
MT-PEG	Methyl-PEG ₄ -Thiol
NA	Numerical Aperture
NC	Nitrocellulose
NP	Nanoparticle
NSB	Non-Specific Binding
NTA-Co	Cobalt (II) Nitrilotriacetic Acid Complex
NTA-M	Metal Ions Nitrilotriacetic Acid Complex
NTA-Ni	Nickel (II) Nitrilotriacetic Acid Complex
O.D.	Optical Density
PAb	Polyclonal Antibody
PDI	Polydispersity Index
PEG	Polyethylene Glycol
PMMA	Poly Methyl Methacrylate
PoC	Point of Care
PPY	4-(1H-Pyrazol-4-Yl)Pyridine
PYOT	5-(Pyridine-4-Yl)-1,3,4-Oxadiazole-2-Thiol
QD	Quantum Dot
Rec	Recombinant
RGB	Red, Green and Blue
rpm	Revolutions per Minute
RRM	Raman Reporter Molecule
RRS	Resonance Raman Scattering
SD	Standard Deviation
SEM	Scanning Electron Microscopy

SERRS	Surface-Enhanced Resonance Raman Scattering
SERS	Surface-Enhanced Raman Scattering
SP	Sample Pad
Sulfo-NHS	N-Hydroxysulfosuccinimide
TEM	Transmission Electron Microscopy
TL	Test Line

Contents

Acknowledgements.....	iv
Abstract.....	v
Abbreviations.....	vi
Contents.....	ix
CHAPTER 1: Introduction	1
1.1. Nanoparticles.....	2
1.1.1. History.....	2
1.1.2. Synthesis of nanoparticles.....	3
1.1.3. Surface modification of nanoparticles.....	4
1.1.4. Optical properties.....	5
1.1.5. Anisotropic nanoparticles.....	7
1.2. Raman Spectroscopy.....	9
1.2.1. Theory.....	9
1.2.2. Surface-Enhanced Raman Scattering (SERS) and Surface-Enhanced Resonance Raman Scattering (SERRS)	11
1.3. Antibody-Conjugated Nanoparticles.....	15
1.3.1. Antibody molecule.....	15
1.3.2. Antibody conjugation methods	19
1.3.2.1. Covalent methods.....	20
1.3.2.2. Non-covalent methods	21
1.3.2.3. Passive adsorption	23
1.3.3. Applications of antibody-conjugated nanoparticles	25
1.3.3.1. Therapy	26
1.3.3.2. Diagnosis	26

1.4. The Lateral Flow Assay	28
1.4.1. Improving sensitivity in lateral flow	30
CHAPTER 2: Gold Nanoparticles for a Universal Conjugation Method of Histidine-Tagged Antibodies	37
2.1. Aims and overview	37
2.2. Results and discussion	39
2.2.1. Modification of AuNPs with polyethylene glycol (PEG).....	39
2.2.2. Attachment of nitrilotriacetic acid (NTA) unit to PEGylated AuNPs.....	43
2.2.3. Metalation study	46
2.2.4. Conjugation of his-tag antibody to metal ions functionalised NTA AuNPs	48
2.2.5. Role of nickel in the conjugation process.....	52
2.2.5.1. Nickel concentration study	52
2.2.5.2. Nickel incubation time study	53
2.2.5.3. Antibody displacement study	53
2.2.6. Antibody concentration study.....	54
2.2.7. Interaction of NTA-Ni AuNPs with poly-L amino acids	56
2.3. Conclusions	59
CHAPTER 3: SERS-based Lateral Flow Immunoassay for the Detection of C-reactive protein	60
3.1. Aims and overview	60
3.2. Results and discussion	62
3.2.1. Raman reporter molecule (RRM) evaluation.....	62
3.2.2. Preparation of MGITC labelled antibody-gold conjugate.....	65
3.2.2.1 Compatibility of MGITC labelled antibody-gold conjugate with LFIA.....	66
3.2.2.2. Comparison of conjugation methods for MGITC labelled antibody-gold.....	67
3.2.3. Sandwich format of SERRS-based LFIA	69

3.2.4. Competitive format of SERRS-based LFIA.....	76
3.2.5. Performance of SERRS-based LFIA in biological samples.....	81
3.3. Conclusions	84
CHAPTER 4: The Use of Gold Nanostars for Highly-Sensitive Lateral Flow Immunoassay	85
4.1. Aims and overview.....	85
4.2. Results and discussion	87
4.2.1. Characterisation of gold nanostars.....	87
4.2.2. Comparison between AuNSs and AuNPs for SERS applications.....	90
4.2.3. Comparison between AuNSs and AuNPs for LFIA applications.....	91
4.2.4. Functionalisation of AuNSs with anti-hCG antibody and MBA.....	92
4.2.5. SERS-based LFIA for the detection of hCG in a buffered solution.....	94
4.2.6. Raman reporter molecule (RRM) evaluation.....	98
4.2.7. Optimisation of the AuNSs@MBA@anti-hCG conjugation method	102
4.2.8. SERS-based LFIA for the detection of hCG in a pseudo-biological matrix	104
4.3. Conclusions	108
CHAPTER 5: Experimental	110
5.1. Materials	110
5.2. Methods and instrumentation.....	111
5.2.1. Extinction spectroscopy.....	111
5.2.2. Dynamic light scattering (DLS).....	111
5.2.3. Scanning electron microscopy (SEM)	112
5.2.4. Raman spectroscopy.....	112
5.3. Gold nanoparticles for a universal conjugation method of histidine-tagged antibodies	113
5.3.1. PEGs concentration study.....	113
5.3.2. Preparation of optimised PEGylated AuNPs.....	113

5.3.3. Preparation of NTA functionalised AuNPs.....	113
5.3.4. Stability of NTA AuNPs in NaCl solutions.....	113
5.3.5. Metals incubation study	114
5.3.6. Optimisation study of NTA AuNPs with nickel and cobalt ions.....	114
5.3.7. His-tag Fab conjugation to metal ions functionalised NTA AuNPs.....	114
5.3.8. Role of nickel in the antibody conjugation	115
5.3.8.1. Nickel concentration study	115
5.3.8.2. Nickel incubation time study	115
5.3.8.3. Antibody displacement study	115
5.3.9. Antibody optimisation study	116
5.3.10. Interactions between NTA-Ni AuNPs and poly-L amino acids.....	116
5.4. SERS-based lateral flow immunoassay for the detection of C-reactive protein.....	117
5.4.1. Raman reporter molecule study.....	117
5.4.2. Preparation of MGITC labelled his-tag Fab NTA-Ni AuNPs.....	117
5.4.3. Compatibility study of MGITC labelled conjugates with LFIA.....	118
5.4.4. Conjugation methods comparison study.....	118
5.4.5. Sandwich SERRS-based LFIA	119
5.4.6. Competitive SERRS-based LFIA.....	119
5.4.7. Biological samples study.....	120
5.4.7.1. Sandwich assay	120
5.4.7.2. Competitive assay	120
5.5. The use of gold nanostars for highly-sensitive lateral flow immunoassay.....	122
5.5.1. Characterisation of BBI AuNSs.....	122
5.5.2. Comparison between BBI AuNSs and AuNPs for SERS applications.....	122
5.5.3. Comparison between BBI AuNSs and AuNPs for LFIA applications.....	122
5.5.4. Functionalisation of AuNSs with anti-hCG antibody and MBA.....	123

5.5.5. SERS-based LFIA for the detection of hCG in buffer solutions	123
5.5.6. Raman reporter molecule evaluation.....	124
5.5.7. Optimisation of the AuNSs@MBA@anti-hCG conjugation method	125
5.5.8. SERS-based LFIA for the detection of hCG in a pseudo-biological matrix	126
CHAPTER 6: Final Conclusion and Future Work.....	127
References	131
APPENDIX A: lateral flow strip assembling and striping procedures.....	156
APPENDIX B: Buffers study for optimal lateral flow performance for his-tag Fab conjugated NTA-Ni AuNPs	158
APPENDIX C: capture antibody line and CRP spot optimisation studies	160
C1. Sandwich format.....	160
C2. Competitive format	161
APPENDIX D: SEM and TEM images of various AuNSs batches	163
APPENDIX E: test line study on lateral flow strips for detection of hCG	165
APPENDIX F: LF strips image for AuNSs@MBA@anti-hCG conjugates optimisation study.	167

CHAPTER 1: Introduction

The origin of nanotechnology is associated with the famous lecture *“There’s plenty of room at the bottom”*, given by the physicist and Nobel Prize winner Richard Feynman at Caltech in 1959.¹ In his talk, Feynman proposed a new field of physics which would take into consideration the problem of understanding, manipulating and controlling things on a small scale.¹ Feynman pointed out that the possibility of rearranging atoms in a predetermined order would allow the synthesis of materials that show novel physicochemical properties. This approach is known as “bottom-up” and forms the foundation of nanochemistry. In contrast, the “top-down” approach is traditionally used by solid state physicists to fabricate nanomaterials.² Feynman was also convinced that the understanding of fundamental biological problems could be solved by *“looking at the thing!”* which means by the development of spectroscopic and microscopic techniques.¹ In the last few decades, nanotechnology has been rapidly expanding in several applications from medicine to electronics, from solar cells to textiles.³ In particular, nanomaterials such as metallic nanoparticles that show an affinity towards biomolecules, have been developed for biomedical applications such as drug delivery, bio-imaging and for the detection of several biomolecules.⁴⁻⁶ More specifically antibody-conjugated nanoparticles are widely used for detection of proteins, viruses, bacteria and other biomolecules.^{7,8} Some of the techniques widely used for bioanalysis are lateral flow immunoassay (LFIA) or surface enhancement Raman scattering (SERS) based assays.^{9,10}

1.1. Nanoparticles

1.1.1. History

Nanoscience is an established area of science that focuses its attention on small objects with size ranging from a few nanometres to around 100 nm; these objects are commonly known as nanoparticles (NPs).¹¹ In chemistry, this range of sizes has historically been associated with colloids, micelles and polymer molecules but in the last few decades, structures such as carbon nanotubes, silicon nanorods or quantum dots have emerged as interesting classes of nanomaterials.^{12,13,14} Furthermore, biology and biochemistry researchers have a deep interest in nanostructures as components of the cell. Many of the most interesting structures in biology – from DNA and viruses to sub-cellular organelles and gap junctions – can be considered as nanostructures.¹⁵ An important class of nanomaterials are metallic NPs such as copper, silver and gold. They display unique characteristics such as electronic, optical, physical and magnetic properties that the same bulk material would not.¹⁶ In the last decade, the field of nanotechnology has undergone remarkable developments, resulting in new procedures for the controlled synthesis of a wide variety of NPs and measurement of their properties. The possibility of tuning these properties by changing the size, shape and composition of the nanostructure has led to the use of NPs in several analytical applications.¹⁷ NPs were used since the ancient times; for instance gold nanoparticles (AuNPs) are related to the history of red-coloured glass. The first milestone in the history of red glass is the Lycurgus Cup (Figure 1), that was made during the Roman Empire in the fourth century.¹⁸ The openwork shows the triumph of Dionysus, Greek god of wine, over Lycurgus, king of the Edoni in Thrace.¹⁹ The glass of the cup is a good example of dichroism. The cup appears red when it is illuminated from the inside due to the transmission of light through gold dispersed in the glass. When the cup is illuminated from the outside it appears green due to the presence of silver NPs which strongly scatter the light.



Figure 1. The Lycurgus Cup, Late Roman, 4th century A.D., in reflected (a) and transmitted (b) light. Scene representing Lycurgus being enmeshed by Ambrosia (a nymph) which is transformed into vines. Image reproduced from The Trustees of the British Museum.²⁰

Another example of use of nanotechnology in ancient time is given by a pigment called Purple of Cassius. This compound was discovered in the 17th century by Andrea Cassius and described in his work *De Auro*.²¹ The compound was prepared by the reduction of gold salt with tin chloride and studies at the beginning of the 20th century confirmed the presence of gold colloids in the pigment.²² The chemistry behind NPs and in particular AuNPs was unknown until 1857, when Michael Faraday delivered the Bakerian Lecture of the Royal Society entitled “*Experimental Relations of Gold (and other Metals) to Light*”.²³ This systematic study on the interaction of light with finely-divided metallic particles marked the birth of the modern colloid science.²⁴ Faraday’s gold colloid was prepared by reducing tetrachloroaurate with phosphorous and carbon disulfide. He discovered that the solution contained diffused gold by observing its interaction with the light.²³ Nowadays NPs of various size, shape and composition are widely produced and commercialised by several companies around the globe, to name a few: BBI Solutions, Innova biosciences, Nano Composix and Merck. In the last few decades a large number of publications have emerged on the use of metallic NPs for analytical and biomedical applications.^{25,26,27}

1.1.2. Synthesis of nanoparticles

Since Faraday’s gold colloids, many methods have been suggested for the preparation of AuNPs. In general, NPs synthesis is performed in aqueous solution and the mechanism involves two processes: nucleation and growth.²⁸ Nucleation is the formation of nuclei (seeds) that act as template for the growing of the NPs. The formation of NPs relies on the reduction of the metal salt in the presence of a reducing/capping agent. Sometimes NPs

synthesis involves the use of molecules that bind their surface in order to prevent flocculation and coagulation.^{29,30} The most popular method of AuNPs synthesis is based on the reduction of tetrachloroauric acid (HAuCl₄) with sodium citrate and it was first developed by Turkevich in 1951.³¹ The resulting AuNPs have negatively charged citrate ions adsorbed on their surface and are thus stabilised by electrostatic repulsion.³² The molar ratio between citrate and HAuCl₄ can be altered in order to make AuNPs of various sizes. This was first investigated by Frens and co-workers in 1973.³³ They prepared AuNPs varying from 16 to 147 nm with a decrease in the citrate-to-HAuCl₄ molar ratio.³⁴ Furthermore, AuNPs with a diameter of 1 to 5 nm can be synthesised by reduction of triphenylphosphine gold chloride with diborane or sodium borohydride and by biphasic reduction of HAuCl₄ by sodium borohydride in the presence of thiol capping agents.^{35,36} Also, silver NPs (AgNPs) can be synthesised in a similar manner described for gold. A method, reported by Lee et al.³⁷ uses silver nitrate combined with a sodium citrate solution which acts as both a reducing and stabilising agent. Many methods have been developed for the preparation of metallic non-spherical NPs such as nanorods or nanostars.^{38,39} Generally, their synthesis involves the use of stabilising agents such as cetrimonium bromide or ascorbic acid.^{40,41}

1.1.3. Surface modification of nanoparticles

Prerequisite for every possible NP application is the proper surface modification that determines their interaction with the environment and ultimately affect their stability.³² NPs can be dispersed in both aqueous and organic solvents according to the ligands that surround their surface. For example hydrophobic ligand molecules such as dodecanethiol or oleic acid can prevent the aggregation of NPs in organic solvents.³² Also amphiphilic ligands molecules such as polyethylene glycol (PEG) can stabilise NPs in a number of solvents with intermediate polarity as well as in aqueous solutions.⁴² The stability of the colloidal depends on the repulsive force between NPs which is due to electrostatic repulsion or steric hindrance. The addition of particular ligand molecules onto the NPs' surface can improve the stability and prevent non-specific aggregations. The ligand can bind the surface by some attractive interactions such as chemisorption, electrostatic attraction or hydrophobic interaction by a head-group of the ligand. For instance, a functional group that shows high affinity toward AuNPs is the thiol group.⁴³ Systematic comparison of the metal–thiolate bond for noble metal monothiolates has shown a degree of covalent binding.⁴⁴ Therefore, ligands that contain thiol groups are the best candidate to anchor onto the surface of AuNPs and avoid displacement.

The electrostatic and the hydrophobic interactions are weaker than chemisorption. Species attached on AuNPs by electrostatic attraction such as sodium citrate, can be easily exchanged by another ligand that contains a thiol group.

1.1.4. Optical properties

For the aim of this thesis, AuNPs are discussed in this section. The widespread use of AuNPs as labels in diagnostics and detection is due to a unique combination of chemical and physical properties that allow biological molecules to be detected at low concentrations.⁴⁵ They display many advantageous properties compared to the other metal NPs such as stronger stability, less toxicity, ease and reproducibility of synthesis.^{46,47} One of the characteristic that makes metallic NPs perfect tools for analytical applications is their optical properties. For example, AuNPs present a unique red colour that is intricately linked with their size. A water suspension of AuNPs with a diameter of 20 nm, shows an extinction spectra with a maximum peak at 520 nm wavelength (λ_{\max}). However, any NPs' surface modification or when two or more NPs interact each other's (i.e. during aggregation) the λ_{\max} shifts, resulting in a colour change of the gold suspension from red to purple (Figure 2).

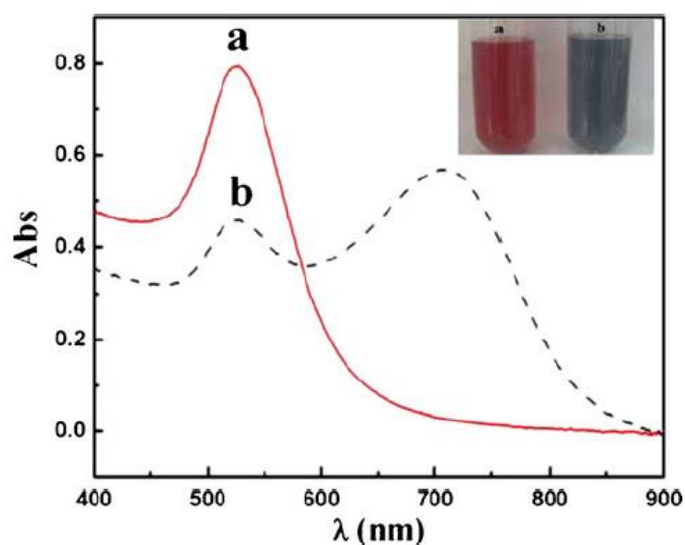


Figure 2. Example of a colour change from red (a) to purple (b) in a water suspension of 15 nm diameter AuNPs due the present of an analyte that causes aggregation. The maximum peak of the extinction spectra is shifted to bigger wavelength after aggregation. Image reprinted with permission from Ya-Nan Chang et al. 2016.⁴⁸ Copyright © 2016, Springer Nature.

This phenomenon is known as localised surface plasmon resonance (LSPR) and the wavelength at the maximum peak is known also as λ_{LSPR} . An approach to explain this phenomenon is described here. The word plasmon corresponds to the quantum energy

associated with a frequency of a plasma oscillation that derives from a free movement of electric charges under the influence of electromagnetic or gravitational forces.¹⁸ For the metallic nanoparticles the plasmon oscillation is due to the conduction electrons which oscillate coherently with an electromagnetic field (Figure 3).

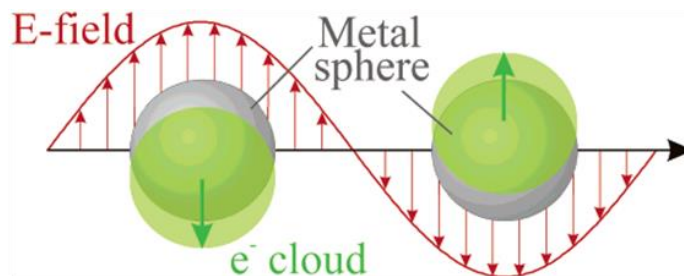


Figure 3. Schematic representation of plasmon oscillation for nanoparticles. Reprinted with permission from K. L. Kelly, E. Coronado, L. L. Zhao, et al., *The Optical Properties of Metal Nanoparticles: The Influence of Size, Shape, and Dielectric Environment*; *The Journal of Physical Chemistry B*. Copyright © 2003 American Chemical Society.

The consequences of the LSPR are a strong absorption of incident light in the visible region and strongly scattered light. In 1908 Mie presented a solution to Maxwell's equation that described the extinction (extinction = absorption + scattering) spectra of spherical particles of arbitrary size.⁴⁹ The electromagnetic fields are expanded in multipole contributions and the expansion coefficients are found by applying the correct boundary conditions for electromagnetic fields at the interface between the metallic nanoparticles and its surroundings.¹⁸ For particles less than 60 nm a dipolar approximation is possible.¹⁸ Therefore, the electric field of the outside of the nanoparticles can be determined using the following equation (Equation 1).

$$\vec{E}_{ext} = \vec{E}_0 - \alpha E_0 \left[-2 \frac{\cos \theta}{r^3} \vec{u}_r - \frac{\sin \theta}{r^3} \vec{u}_\theta \right]$$

Equation 1. Electromagnetic field of nanoparticles.

E_0 is the incident electric field, α is the sphere polarizability and the terms in the square brackets refer to the vectors for the induced dipole electric field that results from polarization of the conduction electrons of the NPs. The La Place equation shows that the polarizability is given by the follow equation (Equation 2).⁵⁰

$$\alpha = \frac{\epsilon_i - \epsilon_0}{\epsilon_i + 2\epsilon_0} a^3$$

Equation 2. La Place equation.

The radius of the sphere is represented by a^3 , ϵ_i is the dielectric constant of the nanoparticles and ϵ_0 is the dielectric constant of the surrounding medium. Therefore, it can be deduced from equations 1 and 2 that the size of the nanoparticles and the medium in which they are dispersed influences the LSPR.

1.1.5. Anisotropic nanoparticles

A special class of nanomaterials is represented by anisotropic nanoparticles. According to the Oxford English Dictionary, the word anisotropic derives from two Greek words “*anisos*” which means unequal and “*tropos*” which means turn.⁵¹ Nanomaterials are defined anisotropic when their physical and optical characteristics depends on the direction the observer stands. Numerous papers and reviews have been published showing many advantages of these materials in several fields of nanotechnology, especially in bioanalytical applications.⁵²⁻⁵⁴ One class of these materials is represented by metal non-spherical nanoparticles (MNNPs). They display intricate shapes such as: wires, rods, stars, urchins, popcorns and flowers.⁵⁵⁻⁶⁰ The common features of MNNPs are protrusions and irregularities on their surfaces that can lead to a localised electric field when they interact with and monochromatic light source. This enhancement is known as “lightning-rod”⁶¹ or “hot-spot”⁶² effect and it gives an advantage over spherical nanoparticles in many analytical applications based on surface enhanced Raman scattering (SERS) and surface enhanced fluorescence (SEF).^{63,64} Indeed, during the analysis, a molecule that is in close proximity of MNNPs’ tips and concavities, is subject to an electric field far stronger than just the intensity of the incident light due to the enhanced local fields.⁶⁵ Anisotropic NPs also exhibit excellent optical properties.⁶⁶ For example, nanorods show higher sensitivity to the local dielectric environment than similarly sized spherical nanoparticles.⁶⁷ The LSPR of MNNPs can be tuned by varying their size or shape making them exceptionally attractive in colorimetric sensing and biomedical applications.^{68,69} For example, silica-gold nanoshells possess highly favourable optical and chemical properties for biomedical imaging and therapeutic applications. By varying the relative core and shell thickness, the optical resonance can be precisely and systematically varied over a broad region of the electromagnetic spectrum (Figure 4).⁷⁰



Figure 4. Visual demonstration of the tunability of metal nanoshells. From left to right the gold shell thickness decreases from 20 to 5 nm. The silica core is 60 nm for each sample.⁷⁰ Image reproduced from Loo C. et al., *Technology in Cancer Research & Treatment*, 2004 (open access article).

Moreover, the LSPR of gold nanostars (AuNSs) can be tuned to the near infrared region where tissue absorption and fluorescence from biomolecules are very low.⁷¹ This is very useful for potential *in vivo* applications such as medical diagnostics and photothermal therapy.^{72,73} The heat coming out from the interaction of MNPs with the electromagnetic field can selectively destroy cancer cells.⁷⁴

1.2. Raman Spectroscopy

1.2.1. Theory

In 1930 Sir Venkata Raman was awarded the Nobel Prize in physics for his work on the scattering of light and for the discovery of the effect named after him.⁷⁵ He discovered that the visible wavelength of a small fraction of the radiation scattered by certain molecules differed from that of the incident beam and furthermore that the shifts in wavelength depended on the chemical structure of the molecules responsible for the scattering.⁷⁶ The scattered photons can be detected by collecting light at an angle to the incident light beam. Figure 5 shows the basic process representing the two main types of scattering process: Raman and Rayleigh.

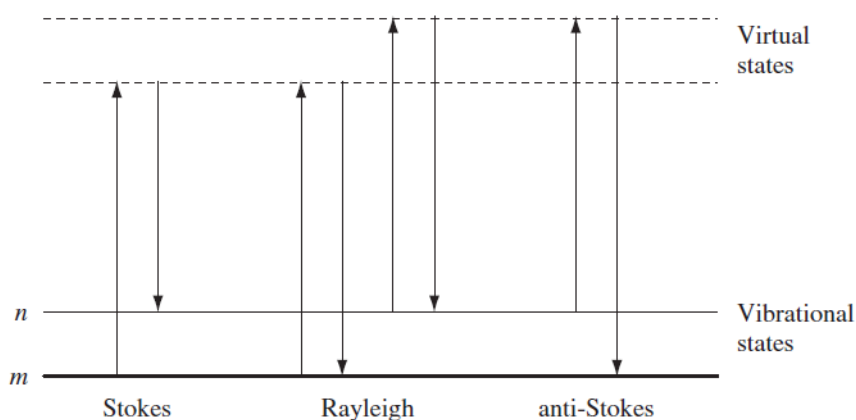


Figure 5. Diagram representing the Rayleigh and Raman (Stokes and anti-Stokes) scattering phenomena. Reprinted with permission from E. Smith and G. Dent, *Modern Raman Spectroscopy – A Practical Approach*. Copyright © 2005, John Wiley and Sons

The Rayleigh scattering is an elastic process where the shift in wavelength is equal to zero as the frequency of absorbed photons is the same of the scattered photons. The Raman scattering is given by the Stokes and anti-Stokes, which are inelastic transitions as the related shift in wavelength is different from zero: Raman shift (Equation 3).

$$\Delta E = |E_n - E_m| = h \nu$$

Equation 3. Energy of the scattered photon (ΔE). h = Planck constant, ν = frequency of the Raman shift. E_n = energy of vibrational state n , E_m = energy of vibrational state m .

The frequency of the Raman shift ν depends on the energy of vibrational states of the molecules responsible for scattering. The average number of molecules in a state is called the population of the state N_i .⁷⁷ Since the population depends on the energy of that level, at

constant temperature (Equation 4), the Stokes transitions will be more frequent than the anti-Stokes'. Therefore, at room temperature the Raman Stokes shift will be the most intense.

$$\frac{N_n}{N_m} = e^{-\frac{(E_n - E_m)}{kT}}$$

Equation 4. Boltzmann distribution for the relative populations for the states m and n .

Where N_n is the average number of molecules in the vibrational states n , N_m is the average number of molecules in the vibrational states m , k is the Boltzmann's constant (1.381×10^{-23} J K⁻¹) and T is the temperature.⁷⁷ One of the many advantages of Raman spectroscopy techniques is that samples can be analysed *in situ* and it is not necessary for any pre-treatment. Additionally, water does not give strong Raman signal so several species can be detected in aqueous condition with low background signal. However, the intensity of a normal Raman band is generally weak (one in a million Raman scattered photons) and it depends on the polarizability of the molecule, the intensity of the source, and the concentration of the active group, as described in the Equation 5.

$$I = K I_L \alpha^2 \nu^4$$

Equation 5. Intensity of the Raman scattering.⁷⁸

Where I is the Raman intensity, K a constant, I_L is the power of the laser, α is the polarizability and ν the frequency. It is evident from Equation 5 that the intensity of the Raman signal can be improved by using a shorter excitation wavelength, which has a higher frequency but this can lead to issues with burning of the sample or decomposition of the analyte.⁷⁹

When the frequency of the laser beam is close to the frequency of an electron transition on the molecule that is analysed, a signal enhancement of the order of $10^3 - 10^4$ can be observed.⁸⁰ This enhancement is called resonance Raman scattering (RRS) and it makes Raman spectroscopy a much more sensitive and selective technique. In RRS the molecule is promoted to the excited electronic state instead of to a virtual state as happens with the non-resonance Raman scattering (Figure 6). An example of an RRS is the analysis of malachite green (absorption maximum ~ 600 nm) with a 633 nm excitation laser. Figure 6 shows that RRS is in competition with fluorescence phenomena therefore Raman spectra can be obscured by the fluorescence background.⁸¹ The use of metallic NPs in combination with Raman spectroscopy can overcome to these issues. This technique is called surface-

enhanced Raman scattering (SERS) and it is the most common enhanced technique used to increase the Raman scattering intensity. SERS is based on the adsorption of the analyte onto roughened metal surface and it will be described in the next section.

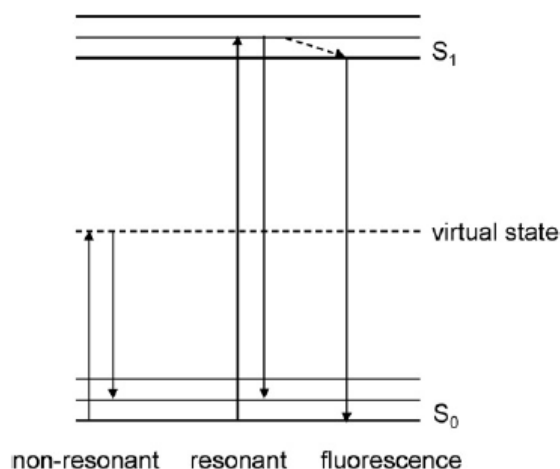


Figure 6. Jablonski diagram representing the comparison between non-resonant Raman scattering (first from the left), resonant Raman scattering and fluorescence. S_1 represents the excited electronic states and S_0 represents the ground electronic state with vibrational levels. Image reprinted with permission from Ariese F. et al., Achievements in resonance Raman spectroscopy review of a technique with a distinct analytical chemistry potential. *Analytica Chimica Acta*. Copyright © 2007 Elsevier B.V.

1.2.2. Surface-Enhanced Raman Scattering (SERS) and Surface-Enhanced Resonance Raman Scattering (SERRS)

SERS has become a mature vibrational spectroscopy technique during the last decades and the number of applications in the chemical, material, and in particular life science is rapidly increasing.⁸² The history of the technique begins in 1974, when Fleischman and co-workers first observed the increase in Raman scattering of adsorbed molecules of pyridine on a roughened silver electrode.⁸³ In order to explain the origin of this enhancement, two separate theories were proposed by independent groups: the electromagnetic enhancement by Jeanmaire and Van Duyne, and the charge transfer by Albrecht and Creighton.^{84,85} Both theories agreed that the effect was due to the electromagnetic interaction of light with the surface of metal as well as the analyte.⁸⁶ They also estimated that magnitude of Raman enhancement due to the presence of metal surface was of the order of 10^6 but recent works suggested enhancement factors as large as 10^{14} .^{80,87} In the electromagnetic enhancement, the analyte is adsorbed onto or is held in close proximity of the metallic surface where electrons from the conduction band are free to move, forming an electric field - i.e. for

metallic NPs the electric field is the LSPR. The electrons in the molecule adsorbed on the surface interact with this field causing greater polarization around the molecule, which increases its Raman scattering. The charge transfer mechanism involves instead the formation of a chemical bond between the analyte and atoms of the metal surface.⁸⁰ According to this theory, Raman scattering will be increased due to electron transfer between the metal and analyte. Only the first layer of the attached molecules can undergo the effect. The most commonly used substrates for SERS experiments are metallic NPs as they have favourable optical properties to sustain good plasmon resonance in the visible/near IR area.⁸⁶

The two theories are now tending to get merged and most researchers agreed that both contributions are causing the enhancement of the Raman scattering. In order to combine the two theories and also taking into account the enhancement due to the molecule itself, Lombardi and co-workers published in 2009 a “unified view of SERS”.⁸⁸ In this study, they formulate a single equation that includes three contributions to the Raman enhancement: (i) the surface plasmon resonance of metallic NPs (from electromagnetic enhancement theory), (ii) a charge transfer resonance involving transfer of electrons between the molecule and the conduction band of the metal and (iii) resonance within the molecule itself. The latter contribution is the RRS that was described in the previous paragraph. In order to understand the degree of contribution from each effect, Lombardi and co-workers provided a systematic approach to the experimental determination of these three effects by combining resonances data of crystal violet molecules absorbed on AgNPs (Figure 7).

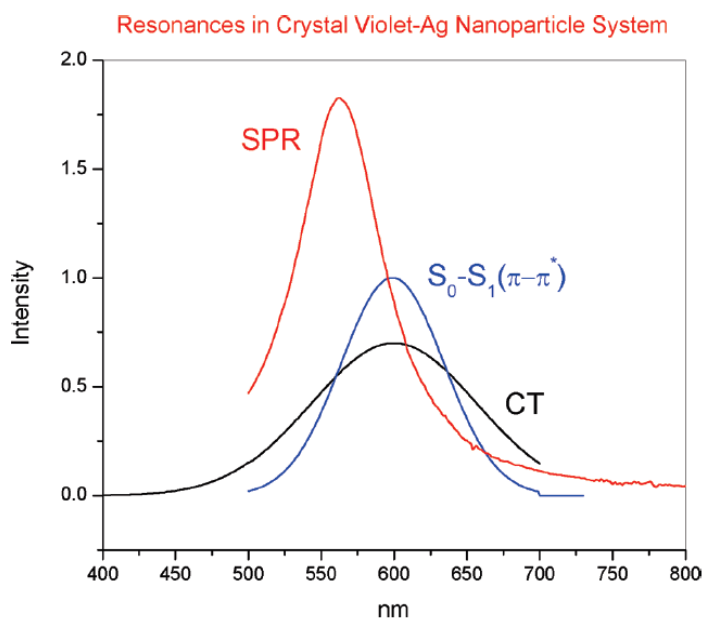


Figure 7. Various resonances of crystal violet adsorbed onto AgNPs. The red plot (SPR) indicates the resonance from electromagnetic enhancement contribution; the blue plot [$S_0-S_1(\pi-\pi^*)$] is the absorbance of crystal violet which indicated the resonance from the molecule itself (RRS) and the black plot represents the charge transfer (CT) contribution which derives from the formation of a charge transfer complex Ag-crystal violet.⁸⁸ Reprinted with permission from Lombardi, J.R. and R.L. Birke, A Unified View of Surface-Enhanced Raman Scattering. Accounts of Chemical Research. Copyright © 2009, American Chemical Society

The graph in Figure 7 shows the observed resonances in the system crystal violet-AgNPs. The surface plasmon resonance (SPR, red plot), which is due to the AgNPs, overlaps at high intensity with the absorbance of the crystal violet (blue plot) at 575 nm. Therefore, if the system crystal violet-AgNPs is excited by a laser with the same wavelength, a strong enhancement is observed. Moreover, the charge transfer resonance (black plot) overlaps with the SPR at circa 600 nm so another enhancement can be observed if the laser has a similar excitation wavelength. The unified theory predicts the possibility of one, two or three resonances simultaneously, depending on the metallic and molecular parameters.⁸⁸ The magnitude of the enhancements, the relative contributions and appearance of the SERS spectra depends crucially on the excitation laser and on the type, size and shape of NPs. In particular, for non-spherical NPs the enhancement is also due to a non-resonant lightning-rod or hot-spot effect.⁶³ A molecule situated in the vicinity of surface protrusions and sharp points will experience an enhanced localised electromagnetic field.⁸⁹ Also these spots can act as preferred binding site for the molecule adsorbed onto the metallic surface. Enhancement due to the hot-spot effect was found to be of the order of $10^4 - 10^5$.⁹⁰ As Lombardi reports, the enhancement due to the combination of laser wavelength with the molecule and the SPR

band is important and this is commonly known as Surface-Enhanced Resonance Raman Scattering (SERRS). The SERRS phenomena was first observed by Stacy and Van Duyne in 1983 and it occurs when the analyte has a chromophore that is close in energy to the frequency of the excitation laser.⁹¹ The enhancement was found out to be of the order of 10^{13} - 10^{14} over normal Raman scattering.⁹² As seen in the previous section, Raman scattering of a chromophore can be masked by fluorescence phenomena. One the main advantages of the SERRS technique is that the fluorescence is here quenched by the metal surface, resulting in much more defined spectra. The use of SERRS in bioanalysis has also an advantage over fluorescence and chemiluminescence based techniques as they do not provide with characteristic structural information of the biomolecule and often show broad emission spectra.¹⁰ SERS and SERRS show the advantage of sensitivity and when possible multiplexed detection as they give sharp fingerprint spectra compared to fluorescence.⁹³

Recent advances have led to many novel applications of SERS for biological analyses, resulting in new insights for biochemistry and molecular biology, the detection of biological warfare agents, and medical diagnostics for cancer, diabetes, and other diseases.⁹⁴ In particular, the combination of molecules that give strong Raman scattering with functionalised NPs has led to the development of several analytical methods for the detection of biomolecules such as proteins or DNA in a fast, efficient and sensitive manner.^{95,96} An example of multiplex detection of DNA by SERRS is given by the work of K. Faulds et al.⁹⁷ They were able to detect six different DNA sequences, corresponding to different strains of the *Escherichia coli* bacterium, by using oligonucleotide-functionalised AgNPs that were labelled with different commercially available Raman dyes. SERS techniques have been used inside living cells in order to gain information about the internal structure and dynamic processes occurring in the intracellular matrix.⁹⁸ Also, native proteins can be multiplex detected with SERS by monitoring the enhancement boost gained from using functionalised AgNPs.⁹⁹ This therefore provided a label free, quantitative identification of proteins and further demonstrated the method could be extended for label-free multiplexing analysis of protein mixtures. Finally, SERS and SERRS have been recently applied in combination with paper-based immunoassays, in order to increase their sensitivity.¹⁰⁰⁻¹⁰² In particular, the application of SERS and SERRS as signal readout of lateral flow immunoassay will be discussed in depth in this thesis.

1.3. Antibody-Conjugated Nanoparticles

Understanding the interactions of nanomaterials with biomolecules is a critical goal in nanoscience. Biomolecules include large macromolecules such as proteins, carbohydrates, lipids and polynucleotide, as well as small molecules such as primary or secondary metabolites and natural products. The conjugation of biomolecules onto inorganic nanostructures can create hybrid materials that have more beneficial properties over the base units. One of these properties is the ability to generate a measurable signal from a specific interaction of these materials with external molecules. This process is the foundation of a nanosensor. Also biomolecules can be exploited for the functionalization or spatial assembly of NPs.³² Amongst biological moieties that can be conjugated to the NPs, there are peptides and proteins such as BSA, antibodies, lectins, polysaccharides, phospholipids, polynucleotides and aptamers.¹⁰³⁻¹⁰⁸ In order to create biomolecule functionalised NPs, it is important to understand the chemistries at the interface of inorganic surface and biological moieties. Generally, interactions at the interface between biomolecules and inorganic nanostructures can be divided into four classes:³²

- ligand-like binding to the surface of the inorganic particle core, commonly by chemisorption of thiol groups;
- electrostatic adsorption of positively charged biomolecules to negatively charged NPs or vice versa;
- covalent binding by conjugation chemistry, exploiting functional groups on both particle and biomolecules;
- non-covalent binding such as affinity-based receptor-ligand systems (i.e. avidin-biotin interaction).

For the aim of this thesis only interaction between antibodies and NPs are discussed in this section. Antibody structure, conjugation methods and applications of antibody-conjugated NPs are also described.

1.3.1. Antibody molecule

An antibody (Ab), also known as immunoglobulin (Ig), is a glycoprotein produced by plasma cells in response to the presence of foreign objects in the body.¹⁰⁹ Abs are important for the immune system as they identify and neutralise the foreign objects, called antigens (viruses, bacteria, parasites, toxins, etc.), by selectively capturing and removing the antigen via

phagocytosis. The antibody-antigen binding is very specific, strong and it is based on supramolecular interactions such as hydrogen bonding, hydrophobic forces, van der Waals forces, π - π interactions and electrostatic effects.¹¹⁰ As with all proteins, Abs are formed by polypeptide chains which are made of amino acid units. These units are covalently bound by an amide bond and contain various functional groups that can be either hydrophobic or hydrophilic in nature. Structurally, Abs are composed of one or more copies of a characteristic element that can be visualised as forming a “Y” shape.¹⁰⁹ Each Y-shaped structure is formed of four polypeptide chains and it is known as immunoglobulin G (IgG) (Figure 8).

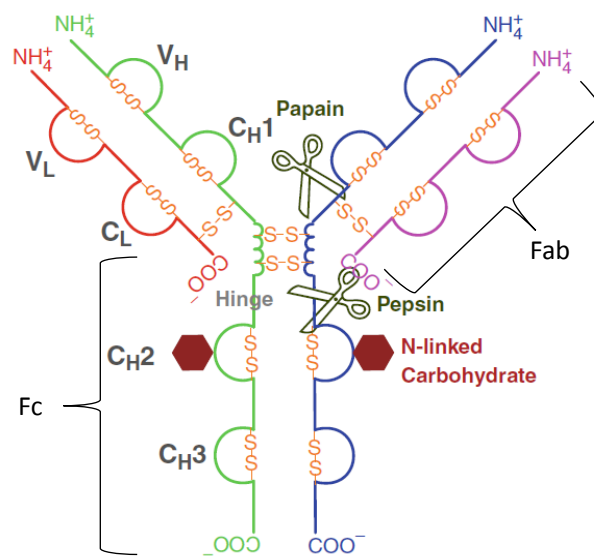


Figure 8. Structure of an antibody IgG, the archetypical immunoglobulin. It consists of 4 polypeptide chains: 2 heavy (blue and green) and 2 light (purple and red) that are connected each other's by disulphide bonds. Each chain are formed of two types of domains: variable (V_H and V_L) and constant (C_H and C_L). Constant domains are decorated with N-linked carbohydrates.¹¹¹ Scissors represent proteolytic cleavage sites by two enzymes: pepsin and papain. Pepsin can cleave IgG so that the fragment antigen-binding is dimeric (Fab₂), but the crystallisable fragment (Fc) is removed. Papain on the other hand cleaves IgG above the disulphide bonds holding the heavy chains together. This results in two independent Fab units and one Fc still intact. Reprinted with permission from Engelbert Buxbaum, Immunoproteins. Fundamentals of Protein Structure and Function, 2^o Edition ©Springer Nature 2015.

An IgG consists of two identical heavy chains (green and blue lines) connected to each other by two disulfide bonds, and two identical light chains (red and purple lines) that are bound to the heavy chains through disulfide bonds. Each chain are formed of two types of domains: variable (V_H and V_L) that are responsible for binding the antigen, and constant (C_H and C_L) that are responsible for the effector functions of the antibody and contain the carbohydrate side chains.¹¹² IgG consists of two fragments: the fragment antigen-binding (Fab) formed by V_L, C_L, V_H and C_{H1} and the fragment crystallisable region (Fc) that is formed by the tail of the

heavy chains. The Fc region is similar among the same species and interacts with specific cells allowing them to trigger an immune response by producing a complementary antibody. Two proteolytic enzymes, papain and pepsin, can attach and break the polypeptide chains at a specific point on the molecule (Figure 8). Papain cleaves IgG above the disulfide bonds holding the heavy chains together. This results in two independent Fab regions and one Fc still not dissociated. Pepsin, instead can cleave IgG so that the Fab is still dimeric, but the Fc is removed.

There are five classes of immunoglobulins in mammals: IgG, IgD, IgE (monomers), IgA (dimer) and IgM (pentamer) (Figure 9).

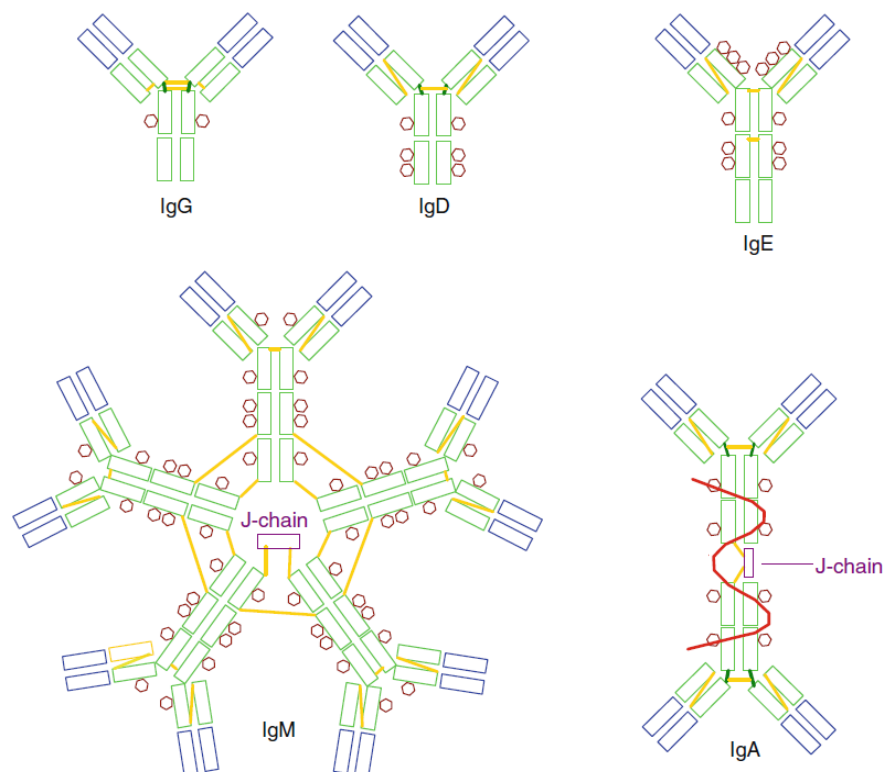


Figure 9. The 5 different immunoglobulins are composed of similar units: variable (blue) and constant (green) domains, forming heavy and light chains. These are held together by disulphide bonds (yellow). The proteins are decorated by sugar side-chains in N-glycosidic bond (purple hexagons). IgA and IgM additionally contain a small J-chain (purple), IgA also a secretion component (red).¹¹¹. Reprinted with permission from Engelbert Buxbaum, Immunoproteins. Fundamentals of Protein Structure and Function, 2^o Edition ©Springer Nature 2015.

The classification is based on the numbers of Y-shaped units and the type of heavy chain they contain. IgG is the “workhorse” of the immunosystem, since it is the isotype most commonly found in circulation and tissues. In the blood of normal adult humans, 70–75% of serum Ig is isotype G and present a molecular weight of 146 kDa on average.¹¹³ IgD is present in small

amounts and its function is primarily as an antigen receptor on B cells.¹¹⁴ IgE is the least abundant of Ig's but it is the most potent of the various Ab classes.¹¹⁵ IgE is associated with allergic reactions and IgE is known to release histamine after binding to the antigen.¹¹⁴ IgA is of special interest because of its predominance in exocrine secretions where it is thought to provide the host with a first line of immune defence against foreign microorganisms.¹¹⁶ Finally IgM is the pentameric form of IgE and it is the first Ab produced during an immune response.¹¹⁷ IgM and IgA consist of an extra joining chain, which comprises of 2 β -sheets folded against one another. The β -sheets are known to have at least 6 cysteine residues, hence the heavy chain of these antibodies are connected via disulphide bridges.¹¹⁸

Abs can be divided into two main categories: monoclonal (MAb) and polyclonal (PAb) antibodies. MAbs were discovered in 1975 when Milstein and Kohler immortalised hybrid cells (hybridomas) derived by B cells and tumour cells to produce a single type of Ab in large quantities.¹¹⁹ This discovery revolutionised many fields of bioscience, in particular diagnostics, as it has been used for antibody directed against specific targets. MAbs can be highly specific towards the antigen as they bind to one specific region (epitope) of the antigen. Often, MAbs are produce from mouse species (murine) and they can be more expensive than PABs as their production involves further biological manipulations. On the other hand, PABs are produced from the inoculation of an immunogen into the animal (mostly rabbit or goat). Blood is then extracted from the animal and Abs are purified by chromatography columns. As PABs are produced from different immune cells, they bind to various epitopes of the antigen. In the 80s, a second-generation of MAbs were produced, called recombinant antibodies.¹²⁰ They are generated *in-vitro* using synthetic genes and they do not need hybridomas and animals in the production process. They are usually expressed in *Escherichia Coli* and the ability to manipulate the antibody genes makes it possible to generate Ab fragments such as Fab or scFv (single-chain variable fragment) with the absence of the Fc region. This is an advantage over non-recombinant Abs, as Fc can cause nonspecific binding in various immunoassays which often leads to higher background, worse signal-to-noise ratio, and decreased sensitivity.¹²¹ Moreover, the conjugation of Fab or scFv fragments to other molecules provide reduced hydrophobicity and reduced steric hindrance compared to an intact IgG. Finally, generation of rec Abs enables manipulation of their sequences, for instance by linking desired amino acid units to the antibody polypeptide chains. These sequences, called also peptide tags, are mostly used for purification of Ab, but also immobilization, detection, enzymatic activities or to create multimeric-binding sites with

increased Abs functional affinity (avidity).¹²¹ A typical example of a peptide tag is the histidine tag (his-tag) which is formed of five to six histidine units. His-tags are generally used for Ab purification.¹²² Another peptide tag used for purification is the StrepII-tag, which shows affinity to streptavidin.

1.3.2. Antibody conjugation methods

The ability to conjugate an Ab to another protein, molecule or to nanostructure, such as metallic NPs, is critically important for many applications in life science research, diagnostics, and therapeutics.¹²³ Antibody conjugates are used in immunoassay techniques such as enzyme-linked immunosorbent assay (ELISA), immunoradiometric assay (IRMA) or lateral flow immunoassay (LFIA). These analytical techniques require the antibody to be conjugated to a “label” such as an enzyme, a radioactive molecule or a nanoparticle. The performance of the assay strictly depends on the functionality and availability of the Ab after it has been conjugated. Hence, it is important to choose the right antibody conjugation method to maximise the performance of the application. As the analytical technique developed in this thesis is LFIA, the methods describe here are intended for conjugation of Ab onto NPs. However, some of the methods described in this thesis are generic and can be used for general biomolecule conjugations. For detailed information about conjugation of Ab to other proteins, enzymes or small molecules, a good textbook to refer to is the *Bioconjugate Techniques, 3rd Edition* by Greg T. Hermanson. The Ab, after conjugation onto NPs, must preserve its binding activity and specificity toward the antigen. Therefore, it is necessary that the binding site of the Ab is available and well oriented to the medium. In general, immobilisation strategies should be mild as Abs can lose their activity if harsh chemicals are used for the conjugation. There are two kinds of immobilisation strategies: random and oriented (Figure 10).¹²⁴ Random immobilisation results in an Ab that is not spatially coordinated onto NPs surface and its position cannot be controlled. During random immobilisation, the antigen-binding site of the Ab could not be accessible due its proximity to the NPs surface. On the other hand, oriented strategies involves the interactions between specific groups either on the Ab or on the NPs.

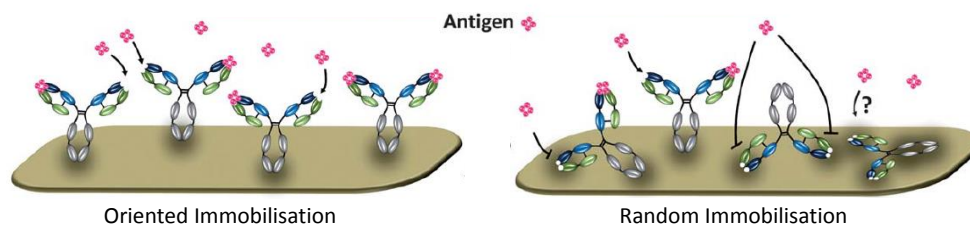


Figure 10. Schematic representation of oriented (left) and random (right) immobilisation strategies of an IgG antibody onto the NPs surface. Image reproduced from A.Trilling *et al.*, Antibody orientation on biosensor surfaces: a mini review. *Analyst*, 2013, 138, 1619.

The main functional groups of Ab that can be involved in the conjugation process are:

- Amines (N-terminus and lysine residues)
- Carboxylic acid groups (C-terminus, glutamic and aspartic acid residues)
- Thiol groups (cysteine residues)
- Carbohydrates linked on amines at the C_{H2} region of the Ab,
- Side-chain groups (i.e. imidazole).

The methods of conjugating Abs onto NPs can be classified into three main groups, depending on the nature of the interaction: covalent, non-covalent and passive.

1.3.2.1. Covalent methods

The covalent conjugation approach involves the formation of a covalent bond between functional groups on the Ab and a linker present on the surface of the NPs. The primary amine of lysine residues or the N-terminus amine groups on an Ab are able to form covalent bonds with aldehyde, ketones or carboxylic acid groups on the surface of the NPs.^{125,126} Covalent conjugation approaches may involve the use of hetero-, homobifunctional or zero length crosslinkers. Heterobifunctional linkers contain two different reactive groups that can couple to two different functional targets on the biomolecules.¹²⁷ Homobifunctional linkers consist of a symmetrical spacer (usually a carbon chain) that connect two identical reactive ends.¹²⁸ Zero length crosslinkers are the smallest available reagent systems for bioconjugation. These compounds mediate the conjugation of two molecules by forming a bond containing no additional atoms.¹²⁹ Usually, covalent conjugation methods involve the formation of an amide bond between the Ab and a linker/molecule present on the NPs surface. An example is provided by the work of Zhong *et al.*¹³⁰ where anti-vascular endothelial growth factor (VEGF) antibody were conjugated onto quantum dots via the zero length crosslinker couple carbodiimide/N-hydroxysuccinimide (EDC/NHS) (Figure 11).

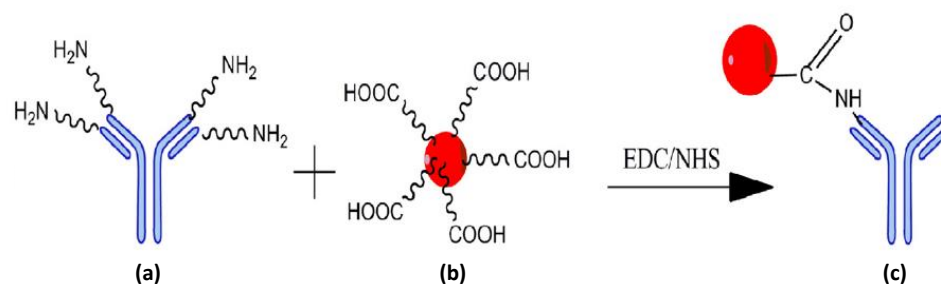


Figure 11. Schematic representation of a covalent conjugation method involving amine groups on the Ab (a) and carboxylic acid groups on the surface of a quantum dot (b). The reaction, which is mediated by the zero length crosslinker couple EDC/NHS, leads to the formation of an amide bond (c). Reprinted with permission from Lili Pang, Hongjing Cui, Yu Liu and Wenyong Zhong. Anti-VEGF antibody conjugated CdHgTe quantum dots as a fluorescent probe for imaging in living mouse. *Journal of Luminescence*, 2016. Copyright © 2016 Elsevier B.V.

Many examples of using the EDC/NHS method for conjugation of various Abs onto various nanoparticles are reported in the literature.^{131–133} Other zero length crosslinkers that are used to conjugate Abs onto NPs are: hydrazide, which reacts with the carbohydrate groups on Abs and maleimide that is able to covalently bind cysteine groups on the Ab chain by forming a thioether bond.^{123,134} The latter is often used to conjugate Abs to drugs.¹³⁵ Finally, an example of covalent conjugation that involves a heterobifunctional crosslinker is provided by the work of Loo *et al.*¹³⁶ where anti-epidermal growth factor receptor 2 (HER2) antibody was conjugated to gold nanoshells. The reaction involved the use of polyethylene glycol (PEG) that contained NHS on one terminus and a thiol group at the other terminus. Firstly, amine groups on the Ab react with the NHS group on the linker and, secondly, the Ab-PEG complex is anchored to the gold surface by gold-sulfur interaction.¹³⁷

1.3.2.2. Non-covalent methods

Non-covalent conjugations are mainly based on bioaffinity methods where interactions such as dative bonds, hydrogen bonding, hydrophobic interactions and van der Waals are present. These interactions are usually weaker than covalent bonds when considered on their own. However, in bioaffinity methods a combination of these interactions is exploited, which can result in very strong and selective binding. The bioaffinity interactions that will be described in this section are: (i) the protein A (or protein G) interaction with the Fc of Ab; (ii) the streptavidin (or avidin)-biotin system and (iii) the interaction of histidine tags with metal ion complexes.

Protein A (or protein G) have natural affinity towards the Fc region of the Abs.^{138–140} These proteins are typically used in affinity columns for Ab purification chromatography. When

protein A and G are adsorbed onto NPs, the Ab is immobilised with the antigen-binding site orientated to medium. Protein A-functionalised AuNPs have been used to visualise Ab binding to antigenic sites in cells or tissue sections (Figure 12A).¹⁴¹ An example given by the work of Hoefsmit *et al.*¹⁴² where 20 nm and 5 nm AuNPs were coated with protein A. Subsequently, MAbs were conjugated to the protein A-functionalised NPs in order to detect plasma membrane antigens in a cell line.

The streptavidin-biotin system is one of the strongest interaction known in biology.¹⁴³ Biotin is a small molecule that contain an ureido ring, that binds the streptavidin, and a carboxylic group that can used for further conjugations. Streptavidin is a 52.8 kDa protein purified from the bacterium *Streptomyces avidinii*. The conjugation methods involves the modification of an Ab with biotin (process called biotinylation) and the coating of NPs (especially gold) with streptavidin. Alike the protein A-functionalised NPs, streptavidin-functionalised NPs can be used to detect, localise or quantify the binding of biotinylated molecules in cells, tissue sections, or blots (Figure 12B).¹⁴¹ An example of the use of streptavidin-biotin interactions is given by the work of Krager *et al.*¹⁴⁴ where a biotin acceptor peptide (BAP) modified protein was conjugated in a single-step with streptavidin-functionalised AuNPs.

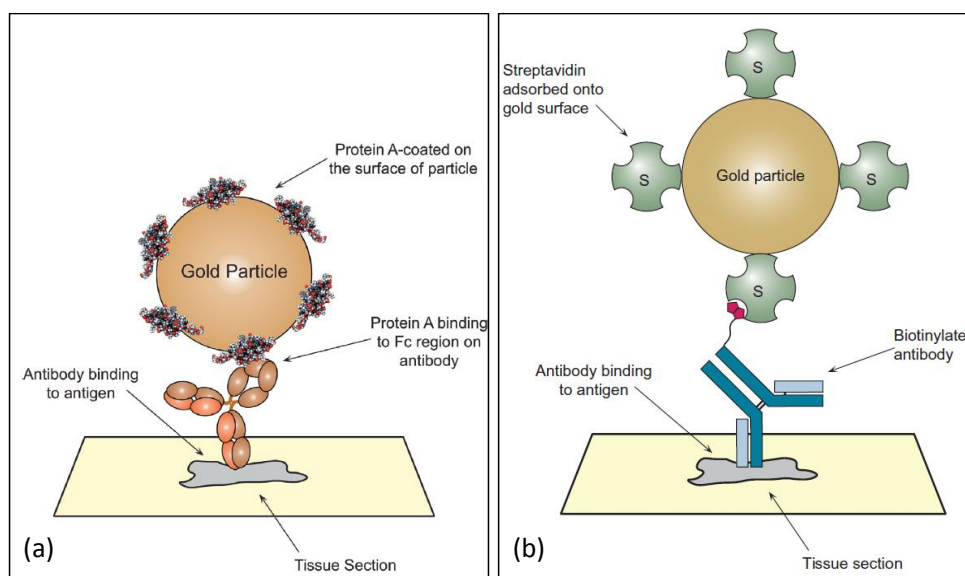


Figure 12. Schematic representation of two non-covalent conjugation methods. An antibody is conjugated to (a) Protein A-functionalised AuNPs and (b) streptavidin-functionalised AuNPs. The diagram shows that the antibodies are bound to specific antigenic determinants on a tissue section.¹⁴¹ Reprinted with permission from Hermanson G.T., Bioconjugate Techniques, Copyright © 2013 Elsevier Inc.

The last non-covalent method described here, involves the use of peptide tags, which can be fused to the N-terminus or C-terminus of a recombinant Ab.¹⁴⁵ As mentioned in Section 1.3.1

of this thesis, peptide tags are usually formed by five or six histidine units (his-tag) and the main use is Ab purification. His-tags show high affinity towards transition metal cations (Cu^{2+} , Ni^{2+} , Zn^{2+} and Co^{2+}) at around neutral pH, as the imidazole rings of the histidine form a dative bond with the metal. In protein purification, this technique is called immobilised-metal affinity chromatography (IMAC).¹⁴⁶ These ions are attached on a solid matrix by ligand molecules, i.e. nitrilotriacetic acid (NTA) or iminodiacetic acid (IDA). By modifying NPs surface with these ligands, the technique can be applied to conjugate his-tag antibodies or protein. Several articles in the last decade have been published about conjugation of his-tag proteins or enzyme onto NPs based on the IMAC principle and some of these works are discussed in Chapter 2 of this thesis. An example of Ab conjugation via his-tag is provided by the work of Nie et al.¹⁴⁷ They describe the conjugation of a single-chain (scFv) anti-EGFR antibody to quantum dots (QDs) or magnetic iron oxide NPs that were functionalised with a nickel complex of NTA. The his-tag/metal ion conjugation method can be reversible with the use of imidazole molecules that displace the Ab. This is an advantage when Ab conjugated NPs are used in systems that requires a carry/release processes or collection of Abs from cell media.

1.3.2.3. Passive adsorption

The methods described previously are based on chemical/biological interactions and external reagents, such as crosslinkers, or the pre-modification of NPs with other biomolecules (i.e. protein A or streptavidin) which are required for the Ab-NP conjugation. On the other hand, passive adsorption is a conjugation method which is mainly based on physical interactions between the NPs surface and Abs. By tuning the pH of an Ab solution, the overall electric charge of the protein can become positive. As NPs are generally negatively charged, the Abs can be adsorbed onto the NPs surface due to electrostatic interactions. Hydrophobic interactions can also be involved in the conjugation process, due to the aromatic groups on Ab side chains which have an affinity for binding to the NPs surface. Moreover, in the case of AuNPs, the Fc region of the Ab can contain cysteine residues that bind naturally to the surface through the gold-sulfur bond.^{148,149} Many examples of passive conjugation can be found in the literature as well as various online protocols.¹⁵⁰ Before proceeding with the conjugation, a pH/Ab concentration study may be necessary to evaluate the best adsorption conditions.

Choosing the right conjugation method depends on a number of factors, such as: the type of nanoparticles (gold surface, QDs, silica, etc.) and antibodies (Fab fragment or whole Abs) or the application the Ab-conjugated NPs is used for. Table 1 summarises the conjugation

methods that are reviewed in this section. Advantages and disadvantages of various conjugation methods are Ab activity, conjugate stability and complexity of the reactions, which are described below.

Table 1. Advantages and disadvantages of various conjugation methods. The “+” symbol indicates an advantage of a particular parameters for the corresponded method. Conversely, the “-” symbol indicates a disadvantage and “=” indicates that the parameter do not have any effect on the conjugation method.

Methods	Conjugation time	Antigen-binding site activity	Conjugate stability	Immobilisation strategy	Notes	Publications
EDC/NHS	-	=	+	Random or Oriented (depending on the pH)	High conjugate yield	<i>Loo et al.</i> ¹³⁶ ; <i>Liedberg et al.</i> ¹³¹
Thiol-maleimides	-	+	+	Oriented	Requires reduced antibodies	<i>Akkapeddi et al.</i> ¹³⁵
Carbohydrate	-	=	+	Oriented	Requires glycosylated antibodies	<i>Kumar et al.</i> ¹³⁴
Passive adsorption	+	-	-	Random	Requires blocking agents	<i>Jazayeri et al.</i> ¹⁵⁰
Protein G/A	+	+	=	Oriented	“Universal” method but non-specific binding	<i>Hoefsmit et al.</i> ¹⁴²
Streptavidin-biotin	=	+	+	Oriented	Requires biotinylated antibodies	<i>Krager et al.</i> ¹⁴⁴
Metal ions affinity	-	+	+	Oriented	Requires his-tag antibodies	<i>Nie et al.</i> ¹⁴⁷

Conjugation time can be relatively fast for passive adsorption and protein A/G conjugation methods where no forming of covalent bonds is required. Indeed, in either method Ab or protein are incubated with the NPs at a specific concentration and pH. These methods are recommended especially for conjugations onto AuNPs. The other methods (covalent and metal ions affinity methods) present a longer conjugation time as pre-functionalisation of the Abs or NPs is required. Regarding the activity of the Ab, it is important that the orientation of the Ab on the NPs allows binding to the antigen. Usually, all the methods listed in Table 1 except for passive adsorption, show an oriented immobilisation strategy. However, for covalent conjugation, it is important to consider the pH of the coupling reactions. For

example, if the conjugation involves reactions of amines on the Ab, then a pH lower than 8, could cause the conjugation to occur at the N-terminal amine groups located at the antigen-binding site, which could lead to partial inactivation of the Ab due to steric hindrance. A stable conjugate can be obtained by modifying the NPs surface with amphiphilic ligands that prevent NPs from coagulation or non-specific binding.^{104,151} Another method to stabilise Ab-conjugated NPs can be the covering of NPs surface with a silica layer.³² During passive adsorption the Ab-conjugated NPs is stabilised by adding a blocking reagent, which can be a surfactant, a polymer or a protein such as casein or albumin. The main function of the blocking reagent is to cover any unreacted metallic surface that could non-specifically interacts with other biomolecules. Careful consideration should be taken to choose any protein-based blocking reagent, as false positives may occur. For examples, if Ab-conjugated NPs are used for the detection of bovine serum albumin (BSA), this protein cannot be used as a blocking reagent.

1.3.3. Applications of antibody-conjugated nanoparticles

Advances in biotechnology has provided researchers with highly selective Abs, which has expanded the use of Ab-conjugated NPs in several scientific fields. The main field of science where these hybrid materials have been developed is the biomedical field. In particular, the applications can be divided into two main groups: therapy and diagnosis, as shown in Figure 13.

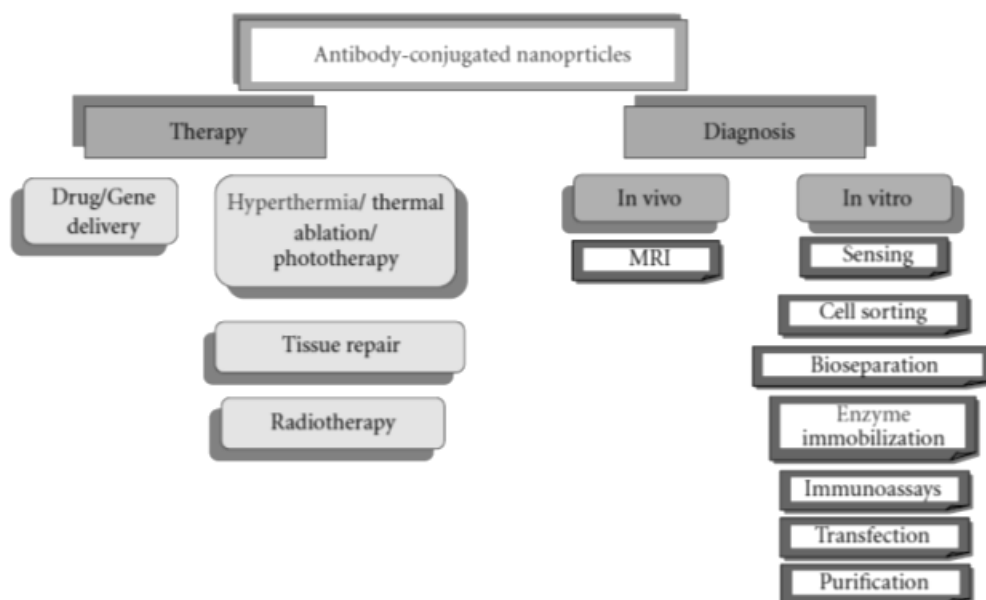


Figure 13. General scheme of the different biomedical applications for antibody-conjugated nanoparticles.¹⁵²

1.3.3.1. Therapy

Therapeutic applications mainly concern the treatment of cancer and cardiovascular diseases, but also inflammatory diseases, infectious diseases and thrombosis.^{153–155} By combining the biological recognition of MAbs and the physical properties of NPs, Ab-conjugated NPs offer great opportunities in the delivery of drugs directly to diseased sites which increases the therapeutic index whilst minimizing off-target side effects.¹⁵⁵ To achieve this, hollow-interior nanocapsules filled with the drug of interest are best candidates for drug delivery applications.¹⁵⁶ Several examples of use of Ab-conjugated NPs for drug delivery can be found in the literature.¹⁵² Tyner et al. reported a system of delivering poorly water-soluble drugs, such as camptothecin, to glioma cells by encapsulating the drug on magnesium–aluminium NPs that were conjugated to specific antibodies.¹⁵⁷ Along with drug delivery, gene delivery, tissue repair, magnetic hyperthermia and photothermal therapies are the main potential therapeutic applications for Ab-conjugated NPs.^{158–162} These applications have in common the selective delivery of a therapeutic carrier that causes the death of malignant cells, the expression of a specific protein or the activation of others, without affecting the surrounding healthy tissues.

1.3.3.2. Diagnosis

In diagnosis, the main applications for Ab-conjugated NPs are cell sorting, magnetic resonance imaging (MRI) and biosensing. Magnetic NPs or microspheres can be conjugated with specific Abs or biomolecules for targeting and collection of certain cells.^{163,164} Moreover, Ab-conjugated super-paramagnetic NPs, developed by Suwa et al., have been used as contrast agents for MRI.¹⁶⁵ Finally, the application that Ab conjugated NPs are more commonly used in, is the highly sensitive detection of biomarker molecules, known as biosensing. In biosensing, the Ab recognises the molecule of interest and the NPs give a physical or chemical signal. The signal that can be obtained from a biosensor could be optical, electric, magnetic or based on mass variations. Like any other sensor, a biosensor has the potential to be cheap, compact, selective, sensitive, portable, reusable, and have a fast readout. A biosensor that contains an Ab as receptor unit is called an immunosensor. Immunosensors are considered to be miniaturised devices, integrating high specificity and selectivity of immunological assays with the accuracy and sensitivity of detection techniques.¹⁶⁶ Utilising these advantages of immunosensors with the capabilities of NPs is a very active and interesting area of research. For the aim of this thesis, examples of biosensors

for diagnosis of diseases/conditions are described below. However, Ab-conjugated NPs can be engaged in various area of research such as environmental monitoring and food safety.^{167,168} Amongst optical biosensors, an example is provided by Tsourkas *et al.* which designed magnetic NPs for diagnosis of inflammatory diseases at early stages by the identification of vascular cell adhesion molecule-1 (VCAM-1) expression on endothelial cells. In this work, functionalised NPs containing anti-VCAM-1 antibodies were able to detect VCAM-1 expression using fluorescence confocal imaging and magnetic resonance imaging in cell culture and in vivo.¹⁶⁹ Moreover, Hirsch *et al.* described the use of Ab-conjugated NPs to detect proteins in saline, serum and whole blood by using near-IR spectroscopy with a sensibility of up to sub-nanogram/mL.¹⁷⁰ Au-coated AgNPs covalently attached to goat anti-mouse IgG and to Raman reporter, were used in biosensing applications by employing SERS.¹⁷¹ Other applications which exploit the properties of Ab-conjugated NPs are cantilevers, quartz crystal microbalances and electrochemical immunosensors.^{172–174} Finally, Au-conjugated NPs are essential for paper based biosensors such as lateral flow devices, which will be discussed in depth in Section 1.4.

1.4. The Lateral Flow Assay

Lateral flow assay (LFA) is a rapid analytical technique that consists of prefabricated strips of a carrier material, usually membranes produced from nitrocellulose, nylon, polyethersulfone, polyethylene or fused silica.¹⁷⁵ The membrane contains reagents that are activated by applying the fluid sample. When the recognition element is formed by antibodies, the technique is called lateral flow immunoassay (LFIA). Ab-conjugated AuNPs are widely used in LFIA, since their strong red colour makes them the ideal choice for optical detection. The technique is especially designed for single use at the point-of-care (PoC) – i.e. outside the laboratory. Over the last few decades, commercially available rapid diagnostic strips have emerged. In particular, the human pregnancy test was one of the first LFIA to be commercialised.¹⁷⁶ It was derived from the development of human chorionic gonadotropin (hCG) beta-subunit radioimmunoassay.¹⁷⁷ Nowadays, commercial tests based on LFA are available for many applications such as: clinical diagnostics, veterinary, food safety, agriculture, environmental monitoring, military defence and drug abuse. Details of these examples can be found in many reviews.^{178–180} LFIAs are usually designed to produce an ON/OFF response, i.e. qualitative assay. The results of an LFA are usually produced in a few minutes. Standard lateral flow devices are fabricated in two separated parts: a paper strip that is supported by a backing card, and a plastic housing (or cassette) in which the strip is enclosed Figure 14.

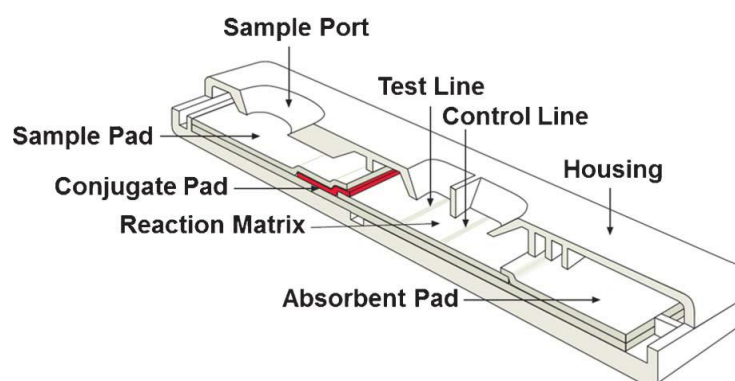


Figure 14. Schematic view of typical lateral flow device.¹⁸¹

The strip is normally subdivided into four sections: sample pad (SP), conjugate pad (CP), absorbent pad (AP) and the reaction matrix (RM) which is usually a nitrocellulose membrane (NC). The fluid sample, which is usually diluted in a buffered solution (running buffer), is applied into the SP which is exposed by a sample port. The CP contains the Ab-conjugated

NPs that react with the sample and migrate through the RM. The immobilised analyte-conjugate (in competitive assay) or the analyte-specific Ab (in sandwich assay) is found in the RM, which constitutes the test line (TL). The majority of the devices also contain a control line (CL) that verifies the functionality of the assay. The CL is usually formed by secondary Abs that bind the antibody present on the Ab-conjugated NPs. Finally, the AP serves to accumulate the excess sample or unreacted Ab-conjugated NPs and it is fundamental for the capillary flow of the sample through the strip. Figure 15 describes the difference in layout and signal generation between two different formats of LFIA: competitive assay (a) and sandwich assay (b). In competitive assays, Ab-conjugated NPs bind to the TL in the absence of analyte to produce a stable signal. Any analyte present on the sample will bind to the Ab-conjugated NPs, thereby hindering the NPs ability to bind to the TL, which decreases the intensity of the signal. Conversely, in sandwich assays, the signal on the TL increases directly with the analyte concentration. Sandwich assays are typically used when testing for larger analytes with multiple antigenic sites, while competitive assays are typically used for the detection of small molecules.

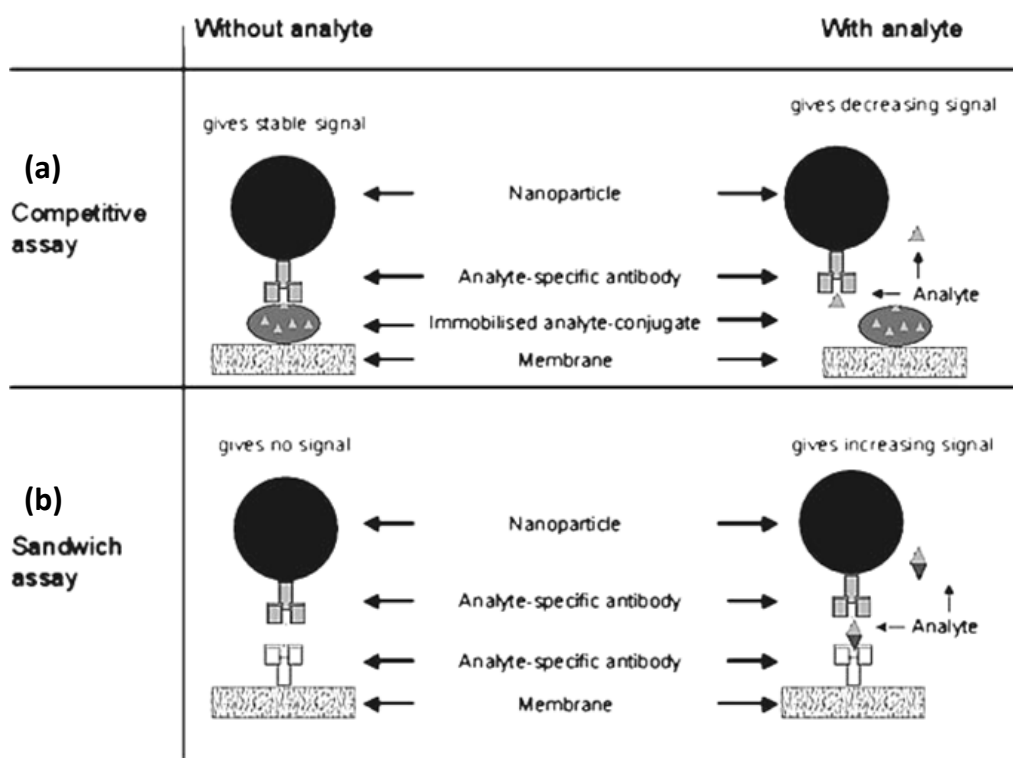


Figure 15. Difference in layout and signal generation between (a) competitive and (b) sandwich LFIA. In the (competitive assay the response is negatively correlated to the amount of analyte in the sample. In the sandwich assay the response is directly proportional to the amount of analyte in the sample.¹⁷⁵ Image reproduced from Posthuma-Trumpie et al., "Lateral flow (immuno) assay: its strengths, weaknesses, opportunities and threats. A literature survey". Analytical and Bioanalytical Chemistry. Copyright © 2008, Springer Nature.

LF devices show several advantages over traditional techniques, which can be summarised using the “ASSURED” acronym: affordable, sensitive, specific, user-friendly, rapid and robust, equipment free and deliverable to end-users.¹⁸² The World Health organisation (WHO) defined this criterion to be crucial for paper-based devices, such as LF. On the other hand, the disadvantages of LFAs include performance limitations, most notably sensitivity, reproducibility and difficulty of multiplexing.¹⁸³ Also, test-to-test variations have prevented quantitative LFAs to compete with larger or more complex clinical analysers.¹⁸³ Recently, progress has been made to overcome these limitations. In the following section, advancements in LFAs are described. Novel nanomaterials, readout systems and signal amplification techniques that can allow sensitive analyte detection and quantification are discussed.

1.4.1. Improving sensitivity in lateral flow

Traditionally, signals from LF devices are detected by the naked-eye. This method of interpretation brings issues of subjectivity into play and makes it virtually impossible to develop quantitative systems.¹⁸⁴ In order to overcome these issues, optical readers are often used as signal readout. Numerous readers are commercially available that can help overcome the issue of user-to-user differences in visually interpreting line colours and also help to improve the sensitivity of the LFA.¹⁷⁵ Multiple optics format is also available such as colorimetric and fluorescent systems.¹⁸⁴ Producing an image of the test and control line of a LF strip is important for a number of reasons, including medical records and law enforcement.¹⁸⁴ Optical readers can be handheld or benchtop systems such as flatbed scanners, but in the last few years, the use of smartphones for analysing LF strips has been rapidly increasing.^{185–187} In order to integrate the LF device to the mobile camera, personalised cartridges and accessories have been developed.¹⁸⁸ For example, Roda *et al.* developed a smartphone-based LFA for the detection of cortisol in saliva by the fabrication of a 3D-printed cartridge and adaptor (Figure 16).¹⁸⁹

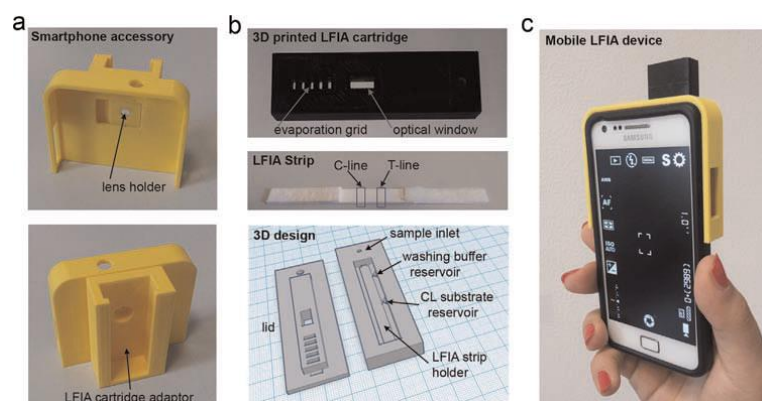


Figure 16. Smartphone accessories for LF signal readout. (a) Smartphone adaptor. (b) 3D-printed cartridge, and strip design. (c) Integrated smartphone-based LF device.¹⁸⁹ Reprinted with permission from Zangheri et al 'A simple and compact smartphone accessory for quantitative chemiluminescence-based lateral flow immunoassay for salivary cortisol detection'. Copyright © 2015 Elsevier Inc.

Smartphone-based LFA could find application in the growing area of home-self-diagnostic device technology for clinical biomarker monitoring.¹⁸⁷ Other handheld devices that are able to analyse LF strips can be found in the literature.¹⁹⁰ These devices are able to transmit the LFA results via Wi-Fi or Bluetooth to a mobile phone.¹⁹¹ The remote detection is fundamental when the test involves high-infectious diseases or difficulties in reaching the samples.

In addition to using an optical reader-based test, the sensitivity of a LFA can be improved by choosing the right materials for building a LF device. The nature of the conjugate pad has an effect on release of labelled conjugate and, therefore, the sensitivity. The wicking rate of the NC and the methods by which the bioreagents are dispensed, dried or blocked play an important role in improving sensitivity of the assay.¹⁷⁸ Moreover, the optimisation of the assay parameters, such as the antibody conjugation method, or pH and composition of the running buffer is a crucial factor for achieving a good level of sensitivity. An interesting piece of research, performed by Tang *et al.* showed that the sensitivity of a LFA could be improved by using different materials integrated into the building of the strip.¹⁹² In this work, a traditional LF strip was modified by inserting a sponge shunt between the CP and the NC. A 10-fold signal enhancement was achieved using the modified strip compared to the unmodified LF test strip. In the last few decades, several research papers have been published using alternative signal readout methods based on thermal contrast, electrochemical, colorimetric, fluorescence and SERS. Some of these works are described below. Wang *et al.* developed a readout system based on thermal contrast amplification (TCA) using Ab-conjugated AuNPs of various size particles.¹⁹³ In this method, TIs were hit with a laser and analysed using an infrared heat sensor showing that the TCA reader could

provide enhanced sensitivity over visual detection or by an optical reader. Many examples of LF signal amplifications by electrochemical detection can be found in a review published by Liu *et al.*¹⁹⁴ In general, electrochemical detection methods with LFA use an Ab conjugated to an electroactive species. After the test is complete, the test zone is cut off and placed in an electrochemical cell for quantitative analysis.

The two methods described above use expensive or non-user-friendly instrumentation and also require trained personnel to perform the analysis. However, signal amplification methods based on colorimetric detection demonstrate the affordable and easy to use way of maximising sensitivity in LFA. For example, Choi *et al.* developed a simple method for signal amplification by adding a second NP-Ab conjugate to a sandwich format LFIA for the detection of troponin I.¹⁹⁵ In this work, AuNP-anti-troponin I conjugate, blocked with BSA, was used as first conjugate and a AuNPs-anti-BSA conjugate, blocked with human serum albumin, as a second conjugate. In this way, in a positive test, the antigen is captured in a sandwich format between the Ab on the TL and the 1st AuNP-Ab conjugate blocked with BSA. Subsequently, the 2nd AuNP-Ab conjugate that contains anti-BSA antibodies binds to the 1st AuNP-Ab conjugate, to give a more intense signal. A schematic representation of the technique used in this work, is shown in Figure 17.

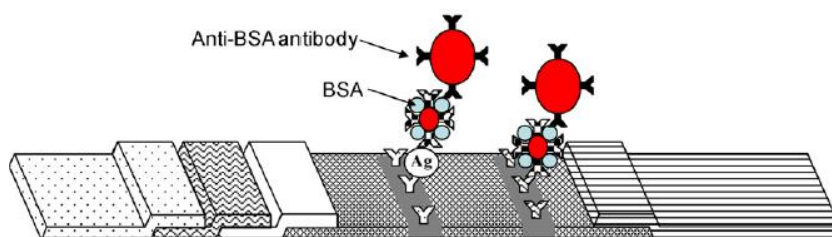


Figure 17. Schematic illustration of a dual AuNP conjugate-based sandwich LFIA. The antigen (Ag) is captured between the antibody on the test line and the 1st Ab-gold conjugate which in turns binds the 2nd Ab-gold conjugate that contain anti-BSA antibody.¹⁹⁵ Reprinted with permission from Choi *et al.* 'A dual gold nanoparticle conjugate-based lateral flow assay (LFA) method for the analysis of troponin I'. Copyright © 2010 Elsevier Inc.

Choi *et al.* claim that using the “dual conjugate” method, the assay sensitivity is increased about 100-folds compared to the conventional LFA. A similar method is described by the work of Tanaka *et al.* which used a dual AuNPs conjugates for the detection of hCG and prostate specific antigen (PSA).¹⁹⁶ Also, the work of Wey *et al.* used AuNP-coated silver conjugates for the detection of abrin-a (a toxic plant protein).¹⁹⁷ Another interesting piece of work that used colorimetric amplification was reported by Duan *et al.*¹⁹⁸ By using Fe₃O₄ magnetic nanoparticle (MNP) conjugated Abs, Duan *et al.* developed a MNP-based LF strip

which was able to detect the glycoprotein of Ebola virus as low as 1 ng/mL, which is 100-fold more sensitive than a LF strip that used AuNP conjugated Abs. MNP showed catalytic properties, so peroxidase chromogenic substrates, such as tetramethylbenzidine (TMB) were used with the LF test to produce a pigmented product that amplifies the intensity of the TL (Figure 18).

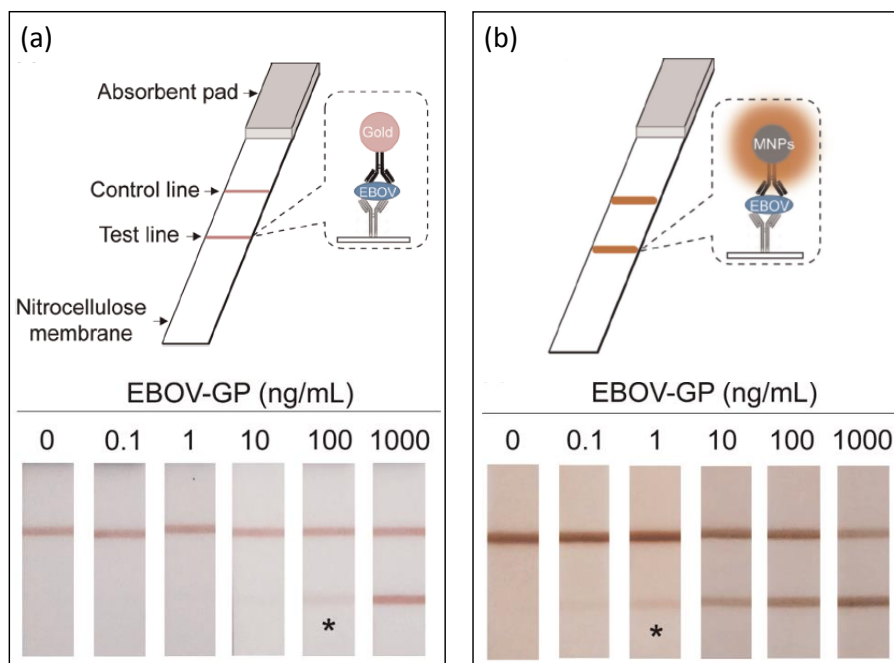


Figure 18. Comparison of AuNPs (a) and catalytic active MNPs-based (b) LFIA for the detection of Ebola virus. The LFIA with MNPs generates a colour reaction with substrates, which significantly enhances the signal so that it can be visualized by the naked-eye. The asterisk (*) indicates the limit of visual detection.¹⁹⁸ Reprinted with permission from Duan et al 'Nanozyme-strip for rapid local diagnosis of Ebola'. Copyright © 2015 Elsevier Inc.

Amplification methods based on fluorescence have also been reported in the last few years.¹⁹⁹ Mainly, fluorescent quantum dots (QDs) have been used to conjugate Abs for LFA, thanks to their high fluorescence quantum yield. Lin *et al.* developed a LF test for the detection of ceruloplasmin, a biomarker for cardiovascular disease or cancer, by using commercially available Qdot[®] nanocrystals and a portable fluorescence strip reader.²⁰⁰ Also, C-reactive protein (CRP), a biomarker that will be discussed in more details in Chapter 3 of this thesis, has been detected using Ab conjugated QDs encapsulated within a polystyrene/acrylamide shell and a fluorescence spectrometer for signal readout.²⁰¹ QDs have also been conjugated to DNA aptamers for the detection of foodborne pathogens in LFA. A 10-fold improvement in the limit of detection was achieved when compared to AuNPs-based LFA.²⁰² Despite the improvement in sensitivity, the amplification of the LF signal by using QDs is not straightforward because, in many cases, the user can only see the LF lines

using a fluorescence reader. Also, covalent conjugation methods are usually required to functionalise the QDs surface with antibodies or aptamers, which increases assay development time and costs. Fluorescence-based LFA that do not use QDs can be found in the literature.¹⁹⁹ For example, Wei-Hua Lai *et al.* reported a comparison of Europium III doped polystyrene nanobeads, fluorescein submicrospheres, QDs and AuNPs as labels in LF for the detection of ractopamine.²⁰³ The authors concluded that by using Eu (III) nanobeads, a lower limit of detection could be achieved. Another interesting material used as a reporter in LFAs is persistent luminescence nanoparticles (PLNPs). PLNPs offer advantages over the conventional photoluminescent probes as signals can be detected by using time-resolved spectroscopy that leads to lower backgrounds and higher sensitivity.²⁰⁴ In this work, Willson *et al.* used PLNPs and AuNPs conjugated to avidin to detect biotinylated hen egg lysozyme (bHEL). Figure 19 shows, the comparison in LF signal between the two different conjugates, showing that PLNPs improved the sensitivity 100 times.

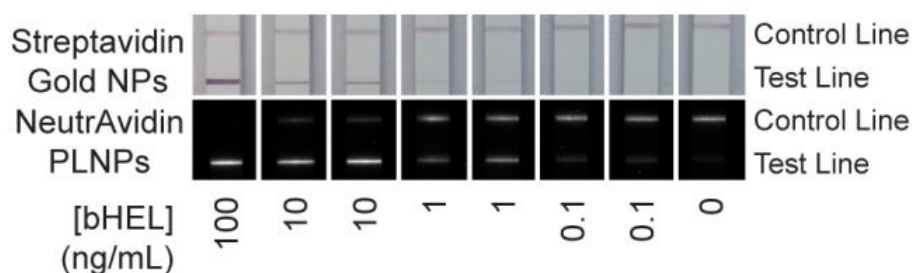


Figure 19. Pictures of the reaction matrix compartment of LF strips showing lysozyme (bHEL) serial dilutions with duplicates. Visual detection by Streptavidin-conjugated AuNPs is shown on top and luminescence detection by NeutrAvidin-conjugated PLNPs is shown at bottom.²⁰⁴ Image reproduced from Willson et al. "Persistent Luminescence Strontium Aluminate Nanoparticles as Reporters in Lateral Flow Assay" *Analytical Chemistry*, 2014. Copyright © 2014 American Chemical Society.

In the last few years, a number of immunoassay applications, which use surface enhanced Raman spectroscopy as detection method, have been developed to improve their sensitivity.²⁰⁵ As described in Section 1.2.2 of this thesis, the Raman scattering from a Raman reporter molecule (RRM) is enhanced when it is in close proximity to a metal surface, producing a unique SERS spectrum. Therefore, by incorporating RRM in Ab-conjugated metallic NPs, the LF signal can be analysed by SERS for quantitative detection of specific targets. Hwang, Lee and Choo developed a SERS-based LFIA for the detection of staphylococcal enterotoxin B by using hollow gold nanospheres (HGN) conjugated to Abs and malachite green isothiocyanate (MGITC).¹⁰² Figure 20 shows a comparison of a conventional and SERS-based LFA strip. With the latter, the presence of a target antigen can be identified

through a colour change in the test zone, but also highly sensitive quantitative evaluation is possible by measuring SERS signals from the test line.¹⁰²

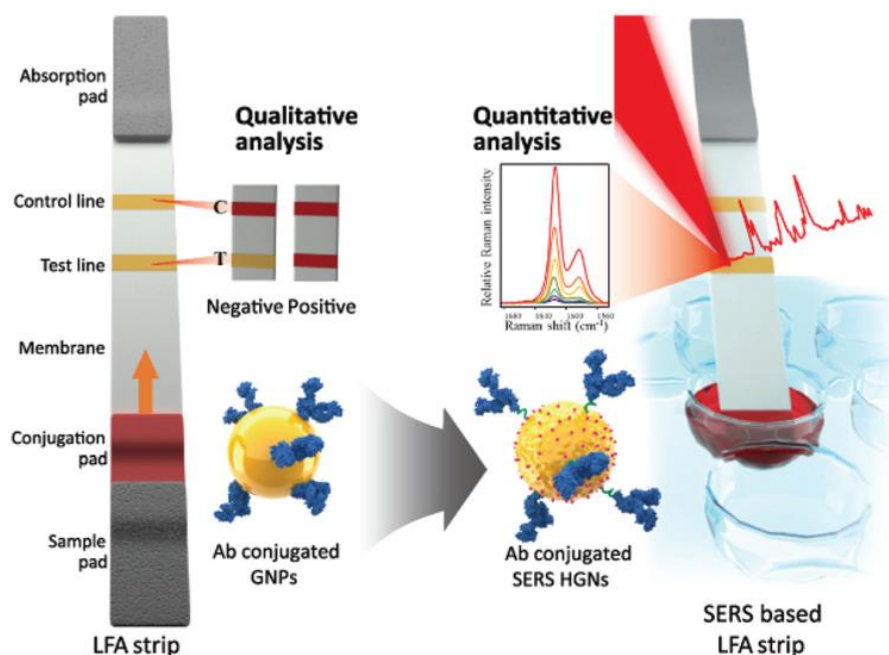


Figure 20. Schematic illustration of a conventional LF strip (left) and a SERS-based LF strip (right). Only a qualitative analysis is permitted with conventional strip, while with the SERS-based LFA strip, highly sensitive quantification of target analytes is possible by monitoring the SERS peak intensity.¹⁰² Image reproduce from Choo et al 'Application of a SERS-Based Lateral Flow Immunoassay Strip for the Rapid and Sensitive Detection of Staphylococcal Enterotoxin B'. *Nanoscale* 2015.

By combining various metal nanomaterials of different shapes and composition with RRRMs and antibodies, several SERS-based LFIA have been developed for the detection of: procalcitonin, influenza A and thyroid-stimulating hormone (TSH).^{100,206,207} Also, if the absorbance of the RRRMs is in resonance with the laser used to analyse the LF lines, a further amplification could be achieved due to the resonance Raman scattering (SERRS). This method was applied by Blanco-Covian *et al.* that showed how Au-coated silver NPs functionalised with rhodamine and antibodies could be used as labelled probes in SERRS-based LFIA for the detection of pneumolysin.²⁰⁸ By using a 532 nm excitation laser, which is in resonance with the RRRM, Blanco-Covian et al. were able to achieve a limit of detection of 1 pg/mL of target. SERS or SERRS amplification methods can also be used for the detection of DNA targets by using single stranded DNA probes instead of antibodies. Xiuli *et al.* demonstrated the use of MGITC on DNA functionalised AuNPs to detect immunodeficiency virus type 1 (HIV-1) DNA with high sensitivity.¹⁰¹ Under optimised conditions, the detection limit of the assay was 0.24 pg/mL, which was at least 1000 times more sensitive, compared to colorimetric or

fluorescence detection methods. Finally, SERS-LFA amplification methods show the advantages of multiplexing. Multiplexing capacity is critical for improving diagnostic efficiency, enhancing the diagnostic precision for specific disease and reducing cost.²⁰⁹ Wang *et al.* reported the simultaneous detection of two DNA targets with high sensitivity: Kaposi's sarcoma-associated herpesvirus (KSHV) and bacillary angiomatosis (BA).²¹⁰ However, multiplexed lateral flow biosensors that are not based on the SERS amplification method have also been developed.²⁰⁹ The availability of bench top and handheld Raman instruments in the last few decades has also provided a boost to the development of SERS-based LFA. The SERS amplification method will be discussed in Sections 3.1 and 4.1 of this thesis as they have been chosen for the detection of CRP and hCG by comparing various nanomaterials, RRMs and different Ab conjugation methods.

CHAPTER 2: Gold Nanoparticles for a Universal Conjugation Method of Histidine-Tagged Antibodies

2.1. Aims and overview

The overall aim of this chapter is to describe the creation and development of a fast and straightforward method for antibody conjugation onto gold nanoparticles (AuNPs). Various conjugation methods were discussed in Section 1.3.2 of this thesis. Antibody-gold conjugates are powerful analytical tools that are able to detect different targets. The stability and binding activity of these tools depend mainly on the interaction between AuNPs surface and polypeptide chains of the antibody. The conjugation approach used in this project is designed for any antibody that contains a poly-histidine tag (his-tag). Those tags are able to bind to metal ions and linked to a AuNPs surface via a non-covalent and reversible coordination bond. This method allows the antibody to face its antigen binding site directly to the surrounding media resulting in a more efficient antigen binding i.e. non steric hindrance. The process involves a one-step synthesis with no use of cross linker reagents or blocking agents that may interfere with the performance of the antibody-gold conjugate. In particular, the conjugation method that was investigated in this research is based on the coordination between imidazole rings that constitute the his-tag and transition metal ions such as nickel (II), cobalt (II), copper (II) and zinc (II).²¹¹ This strategy is the basis of immobilised-metal affinity chromatography (IMAC) that is widely used to purify his-tag proteins.^{145,146} In this technique, the transition metal itself is usually immobilised to a solid matrix via a chelating group such as iminodiacetic (IDA) or nitrilotriacetic acid (NTA). These metal complexes exhibit varying affinities and specificities toward histidines as shown in Figure 21.

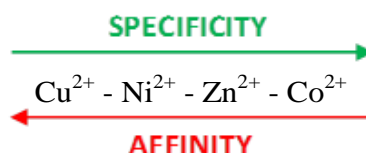


Figure 21. Specificity and affinity of transition metals towards histidines.

While nickel ions show a high affinity but low specificity, cobalt ions are more specific but with reduced binding affinity and are therefore, an option to reduce non-specific protein binding.²¹²⁻²¹⁴ Many examples on how to adapt the IMAC principle to nanoparticle systems in order to develop structures capable to bind, carry and recognise his-tag proteins have been developed in the last few decades.²¹⁵⁻²¹⁸ For example, Rotello *et al.* synthesised 5 nm AuNPs functionalised NTA that bound his-tag green fluorescence protein in the presence of NiCl₂.²¹⁹ Susumu *et al.* designed luminescent quantum dots (QDs) modified with terminal nickel-NTA capable to bind selectively maltose-binding proteins which contain 5 his-tags.²²⁰ Also, his-tag proteins can be purified by magnetism as described by Zhang *et al.* who synthesised superparamagnetic Fe₃O₄/Au NPs that contain NTA-Co (II) functions.²²¹ The bivalent cobalt ions provided a very selective docking site for histidines and the functionalised nanoparticles exhibited excellent performance in the direct separation of his-tag proteins from cell lysate. Moreover, a spectrophotometric nanosensor was developed by Wright *et al.* using AuNPs and AgNPs functionalised with a NTA-Ni (II) complex.²²² In order to develop a rapid diagnostic test for malaria, plasmodium falciparum histidine-rich Protein II was used as analyte. The colour change due to NP aggregation indicated the interaction between NTA-Ni (II) and protein.

In order to create functionalised AuNPs that contain metal ions available to coordinate the histidine tag on the antibody, it was necessary to develop an appropriate linker. The linker should be able to anchor strongly to the AuNPs surface while binding the metallic ion. For this purpose a chelating agent such as NTA was used for the development project. A CRP antibody that contains 7 histidine residues is evaluated as model target during this research. The antibody is a recombinant monoclonal Fab fragment and its biological activity, after its conjugation onto AuNPs, is assessed by lateral flow immunoassay.

2.2. Results and discussion

2.2.1. Modification of AuNPs with polyethylene glycol (PEG)

An approach to eliminate non-specific interaction between biomolecules and nanoparticles involves covering the AuNPs with poly ethylene glycol (PEG).¹⁵¹ PEG is a linear polymer consisting of repeated units of $-\text{CH}_2-\text{CH}_2-\text{O}-$, it is very soluble in water as well as in polar organic solvent such as DMSO. The reason to use PEG is because of its inertness, biocompatibility and the ability to make gold nanoparticles non-toxic (for possible in vivo applications). The possibility to form self-assembled monolayers, that can protect the nanoparticles from aggregation or non-specific binding (NSB) is another advantage of PEG molecules.²²³ PEG can be modified to contain different functional groups as a terminal component. Carboxyl-thiol (Figure 22A) and methyl-thiol (Figure 22B) PEGs were used in this project for AuNPs surface modification.

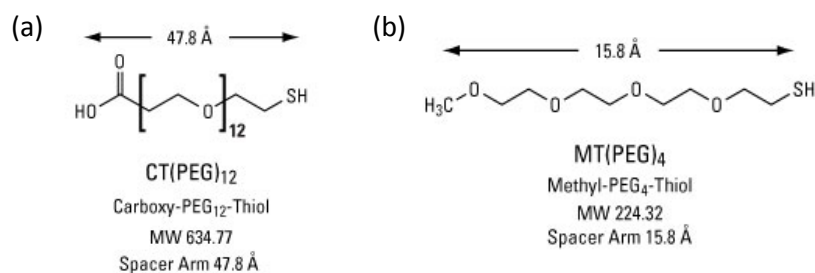


Figure 22. Chemical structure and properties of (a) carboxy-PEG₁₂-thiol (CT-PEG) and (b) methyl-PEG₄-Thiol (MT-PEG).^{224,225}

These PEG molecules contain a terminal monodentate thiol group that is able to anchor the PEGs onto the AuNPs surface, because of the strong gold-sulfur bond. The carboxylic acid group, at the CT-PEG chain terminus, allows further covalent attachments of other molecules on the AuNPs surface. The MT-PEG was used as a spacer to discourage steric hindrance between PEGs. A PEGylation method developed by Qian *et al.* was followed in this work.²²⁶ The method is based on a two steps process where AuNPs were incubated first with a solution of CT-PEG and subsequently with a MT-PEG solution that contained the same concentration of the CT-PEG. Therefore, following this methodology, commercially available monodisperse 40 nm AuNPs, which were characterised by extinction spectroscopy and dynamic light scattering (DLS) (Figure 23), were immersed in a solution containing CT-PEG and MT-PEG as described in Section 5.3.1.

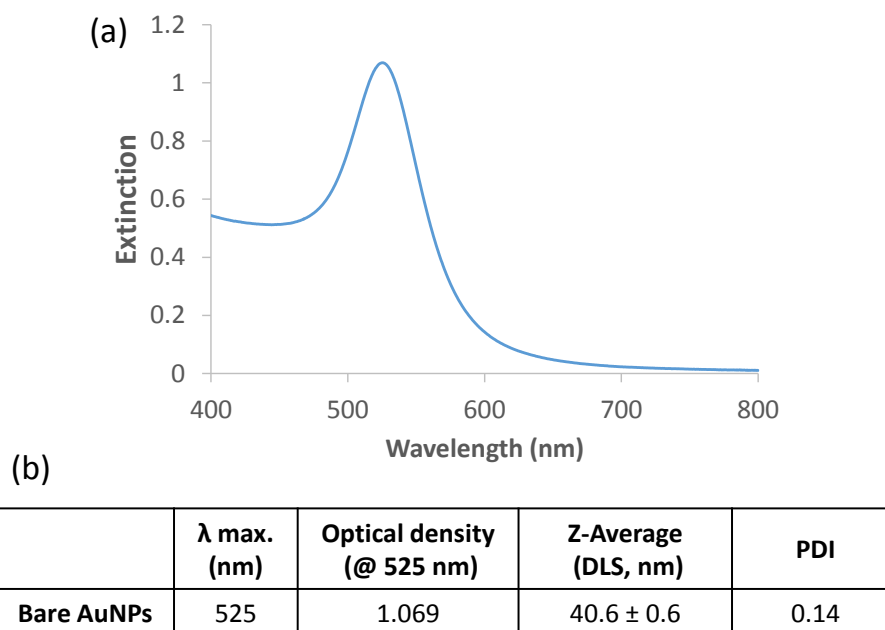


Figure 23. Extinction spectroscopy (a) and data representing LSPR, hydrodynamic diameter (Z-Average) and polydispersity index (PDI) measured by DLS (b) of commercially available 40 nm AuNPs used in this work.

In order to determine the optimal amount of PEGs for stable AuNPs and to assure a full surface coverage, a concentration study was performed. After an incubation time, the PEGs functionalised AuNPs (PEGylated AuNPs) were purified by a centrifugation step. Experimental details of the study are described in Section 5.3.1. Success of PEGylation was examined via extinction spectroscopy and DLS. Figure 24 shows DLS measurements of AuNPs that were incubated with various PEG solutions from 0.05 to 222.2 μ M. This wide concentration range was chosen on the basis of previous published works on PEGylation procedures.^{223,227,228} Measurements were taken before and after the centrifugation step. An increase of AuNPs' hydrodynamic diameter was expected due to the presence of PEG molecules at the gold surface.

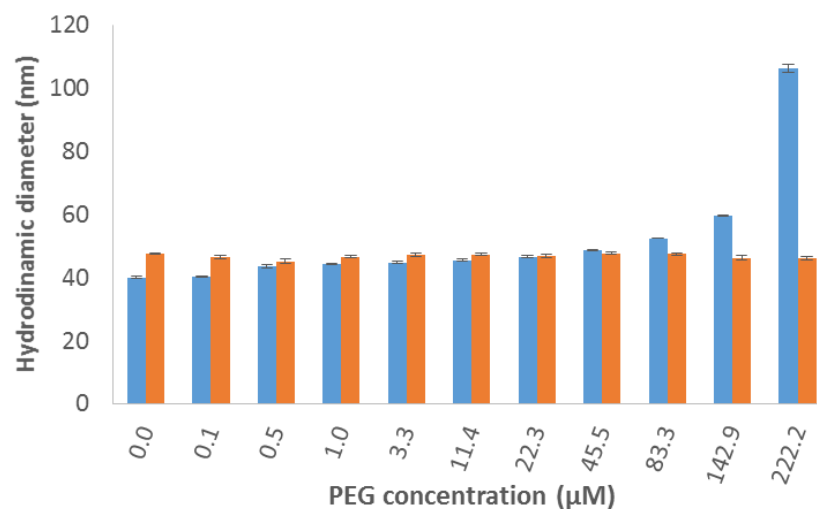


Figure 24. Z-Average DLS sizing of PEGylated AuNPs, before (blue) and after (orange) centrifugation step. Error bars represent the standard deviation of three measurement for each sample. Incubation time, volumes of colloids and details on the centrifugation procedure are described in Section 5.3.1.

The graph in Figure 24 shows that before the centrifugation step, the hydrodynamic diameter increases from 40 nm (0.05 µM of PEG) to circa 120 nm (222.2 µM of PEGs). Although, measurements taken after the centrifugation step, showed no significant changes in the particle size. This suggested that, for PEG solutions with concentrations lower than 22.3 µM, the size increase was due to the centrifugation step rather than the presence of PEG on the surface. On the other hand, AuNPs that were incubated with a solution of 45.5 µM and higher, a decrease of hydrodynamic diameter due to the centrifugation step was noted. This suggested that some of the PEGs were not attached to the AuNPs surface and therefore, they were discharged by the centrifugation step. The DLS results suggested that the optimum PEG concentration should not be lower than 22.3 µM or higher than 45.5 µM. In order to confirm these results, extinction spectra of PEGylated AuNPs were also taken after the centrifugation step (Figure 25A). Typically, a change of nanoparticles surrounding medium can lead to a change of extinction spectrum.¹⁸ In particular, a bathochromic (red) or hypsochromic (blue) shift for the maximum peak of the spectra (λ max.) could be noted. The presence of PEGs at the AuNPs surface caused a redshift between 0.5 and 3 nm (Figure 25B), depending on concentration of PEGs used in the incubation.

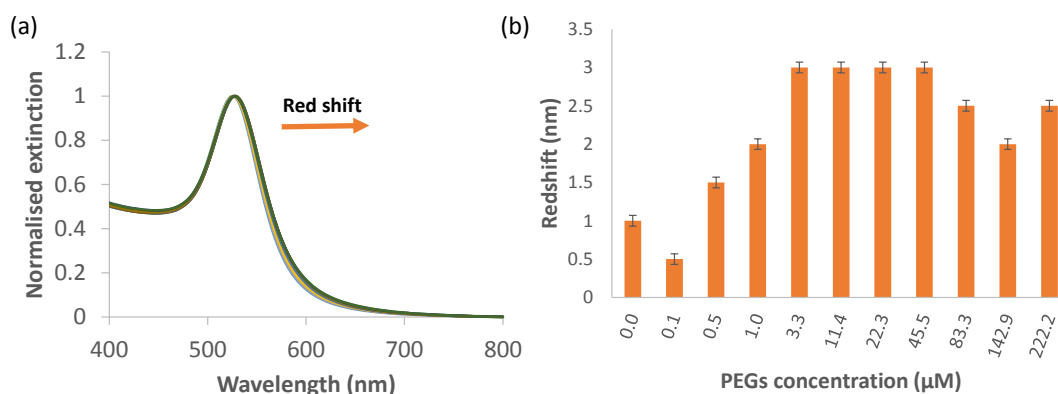


Figure 25. (a) Extinction spectroscopy of PEGylated AuNPs at various concentration of PEG after the centrifugation step. (b) Columns chart that represents the redshift calculated as the difference between the λ max of PEGylated AuNPs and bare AuNPs (λ max = 525 nm). Error bars represent the wavelength accuracy of the instrument at 541.94 nm.

Extinction spectra showed that the greatest redshift was obtained for PEG concentrations between 3.3 and 45.5 μ M, indicating a full surface coverage. The combination of these results with the DLS measurements suggested that the optimum concentration of PEG should be between 22.3 and 45.5 μ M. Therefore, AuNPs were incubated with PEG solution with a concentration of 33.9 μ M (average value) and characterised by extinction spectroscopy and DLS (Figure 26). Incubation time and pH of the optimised PEGylation procedure are described in Section 5.3.2.

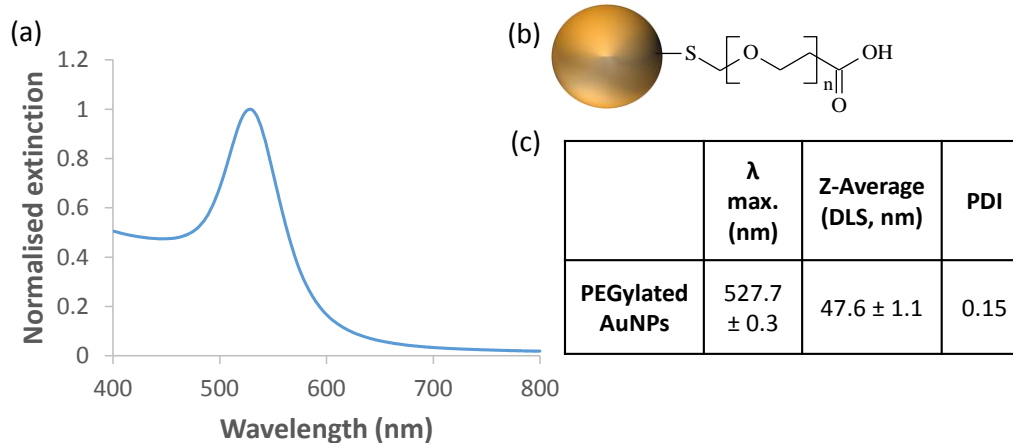


Figure 26. Extinction spectroscopy (a), schematic representation (b) (not in scale) and (c) data representing local surface plasmon resonance, hydrodynamic diameter (Z-Average) and polydispersity index (PDI) measured by DLS optimised of PEGylated AuNPs.

Results in Figure 26 showed that optimised PEGylated AuNPs have a hydrodynamic diameter of 47.6 nm and a localised surface plasmon resonance peak at 527.7 nm. The size increase of

hydrodynamic diameter of around 7 nm (bare AuNPs diameter is 40.6 nm, see Figure 23) can be explained by the AuNPs modification with the CT-PEG₁₂ molecules, which display a space arm of 4.7 nm (Figure 22A).

2.2.2. Attachment of nitrilotriacetic acid (NTA) unit to PEGylated AuNPs

In order to obtain nanostructures that contain binding sites for histidine, a nitrilotriacetic acid (NTA) unit was covalently attached to the PEGylated AuNPs by using the water soluble coupling reagents EDC and sulfo-NHS. This method has been successfully used in various biomolecule conjugations and nanoparticle modifications.^{129,229} The reaction involves the formation of an amide bond between the carboxylic acid on the PEGylated AuNPs and the primary amine on the NTA unit (Figure 27). Experimental details of the reaction are described in Section 5.3.3.

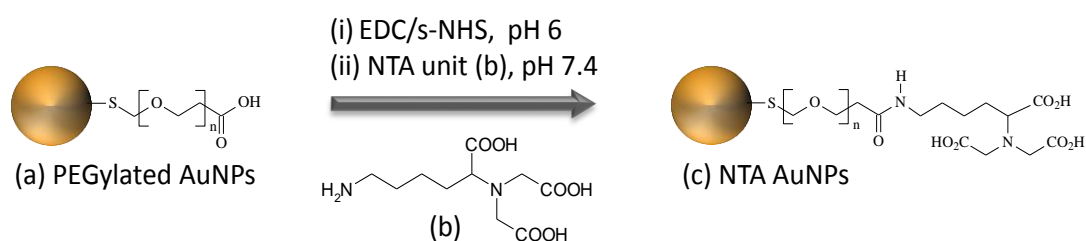


Figure 27. Reaction scheme for the synthesis of (c) NTA AuNPs. The reaction involves a first step (i) where (a) PEGylated AuNPs react with the water soluble coupling reagents EDC and sulfo-NHS at pH 6. The second step (ii) involves the addition of the NTA unit (b) at pH 7.4 in order to form the amide bond.

The mechanism of the amide bond formation is schematised in Figure 28. The carboxylic acid group react with the carbodiimide EDC and an active ester leaving group is formed. This intermediate (*O*-acylisourea) is unstable and can hydrolyse very quickly. The presence of sulfo-NHS causes the reaction to form a stable and water soluble ester intermediate that reacts quickly with primary amines. Therefore, a stable amide linkage can be obtained.

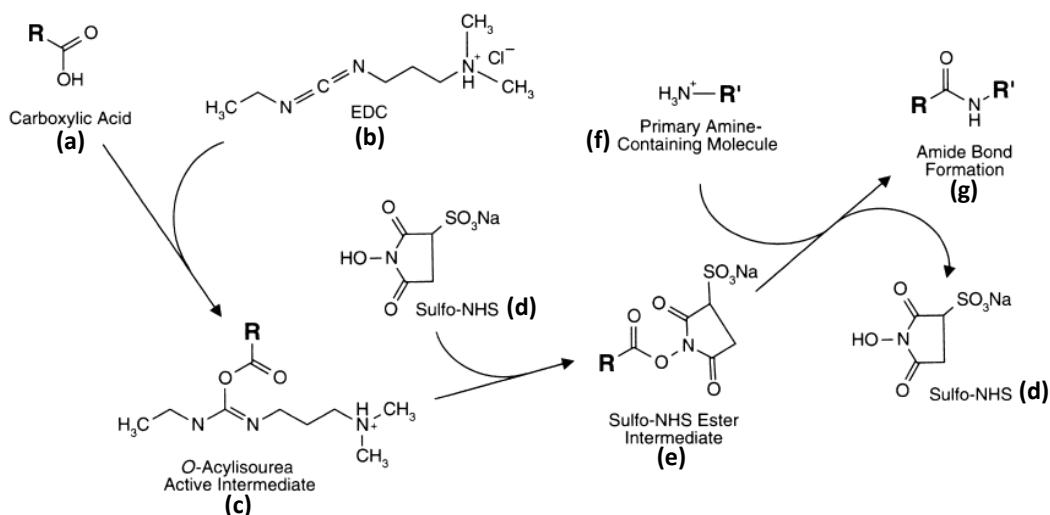


Figure 28. Mechanism of the amide bond formation between carboxylic acid (a) and primary amine (f). The reaction is mediated by the zero length crosslinkers reagents EDC (b) and sulfo-NHS (d). The intermediate of the reactions are the O-acylisourea (c) and the sulfo NHS-ester (e).

The crucial factor for amide formation success was using the correct pH conditions during the reaction. The formation of the stable sulfo-NHS ester intermediate was possible by using a buffered solution at pH 6. This condition could prevent any unwanted hydrolysis of the intermediate before the primary amine was added.²³⁰ The addition of the NTA unit, that contained a primary amine, was performed instead in a buffered solution at pH 7.4. At this pH the amine was not protonated and was active for nucleophile attack.¹²⁹ The NTA functionalised AuNPs were then purified by a centrifugation step and characterised by extinction spectroscopy and DLS (Figure 29).

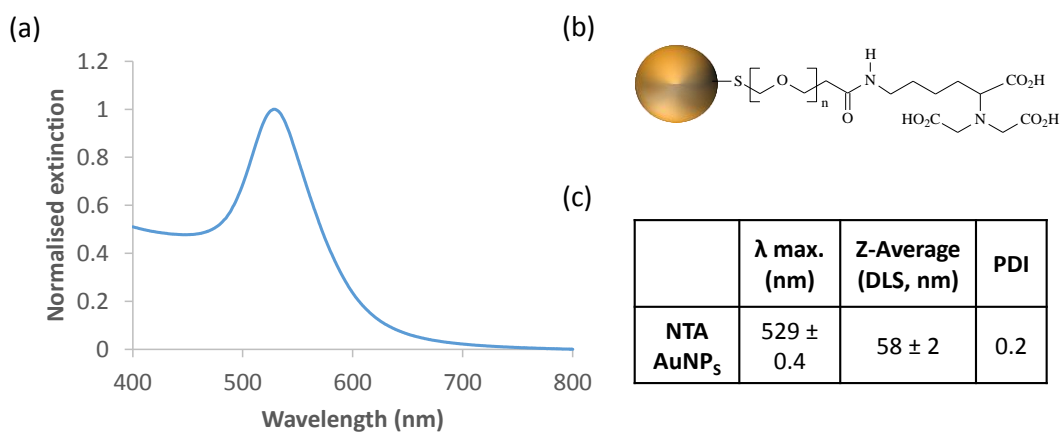


Figure 29. (a) Extinction spectroscopy, (b) schematic representation and (c) data representing local surface plasmon resonance, hydrodynamic diameter (Z-Average) and polydispersity index (PDI) measured by DLS of NTA AuNPs.

The results in Figure 29 shows that the maximum peak of the extinction spectrum (λ max.) shifted to longer wavelengths (redshift), if compared to extinction spectrum of PEGylated AuNPs (Figure 26). This may be due to an increase of dielectric constant of the media, caused by the formation of NTA layers around the NPs. Also, DLS measurements showed an increase of hydrodynamic diameter for the NTA functionalised AuNPs of circa 10 nm compared to the PEGylated AuNPs and a PDI of 0.2 indicates a monodisperse colloidal suspension (see Section 5.2.2). Such an increase can be explained by the formation of various layers of NTA unit, resulting in a dendrimeric structure. High stability of AuNPs in physiological environments is a fundamental pre-requisite for successful assay preparation. Therefore, prior to antibody conjugation, it was necessary to evaluate the behaviour of the NTA AuNPs in salt solutions. Experimental details of the stability study are shown in Section 5.3.4. Briefly, various concentrations of sodium chloride (NaCl) were added to both NTA AuNPs and bare AuNPs. The state of AuNPs aggregation was monitored by measuring the extinction value at 650 nm after the addition of each NaCl aliquot (Figure 30).

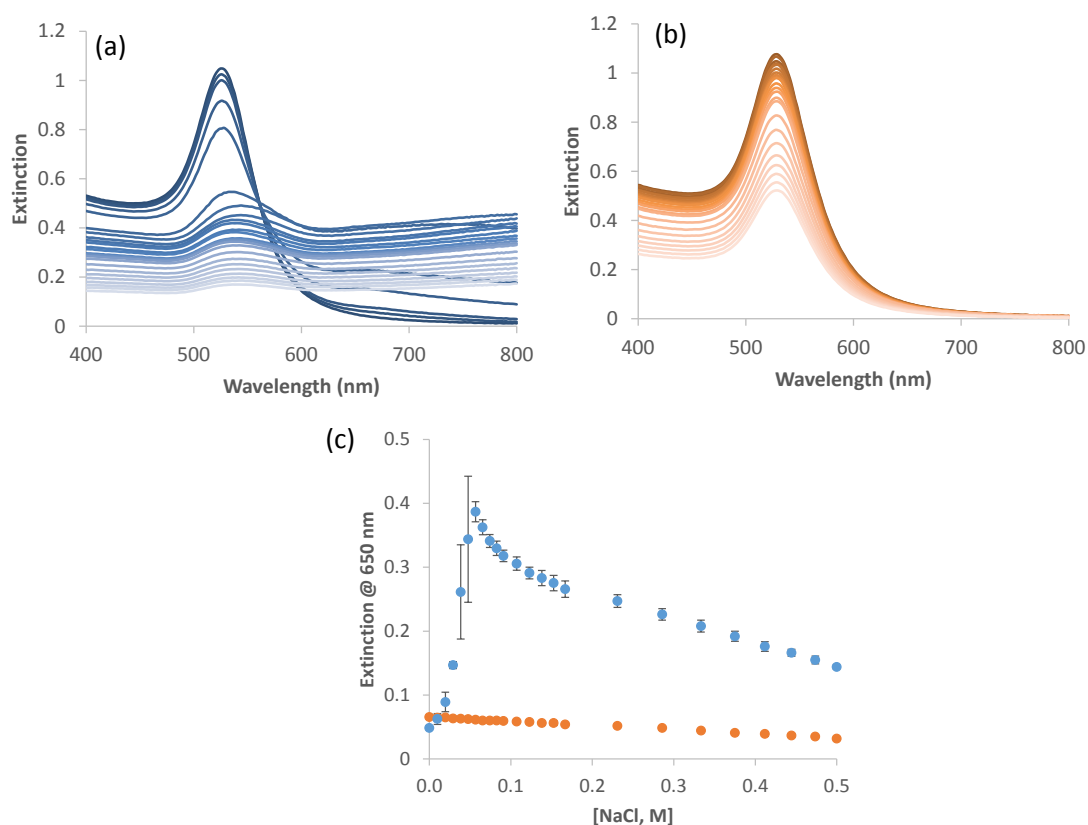


Figure 30. Extinction spectra of (a) bare AuNPs and (b) NTA AuNPs that were incubated with various solutions of NaCl. Concentrations vary from 0 to 0.5 M. The additions of different aliquot of NaCl are described in Section 5.3.4. Aggregation is monitored by the increase of (c) extinction value at 650 nm versus NaCl concentration. Error bars represent the standard deviation of three replica.

Figure 30 results show that the NTA AuNPs remained stable when incubated with NaCl solutions up to 0.5 M as no redshift or extinction value increase at 650 nm is noted. Control experiments, using bare AuNPs showed that NaCl causes nanoparticles aggregation, even at concentrations lower than 0.05 M. The NTA AuNPs can therefore be used in harsh environments such as urine or blood serum that may contain high levels of NaCl.

2.2.3. Metalation study

NTA can form various complexes with transition metal ions, such as Ni (II), Co (II), Zn (II) and Cu (II). In order to establish which metal ions shows the strongest affinity for NTA AuNPs without causing non-specific nanoparticles aggregation, a metalation study was performed. The experimental of this study is described in Section 5.3.5. NTA AuNPs were incubated with 4 aqueous solutions of bivalent metal ion salts: NiCl₂, CoCl₂, CuSO₄ and ZnCl₂. Extinction spectroscopy was performed to monitor the stability of NTA AuNPs in different metal ion solutions (Figure 31).

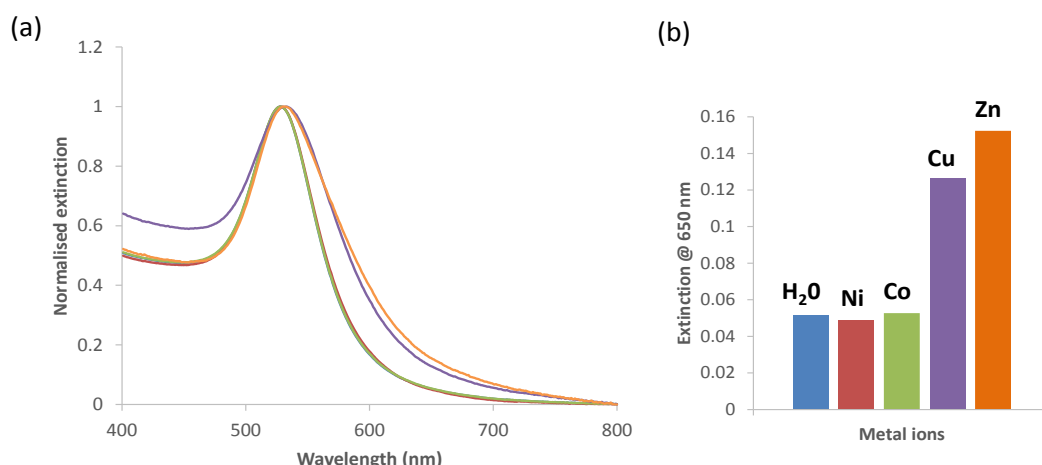


Figure 31. (a) Normalised extinction spectra of NTA AuNPs that were incubated with various solutions of 600 μ M of metal ions: nickel (red), cobalt (green), copper (purple), zinc (orange) and MilliQ water (blue). Spectra were registered at 20 minutes after incubation. (b) Extinction values at 650 nm of NTA AuNPs incubated for 20min with various metal ions.

Figure 31 results shows that when NTA AuNPs were incubated with CuSO₄ and ZnCl₂, the extinction values at 650 nm increased considerably, suggesting NTA AuNPs destabilisation. On the other hand, NiCl₂, CoCl₂ did not give any NTA AuNPs aggregation as their extinction values at 650 nm are comparable with the control sample (Figure 31B). Therefore, only Ni (II) and Co (II) were further investigated. In order to determine the metal ions optimum concentration for NTA AuNPs functionalisation, a theoretical calculation was developed.

Equation 6 describes the moles of metal ions required to bind all the coordination sites present on the NTA AuNPs (1 equivalent). The following considerations were made: each thiol-PEG occupies an area (foot print) of 0.35 nm² per AuNPs²²⁷, a full monolayer of PEGs was reached and the yield of the NTA coupling was equal to 100 % entirely, so for each CT-PEG attached on AuNPs, a NTA unit is formed.

$$\text{moles of metal ions} = \text{moles of PEG} = \frac{4 \pi r^2 \times \text{moles of AuNPs}}{\text{PEG foot print}}$$

Equation 6. Theoretical calculation for moles of metal ions in order to full cover the NTA coordination sites on the NTA AuNPs (1 equivalent). “*r*” is the hydrodynamic radius of bare AuNPs, “PEG foot print” is the area of AuNPs surface occupied by thiol-PEGs. “Moles of AuNPs” is calculated according to the Beer-Lambert law.

The equation was solved for a 10 μL solution of NTA AuNPs that had a concentration (calculated using the Beer-Lambert law, see Section 5.2.1) equal to 0.5 nM. The radius “*r*” in the equation 6 is the hydrodynamic radius measured of bare AuNPs, equal to 20.3 nm. By replacing these values in the equation 6, the metal ions concentration was found to be equal to 2.23 μM. This concentration value corresponds to 1 equivalent (eqv) of metal ions to AuNPs. As the equation does not take consideration of the possible ramification of the NTA unit, this concentration is a theoretical maximum. Therefore NTA AuNPs were incubated overnight with 5 solutions of NiCl₂ and 5 solutions CoCl₂ with the following concentrations: 2.23 (1 eqv), 11.15 (5 eqv), 22.3 (10 eqv), 111.5 (50 eqv) and 223 μM (100 eqv). Experimental details of the incubation procedure are described in Section 5.3.6. Extinction spectroscopy was then performed to evaluate any nanoparticle aggregation (Figure 32).

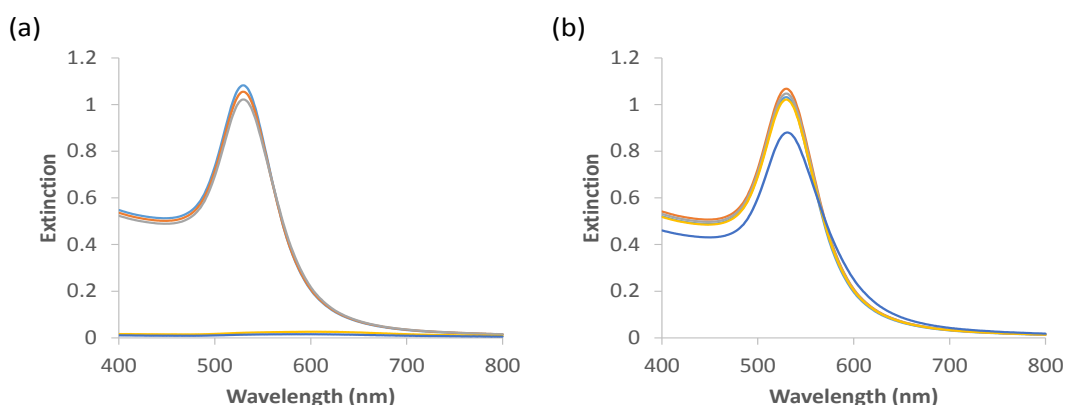


Figure 32. Extinction spectra of (a) nickel and (b) cobalt functionalised NTA AuNPs. Spectra were taken after an overnight incubation. Samples contained various concentrations of metal ions [μM]: 2.23 (light blue), 11.15 (orange), 22.3 (grey), 111.5 (yellow) and 223 (dark blue).

Results in Figure 32 suggest that the optimum metal ions concentration for stable nickel functionalised NTA AuNPs is equal to 22.3 μM (10 eqv) and the cobalt functionalised NTA AuNPs is equal to 113 μM (50 eqv). Figure 33 shows a schematic representation of metal ion functionalised NTA AuNPs which contain two free coordination binding sites for histidine.

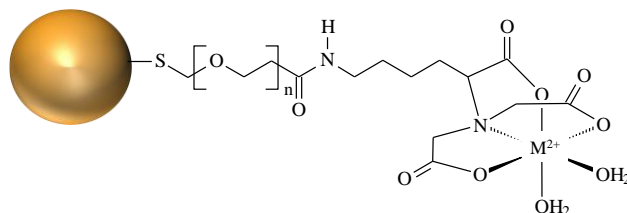


Figure 33. Schematic representation of metal ions functionalised NTA AuNPs (NTA-M AuNPs). M^{2+} = nickel (II) or cobalt (II).

2.2.4. Conjugation of his-tag antibody to metal ions functionalised NTA AuNPs

In order to assess which complex, between NTA-Ni and NTA-Co shows stronger affinity towards histidine-tagged antibodies, a recombinant Fab (fragment antigen-binding) anti-CRP antibody that contains 7 histidine units (his-tag Fab) (Figure 34A) was incubated with both the NTA-M functionalised AuNPs for 1 hour at pH 7.4 (Figure 34B). Details of the conjugation method are described in Section 5.3.7.

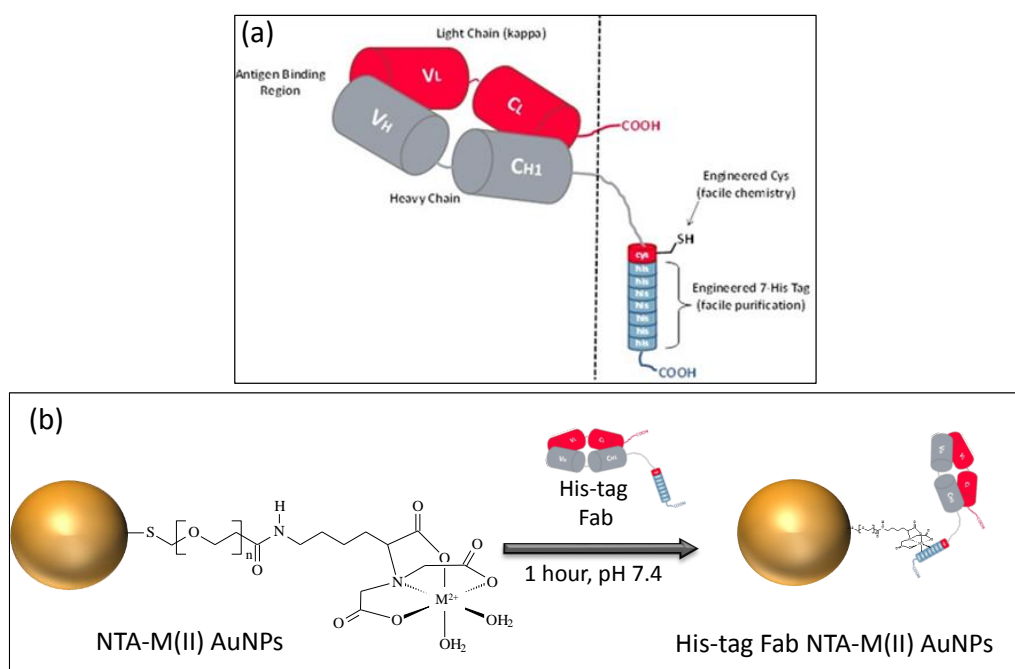


Figure 34. (a) Schematic representation of the recombinant Fab antibodies which are tagged with 7 histidine residues (his-tag Fab), (credit to BBI Solutions where image was reproduced from). (b) Schematic representation of his-tag Fab conjugation to metal ions functionalised NTA AuNPs.

The NTA-*M* (II) AuNPs (*M* = Ni or Co) were conjugated with a concentration of his-tag Fab equal to 1 µg/mL. Considering that the molecular weight of a Fab fragment is approximately 13.5 KDa, 1 µg/mL of his-tag Fab corresponds to a molarity of 74 µM (mole = mass/molecular weight). This concentration is theoretically (see Section 2.2.3) in excess compared to the metal ions functionalised NTA AuNPs.

The biological functionality of the two his-tag Fab conjugates towards the antigen was evaluated by lateral flow (LF) assay. In particular a “half-dipstick” test, which is usually used as a method for screening antibodies, was performed.¹⁸⁴ The test was also used to compare the binding efficiency of the NTA-Ni (II) and the NTA-Co (II) towards the histidine units. Information about the LF strips that were used in this experiment, can be found in Appendix A. The “half-dipstick” test procedure is schematised in Figure 35. LF strips that contained four lines of CRP striped onto the nitrocellulose (NC) were used for this experiment. His-tag Fab conjugated to NTA-Ni (II) AuNPs or to NTA-Co (II) AuNPs were placed on the conjugate pad (CP) and a solution, called running buffer, was placed on the sample pad (SP) to allow the conjugate to flow through the strip (Figure 35A). A HEPES buffer solution at pH 7.4 was chosen over other 3 conventional running buffers as its use resulted in the greatest line intensity (see Appendix B).

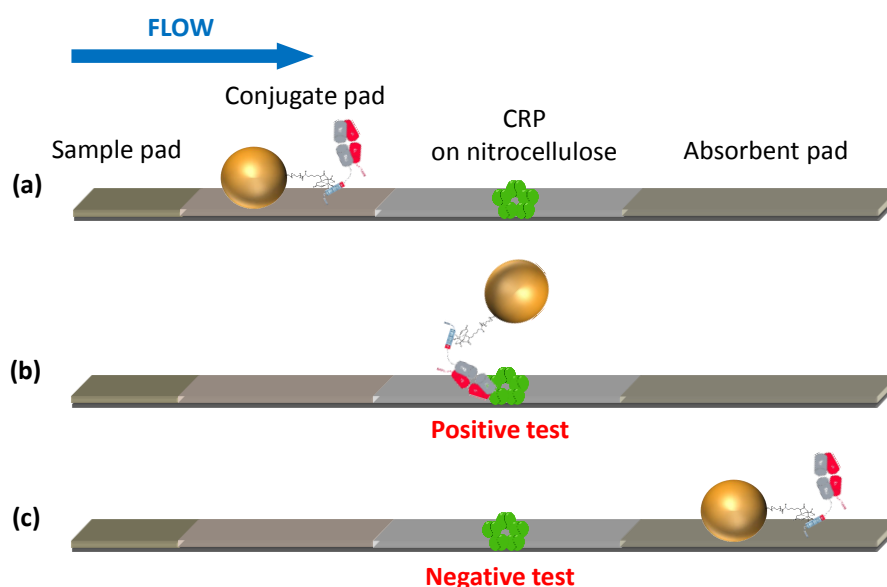




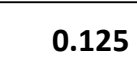

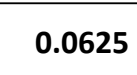



Figure 35. Schematic representation of lateral flow testing used to assess the more efficient conjugate between NTA-Co and NTA-Ni AuNPs antibody conjugates. C-reactive protein was previously absorbed on to nitrocellulose. The conjugate pad was loaded with the anti-CRP his-tag Fab conjugates. A HEPES solution was placed on the sample pad to allow the conjugate to flow through the strip. (a) Before the test, (b) positive test and (c) negative test. Experimental details of the test are described in Section 5.3.7.

Generally, a positive test (Figure 35B) is achieved when the conjugate is able to bind the CRP so red lines should appear on the NC compartment. If conjugate is not able to bind to the antigen, the NC should not show any red colour: negative test (Figure 35C). After the his-tag Fab conjugate migrated to the absorbent pad, strips were placed horizontally and left to dry. The test was complete in approximately 5 minutes. The flowing time depends on the NC's pores. For the work described herein NC with pores size equal to 15 μm was used. Photographs of the LF strips were taken in order to compare the intensity of red lines between NTA-Ni and NTA-Co his-tag Fab conjugates. Results are shown in Table 2.

Table 2. Photographs of the nitrocellulose compartment of the LF strips after the “half-dipstick” test was performed. Strips were previously loaded with 4 different concentrations of CRP (red lines). Tests were performed using anti-CRP his-tag Fab conjugated (a) NTA-Ni and (b) NTA-Co AuNPs. Tests were performed in triplicate.

[CRP, mg/mL]	(a)	(b)
0.5		
0.25		
0.125		
0.0625		

The photographs in Table 2 show that when NTA-Ni AuNPs conjugates were used, red lines appeared more intense (Table 2A) compared to strips that contained NTA-Co AuNPs conjugates (Table 2B) These results suggested that the NTA-Ni AuNPs have the strongest affinity towards histidine-tagged antibodies. Therefore nickel ions were preferred over cobalt ions in the metalation of NTA AuNPs. Herein, NTA-Ni AuNPs that were previously incubated with 22.3 μM of NiCl_2 , were characterised by extinction spectroscopy, DLS and scanning electron microscopy (SEM) (Figure 36).

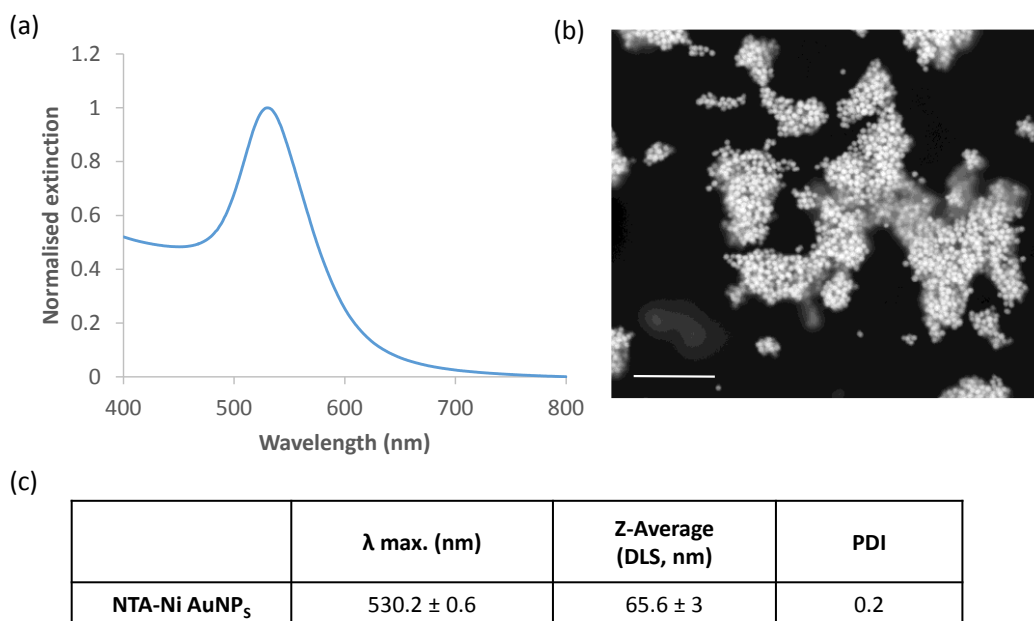


Figure 36. (a) Extinction spectroscopy, (b) SEM image and (c) data representing local surface plasmon resonance, hydrodynamic diameter (Z-Average) and polydispersity index (PDI) measured by DLS of NTA-Ni AuNPs. SEM image's scale is 500 μ m. PDI of 0.2 indicates a monodisperse colloidal suspension (see Section 5.2.2).

Moreover, a time stability study was performed on the optimised NTA-Ni AuNPs. They were stored at temperature of 4-8 °C for several weeks. Extinction spectra were taken over time (Figure 37) and results suggested that the NTA-Ni AuNPs were stable for at least 3 months as no significant changes of the spectra profile were noted.

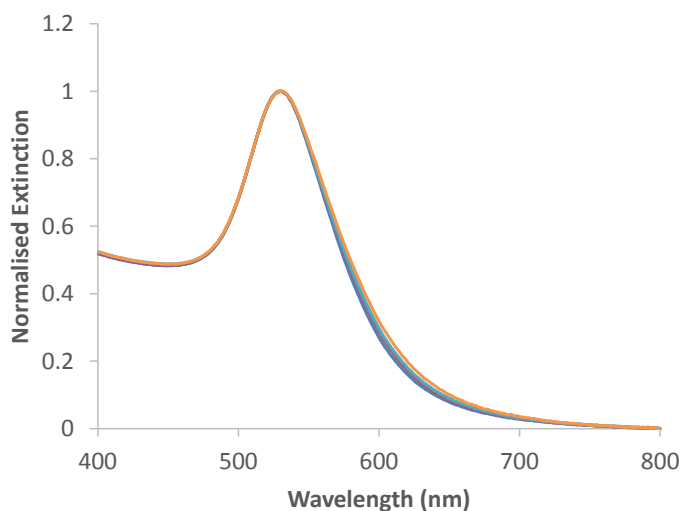


Figure 37. Time stability study. Extinction spectra of NTA-Ni AuNPs: 3 (dark blue), 6 (red), 13 (green), 20 (purple), 27 (light blue) and 134 days (orange).

2.2.5. Role of nickel in the conjugation process

In order to investigate the role of nickel in the antibody conjugation process, a nickel concentration study, an incubation time study and an antibody displacement study were performed. Experimental details of the studies are shown in Section 5.3.8.

2.2.5.1. Nickel concentration study

4 samples of NTA-Ni AuNPs were incubated with different concentrations of NiCl₂. After a fixed incubation time, samples were centrifuged and conjugated with a solution of 1 µg/mL of his-tag Fab. The conjugates were tested on LF strips containing 4 lines of CRP on the NC strips. The principle of the test is the same reported in the previous section (Figure 35) and competitive format test strips with a CRP gradient were used in this experiment (see Appendix A). The functionality and the quantity of antibody loaded on the NTA-Ni AuNPs was estimated on the visual readout of the CRP lines. The results are shown in Table 3.

Table 3. Nickel concentration study. Lateral flow tests were performed using his-tag Fab conjugated NTA-Ni AuNPs that contained various nickel concentrations. Strips were previously loaded with 4 lines of C-reactive protein solutions and left to dry (from 62.5 to 500 µg/mL). The strips demonstrated that increasing the nickel concentration led to an increased uptake of antibody on to NTA AuNPs. The experiment was performed in triplicate. Control strips showed the absence of non-specific binding when antibody was not loaded on to NTA AuNPs.

C-reactive protein (mg/mL)	Incubation his-tag Fab 1 µg/mL				Control (No his-tag Fab)	
	0 eqv Ni	1 eqv Ni	5 eqv Ni	10 eqv Ni	0 eqv Ni	10 eqv Ni
0.5						
0.25						
0.125						
0.0625						

Results indicate that when no nickel was present on the NTA AuNPs, no red lines appeared. Samples that contained 1 equivalent (eqv) of NiCl₂ (2.23 µM) showed very pale red lines. Samples that contained 5 and 10 eqv of NiCl₂ showed red lines, but the latter condition was more intense. Results suggested that NiCl₂ controls the quantity of antibody that is attached on to NTA-Ni AuNPs. A control test was run using NTA-Ni AuNPs that were not conjugated with antibodies. No red lines appeared on the control strips.

2.2.5.2. Nickel incubation time study

A nickel incubation time study was conducted using 3 samples of NTA-Ni AuNPs that all contained 10 eqv of NiCl₂. NTA AuNPs samples were incubated with NiCl₂ for 16, 20 and 44 hours respectively. After these times, nanoparticles were incubated with his-tag Fab. In order to evaluate a possible correlation between the quantity of antibodies conjugated to nanoparticles and nickel incubation time, an experiment were performed using the same LF format seen in the concentration study. The results are shown in Table 4. For the positive test, conjugate pads were loaded with 3 samples of NTA-Ni AuNPs (16 h, 20 h and 44 h). A control test where no nickel was added on to the NTA AuNPs was also performed for each time point. Photographs in Table 4 showed that samples that were incubated with nickel for a longer time, displayed more intense red lines. This suggested that a longer nickel incubation time with NTA AuNPs, led to an increase of antibody binding to the AuNPs.

Table 4. Nickel incubation time study. Lateral flow tests were performed with his-tag Fab conjugated NTA-Ni AuNPs that were incubated with nickel for an incrementally increasing number of hours during functionalisation. Strips were previously loaded with 4 lines of C-reactive protein solutions and left to dry (from 62.5 to 500 µg/mL). Test strips showed that increasing nickel incubation time led to increased uptake of antibody on to the AuNPs. Experiments were performed in triplicate. Control strips showed the absence of antibody on to NTA AuNPs when nickel was not added.


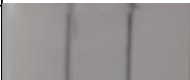

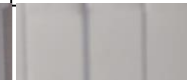
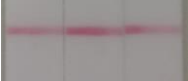


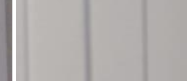

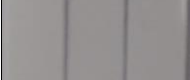






C-reactive protein (mg/mL)	Incubation time (Ni 10 eqv) – his-tag Fab 1 µg/mL					
	16 h		20 h		44 h	
	NTA-Ni	NTA	NTA-Ni	NTA	NTA-Ni	NTA
0.5						
0.25						
0.125						
0.0625						

2.2.5.3. Antibody displacement study

In order to confirm that his-tag Fab was binding to the NTA-Ni AuNPs through the histidine group, an experiment involving the use of imidazole was conducted. Imidazole solutions are often used to displace proteins from IMAC columns.²¹³ In this project, his-tag Fab conjugated NTA-Ni AuNPs were incubated with an aqueous solution of imidazole. After purification by centrifugation, LF tests were performed and the results are shown in Table 5. Red lines appeared when the conjugate was not treated with imidazole. When the same sample was treated with imidazole, no red lines appeared. This suggested that the imidazole displaced

his-tag Fab antibodies from the NTA-Ni AuNPs. Control tests, in which no nickel was added, were also performed and did not display any non-specific binding. These results confirmed that the binding site between antibodies and NTA-Ni AuNPs is specific at the histidine tag. The binding site can be tuned by nickel concentration/incubation time and could also be reversible with the use of imidazole solutions for displacement.

Table 5. Antibody displacement study. Lateral flow tests were performed before and after imidazole treatment. Strips were previously loaded with 4 lines of C-reactive protein solutions and left to dry (from 62.5 to 500 $\mu\text{g/mL}$). Subsequently, his-tag Fab NTA-Ni conjugates were incubated with a solution of Imidazole. Lateral flow strips did not display lines. Control strips showed the absence of antibody on to NTA AuNPs when nickel was not added.

C-reactive protein (mg/mL)	Before imidazole treatment		After imidazole treatment	
	His-tag Fab NTA-Ni	His-tag Fab NTA	His-tag Fab NTA-Ni	His-tag Fab NTA
0.5				
0.25				
0.125				
0.0625				

2.2.6. Antibody concentration study

NTA-Ni AuNPs that were previously incubated with 22.3 μM of NiCl_2 for at least 44 hours were used for an antibody concentration study. Herein, various solutions of his-tag Fab were incubated with NTA-Ni AuNPs for 1 hour and after a centrifugation step, conjugates were tested by extinction spectroscopy (Figure 38) and “half-dipstick” LF test. Details of the concentration study are described in Section 5.3.9.

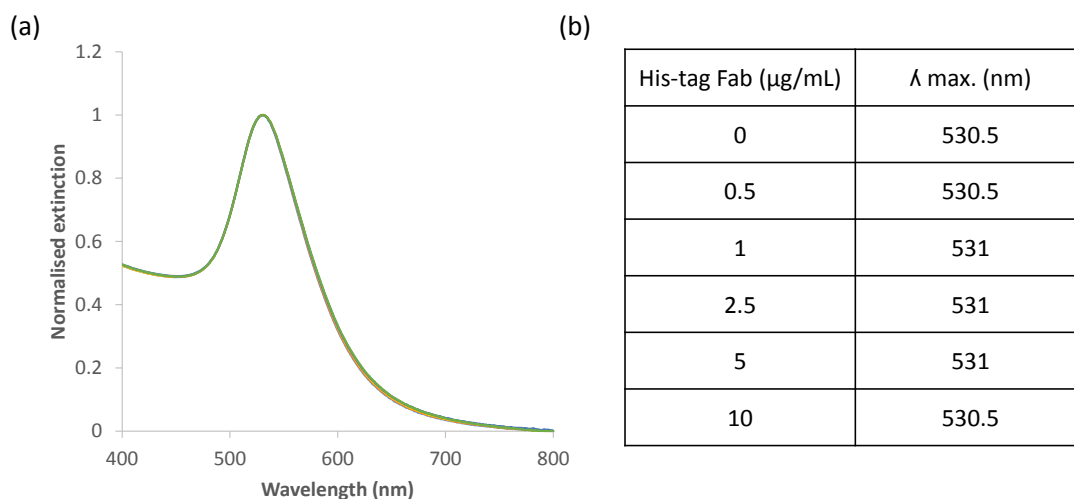


Figure 38. (a) Extinction spectra of NTA-Ni AuNPs that were conjugated to various solutions of his-tag Fab anti-CRP antibody: 0/control (light blue), 0.5 (red), 1 (grey), 2.5 (yellow), 5 (dark blue) and 10 $\mu\text{g/mL}$ (green). (b) LSPR resonance data. Spectra have the same profile and there is no significant difference on LSPR values.

Results in Figure 38 suggest that the NTA-Ni AuNPs remained stable when incubated with various concentrations of his-tag Fab as no increase of extinction value at 650 nm nor shift of the λ_{max} was noted. Also, no LSPR shifts were noted. LSPR is generally influenced by the nanoparticles surrounding, but in this case the antibodies are too distant from the surface to cause a shift of the λ_{max} . The “half-dipstick” LF test was performed by using strips that were spotted with a solution of CRP (0.5 mg/mL) in the middle of the NC compartment and left to dry for 30 minutes at room temperature. The conjugates were loaded on the CP and a buffer solution was run from the SP. Photographs of the LF strips are shown in Figure 39.

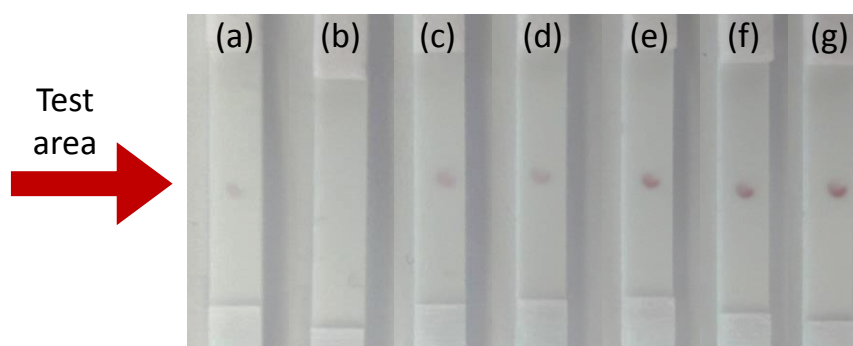


Figure 39. Photographs of nitrocellulose compartment of lateral flow strips for the evaluation of optimum antibody incubation concentration. Nitrocellulose was previously spotted with a solution of CRP and dried at room temperature. Strips were run with the following conjugates. (a) Commercially available BBI Fab anti-CRP gold conjugate, (b) NTA-Ni AuNPs (control sample). From (c) to (g), NTA-Ni AuNPs with various concentration of his-tag Fab conjugates: (c) 0.5, (d) 1, (e) 2.5, (f) 5 and (g) 10 $\mu\text{g/mL}$.

Results in Figure 39 show that the intensity of red spots on the test area increased with the antibody concentration. A control strip where no antibody was added, suggested the absence of NSB. The antigen binding efficiency of his-tag Fab NTA-Ni AuNPs conjugate was compared with commercially available anti-CRP gold conjugate (Figure 39A). Results showed that the NTA-Ni conjugates gave a more intense spot than the commercially available conjugate formed by the same his-tag Fab antibody and 40 nm AuNPs. The reason why commercially available conjugate is given a worse signal than his-tag Fab NTA-Ni AuNPs conjugate can be ascribed to the different conjugation method used to prepare the antibody-gold conjugate. Indeed, the commercial conjugate is prepared by using the passive method (see Section 1.3.2.3) which leads to a lower Ab binding activity compared to the his-tag conjugation method. LF results and conjugates extinction data suggested that the optimum concentration of his-tag Fab to conjugate the NTA-Ni AuNPs was equal to 5 $\mu\text{g/mL}$.

2.2.7. Interaction of NTA-Ni AuNPs with poly-L amino acids

It was established from the experiments described previously in Sections 2.2.4 and 2.2.5 that the NTA-Ni AuNPs were able to bind to his-tag Fab antibodies and that the presence of nickel controlled the binding. In order to investigate whether the NTA-Ni AuNPs could potentially bind every biomolecule that contains histidine, their interaction with selected poly-L amino acids was studied. NTA-Ni AuNPs were incubated with solutions of poly-L histidine, lysine, arginine and glutamic acid (Figure 40). The experimental data is described in Section 5.3.10.

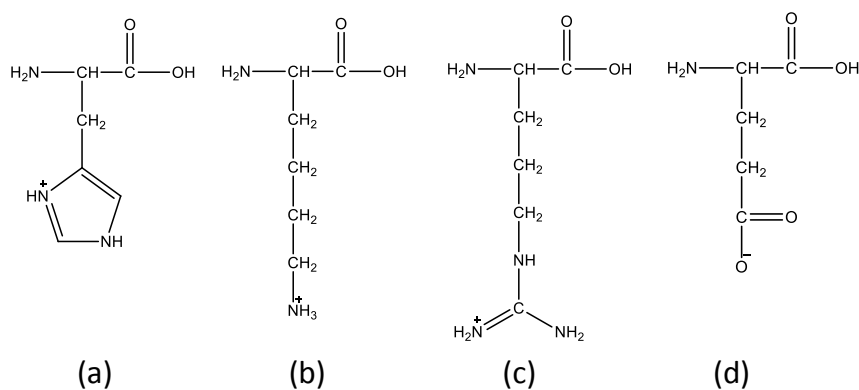


Figure 40. Chemical structure of the monomeric unit of poly-L-amino acids at physiological pH that were incubated with the NTA-Ni AuNPs. (a) Histidine, (b) lysine, (c) arginine and (d) glutamic acid.

Arginine and lysine contain positively charged side chains at physiological pH that could interact with the NTA-Ni AuNPs by electrostatic interactions or dative bonds. Poly-L glutamic acid was used as a control with the purpose of investigating non-specific interactions

between the NTA-Ni AuNPs and the peptide chain itself. The NTA-Ni AuNPs were incubated with the selected poly-L amino acids and extinction spectra were registered over 100 minutes (Figure 41).

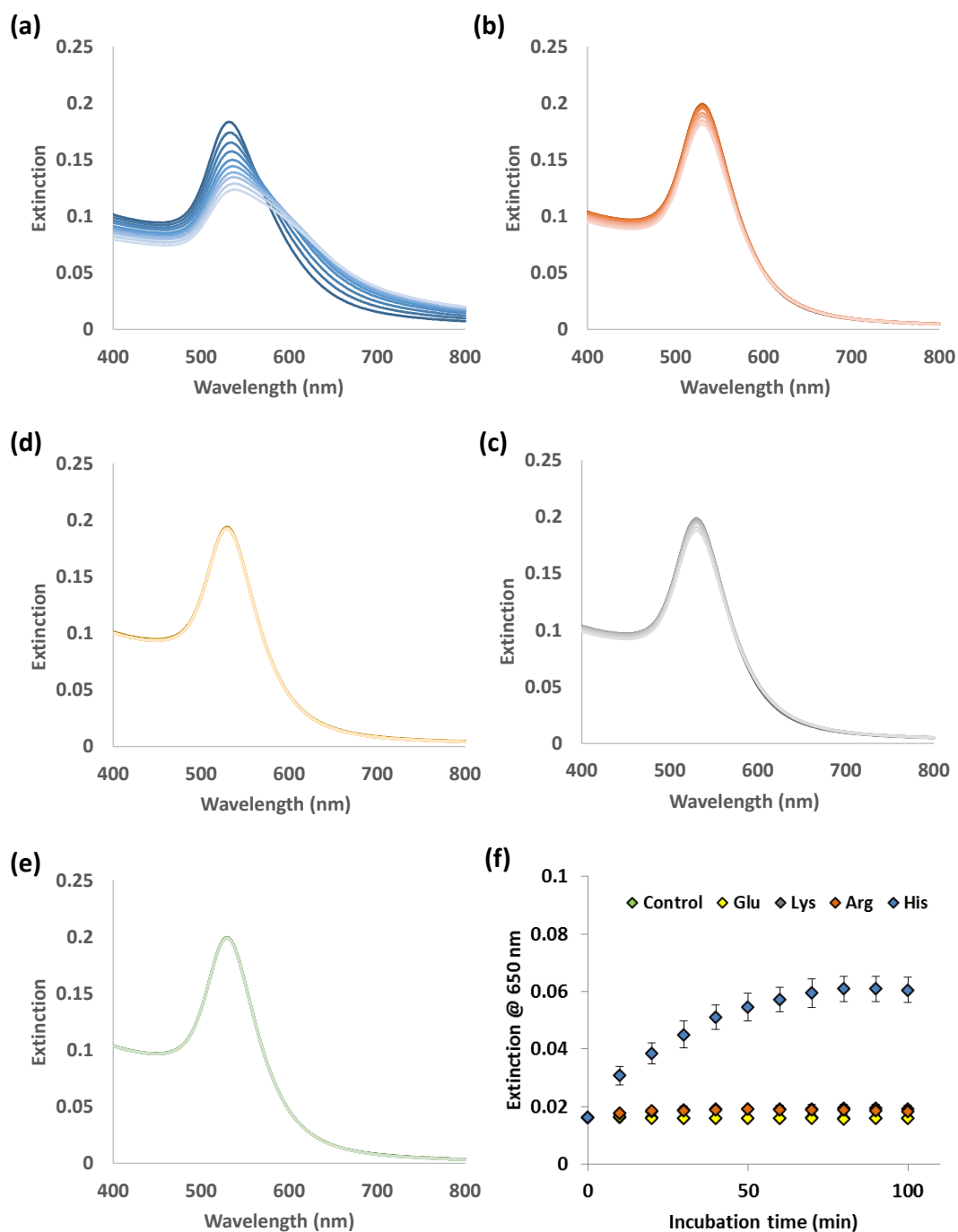


Figure 41. Extinction spectra of 5 samples of NTA-Ni AuNPs in 25 mM HEPES buffer pH 7.4 that were incubated with (a) poly-L-histidine, (b) poly-L-arginine, (c) poly-L-lysine, (d) poly-L- glutamic acid, (e) MilliQ water (control). Spectra were taken every 10 minutes for 100 minutes. (f) Extinction values at 650 nm of the various samples vs incubation time: control (green), glutamic acid (yellow), lysine (grey), arginine (red) and histidine (blue). Error bars indicate standard deviation of three replicates for each sample.

Results in Figure 41 suggested that the NTA-Ni AuNPs strongly interact with poly-L-histidine as the plasmonic band has significantly broadened. In contrast, the inclusion of poly-L-arginine, poly-L-lysine and poly-L-glutamic acid to the NTA-Ni AuNPs did not cause any changes in their extinction profiles. A control experiment where no poly-L-amino acids were added was also performed for assuring the stability under buffer conditions. The plots in Figure 41F clearly show the different behaviour of NTA-Ni AuNPs with poly-L-histidine compared to the other samples. The extinction value at 650 nm increased considerably over 100 minutes only when NTA-Ni AuNPs are incubated with poly-L-histidine. The nature of this interaction is due to the coordination bond between NTA-Ni complexes and imidazole rings of poly-L-histidine, i.e. the pre-organization of the ligand increases the strength of the bond and intramolecular interactions are formed as a results (Figure 42). The poly-L amino acid study confirmed that NTA-Ni AuNPs developed here, have affinity towards histidine and selectivity against lysine, arginine and glutamic acid.

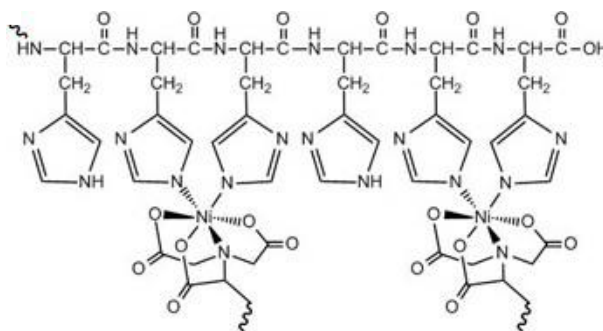


Figure 42. Schematic representation of the coordination bonds between NTA-Ni complexes and imidazole groups on the side chain of the poly-L histidine.

2.3. Conclusions

A nanosystem capable of selectively binding histidine units was successfully developed. 40 nm AuNPs were modified with PEG molecules which prevented any non-specific interactions and protected the AuNPs from aggregations. The NTA group, that it is known to form metal complexes, was covalently attached to the PEGylated AuNPs by using water soluble coupling reagents, EDC/sulfo-NHS. A metalation study also suggested that nickel ions performed best in the metal ion functionalisations of NTA AuNPs. The NTA-Ni AuNPs exhibited maximum stability and a stronger interaction towards the his-tag Fab anti-CRP antibody. It was established that nickel ions drove antibody uptake and they are key to the nanoparticles/biomolecules interactions. The conjugation method developed in this project was fast (1 hour incubation time), straightforward and no external reagents were necessary during the conjugation process. Due to the simplicity of this methodology, NTA-Ni AuNPs could potentially be used to conjugate any commercially available his-tagged antibody for immunoassay research and development or in routine analysis. With further optimisation the NTA-Ni AuNPs could be used for the purification of recombinant his-tag antibodies from cell media.

CHAPTER 3: SERS-based Lateral Flow Immunoassay for the Detection of C-reactive protein

3.1. Aims and overview

C-reactive protein (CRP) is a ring shaped protein that consist of 5 identical polypeptide subunits, which interact with each other's via non-covalent bonds (Figure 43). In human and other animal species, CRP is a major acute-phase plasma protein displaying rapid and pronounced rise of its serum concentration in response to infection or tissue injury.²³¹ In combination with high levels of cholesterol in blood, the monitoring of CRP concentration has been also used to provide an assessment of the risk in developing cardiovascular disease.²³²

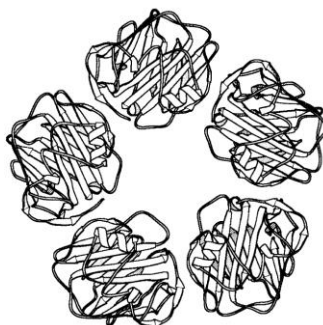


Figure 43. Representation of the C-reactive protein pentameric structure. Image reproduced from Human C-reactive protein: expression, structure, and function. John E. Volanakis. *Molecular Immunology* 38 (2001) 189–197.

CRP detection on clinical samples is usually performed by rate nephelometry and turbidimetry.²³³ Also, enzyme-linked immunosorbent assay (ELISA) is commonly used by researchers and kits for CRP detection are commercially available. Several advanced immunoassays for CRP detection have also been developed in the last few years.²³⁴ In particular, lateral flow immunoassays (LFIA) have emerged due to their robustness, rapidity and simplicity of the test.^{235,236} However, there is a lack of sensitivity and precision at low concentrations when visual test interpretation is required. Hence there is a need for a signal

amplification method that increases the sensitivity of the tests and at the same time, allows for the quantification of the analyte. Examples of CRP detection by LFIAs that use amplification methods such as fluorescence and electrochemistry are available in the literature.^{237–239} As described in Section 1.4.1 of this thesis, several amplification methods that improve the sensitivity of the LFA exist. In this research, an amplification method based on surface enhanced resonance Raman spectroscopy (SERRS) was developed. This method combines the robustness and rapidity of the LFIA with the sensitivity of a SERRS-based assays. The simple and straightforward process by which Ab conjugated NPs can be labelled with Raman reporter molecules (RRMs), along with their wide selection (fundamental for multiplexing assays) gives the SERRS technique an advantage over other amplification methods. SERRS-based immunoassays for the detection of CRP have been previously investigated using techniques such as ELISA or most recently a silver-linked immunosorbent assay (SLISA).^{240,241}

The aim of this research was to develop a SERRS-based LFIA for the detection of CRP. The choice of the Raman reporter molecule (RRM) and its compatibility on LF devices are discussed in this chapter. Also, Ab conjugated NPs that were prepared via the NTA-Ni (II) conjugation method in the previous chapter, were evaluated for SERRS performance and compared to passively absorbed conjugates. In order to increase the dynamic range and the sensitivity of the assay, two different LF formats were developed: sandwich-like assay, where the amount of CRP is directly proportional to the intensity of the signal, and competitive assay, where the signal decreases with the CRP concentration as the analyte competes with immobilised CRP on the LF device. Finally, the possibility of analysing CRP in biological matrices such as serum was evaluated, conveying the usefulness of the LFIA for PoC analysis.

3.2. Results and discussion

3.2.1. Raman reporter molecule (RRM) evaluation

In order to evaluate a suitable RRM which would be used to label antibody-gold conjugates for their use in LFIA, 4-mercaptobenzoic acid (MBA) and malachite green isothiocyanate (MGITC) were used in this project. Both molecules are known to be Raman active and they also contain thiol groups that strongly bind to the nanoparticles surface by the Au-S bond (Figure 44).

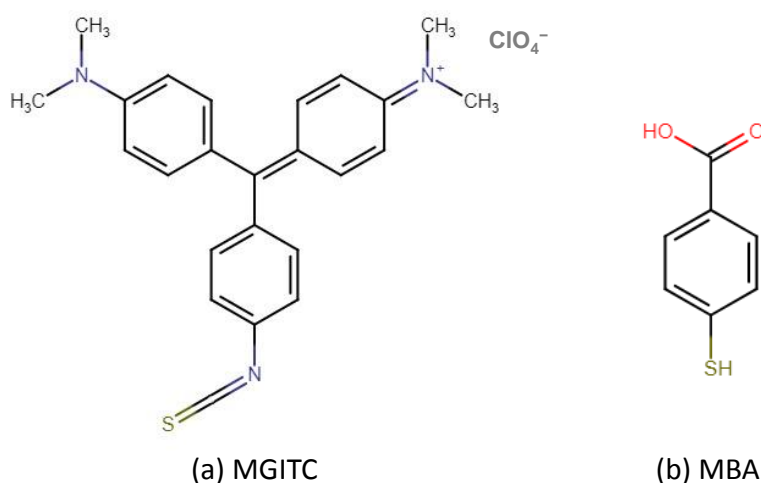


Figure 44. Molecular structures of (a) malachite green isothiocyanate (MGITC) and (b) 4-mercapto benzoic acid (MBA).

The RRM were incubated overnight with the antibody-gold conjugates based on the NTA-Ni conjugation method that was previously developed in this research (his-tag Fab NTA-Ni AuNPs, Figure 34B). The solutions were then centrifuged to remove unbound dye and resuspended in water and the effectiveness of the conjugation evaluated by the “half-dipstick” LF test. Two strips that contain 4 lines of CRP concentration gradient from 500 to 62.5 $\mu\text{g}/\text{mL}$ were used in this experiment. The RRM labelled his-tag Fab NTA-Ni AuNPs were placed on the conjugate pad and HEPES buffer was run from the sample pad to allow conjugates flow through the strip. Photographs of the nitrocellulose area of the strips are shown in Table 6.

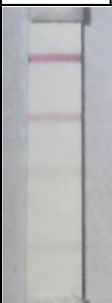

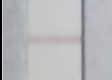
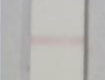

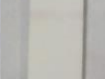
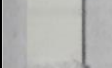

CRP lines ($\mu\text{g/mL}$)	MBA	MGITC
500		
250		
125		
62.5		

Table 6. Photographs of NC compartment of lateral flow strips performed to evaluate the Raman reporter molecule. Strips contain 4 lines of CRP gradient from 500 to 62.5 $\mu\text{g/mL}$. Conjugate pads were loaded respectively with MBA and MGITC labelled his-tag Fab NTA-Ni AuNPs.

Results in Table 6 shows that both MBA and MGITC labelled conjugates are able to bind to the CRP on the strip. Intensities of the red lines decreases with the CRP concentration and there are not significant differences between the two strips. Lines containing 500 and 250 $\mu\text{g/mL}$ of CRP are very noticeable to the naked-eye. However, the lines with 125 and 62.5 $\mu\text{g/mL}$ of CRP are paler and harder to visualise to the naked-eye. A Raman microscope was used to evaluate the eventual SERS signals coming from the CRP lines. A 633 nm laser excitation was chosen as the incident beam, because it is known that gold spherical nanoparticles give better surface enhancement with this laser wavelength.⁸⁰ Strips, were placed under a Raman microscope as shown in Figure 45 and SERS spectra were collected on each test lines (Figure 46).



Figure 45. Photograph of a Raman microscope used for analysing LF strips.

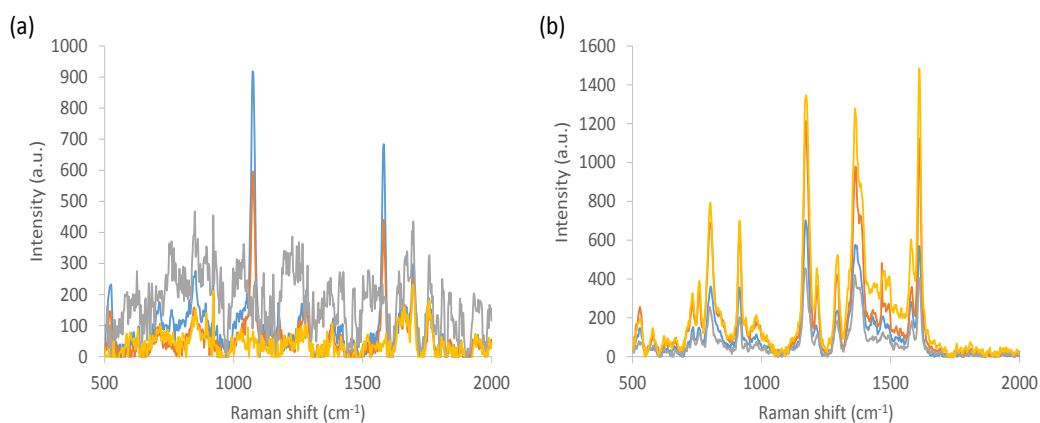


Figure 46. Baselined SERS spectra from LF strips lines of (a) MBA and (b) MGITC labelled his-tag Fab NTA-Ni AuNPs. Each lines is striped with a different CRP concentration ($\mu\text{g/mL}$): 500 (blue), 250 (orange), 125 (grey) and 62.5 (yellow). Spectra were baselined and averaged out of three measurements taken from each line. The integration time for all the 4 spectra of the MBA sample was 10 second; For the MGITC sample, the blue spectra (500 $\mu\text{g/mL}$ CRP) was taken at 0.1 second of integration time, however the remained three spectra (250, 125 and 62.5 $\mu\text{g/mL}$) were taken at 1 second.

The spectra in Figure 46A demonstrate that the strip containing MBA labelled antibody-gold conjugate, only gave SERS signals from two lines which had the highest CRP concentration (500 and 250 $\mu\text{g/mL}$). The two peaks at around 1070 and 1575 cm^{-1} are assigned to the aromatic ring vibrations of the MBA.²⁴² The other two lines (125 and 62.5 $\mu\text{g/mL}$) did not show any significant peaks from the MBA labelled conjugate. On the other hand, the spectra in Figure 46B show that the strip containing MGITC labelled conjugates gave strong SERS signals from all the four CRP lines. However, the intensity of the signals is not proportional to the CRP concentration lines. SERS is a very sensitive technique and in this experiment only three measurements were taken for each line. Despite the lines appearing quite homogeneous by the naked-eye, they show areas with various colloidal density when observed with a microscope. This effect is due to the heterogeneous structure of nitrocellulose. The importance of the collection area for a fair representation of the sample will be discussed later in this chapter. Results suggested that MGITC is a better RRM than MBA for labelling antibody-gold conjugates as SERS signals were detected from the 125 and 62.5 $\mu\text{g/mL}$ CRP lines. Moreover, the integration time used to analyse the MBA strip was 10 times longer than the time used for the MGITC strip. Therefore the use of MGITC labelled conjugate may reduce operational times. MGITC has its maximum absorption peak at around 630 nm which is in resonance with the 633 nm laser used in the experiment. As described in the introduction of this thesis, the technique is called surface-enhanced resonance Raman scattering (SERRS) and it has the sensitivity to rival or surpass that achievable with

fluorescence.⁸⁰ Due to the SERRS effect and the decreased analysis time need to achieve a reasonable signal, MGITC was chosen as RRM for the antibody-gold conjugates to be used in future experiments. Experimental details of the work in this paragraph is found in Section 5.4.1.

3.2.2. Preparation of MGITC labelled antibody-gold conjugate

Figure 47 shows a schematic representation for the optimised MGITC labelling process to the his-tag Fab NTA-Ni AuNPs with the synthesis discussed in Section 2.2. A MGITC concentration of 0.1 μ M was incubated with the conjugate for 30 minutes at room temperature. The MGITC intercalates between AuNPs surrounding and binds the metal surface by its thiol group.

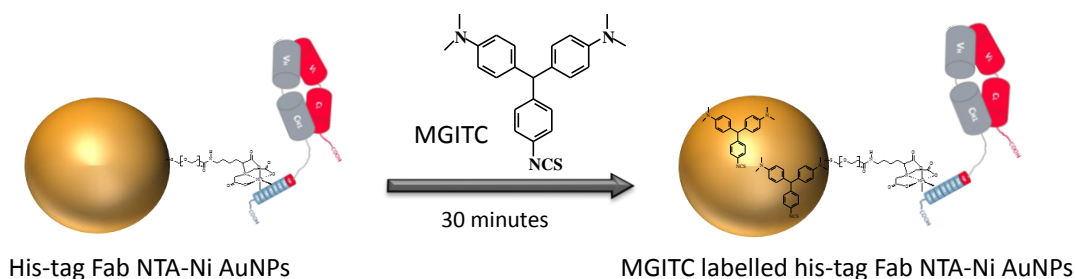


Figure 47. Schematic representation of the reaction of his-tag Fab NTA-Ni AuNPs with malachite green isothiocyanate (MGITC). Experimental data of the reaction is found in Section 5.4.2.

In order to estimate the enhancement factor of the MGITC signals due to its proximity to the gold surface, MGITC labelled his-tag Fab NTA-Ni AuNPs were then analysed by using a 638 nm laser Raman reader and compared with an equimolar solution of MGITC in HEPES buffer (Figure 48A). For details of experimental parameters see Section 5.4.2. Results show that MGITC signals are more intense when the antibody-gold conjugate are present, due to the SERRS effect. The vibration frequencies, showed as Raman shift, for the particular groups of the MGITC are: 1614 and 1585 cm^{-1} (ring C-C stretching); 1391 and 1366 cm^{-1} (N-phenyl stretching); 1220 cm^{-1} (C-H rocking) and 1174 cm^{-1} (in plane vibrations of ring C-H).²⁴³ A peak at around 1300 cm^{-1} is visible for both MGITC solution and MGITC labelled conjugate. This peak may be due to the presence of HEPES buffer in both samples. The peak at 1614 cm^{-1} was found to have the highest intensity, therefore it was chosen as signal readout for the SERRS-based LFIA. Moreover, extinction spectroscopy demonstrated that his-tag Fab NTA-Ni AuNPs remained stable after the MGITC functionalisation (Figure 48B).

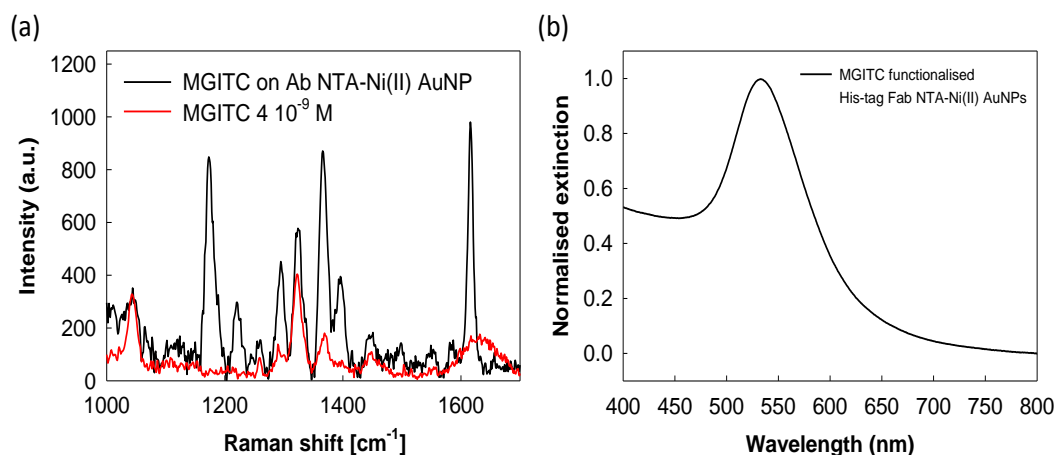


















Figure 48. (a) Raman spectrum of MGITC (red) and SERRS spectrum of MGITC labelled his-tag Fab conjugated NTA-Ni AuNPs (black). Spectra were taken using a 638 nm Raman spectrometer, laser power 40 mW, integration time 5 seconds. (b) Extinction spectroscopy for MGITC labelled his-tag Fab NTA-Ni AuNPs, $\lambda_{\max} = 533.5 \pm 2.7$ nm.

3.2.2.1 Compatibility of MGITC labelled antibody-gold conjugate with LFIA

It is important to evaluate the compatibility of MGITC labelled conjugates with the LFIA. The functionalisation of MGITC onto antibody-gold conjugates can cause interferences with the assay as non-specific bindings (NSB) can occur, which could lead to false positives or negatives.²⁴⁴ Therefore, an experiment to evaluate the degree of NSB that could occur, was required for the MGITC labelled conjugate. LF strips that contained 4 lines of CRP gradient from 500 to 62.5 $\mu\text{g}/\text{mL}$ were used in this experiment. The antigen-binding efficiency was evaluated by comparing the performance of MGITC labelled conjugate (Table 7B) with a non-labelled conjugate (Table 7A). Also, two control samples were run on LF strips: a MGITC labelled NTA-Ni AuNPs sample that contained no antibody (Table 7C) and a NTA-Ni AuNPs sample that contained no antibody and no MGITC (Table 7D). These two controls could assess the possibility that the lines on LF strips are due to the antibody-CRP binding or NSB. Experimental data of the study is described in Section 5.4.3. Results showed that the non-labelled antibody-gold conjugates produced lines with higher intensities compared to the MGITC labelled conjugate's lines. This can be explained by the partial inactivation of the antibody molecules caused by the reaction between isothiocyanate groups of the MGITC and primary amines situated on the antigen binding site.²⁴⁵ Finally, LF strips that contained MGITC NTA-Ni AuNPs and NTA-Ni AuNPs on the conjugate pads, did not show any red lines suggesting that no NSB occurred when conjugates is labelled with MGITC.


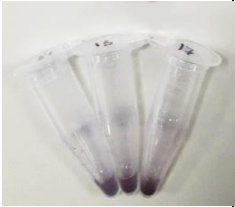
Table 7. Photographs of NC compartment of lateral flow strips performed to evaluate non-specific bindings. Strips used on this experiment contain 4 lines of CRP gradient from 500 to 62.5 $\mu\text{g}/\text{mL}$ (indicated by arrows). Conjugate pads were loaded respectively with (a) his-tag Fab NTA-Ni AuNPs, (b) MGITC labelled his-tag Fab NTA-Ni AuNPs, (c) MGITC labelled NTA-Ni AuNPs and (d) NTA-Ni AuNPs.

CRP lines ($\mu\text{g}/\text{mL}$)	(a)	(b)	(c)	(d)
500 →				
250 →				
125 →				
62.5 →				

3.2.2.2. Comparison of conjugation methods for MGITC labelled antibody-gold

The NTA-Ni AuNPs showed good stability and they were able to efficiently bind his-tag Fab antibodies in a straightforward manner, as discussed in Chapter 2 of this thesis. However, in order to attach the NTA-Ni group on AuNPs, external crosslinkers were required. Various conjugation methods were discussed in Section 1.3.2. Amongst them, passive absorption is one of the fastest, cheapest and straightforward method to conjugate antibodies. A comparison study between passive absorption and histidine/nickel conjugation was carried out for MGITC labelled conjugate. For the passive absorption, commercially available citrate capped AuNPs were incubated first with his-tag Fab antibodies (4 $\mu\text{g}/\text{mL}$) and then with MGITC (0.1 μM). For the histidine/nickel conjugation, the same amount of his-tag Fab antibodies and MGITC were added to the NTA-Ni AuNPs. Experimental details of this study are described in Section 5.4.4. The stability of the conjugates was evaluated by extinction spectroscopy and DLS (Table 8).

Table 8. Comparison between passive adsorption and NTA-Ni conjugations. The same amount of his-tag Fab antibody and MGITC was used for both methods. Table shows visual evaluation, DLS measurements and extinction spectroscopy parameters of the two different conjugates. Experiments were performed in triplicate.

Conjugation method	Antibody ($\mu\text{g/mL}$)	MGITC (μM)	Visual Evaluation	Z-Average (DLS, nm) & PDI	λ max. (nm)	O.D. _{@530 nm} (a.u.)
His-tag/ NTA-Ni	4	0.1		69 ± 7 & 0.22	531 ± 1	6.7 ± 0.6
Passive absorption	4	0.1		8539 ± 13185 & 0.71	551 ± 1	1.4 ± 0.3

A visual evaluation of the conjugates suggested that the passive absorption method led to unstable conjugate as the solution turned purple. This is due to the plasmonic coupling of two or more nanoparticles that interact with each other. DLS measurements confirmed the formation of aggregated particles for the passive absorption conjugation (PDI higher than 0.7). Finally, extinction spectroscopy indicated that the NTA-Ni conjugate was stable as it showed a LSPR of 531 nm and optical density (O.D.) equal to 6.7. On the other hand, passive conjugates showed a very low O.D. and a LSPR of 551 nm, suggesting a plasmonic coupling effect. These results suggested that conjugation methods where antibodies are well oriented on the AuNPs surface, such as the NTA-Ni/histidine method can improve the stability of MGITC labelled conjugates. The passive absorption method is not recommended for this application as his-tag Fab antibodies are not able to stabilise citrated capped AuNPs when MGITC is present. Therefore, his-tag Fab NTA-Ni AuNPs were chosen over passively adsorbed conjugates for the detection of CRP through the SERRS-based LFIA.

3.2.3. Sandwich format of SERRS-based LFIA

Stable MGITC labelled his-tag Fab NTA-Ni AuNPs were successfully synthesised and could be used in the development of a SERRS-based LFIA for the detection of human CRP in a sandwich-like format. The principle of the assay is schematised in Figure 49. Specifications of the LF strips used in this assay are found in Appendix A.

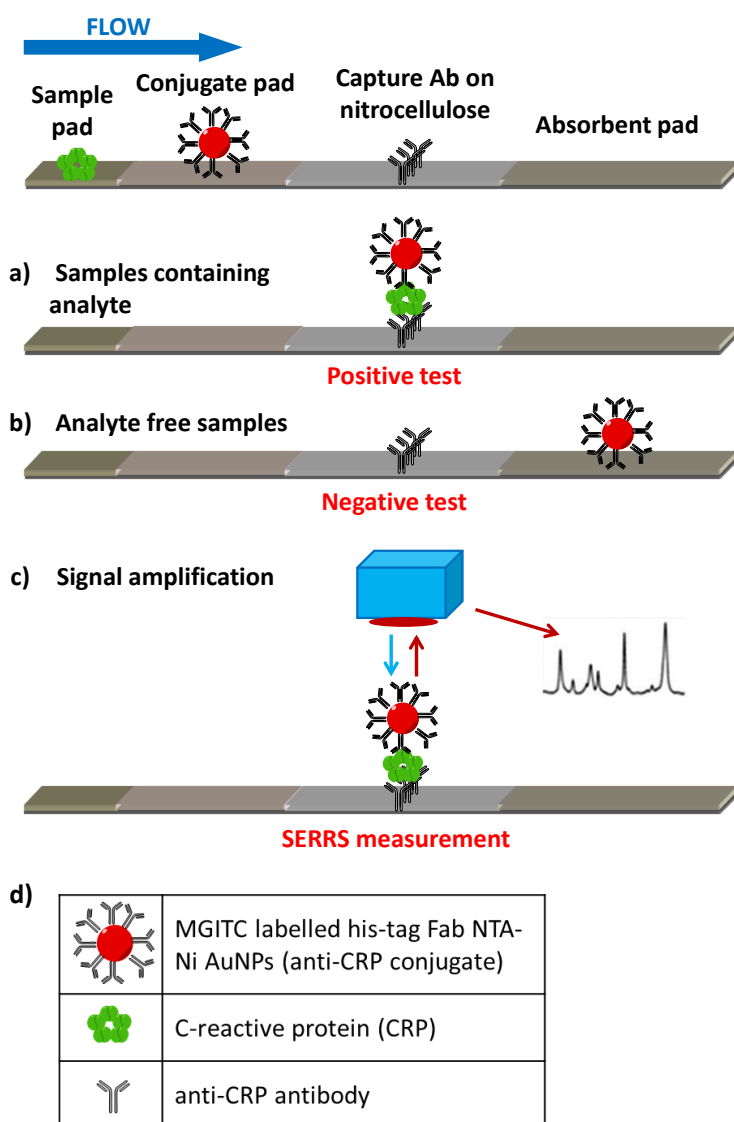
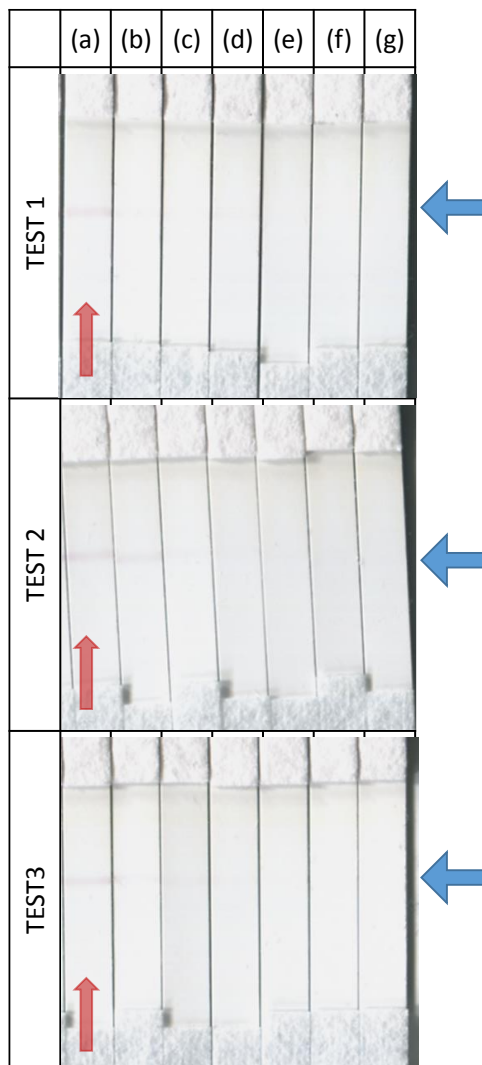


Figure 49. Schematic representation of the sandwich SERRS-based lateral flow immunoassay. Anti-C-reactive protein antibody (capture Ab) was placed to dry on the middle of nitrocellulose (test area). The conjugate pad was loaded with the MGITC labelled his-tag Fab NTA-Ni AuNPs (anti-CRP conjugate). Various concentration of C-reactive protein (analyte) were then placed on the sample pad to allow the anti-CRP conjugate to flow through the lateral flow strip. If the analyte is present in the sample, it binds both the conjugate and the capture Ab in a “sandwich” manner so a red line or spot appears in the test area (a). If the sample is analyte free, the conjugate will flow through the strip and no red line appears (b). After the strip was dry, test area is analysed using a 633 nm Raman spectrometer for signal amplification (c). Key legend (d).

The sandwich assay consists of a direct response signal/analyte. If the sample contains a specific amount of analyte, a binding process between the conjugate and the analyte occurs. The complex conjugate/analyte then flows through the strip until it binds the capture Ab placed in the middle of the nitrocellulose (Figure 49A). A red line should appear in this area and the test is positive if the CRP has been detected. If the sample does not contain any analyte, the conjugate should flow through the strip and no red line appears on the middle of the NC (negative test, Figure 49B). However, sometimes the concentration of the analyte is so low that a red line is difficult to perceive by the naked-eye. To overcome the limitation of a visual readout, a Raman microscope equipped with a 633 nm laser was used to amplify the signal from the test line (Figure 49C). The intensity of the SERRS signal can give an indication of the amount of analyte that is present in the sample. An optimisation study, shown in Appendix C1 was performed for the capture Ab. Three different capture Ab concentrations were evaluated: 0.1, 0.5 and 1 mg/mL. The study showed that the sensitivity of the assay improves when 0.5 mg/mL of capture Ab is used. These strips were prepared by striping a line of capture Ab on the NC using an Isoflow dispensing systems (for further information see Appendix A). As seen in other detection techniques, when high concentrations of CRP are present, there should be more NPs and MGITC present which should lead to a larger SERRS signal.²⁴¹ As the concentration of CRP decreases, so does the concentration of NPs that bind to it resulting in a lower SERRS signal. Therefore the concentration of CRP should be related to the SERRS signal and a limit of detection can be achieved.

In order to quantify the amount of CRP in a sample, a concentration study was necessary in order to understand the correlation between the SERRS signal and CRP concentration. The quantification study was carried out in HEPES buffer at pH 7.4 using MGITC labelled his-tag Fab NTA-Ni AuNPs conjugate that was prepared as discussed in Section 3.2.2. The his-tag Fab used in this assay was an anti-human CRP monoclonal antibody. LF strips were performed in triplicate and CRP solutions with concentrations from 1 to 100 ng/mL were used. Experimental data of the sandwich assay is described in Section 5.4.5. Pictures of the LF strips are shown in Table 9.

Table 9. Photographs of the nitrocellulose compartment of the lateral flow strips used for the sandwich assay. Conjugate pad was loaded with 5 μL of MGITC labelled his-tag Fab NTA-Ni AuNPs conjugate (O.D. 6.25). Test areas (blue arrows) were previously loaded with monoclonal anti-CRP antibody (capture Ab, 500 $\mu\text{g}/\text{mL}$). The assay was performed using various samples of CRP solutions in HEPES buffer at pH 7.4. CRP concentrations were as follows: (a) 100, (b) 50, (c) 25, (d) 10, (e) 5 and (f) 1 ng/mL. A blank sample (g) was run using only HEPES buffer at pH 7.4. Red arrows represent the flow direction of the sample through the strip. A pale red line is visible for samples with CRP concentration higher than 25 ng/mL (c), indicating that CRP was detected. For samples that contained CRP concentrations lower than 25 ng/mL (c), red lines were not visible at the naked-eye. The experiment was performed in triplicate using one batch of conjugate.



Results (shown in Table 9) suggest that a decrease of CRP concentration leads to a decrease of line intensity. However, the visual readout was challenging for CRP concentrations below 25 ng/mL. Therefore, in order to increase the limit of detection of the assay, LF strips were analysed by SERRS. A Raman microscope equipped with a 633 nm laser excitation was used to measure the SERRS intensity on the test area. The choice of the right magnification lens used in the measurements, had to take into consideration the sampling error that is related to a small size of the focused laser spot. A study by Crawford *et al.* indicated that a smaller

laser spot leads to a larger deviation in the accuracy and a greater imprecision of the measurement.²⁴⁶ This can be explained by the equation which relates the diameter of the laser spot (d) to the numerical aperture (NA) by the Abbe resolution limit (Equation 7).²⁴⁷

$$d = \frac{\lambda}{2 NA}$$

Equation 7. Abbe diffraction limit. λ is the wavelength (nm) of the incident beam, NA is the numerical aperture and (d) the diameter of the spot.

Equation 7 shows that if the laser wavelength is constant (λ), the smaller NA and the bigger the spot. Therefore, in order to obtain a big diameter laser spot, a 5 times magnified objective with a numerical aperture (NA) equal to 0.12 was chosen amongst other objectives available with bigger NA. A laser spot diameter of 2.63 μm was found for the objective used in this test. Each strip was placed under the microscope and test area was investigated. Before sampling each strip, it is important to identify the centre of the test area so that the spectra are taken on the right position. Therefore, a “find the line” experiment was carried out by taking an arbitrary number of spectra across the nitrocellulose in an imaginary line that is perpendicular to the test area (Figure 50).

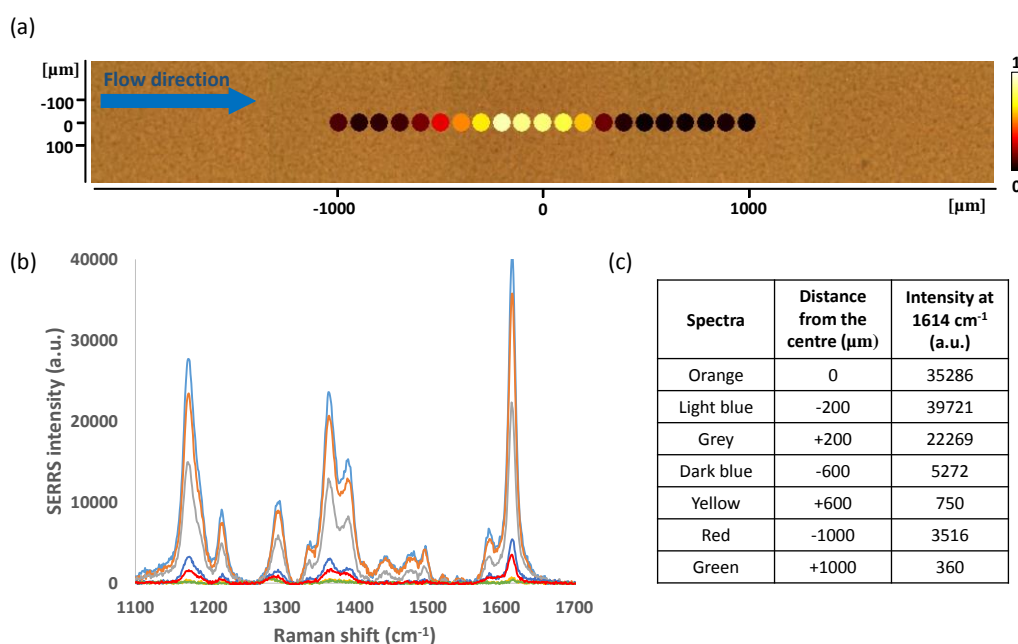


Figure 50. The “find the line” experiment. (a) 5x magnified image of the middle of nitrocellulose where capture antibody was dried. The 21 points represent single SERRS measurements that were taken at a distance of 100 μm from each other’s. (b) SERRS spectra of the test area at different distance position form an arbitrary centre. (c) Table representing spectra colours with relatives positions on the test area and their signal intensity at 1614 cm^{-1} .

Each spectrum was taken at 100 μm apart. The intensity of the peak at 1614 cm^{-1} for each spot were then compared and the most intense spectrum chosen for the centre of the test area. Figure 50 shows an example of the “find the line” experiment. In this case, the most intense signal was achieved at a position of -200 μm . Consequently, the strip was moved 200 μm to the left, and that position on the NC became the centre of the test area. An area of 600 x 3600 μm was then Raman mapped using a rectangular mapping mode. 91 spectra each map were collected and results are shown in Table 10.

Table 10. 5x magnified map images of the test area for the sandwich lateral flow strips at various CRP concentrations. Map value scale represents the intensity to baseline of the Raman shift region between 1600 and 1630 cm^{-1} . Each map represents 91 single spectra taken in a rectangular distribution: 7 spectra every 100 μm on the x axis and 13 spectra every 300 μm on the y axis. Measurements were carried out using a Renishaw Raman microscope equipped with a 633 nm laser. Test was performed in triplicate.

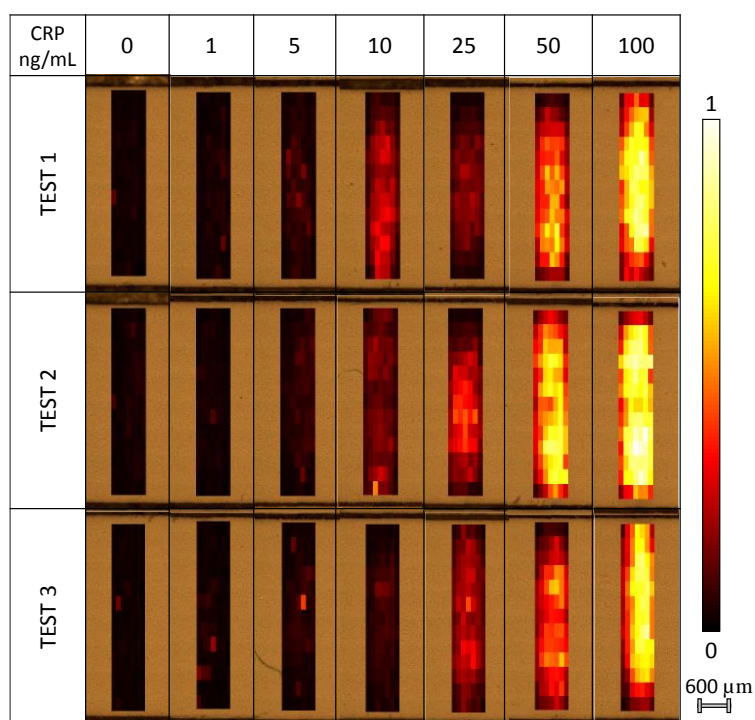


Table 10 shows the map images of the test area of strips used for the concentration study. The map scale value represents the intensity to baseline of the peak between 1600 and 1630 cm^{-1} of the MGITC labelled his-tag Fab NTA-Ni AuNPs conjugate. Black areas represent mapped surface that showed the lowest SERRS intensity. On the other hand, white areas showed the highest SERRS intensity. Map images were normalised within the test from an arbitrary value of 0 (black) to 1 (white). Results suggested that as the CRP concentration increases, the SERRS signal of the test area increases due to the presence of MGITC labelled conjugate. Signal was present across all the samples from 100 (yellow and orange areas) to

1 ng/mL of CRP (red areas). Also, the signal is homogenous across the area with stronger intensity near the centre. When comparing these results with the visual readout shown in Table 9, it is evident that SERRS can amplify the LFIA lines up to 25 times. Figure 51 shows the averaged intensities of the 1614 cm^{-1} peak for each map and replica.

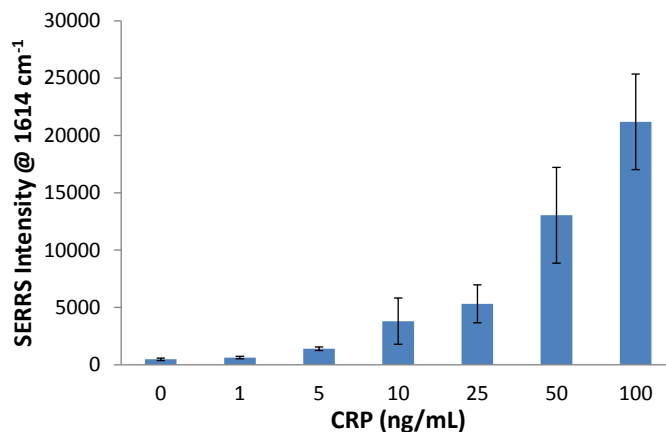


Figure 51. Bars chart representing averaged SERRS intensity values at 1614 cm^{-1} from the maps on test area of the sandwich lateral flow immunoassay. Error bars represent the standard deviation of three replica.

Results in Figure 51 show that the SERRS signal increases with the CRP concentration. Although, a weak SERRS signal was also detected for blank samples (CRP concentration equal to 0). This phenomenon could be attributed to the retention of conjugate in the nitrocellulose or could be due to NSB occurring between conjugate and capture antibody. In order to determine the cause of this signal, the nitrocellulose of each strip was analysed by taking 20 spectra before and 20 after the test area as shown by orange squares in Figure 52A. The 40 spectra were then baseline corrected and the intensities of peak at 1614 cm^{-1} were averaged.

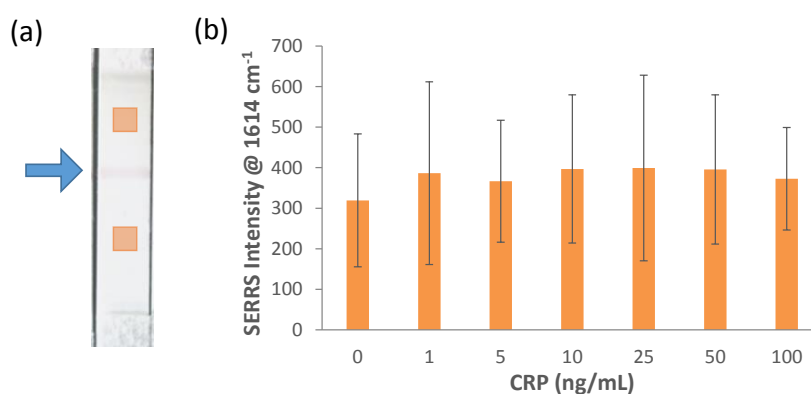


Figure 52. (a) Photograph of the nitrocellulose part of the sandwich lateral flow immunoassay. Orange squares represent the collection area for background signal investigation. The blue arrow represents the test area. (b) Bars chart representing background signals at 1614 cm^{-1} on the nitrocellulose compartment, away from the test area. 40 spectra per strip were taken and averaged (20 before and 20 after the test area). Errors bar indicate standard deviation of three replica.

Results shown in Figure 52B suggest that background signals have the same intensity no matter what CRP concentration was run on the strip. Therefore the background signal is attributed to the retention of conjugate during its flow through the nitrocellulose. In order to obtain the true SERRS spectra for each CRP concentration, this background signal was subtracted for the averaged spectra on the test area (Figure 53A). A calibration curve was created by plotting the intensities at 1614 cm⁻¹ of the background subtracted spectra against the CRP concentration (Figure 53B).

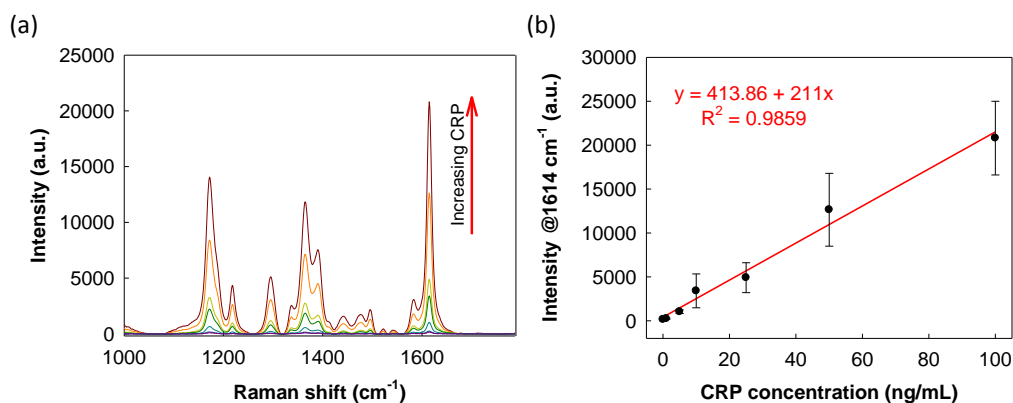


Figure 53. (a) Averaged and background corrected SERRS spectra for the sandwich assay. Each spectrum corresponds to a fixed concentration of CRP: 100 (burgundy), 50 (orange), 25 (light green), 10 (dark green), 5 (light blue), 1 (dark blue) and 0 (purple) ng/mL. An accumulation time of 5 seconds was used for each spectrum. (b) Corresponding calibration curve of the peak intensity at 1614 cm⁻¹ against CRP concentrations with a line of best fit. Three lateral flow tests were performed for each concentration. Error bars indicate the standard deviation obtained from three replicates for each concentration.

Results in Figure 53B suggested that the SERRS intensity was directly proportional to the CRP concentration. A linear regression line of the best fitted points shows a correlation coefficient (R^2) equal to 0.9859. A limit of detection (LOD) was calculated for this assay as shown in Equation 8.

$$LOD = \frac{3 * SD_{blank}}{slope}$$

Equation 8. Calculation of the limit of detection (LOD) for the sandwich lateral flow immunoassay.

SD_{blank} is the standard deviation of the blank tests (CRP concentration equal to zero), and it was found to be equal to 129.38. The slope of the regression line was found to be equal to 211.01. By replacing these values in the Equation 8, a calculated LOD was found to be equal to 1.84 ng/mL. This value is the same order of magnitude of LODs calculated for other LFIA for the detection of CRP.^{235,237,239}

A wider CRP concentration range was also investigated for the sandwich assay in HEPES buffer. Test strips were also run using various solutions of CRP from 100 to 5000 ng/mL. Strips were analysed by SERRS as shown previously and the results of the calibration curve is shown in Figure 54.

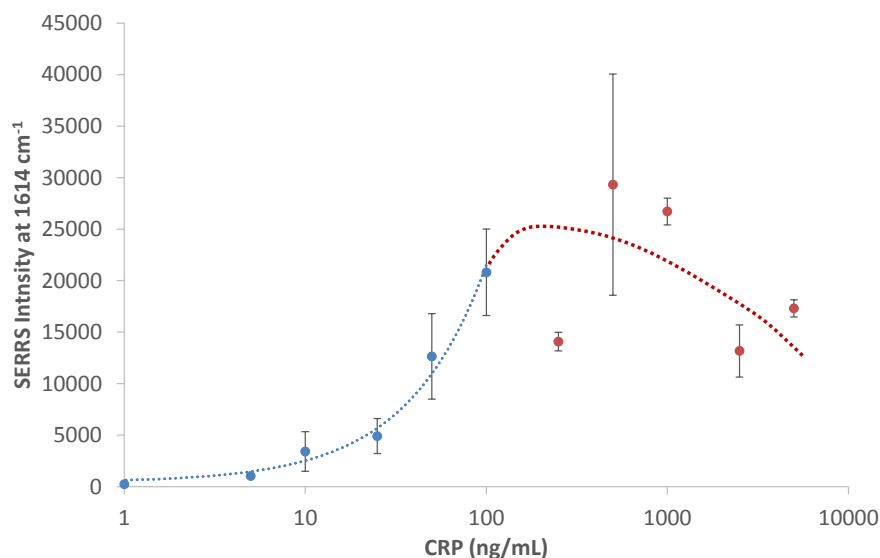


Figure 54. Graph representing the hook effect for high concentration of CRP in the sandwich lateral flow assay. Blue dots represent the linear range and red dots represents the non-linear range where the hook effect occurs. The x axis is shown as \log_{10} for better understanding of the data. Error bars represents standard deviation of three replica.

The graph in Figure 54 shows the limitation of the sandwich assay for detecting a wide range of CRP. The intensity is linear with the concentration until 100 ng/mL, after this value, the signal stops increasing for higher CRP concentrations. This phenomenon is called the “hook effect” and it is very common in sandwich immunoassays. The major cause is the high-dose of antigen that saturates both capture antibody and conjugate binding sites.²⁴⁸ An efficient method to overcome to this effect is to redevelop the assay wherever possible, by using the competitive format instead of the sandwich-like format.²⁴⁹ Therefore, a competitive SERRS-based LFIA for the detection of CRP was developed and it is discussed in the next section.

3.2.4. Competitive format of SERRS-based LFIA

One of the reasons to develop a competitive assay is the possibility to quantify the analyte in a wider concentration range. This is important as the diagnosis of diseases, such as rheumatoid arthritis and sepsis, CRP values in serum are found respectively in a range from 1 to >100 $\mu\text{g/mL}$ and >250 $\mu\text{g/mL}$.²⁵⁰ Moreover, sometimes antigens contain only one binding site towards their antibodies, therefore sandwich format assays cannot be performed. A

convenient way to carry out an immunoassay when capture antibody is not available is the competitive format. In this format the antigen (analyte) is immobilised on the nitrocellulose and the lateral flow signal is inversely proportional to the analyte concentration. Schematic representation of the competitive SERRS-based lateral flow assay described in this paragraph is shown in Figure 55.

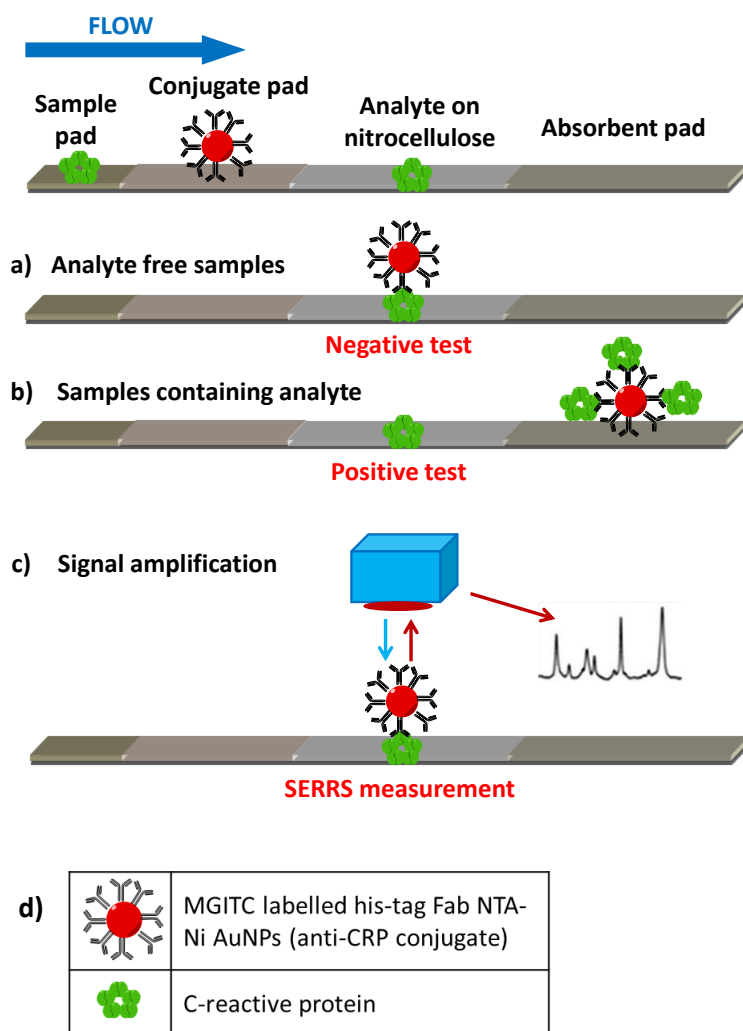

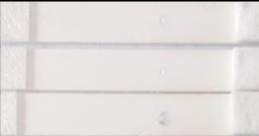
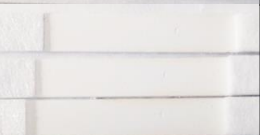
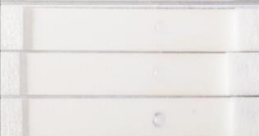
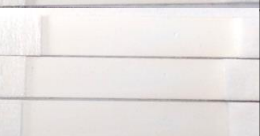
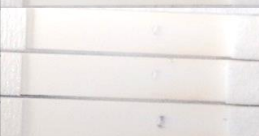
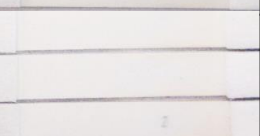
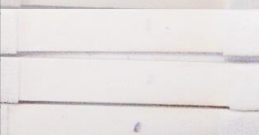
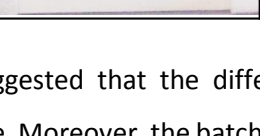
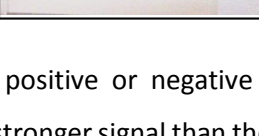
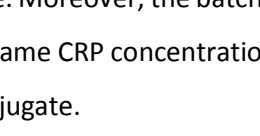
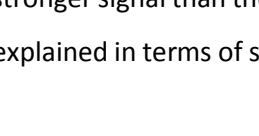
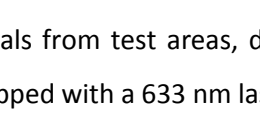
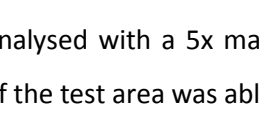
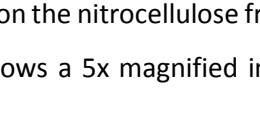
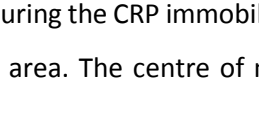








Figure 55. Schematic representation of the competitive SERRS-based lateral flow immunoassay. A fix concentration of C-reactive protein (CRP) was previously placed to dry on the middle of nitrocellulose (test area). The conjugate pad was then loaded with the MGITC labelled his-tag Fab NTA-Ni AuNPs (anti-CRP conjugate). Various concentrations of CRP (analyte) were then placed on the sample pad to allow the anti-CRP conjugate to flow through the strip. If the sample does not contain analyte, the conjugate binds the CRP that is immobilised on the nitrocellulose (a). If the analyte is present, it binds the conjugate which flows through the strip without any binding on the nitrocellulose (b). After the strip was dry, test area was analysed using a 633 nm Raman spectrometer for signal amplification (c). Key legend (d).

As seen in the previous section, the NC compartment of LF strips are usually striped with lines of antibody or protein solutions by a suitable dispensing system.¹⁸³ Unfortunately, due to limited access to this instrument, test areas for this assay were prepared by pipetting 0.5 μ L

of CRP in the middle of the NC. The optimised concentration of CRP immobilised onto the NC was found to be equal to 50 µg/mL. The optimisation study is described in Appendix C2. In order to evaluate a wide dynamic range, CRP samples at concentrations from 0.001 to 500 µg/mL were used in this assay. Moreover, the reproducibility of the assay was evaluated by using three different batches of antibody-gold conjugate that were prepared on different days. Experimental data of this assay is described in Section 5.4.6. Photographs of the test strip for the competitive assay are shown in Table 11.

Table 11. Photographs of the nitrocellulose compartment of lateral flow strips for competitive assay. Test area were prepared by spotting 0.5 µL of CRP (50 µg/mL) and let it to dry for 1 hour at 37 °C. Three different batches of MGITC labelled his-tag Fab NTA-Ni AuNPs were placed on the conjugate pads (5 µL). The experiment was performed using various concentration of CRP, from 0.001 to 500 µg/mL. Pictures were taken few days after the test was complete. The black spots, initially red, of the batch n° 3 were due to aggregation of the conjugate on nitrocellulose over time.

CRP (µg/mL)	Batch no	Test area ↓	CRP (µg/mL)	Batch no	Test area ↓
500	1		0.1	1	
	2			2	
	3			3	
100	1		0.01	1	
	2			2	
	3			3	
10	1		0.001	1	
	2			2	
	3			3	
1	1		0	1	
	2			2	
	3			3	

Results in Table 11 suggested that the difference between positive or negative test is challenging to determine. Moreover, the batch n° 3 provided a stronger signal than the other two batches within the same CRP concentration. This could be explained in terms of stability of the third batch of conjugate.

In order to amplify signals from test areas, dry strips were analysed with a 5x magnified Raman microscope equipped with a 633 nm laser. The centre of the test area was able to be identified by a mark left on the nitrocellulose from the pipette during the CRP immobilisation procedure. Figure 56 shows a 5x magnified image of the test area. The centre of mark is

highlighted by the intersection of the blue lines. The big blue square represents an area of 1200 μm per side where SERRS spectra were collected (map area).

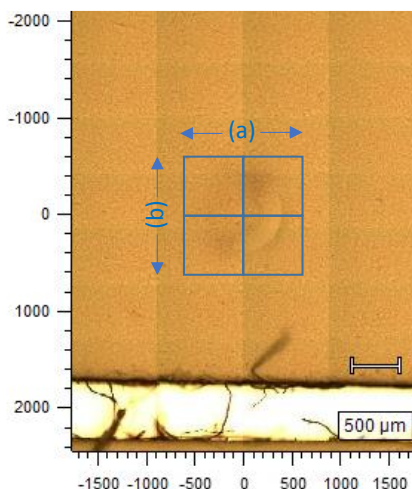
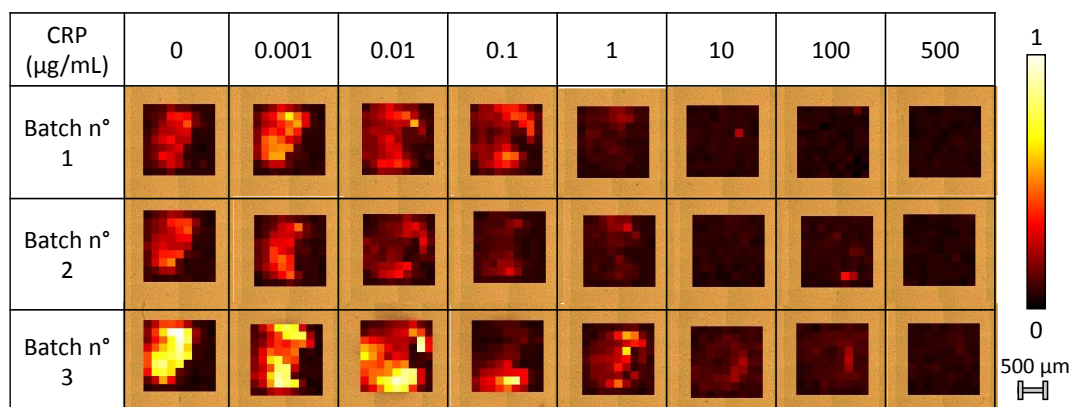


Figure 56. 5x magnified images from the white light of the Raman microscope representing test area of the competitive lateral flow immunoassay strips. The blue square represents the area where spectra were collected (map area). The intersection of the blue lines represents the centre of the test area. The side “a” and “b” are 1200 μm length.

Once the centre of the test area was identified for each strip, 81 spectra (9 spectra along the x axis and 9 spectra along the y axis) were taken using a square mapping mode. Results are shown in Table 12.

Table 12. 5x magnified map images of the test area for the competitive lateral flow strips at various CRP concentrations. Map value scale represents the intensity to baseline of the Raman shift region between 1600 and 1630 cm^{-1} . Each map represents 81 single spectra taken in a square distribution: 9 spectra every 100 μm on the x axis 9 on the y axis. Measurements were carried out using a Renishaw Raman microscope equipped with a 633 nm laser. Test was performed in triplicate using three different batch of anti-CRP conjugate.



The map images in Table 12 demonstrated that SERRS amplification allowed the visualisation of the test areas that otherwise were very challenging to see by the naked-eye (Table 11). The map scale value on the right side of Table 12 represents the arbitrary intensity to baseline

of the MGITC labelled conjugate peak between 1600 and 1630 cm^{-1} . Samples that contained none or low CRP concentration showed the highest SERRS intensity. As the concentration increased, less MGITC labelled conjugate was able to bind to the test area, hence the SERRS intensity decreased. This inverse correlation signal/concentration is expected for competitive format assays. Each conjugate batch was able to detect CRP, however differences in intensities were found for the same CRP concentration, across different batches. Batch n° 3 showed higher SERRS intensity than batches n° 1 and 2. Subsequently, SERRS spectra for each CRP concentration were averaged (Figure 57A) and the peak at 1614 cm^{-1} was plotted against the logarithmic of the concentration as shown in Figure 57B.

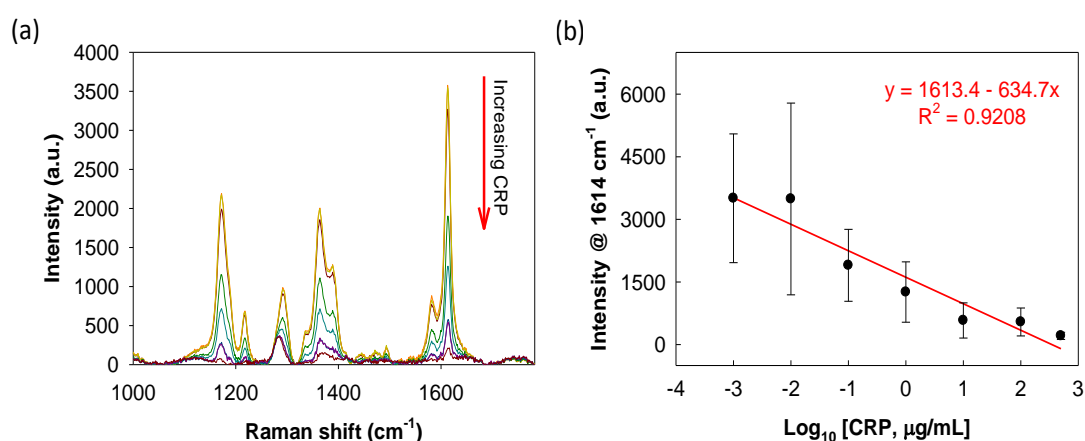


Figure 57. (a) Averaged SERRS spectra on the test area of the strips for the competitive lateral flow assay. Each spectrum corresponds to a fixed concentration of C-reactive protein: 0 (brown), 0.001 (orange), 0.01 (light green), 0.1 (dark green), 1 (light blue), 10 (dark blue), 100 (purple) and 500 (red) $\mu\text{g}/\text{mL}$. Three replica were performed for each CRP concentration. Each measurement is the average of 81 spectra. $\lambda_{\text{ex}} = 633 \text{ nm}$, 3 seconds exposure time, laser power 100% (8 mW). (b) Corresponding calibration curve of the peak intensity at 1614 cm^{-1} against the logarithm of the C-reactive protein concentration with a line of best fit. Error bars indicate the standard deviation obtained from the three conjugate batches.

An inverse regression line of the best fitted points was calculated for CRP concentration from 0.001 to 500 $\mu\text{g}/\text{mL}$. A correlation coefficient (R^2) equal to 0.9208 demonstrates a linear response between \log_{10} CRP and SERRS signal. Although, it is evident from the graph in Figure 57B that the error bars, that represent standard deviations of three different measurements, are bigger for lower CRP concentrations. This issue can be explained considering that the assay was performed in replica using three different batches of MGITC labelled conjugates. An LOD for the competitive assay was calculated as 90% of the highest intensity obtained with the presence of CRP.²⁵¹ The linear correlation between log CRP and Intensity is ruled by the Equation 9.

$$SERRS\ Intensity = 1613.4 - 634.7 \log[CRP]$$

Equation 9. Correlation between SERRS Intensity and CRP concentration in the lateral flow competitive assay.

The highest intensity on the equation was found to be equal to 3505.73 which corresponds to 1 ng/mL of CRP. The 90% of this value is 3155.16 and by substituting this value in to Equation 9, the LOD was found to equal to 3.7 ng/mL. Even if the LOD is higher than the value found for the sandwich assay, it is now possible to have a linear correlation with higher CRP concentrations. It is always important to have a wide dynamic range, especially with analytes such as CRP that are present in biological samples at high levels. The hook effect, that was limiting the detection of high CRP concentrations for the sandwich assay, is now removed by performing a competitive assay. Also, competitive formats are important for the detection of small molecules where sandwich assays are not available because of the presence of one binding site antigen-antibody.

3.2.5. Performance of SERRS-based LFAs in biological samples

In order to assess the validity of the SERRS-based LFAs in biological environments, both sandwich and competitive tests were performed in a solution containing foetal bovine serum (FBS). FBS is the blood fraction from a bovine foetus that has naturally coagulated and then centrifuged to eliminate blood cells. This product contains an array of various proteins and it can be used as an alternative to human blood serum to develop immunoassays techniques. The selectivity of the assay was also determined using a non-specific antigen such as human chorionic gonadotropin (hCG). The concentration of CRP in human blood, for a healthy patient is normally less than 1 µg/mL.²³³ Concentrations between 1 and 3 µg/mL are considered as average cardiovascular risk, 3.1 and 10 µg/mL high risk and if the CRP concentration is higher than 10 µg/mL the risk of cardiovascular diseases become very high. Therefore, a concentration of CRP which has biological significance was used in this experiment. For details of experimental data see Section 5.4.7.

For the sandwich assay, three different samples that contained a 50% solution of FBS were run on sandwich LF strips that contained 1 mg/mL of capture Ab. Sample pads were loaded with: CRP solutions of 5 µg/mL (Figure 58A), hCG solutions of 5 µg/mL (Figure 58B) and blank solutions containing only FBS in HEPES buffer (Figure 58C). The pH of the samples was kept under buffer conditions using a HEPES solution at pH 7.4. Tests were performed in triplicate.

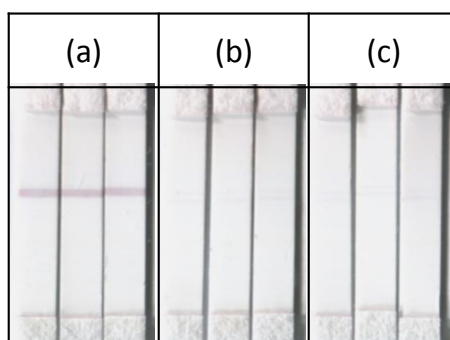


Figure 58. Photographs of sandwich lateral flow test strips used for the biological conditions experiment. Nitrocellulose were striped with a 1 mg/mL solution of capture Ab. MGITC labelled his-tag Fab NTA-Ni AuNPs were used as conjugate. Sample pads were loaded with a 50% solution of FBS that contained: (a) 5 $\mu\text{g}/\text{mL}$ of CRP, (b) 5 $\mu\text{g}/\text{mL}$ of hCG and (c) HEPES buffer (blank). Tests were performed in triplicate.

The strips were then analysed with a 633 nm laser Raman microscope. 49 spectra were taken on the test areas of each strip and intensities of the peak at 1614 cm^{-1} were averaged in order to determine the ratio between positive and negative samples (Figure 59).

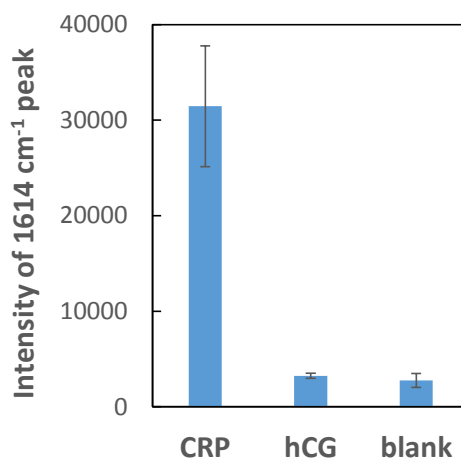


Figure 59. Bars chart representing averaged peak intensity at 1614 cm^{-1} of 49 spectra taken on the test area of sandwich lateral flow strips for biological conditions experiment. Error bars represent standard deviation of three replica.

Results in Figure 59 show that the intensity for the positive test (CRP) is circa 10 times higher than the intensity measured for the negative (hCG) and blank samples. This suggested that the sandwich format of the SERRS-based LFIA developed in this work is valid in biological environment and it can be applied for the detection of CRP in biological matrices.

The same test was performed for the competitive assay. Three different samples that contained a 50% solution of FBS were used during this assay. LF strips contained 50 $\mu\text{g}/\text{mL}$ of CRP immobilised on nitrocellulose. Sample pads were loaded with: CRP solutions of 5 $\mu\text{g}/\text{mL}$

(Figure 60A) hCG solutions of 5 $\mu\text{g}/\text{mL}$ (Figure 60B) and blank samples containing only FBS in HEPES buffer (Figure 60C). The pH of the samples was kept under buffer conditions using HEPES solution pH 7.4. Tests were performed in triplicate.

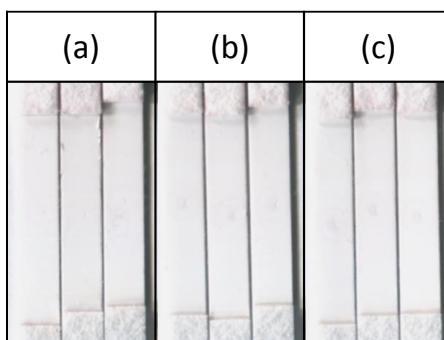


Figure 60. Photographs of competitive lateral flow test strips used for the biological conditions experiment. A 50 $\mu\text{g}/\text{mL}$ solution of CRP was placed on the middle of the nitrocellulose and left to dry for 1 hour. MGITC labelled his-tag Fab NTA-Ni AuNPs were used as conjugate. Sample pads were loaded with a 50% solution of FBS that contained: (a) 5 $\mu\text{g}/\text{mL}$ of CRP, (b) 5 $\mu\text{g}/\text{mL}$ of hCG and (c) HEPES buffer (blank). Test were performed in triplicate.

The strips were then analysed with a 633 nm laser Raman microscope. 37 spectra were taken on the test areas of each strip. Spectra were averaged and the intensities of the peak at 1614 cm^{-1} was used to determine the ratio between positive and negative tests (Figure 61).

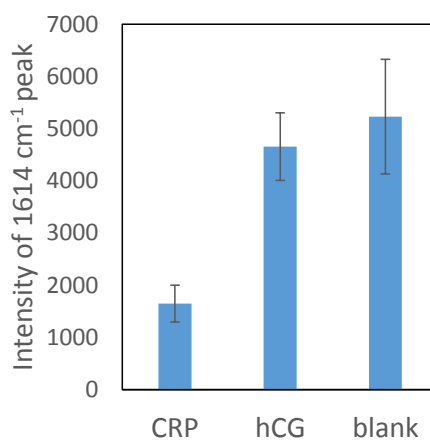


Figure 61. Bars chart representing averaged peak intensity at 1614 cm^{-1} of 37 spectra taken on the test area of competitive lateral flow strips for biological conditions experiment. Error bars represent standard deviation of three replica.

Results in Figure 61 show that the intensity for the positive test (CRP) is circa 3 times smaller than the intensity measured for the negative (hCG) and blank (test). These result suggested that competitive format of SERRS-based LFIA is also valid in biological environment and it can be applied for the detection of CRP in matrices such as serum or blood plasma.

3.3. Conclusions

LFIA is a rapid, robust and cost-effective analytical method for the detection of a wide range of biomolecules. Although, the sensitivity of this technique is often low, due to the limitation of naked-eye detection. In order to increase the sensitivity of the LF test for the detection of CRP, a SERRS amplification method was developed in this chapter. It was demonstrated that the use of the SERRS technique increases the sensitivity of the LF test up to 25 times more compared to visual detection. Moreover, conjugation methods performed in order to create SERRS active antibody-gold conjugates were investigated. The results showed that the NTA-Ni conjugation method, developed in Chapter 2 of this thesis, demonstrated better stability than passively absorbed conjugates. The possibility of developing two different formats for the detection of CRP was another fundamental achievement of this project. The compatibility of the SERRS active conjugates for competitive and sandwich format LFIA was fully demonstrated. The lowest LOD was achieved by using the sandwich format and it was equal to 1.84 ng/mL. This value is the same order of magnitude of calculated LODs for other advanced LFIAs. For example Oh *et al.* have found a value of 0.65 ng/mL by using a three-line strip test.²³⁵ Also, other LFIAs which amplification methods are based on fluorescence and chemiluminescence can detect respectively 8.5 and 1.05 ng/mL of CRP.^{237,239} Also, the competitive LFIA developed here was able to overcome assay interferences such as the hook effect. Finally, it was shown that the SERRS-based LFIA can be performed in biological samples without losing the selectivity towards the analyte. A consideration for future work would be that SERRS active NTA-Ni AuNPs developed in this project may be used for multiplexed analysis due to the simplicity of the conjugation/labelling methodology and the potential for PoC analyte detection with the emergence of portable Raman readers.

CHAPTER 4: The Use of Gold Nanostars for Highly-Sensitive Lateral Flow Immunoassay

4.1. Aims and overview

In the last decade a large number of publications have focused on the advantages of integrating gold nanostars (AuNSs) into various immunoassays as an alternative to spherical AuNPs. Park *et al.* demonstrated that using AuNSs improves the sensitivity of plasmonic assays compared to spherical AuNPs where the group used streptavidin as a model target.²⁵² Mehn *et al.* developed a paper-based SERS active substrate for the detection of apomorphine. They compared spherical gold and star-shaped nanoparticles, concluding that the latter showed better sensitivity.²⁵³ More recently, AuNSs have been used as antibody labels in LFIA. As described in Section 1.4 of this thesis, LFIA is a rapid and robust analytical method that is able to detect various analytes. LFIA can suffer due to lower sensitivity, there are however several amplification methods in development in order to surpass this limitation. AuNSs play an important role in the development of highly-sensitive LFA when the signal amplification is performed by SERS. Maneepprakorn *et al.* in 2016 developed a SERS-based LFIA for the detection of influenza A. AuNSs were conjugated with antibody and 4-aminothiophenol, leading to an improvement in sensitivity of over 300 times greater than visual detection and over 37 times compared to fluorescence.²⁰⁷ Another example that shows the advantages of using AuNSs in LFIA is demonstrated by the research of Serebrennikova *et al.*²⁰⁶ A LFIA for the detection of prolactin was developed using stars and popcorn-shaped nanogold labels. A limit of detection of 0.1 ng/mL was reached using these anisotropic materials.

In this chapter the advantages of using AuNSs in the development of a LFIA for the detection of human chorionic gonadotropin (hCG) will be shown. Together with luteinizing hormone (LH), follicle stimulating hormone (FSH) and thyrotropin (TSH), hCG is part of the glycoprotein hormones family. They consist of two subunits: α (alpha) which is identical in all four hormones and β (beta) which is characteristic of the individual hormone.²⁵⁴ hCG is produced by the syncytiotrophoblast of the placenta and can be found in urine or blood during pregnancy. Levels of hCG can be monitored to detect early pregnancy, threatened abortion,

ectopic pregnancy or Down's syndrome.²⁵⁴ Moreover, high levels of β -hCG combined with α -fetoprotein in blood can be an indication of cancer.^{255,256} One of the first analytical methods used to detect hCG and understand its biology was a radioimmunoassay developed by Vaitukaitis and co-workers.¹⁷⁷ Their research was the driving force for the early development of LFIAs (pregnancy test). Nowadays, pregnancy tests are commercially available. However, their sensitivity is variable and the limit of detection does not exceed 25 ng/mL.²⁵⁴ This value allows the detection of pregnancy at approximately 7 days after conception. However, the need for a more sensitive assay is crucial for the monitoring of hCG-related diseases such as trophoblastic tumours of placental and germ cell origin.²⁵⁷

The aim of this chapter is to develop a LFIA which is capable of detecting a very low concentration of hCG by using AuNSs as antibody labels. Various batches of prototype AuNSs were acquired from BBI Solutions and characterised by SEM, extinction and Raman spectroscopy. In order to show the advantages of AuNSs in SERS and LFIA a direct comparison with spherical AuNPs was carried out. Moreover, the evaluation of AuNSs with various RRM and conjugation with anti-hCG antibodies are reported. Finally, a SERS-based LFIA for the detection of hCG in pseudo-biological matrix with a comparison between SERS and visual signal readouts were performed.

4.2. Results and discussion

4.2.1. Characterisation of gold nanostars

Various batches of gold nanostars (AuNSs) were supplied by BBI Solutions. The fabrication of AuNSs involved use of sodium citrate as reducing agent and no surfactants were added during the preparation. AuNSs batches differ from each other by the reaction volume, although experimental data of AuNSs used during this project was limited because the work is commercially sensitive. AuNSs synthesis that have been published in the last few decades are based on a two-step process known as “seed-mediated growth”.⁴⁷ In the first step, smaller spherical particles are formed (seeds). In the second step, more gold ions are added along with possible surfactants such as cetrimonium bromide and reducing agents so seeds can grow into larger anisotropic particles. By adjusting the ratio seed/growth solution is possible to tune shape and morphology of AuNSs.²⁵⁸ The optical properties of BBI AuNSs were analysed by extinction spectroscopy and DLS (see Section 5.5.1 for experimental data). Table 13 shows LSPR peaks and optical density values of 10 different AuNSs batches. In order to evaluate the stability of AuNSs, these parameters were rechecked 30 days later from the acquisition of the batch.

Table 13. LSPR peak (λ_{\max}) and optical density (O.D.) of each AuNSs batch on the first day and after 30 days of storage at 8 °C. $\lambda_{30 \text{ days}}$ represents the λ_{\max} after 30 days. λ_{1d} represents the λ_{\max} on the first day. The O.D. decrease (%) was calculated as: $(\text{O.D.}_{\text{day 1}} - \text{O.D.}_{30 \text{ days}}) \times 100$.

Batch N°	Day 1		30 days later (stored at 8°C)		$\lambda_{30d} - \lambda_{1d}$ blueshift (nm)	O.D. decrease (%)
	λ_{\max} (nm)	O.D.	λ_{\max} (nm)	O.D.		
16967	674	1	599	0.94	75	6
16975	724	1.07	701	1.03	23	4
16976	714	0.98	677	0.88	37	5
16977	691	1.06	661	1.02	30	4
16978	661	1.13	630	1.15	31	-2
16979	657	0.97	623	0.95	34	2
16980	726	0.94	717	0.94	9	0
16981	817	1.16	774	0.99	43	15
13098	838	1.22	821	1.16	17	5
17003	718	1.18	688	1.1	30	7

Results in Table 13 showed that the λ_{\max} for each batch of AuNSs was shifted to smaller wavelengths (blueshift) over 30 days. However, optical densities (O.D.) did not change significantly over time, suggesting that AuNSs remained stable. The observed blueshift

suggests that a process of Ostwald ripening occurred over time. This phenomenon leads to the gradual transformation of the AuNSs into spherical particles. It is caused by the dissolution of small crystals or sol particles and the redeposition of the dissolved species on the surfaces of larger crystals or sol particles.^{259,260} The presence of small particles, that causes the AuNSs degradation, can be evaluated by DLS measurements (Figure 62).

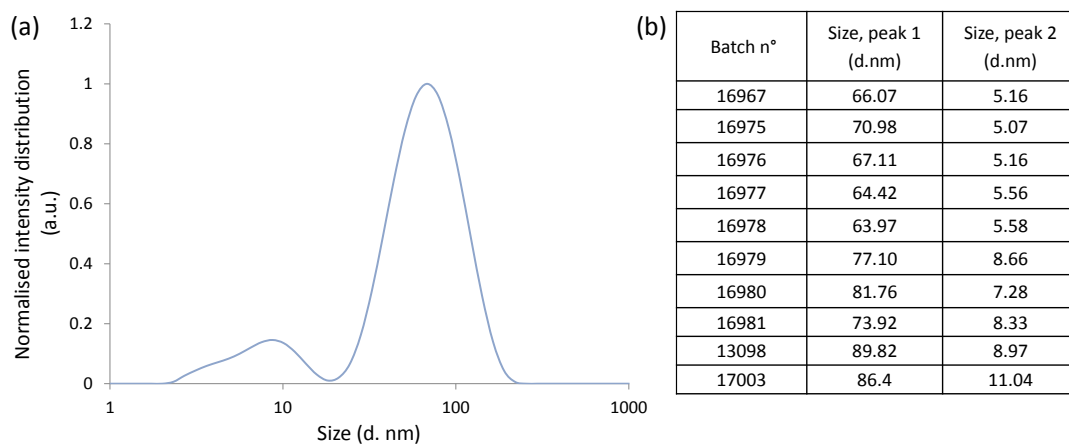


Figure 62. DLS analysis of AuNSs. (a) Intensity distribution vs hydrodynamic diameter of batch n° 16981 and (b) hydrodynamic diameter peaks of various AuNSs batches.

DLS results showed two peaks for hydrodynamic diameter for each AuNSs sample. The peak with a higher intensity distribution (Figure 62B “peak 1”) shows an average size from 63.97 (batch n° 16978) to 89.82 nm (batch n° 13098) while the second peak (Figure 62B “peak 2”) goes from 5.07 (batch n° 16975) to 11.04 nm (batch n° 17003). The second peak shows an intensity distribution of 20% circa of the entire sample. These peaks could be caused by the presence of small particles which were used for the fabrication of AuNSs. Furthermore, shape and morphology of AuNSs were investigated by SEM and TEM analysis (Figure 63). For experimental procedure of SEM analysis see Section 5.5.1.

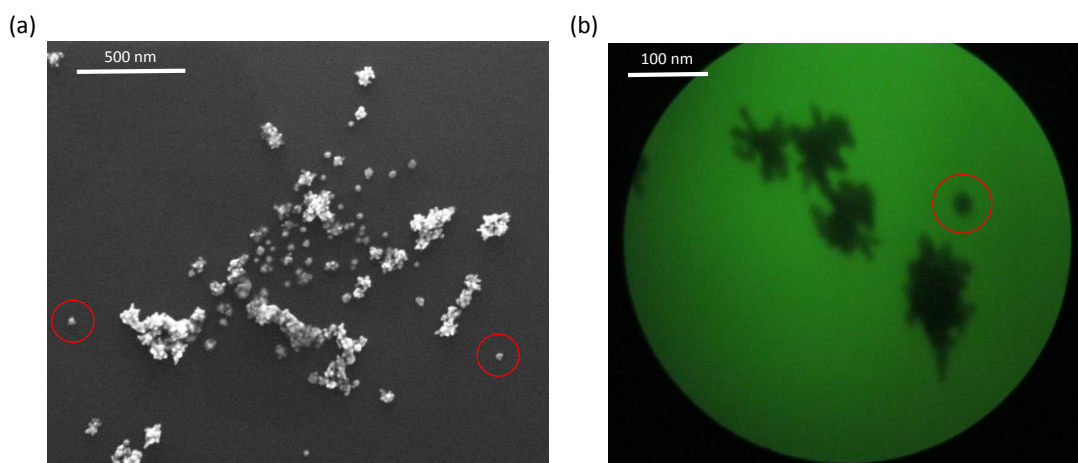


Figure 63. (a) SEM and (b) TEM images of AuNSs batch n° 16981. TEM images reproduced with the courtesy of BBI solutions. Red circles highlight the presence of small spherical particles.

Images in Figure 63 show the variety of size and shapes in a single batch of AuNSs. Particles have a spherical core surrounded by several branches and concavities. The average particle diameter calculated from the TEM image of batch n° 16981 (Figure 63B) was found to be equal to 79.8 nm. This value matches with the value found during the DLS experiment. Moreover, SEM and TEM images of AuNSs confirm the presence of small spherical particles that were used during the synthesis of AuNSs. Images for each AuNSs batch (Appendix D) show the same characteristic found for batch n° 16981. In conclusion, in order to determine the long term stability, AuNSs batch n° 17003 was monitored by extinction spectroscopy over a year. Results in Figure 64 show that blueshift occurred gradually over time. However, the blue-shift reaches a plateau after 400 days.

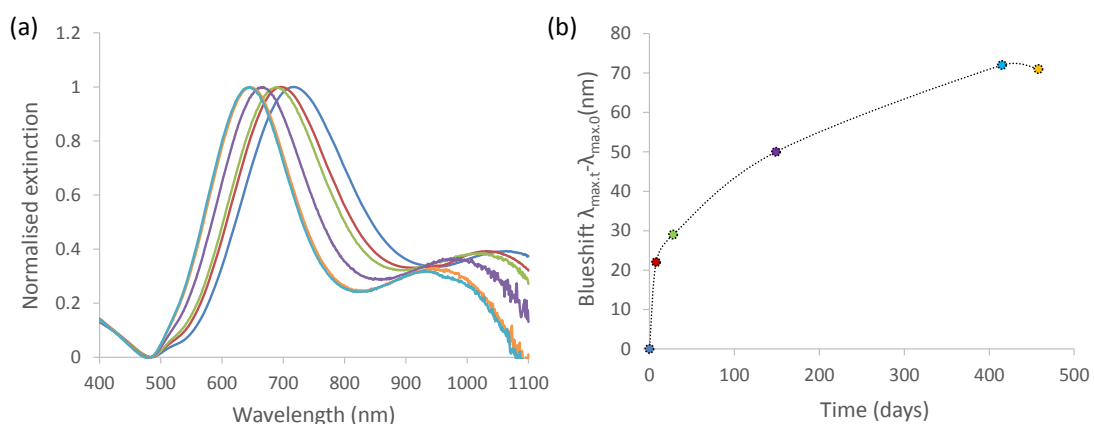


Figure 64. Extinction spectra (a) and graph representing the blueshift over time of AuNSs batch n° 17003. Spectra were taken on the day of arrival (dark blue) and after several days: 8 (red), 28 (green), 149 (purple), 415 (light blue) and 458 (orange).

AuNSs batch n° 17003 showed better stability than others batches and it also presents better SERS properties as it will be discussed in the next paragraph. Therefore AuNSs batch n° 17003 was chosen for further experiments performed during this project.

4.2.2. Comparison between AuNSs and AuNPs for SERS applications

The morphology of anisotropic particles gives an advantage over spherical particles in SERS applications. This is widely demonstrated in various publications as seen in the introduction of this chapter. A direct comparison between BBI AuNSs and AuNPs are described in this paragraph. Two different batches of AuNSs that show different LSPR peaks were also compared. Experimental details of this study are described in Section 5.5.2. Photographs of gold colloids are shown in Figure 65. AuNSs present various shades of blue while AuNPs present their distinctive red colour.

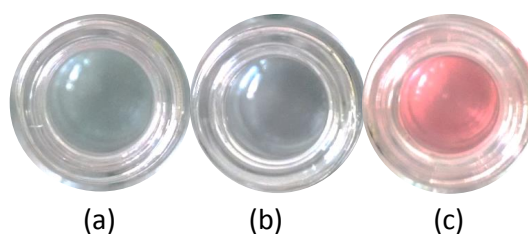


Figure 65. Gold colloids analysed for comparison study. AuNSs batch n° 17003 (a), n° 13098 (b) and BBI commercially available 40 nm AuNPs (c).

A laser wavelength of 785 nm was used in this experiment. The choice of the laser wavelength is driven by the fact that the 785 nm laser shows an advantage in terms of SERS in-vivo detection. Tissues are more likely to be damaged with more energetic lasers such as 532 and 633 nm. Also, previous experiments were conducted using a 633 nm where they showed weaker SERS signals compared to a 785 nm laser. The comparison was performed using 4-mercaptobenzoic acid (MBA) as Raman reporter molecule. Gold colloids were incubated with a solution of MBA and they were analysed by extinction and Raman spectroscopy (Figure 66).

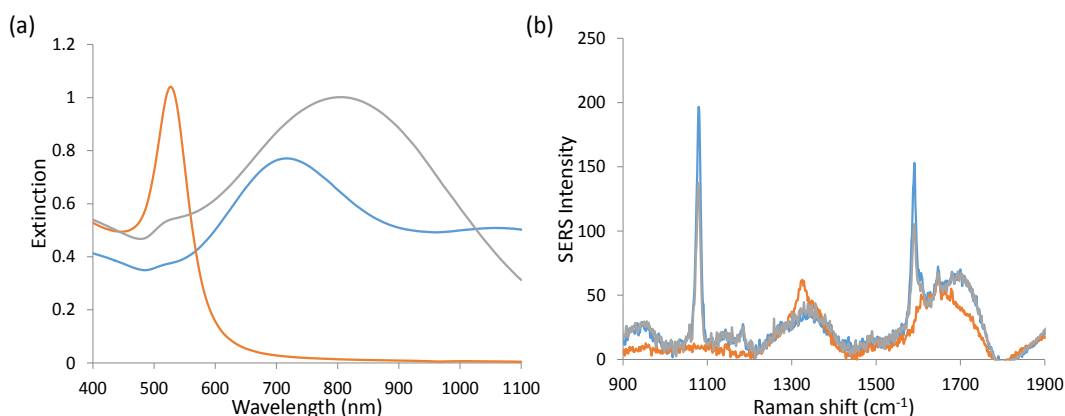


Figure 66. (a) Extinction spectra and (b) SERS spectra of MBA functionalised particles: AuNPs (orange), AuNSs n°17003 (blue) and AuNSs n° 13098 (grey). Colloids show the following LSPR peak: 718 (AuNSs n°17003), 805 (AuNSs n°13098) and 530 nm (AuNPs).

Figure 66A shows extinction spectra of MBA functionalised with AuNPs (orange plots) and two different batches of AuNSs (grey and blue plots) that show different LSPR peaks. The colloids show similar optical density at their λ_{max} : 0.99 (AuNSs n° 13098), 0.77 (AuNSs n° 17003) and 1.04 (AuNPs). Moreover, no visible aggregation was noted upon the addition of MBA onto the colloids. Figure 66B shows the SERS spectra of MBA absorbed onto different colloids. The two peaks at circa 1080 and 1590 cm^{-1} are due to the vibrations of the aromatic ring of MBA. Results demonstrated that AuNSs which show an LSPR peak at 718 nm (blue plot of Figure 66A) give higher SERS intensity (blue plot of Figure 66B) than the other colloids. Also spherical AuNPs did not show any MBA SERS signals. According to these results, AuNSs batch n° 17003 was chosen for the development of immunoassays based on SERS measurements.

4.2.3. Comparison between AuNSs and AuNPs for LFIA applications

A comparison between AuNSs and AuNPs was also performed to evaluate which colloid showed the best performance in LFIAs. Experimental details of this study are described in Section 5.5.3. AuNSs and AuNPs were conjugated to a model antibody (anti-CRP mAb) and tested in various LF devices. Three different tests were carried out during this study. The first test compared CRP line intensities when antibody conjugated AuNPs (Table 14A) or AuNSs (Table 14B) were used to run the test. The results show that when AuNS conjugates were used, the intensity of the lines was greater than AuNPs samples. The second test evaluated any possible NSB between bare AuNPs or AuNSs towards CRP lines on the strips (Table 14C and 14D). The results show no visible NSB. The last test was to check if antibody-gold

conjugates were binding in a specific manner or not. Conjugates were run in strips that contained a spot of a non-specific antigen such as brain natriuretic peptide (BNP). The results in Table 14E and Table 14F demonstrated that both conjugates did not bind to BNP, therefore the specificity of antibody was confirmed. This study suggested that AuNSs were showing a better performance in LFIA than AuNPs. This result could be explained by considering that the different surface area of AuNSs and AuNPs. The morphology of the AuNS surface allows to allocate more antibodies in a more oriented manner, compared to spherical particles.

Table 14. Photographs of nitrocellulose compartments of LF strips used to compare the performance AuNSs with AuNPs in LFIAs. (a) AuNPs@anti-CRP and (b) AuNSs@anti-CRP conjugates used in LF strips containing 4 lines of CRP gradient. (c) Bare AuNPs and (d) bare AuNSs used in LF strip containing 4 lines of CRP gradient (control 1). (e) AuNPs@anti-CRP and (f) AuNSs@anti-CRP conjugates used in LF strip containing a spot of BNP 500 µg/mL (control 2).

CRP lines (µg/mL)	(a)	(b)	(c)	(d)	BNP spot (µg/mL)	(e)	(f)
62.5					500		
125							
250							
500							

4.2.4. Functionalisation of AuNSs with anti-hCG antibody and MBA

Previous evidence shows that BBI AuNSs can increase the sensitivity in SERS and LFIA applications, when compared to spherical AuNPs. Therefore, AuNSs labelled with MBA were chosen for the development of a SERS-based LFIA for the detection of human chorionic gonadotropin (hCG). Two different conjugation protocols were investigated during this experiment. Both methods consist of the passive adsorption of anti-hCG antibodies onto AuNSs at physiological pH. In method n° 1 (Figure 67A), antibodies were incubated overnight to maximise the absorption and MBA was subsequently added and allowed to conjugate to the AuNSs surface for 1 h. In method n° 2 (Figure 67B), AuNSs were first incubated with MBA for 30 min, antibodies were then added and the solution was mixed for 1 h. Both sets of functionalised AuNSs were then incubated with a solution of bovine serum albumin (BSA) to cover any non-reacted AuNSs surface and purified by a centrifugation step.

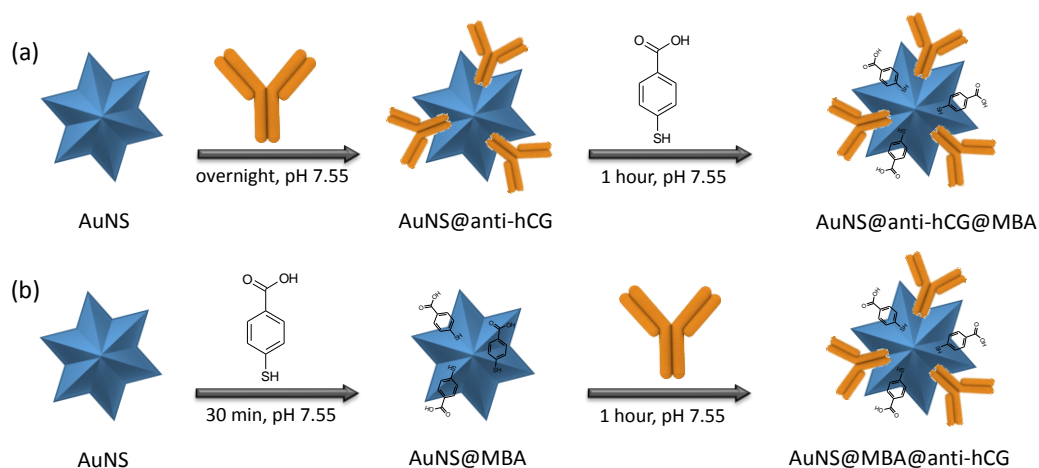


Figure 67. Schematic representation of anti-hCG antibody and MBA functionalisation of AuNSs performed in this research. (a) Method n° 1 consisted of an overnight incubation with antibodies and subsequently labelling with MBA. (b) Method n° 2 consisted of a 30 min incubation with MBA and subsequently antibody incubation for 1 hour. Experimental details of the conjugation methods are described in details in Section 5.5.4.

In order to evaluate which method gave a better conjugate, extinction spectroscopy and SERS were performed on the colloids. Figure 68A shows that both protocols produced stable conjugates as their extinction profile did not broaden and the λ_{\max} was equal to 660 nm for AuNSs@anti-hCG@MBA and 662 nm for AuNSs@MBA@anti-hCG. However, SERS spectra (Figure 68B) showed that conjugates prepared by method n° 2 give greatest MBA signal. SERS peaks at circa 1590 and 1080 cm^{-1} are associated with the stretching of the C-C bonds in the aromatic rings (breathing mode), whilst the broad peak at around 1360 cm^{-1} is due to the stretching of the carboxyl group of MBA.²⁴² Therefore, in light of these results, method n° 2 was chosen for the preparation of MBA labelled anti-hCG AuNSs that were using during this research project.

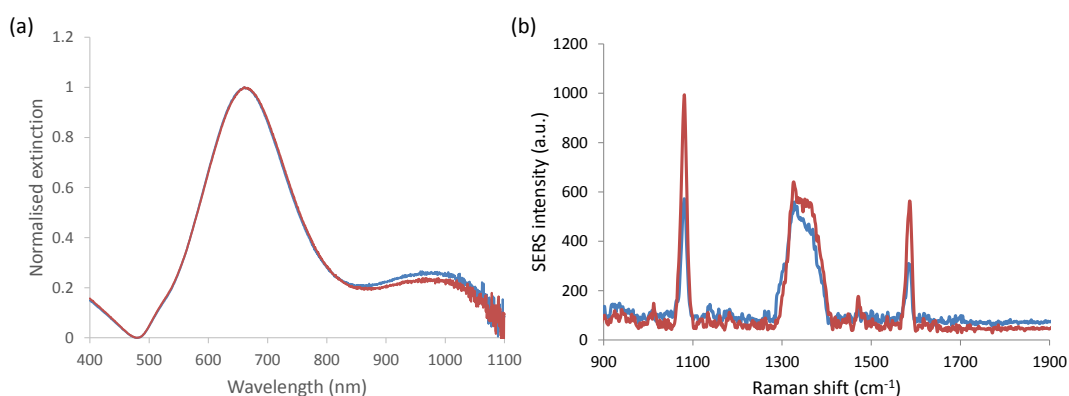


Figure 68. (a) Extinction spectra and (b) SERS spectra of AuNSs@anti-hCG@MBA (blue) and AuNSs@MBA@anti-hCG (red). Experimental data is described in details in Section 5.5.4.

4.2.5. SERS-based LFIA for the detection of hCG in a buffered solution

The sandwich immunoassay for the detection of hCG is schematised in Figure 69. LF strip design and components are described in Appendix A while experimental parameter of the assay is described in Section 5.5.5. Briefly, LF strips that contained one homogeneous line of capture Ab (test line, TL) and one line of secondary Ab (control line, CL) were used for this assay. A capture Ab concentration of 0.25 mg/mL was chosen for the TL, after an optimisation study that is described in Appendix E. To perform the assay, the AuNSs-antibody conjugate (AuNSs@MBA@anti-hCG) was placed on to the conjugate pad and various solutions containing hCG were run from the sample pad. As previously discussed in Section 1.4, a sandwich assay consists of a direct response between signal/analyte (direct assay). If the sample contains a specific amount of hCG, it binds to the AuNSs-antibody conjugates and they flow through the nitrocellulose until the TL, where a blue line appears (Figure 69A). If the sample does not contain any hCG, the conjugate should flow through the strip and only the CL appears blue (Figure 69B). After the test is performed, the TL is analysed by a Raman microscope (Figure 69C). In conclusion, a visual detection of the CL is needed to evaluate whether the assay is valid or not: if CL does not appear, the test is considered invalid.

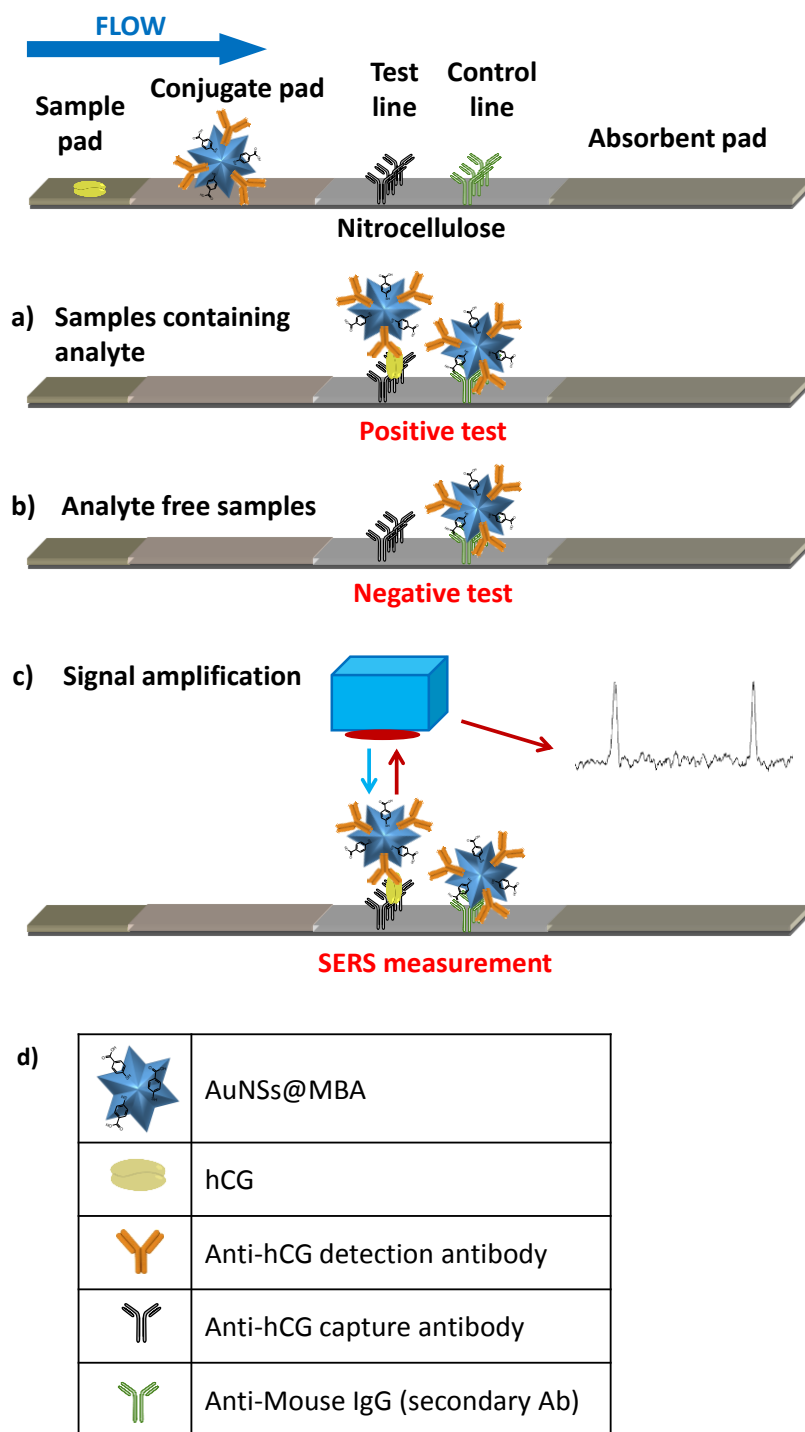


Figure 69. Schematic representation of the SERS-based LFIA for the detection of hCG. Nitrocellulose membrane contains TL of Anti- α subunit hCG and CL of anti-mouse IgG. Conjugate pad was loaded with the AuNSs@MBA@anti-hCG. Various concentration of hCG (analyte) were then placed on the sample pad to allow the AuNSs conjugate to flow through the strip. If the analyte is present in the sample, both TL and CL should bind the complex conjugate/hCG (a, positive test). If the sample is analyte free, the conjugate will bind only the CL (b, negative test). After the strip was dry, TL was analysed using a 785 nm Raman spectrometer for signal amplification (c). Key legend (d).

The assay was performed using buffer solutions at pH 7.5 that contained hCG from 0 to 50 ng/mL. Moreover, commercially available anti-hCG conjugated AuNPs were also tested as a reference with the same hCG solutions. Photographs of the nitrocellulose compartment of LF test strips that were performed using AuNSs and AuNPs are shown respectively in Table 15 and Table 16. Three replicates of each test were performed. Through general observation, it is evident that both assays were not able to detect hCG solutions lower than 0.5 ng/mL as no TLs appeared. The presence of CLs suggested that tests were valid. However, TLs appeared for hCG at concentrations higher than 0.5 ng/mL. The strips were then scanned in order to determine the red, green and blue (RGB) values of their images. These RGB values were extrapolated for each TL using the image processor software Image J. Results are shown in Figure 70.

Table 15. Scanned images of the nitrocellulose compartment of LF test strips for the detection of hCG using AuNSs@MBA@anti-hCG in the conjugate pad.

hCG (ng/mL)	Test N°	Lines: T C	hCG (ng/mL)	Test N°	Lines: T C
50	1		0.1	1	
	2			2	
	3			3	
10	1		0.05	1	
	2			2	
	3			3	
5	1		0.01	1	
	2			2	
	3			3	
1	1		0.005	1	
	2			2	
	3			3	
0.5	1		0	1	
	2			2	
	3			3	

Table 16. Scanned images of the nitrocellulose compartment of LF test strips for the detection of hCG using commercially available BBI anti-hCG in the conjugate pad.

hCG (ng/mL)	Test N°	Lines: T C	hCG (ng/mL)	Test N°	Lines: T C
50	1		0.1	1	
	2			2	
	3			3	
10	1		0.05	1	
	2			2	
	3			3	
5	1		0.01	1	
	2			2	
	3			3	
1	1		0.005	1	
	2			2	
	3			3	
0.5	1		0	1	
	2			2	
	3			3	

The bars charts in Figure 70 shows the red, green and blue (RGB) values calculated from the TLs for the assays performed with AuNSs (Figure 70A) and AuNPs (Figure 70B). RGB was calculated by subtracting values on nitrocellulose (blank) or the values obtained on each TL. Results demonstrated that AuNSs conjugates were 10-times more sensitive than AuNPs as the scanner was able to measure RGB values for samples at 0.5 ng/mL of hCG, but only TLs at 5 ng/mL were detected for AuNPs. It is worth noting that the red channel worked better than green and blue for AuNSs, while the green channel was more sensitive for AuNPs.

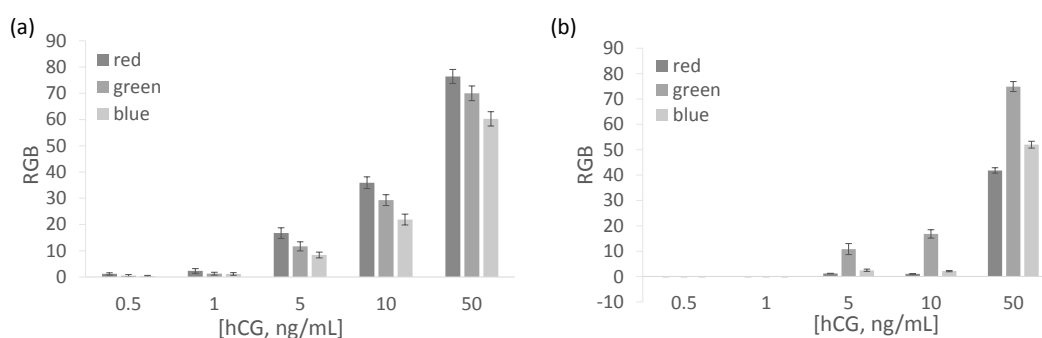


Figure 70. RGB scale of TLs from lateral flow strips performed by using (a) AuNSs and (b) AuNPs conjugates. The values were calculated by subtracting the averaged RGB values of blank nitrocellulose minus the RGB value of the TLs. Error bars indicate standard deviations of three replica.

Analysis of the AuNSs strips was then carried out on a Raman microscope for amplification of the signal. SERS maps were created of the lines, using a method that was described in

Section 3.2.3. In order to create a calibration curve for the assay, the intensity of the MBA peak at 1082 cm^{-1} for each sample was plotted against the concentration of hCG as shown in Figure 71.

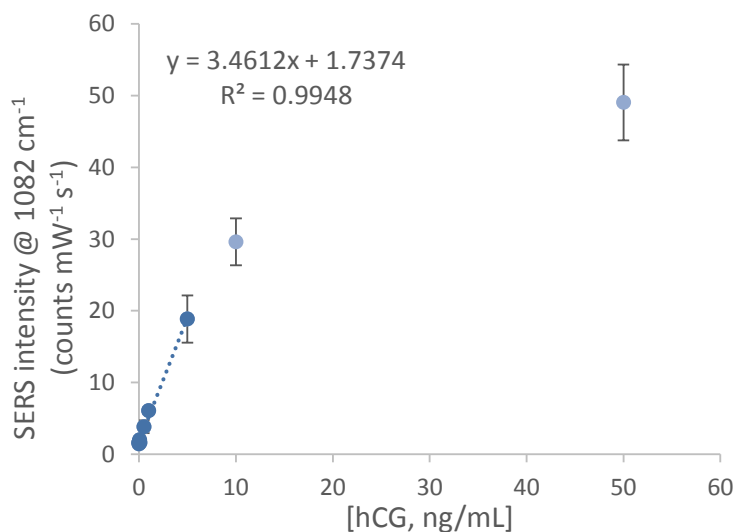


Figure 71. Calibration curve of the peak intensity at 1082 cm^{-1} against hCG concentrations with a line of best fit between 0 and 5 ng/mL of hCG. Three lateral flow tests were performed for each concentration. Error bars indicate the standard deviation obtained from three replicates for each concentration.

A linear range was found between 0 and 5 ng/mL, therefore a regression line was calculated for these points. For concentrations higher than 5 ng/mL the signal became saturated. An LOD was calculated as three times the standard deviation of the blank ($SD_{\text{blank}} = 0.71$) divided by the gradient of the regression line (gradient = 3.46). A value of 0.62 ng/mL of hCG was found for the SERS-based LFIA using AuNSs. This value is 40 times more sensitive than LODs of commercially available pregnancy tests.²⁵⁴ However, the assay presented here was performed in buffer solutions, so for a real comparison it is necessary to perform the assay in a biological matrix. Moreover, the AuNSs@MBA@anti-hCG used during this experiment were not optimised. In the following paragraphs, optimisation studies and detection of hCG in complex matrices will be described.

4.2.6. Raman reporter molecule (RRM) evaluation

One of the many advantages of SERS is the ability to simultaneously detect multiple analytes.²⁶¹ It has already been demonstrated that MBA is an efficient Raman reporter molecule (RRM) as it gives distinctive and strong signals when coupled to AuNSs and analysed using a 785 nm laser. Also, MBA is compatible with LFIA applications. Three RRM containing

aromatic amine or thiol attachment groups, such as 1,2-bis(4-pyridyl)ethylene (BPE), (4-(1H-pyrazol-4-yl)pyridine (PPY) and 5-(pyridine-4-yl)-1,3,4-oxadiazole-2-thiol (PYOT) were investigated and compared to the MBA. Detailed experimental information of the study is reported in Section 5.5.6. In this study, the RRM s shown in Figure 72 were added to the AuNSs followed by the conjugation of anti-hCG antibodies and BSA as blocking agent.

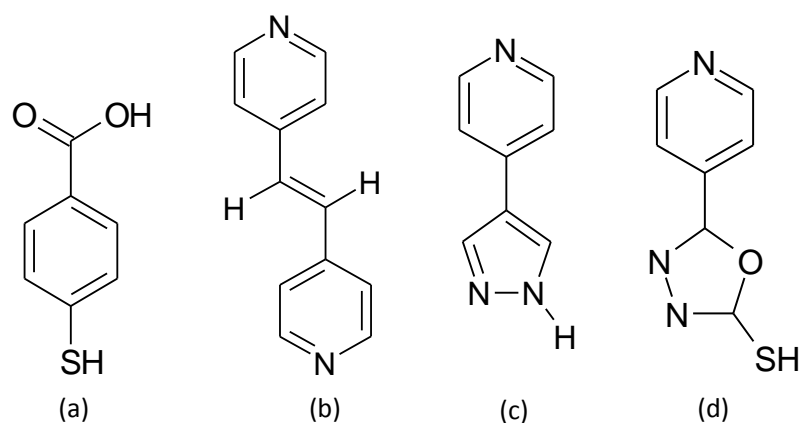


Figure 72. Molecular structures of four RRM s used in this study: (a) 4-mercaptobenzoic acid (MBA), (b) 1,2-bis(4-pyridyl)ethylene (BPE), (c) 4-(1H-pyrazol-4-yl)pyridine (PPY) and (d) 5-(pyridine-4-yl)-1,3,4-oxadiazole-2-thiol (PYOT).

AuNSs were incubated with a 0.5 μM solution of RRM s and conjugated to anti-hCG antibodies. Conjugates were then characterised using extinction spectroscopy and DLS. Results are shown in Table 17. Results demonstrated that AuNSs samples were successfully functionalised with RRM s and antibodies as their λ_{max} and the hydrodynamic diameter changed when compared to bare AuNSs.

Table 17. Extinction spectroscopy and DLS data of AuNSs@RRMs@anti-hCG and bare AuNSs before the functionalisation with RRM s and anti-hCG.

RRMs	MBA	BPE	PPY	PYOT	(bare)
Conc. (μM)	0.5	0.5	0.5	0.5	-
Size (d.nm)	83.17 \pm 1.3	76 \pm 0.3	82.5 \pm 0.7	77.65 \pm 0.15	57 \pm 3
λ_{max}	667.5	662	662	662	646

In order to evaluate the SERS performance of the RRM, colloid suspension of AuNSs@RRMs@anti-hCG were also analysed with a 785 nm Raman spectrometer. Results are shown in Figure 73.

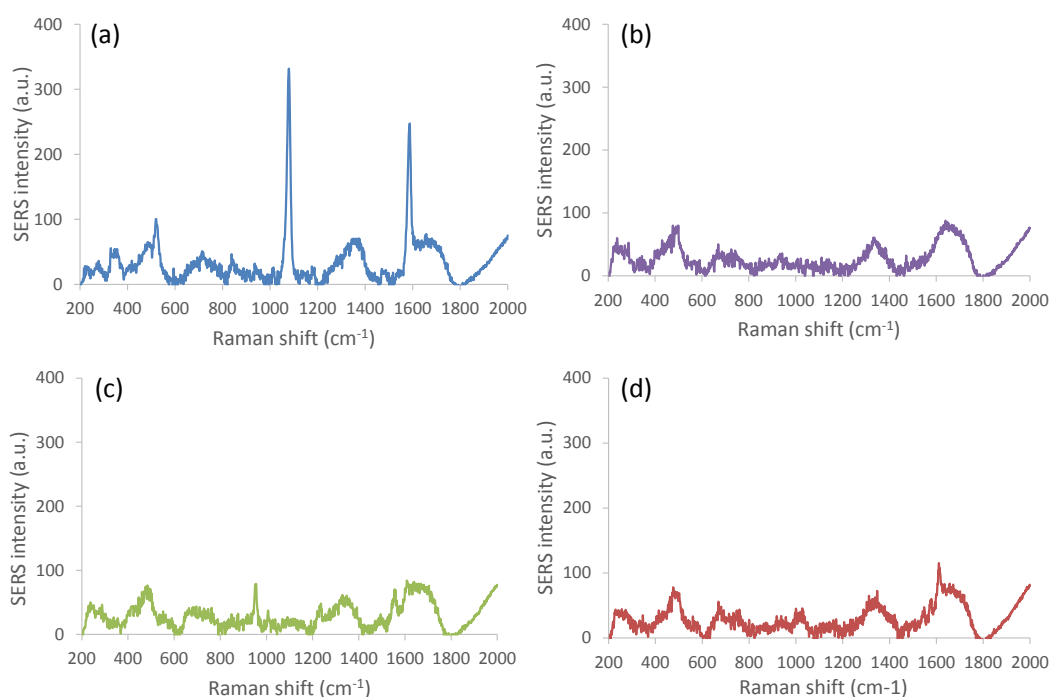


Figure 73. SERS spectra of AuNSs@RRMs@anti-hCG in borate buffer, taken with Raman spectrometer equipped with a 785 nm laser. RRM are: (a) MBA, (b) BPE, (c) PPY and (d) PYOT.

Results in Figure 73A suggest that only conjugates embedded with MBA were capable of realising a strong SERS signal. Conjugates containing BPE showed only background noise (Figure 73B). PPY (Figure 73C) and PYOT (Figure 73D) conjugates showed respectively weak SERS peaks at around 960 cm⁻¹ and 1610 cm⁻¹. However, these measurements were solution-based, so it was decided to perform the assay and analyse the RRM functionalised AuNSs on TLs of LF strips. Conjugates containing different RRM were tested on LF devices using various solutions of hCG. Images of the NC compartment of the strips are shown in Table 18.

Table 18. Images of the nitrocellulose compartments of LF strips performed using AuNSs-antibody conjugates that contained four different RRM.

Dyes:	MBA		BPE		PPY		PYOT	
[hCG, ng/mL]	lines:	T C	lines:	T C	lines:	T C	lines:	T C
10								
1								
0.1								
0								

Naked-eye evaluation of the LF strips shown in Table 18 suggested that all the conjugates gave strong TLs for 10 ng/mL of hCG. For samples at hCG concentration of 1 and 0.1 ng/mL, conjugates showed weak TLs with some intensity variations observed. LF strips that were run with 10 ng/mL of hCG solution were analysed using Raman. Results in Figure 74A shows the averaged SERS spectra taken on the TLs. No SERS signals were detected with BPE and PPY samples. Instead, strong SERS signals were obtained on strips that contained MBA and PYOT conjugates. These two molecules contained a thiol group, which is known to strongly bind to the gold surface. In order to determine which conjugate gives better sensitivity on LFIA, strips containing only buffer (blank samples) were also analysed and compared with the 10 ng/mL samples. Bar charts in Figure 74B show the SERS intensities of the peak at 1082 cm^{-1} for MBA strips (blue) and 1612 cm^{-1} for PYOT strips (red). The ratio positive/negative was found to be higher for MBA than PYOT. Therefore, MBA was kept as RRM for the development of the SERS-based LFIA for the detection of hCG.

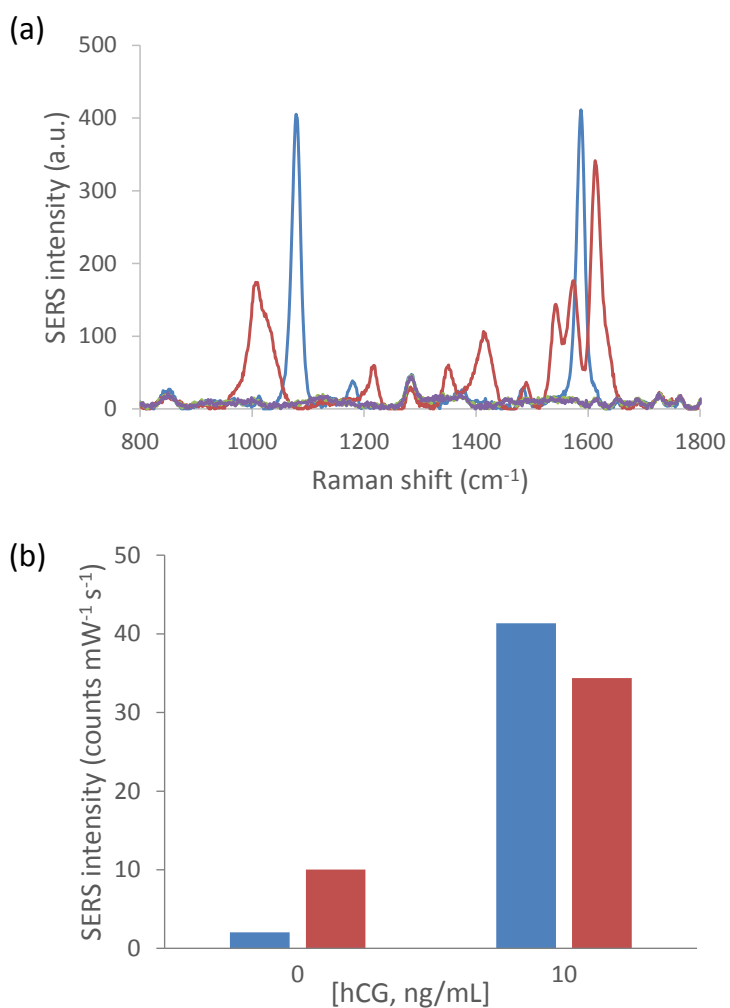


Figure 74. (a) Averaged SERS spectra on TLs of LF strips for 10 ng/mL of hCG that contained AuNSs@RRMs@anti-hCG conjugates. RRM are: MBA (blue), BPE (purple), PPY (green) and PYOT (red). (b) Bar chart representing the averaged SERS intensity on test lines of strips containing AuNSs@MBA@anti-hCG (blue) and AuNSs@PYOT@anti-hCG (red). The SERS intensities were chosen from peaks at 1082 cm^{-1} for MBA and 1612 cm^{-1} for PYOT. The ratio blank/positive was found to be equal to 20.2 for MBA and 3.4 for PYOT conjugates.

4.2.7. Optimisation of the AuNSs@MBA@anti-hCG conjugation method

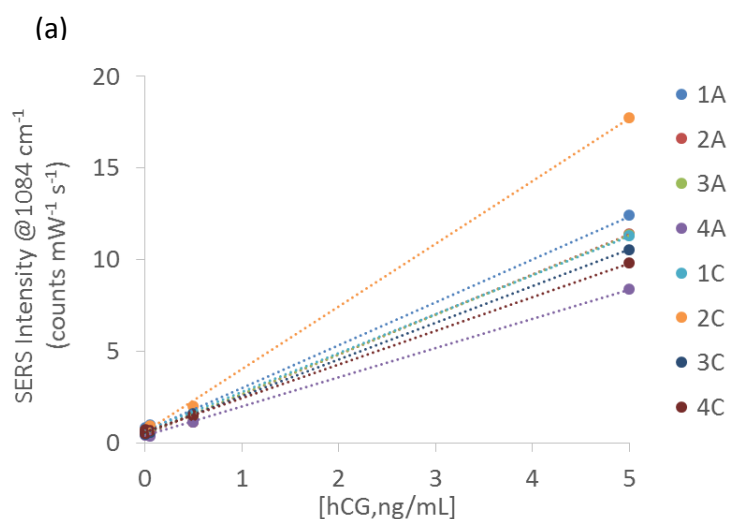
In order to increase the sensitivity of the LFIA assay, it is necessary to optimise the AuNSs@MBA@anti-hCG conjugates. Usually NSB reduces LFIA sensitivity and one efficient method to eliminate this is to add BSA onto the surface of the conjugates. Centrifugation of colloids can also lead to a more purified conjugate, therefore reducing NSB. The optimisation study consisted of a combination of various BSA solutions and centrifugation steps. AuNSs were initially functionalised with MBA and anti-hCG as described in Section 4.2.4. Subsequently, conjugates were then incubated with BSA at a range of concentrations and

various centrifugation steps were performed. Experimental details are described in Section 5.5.7. Table 19 shows eight different conjugates that were used in this study.

Table 19. Experimental data for the optimisation of AuNSs@MBA@anti-hCG conjugates. (*) 1st centrifugation step was performed at 4000 rpm for 15 min while the 2nd centrifugation step was at 3500 rpm for 10 min.

Samples	MBA (μM)	Anti-hCG ($\mu\text{g}/\text{mL}$)	% BSA	N° centrifugation steps*
1A	0.5	2.5	0.5	1
1C	0.5	2.5	0.5	2
2A	0.5	2.5	1	1
2C	0.5	2.5	1	2
3A	0.5	2.5	1.5	1
3C	0.5	2.5	1.5	2
4A	0.5	2.5	2	1
4C	0.5	2.5	2	2

It is important to determine the optimum BSA concentration as BSA covers any exposed AuNSs surface. However, an excess of BSA can cause steric hindrance and reduce the sensitivity of the assay. Centrifugation steps are important for purifying the conjugate and removing excess of antibodies that are unbound to the AuNSs surface. The eight conjugates were then tested in SERS-based LFIA. Experimental details are described in Section 5.5.7. Each conjugate was used in a concentration study with solutions of hCG varying from 0 to 5 ng/mL. Images of LF strips are shown in Appendix F. TLs of each strip were then analysed by Raman microscopy at 785 nm. In order to create a calibration curve, the SERS intensity of the MBA peak at 1082 cm^{-1} for each strip was plotted against hCG concentration (Figure 75A). The regression line for each conjugate was then calculated and parameters are shown in Figure 75B.



(b)

Samples	Intensity ratio hCG/blank	Slope	Correlation coefficient (R^2)
1A	18.1	2.34	0.9978
1C	17.2	2.13	0.9997
2A	20.1	2.19	0.998
2C	25.3	3.42	0.9994
3A	23.9	2.17	0.9992
3C	16.3	1.99	0.9998
4A	17.4	1.6	0.9996
4C	19.1	1.84	0.9997

Figure 75. (a) Calibration curves of LF tests from 0 to 5 ng/mL of hCG for 8 different samples of AuNSs@MBA@anti-hCG conjugates. (b) Accompanying Table shows the parameters of each experiment applied to create the regression lines and intensity ratios of the signal at 5 ng/mL to blank strips.

Results showed that the highest ratio of the signal for strips at 5 ng/mL and blank strips was found for the sample 2C. This demonstrated that an optimised conjugate was obtained by adding 1% of BSA and by employing two centrifugation steps. These optimised parameters were then used for the preparation of more AuNSs@MBA@anti-hCG conjugates used in the detection of hCG present in biological matrices by SERS-based LFIA.

4.2.8. SERS-based LFIA for the detection of hCG in a pseudo-biological matrix

Optimised AuNSs-antibody conjugate (sample 2C), described in Section 4.2.7, was then used in LF devices for the detection of hCG in complex matrices. Synthetic urine (Surine™), a certified reference material, was used as a pseudo-biological matrix. Various hCG solutions that contained 90% of Surine were tested by SERS-based LFIA. The LF strips that were run

with hCG samples from 0 to 10 ng/mL are shown in Table 20. Experimental data of the assay is described in Section 5.5.8.

Table 20. Images of nitrocellulose compartment of LF strips containing hCG from 0 to 10 ng/mL. hCG solutions were prepared in borate buffer pH 7.5 that contained 90% of synthetic urine. Tests were performed in triplicate.

N° replicas:	(1)		(2)		(3)	
[hCG, ng/mL]	lines:	T C	lines:	T C	lines:	T C
0						
0.078						
0.1563						
0.3125						
0.625						
1.25						
2.5						
5						
10						

Images in Table 20 show that TLs were visible with the naked-eye until a concentration of 0.1563 ng/mL. The sensitivity of the assay has now increased compared to when the unoptimised conjugate was used. RGB values of the TLs were measured by a flatbed scanner model Epson V370 Perfection. As seen in previous experiments, the red channel gives better sensitivity than blue and green channels when a blue object (AuNSs) is analysed. In order to generate a calibration curve, red channel values were plotted against the hCG concentration (Figure 76).

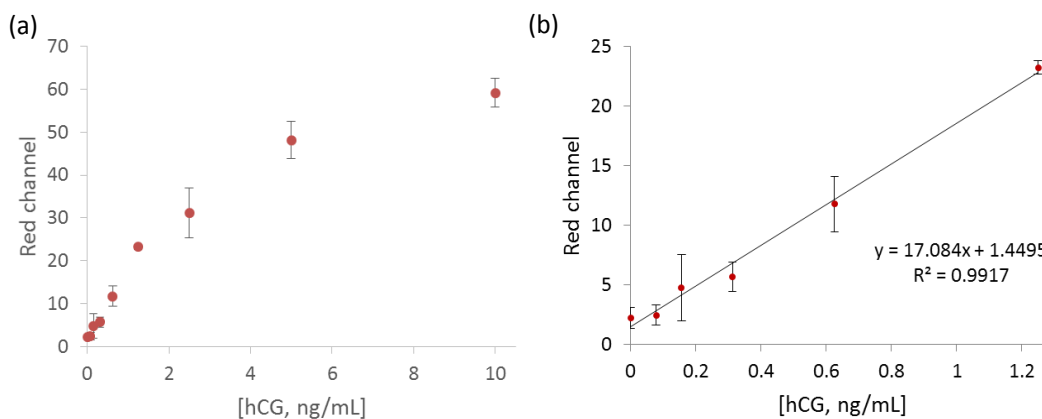


Figure 76. (a) Red channel values of TLs of LF strips with various hCG solutions in 90% synthetic urine. (b) Red channel values for samples between 0 and 1.25 ng/mL of hCG with line of the best fit. Error bars represent the standard deviation of three replicates.

The regression line in Figure 76B was calculated for the concentration range 0 to 1.25 ng/mL. After this concentration the TLs intensities stopped increasing in a linear manner with respect

to the hCG concentration as a result of signal saturation. An LOD was calculated from the RGB values by using the formula shown in Equation 8 (Section 3.2.3) and it was found to be equal to 155.24 pg/mL. TLs were analysed by a Raman microscope equipped with a 785 nm laser. SERS intensities of the MBA peak at 1082 cm^{-1} are shown in Figure 77.

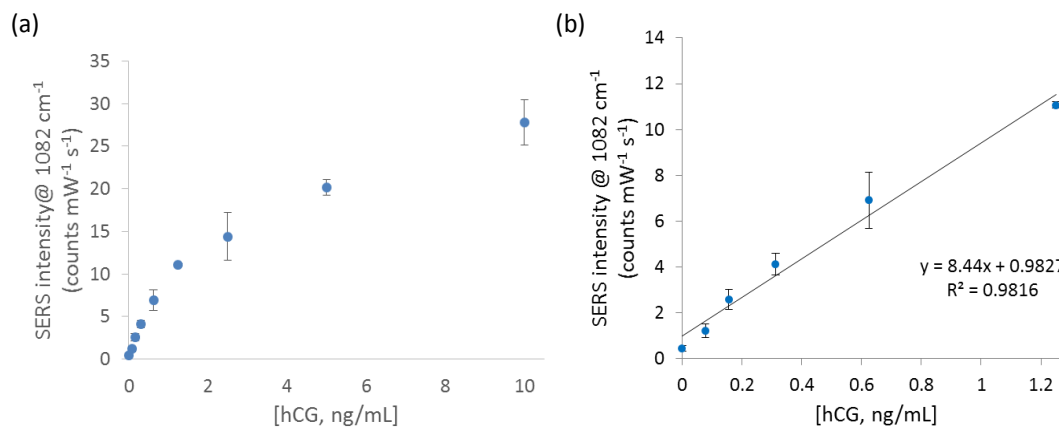


Figure 77. (a) SERS intensity of TLs of LF strips with various hCG solutions in 90% synthetic urine. (b) SERS intensity for samples between 0 and 1.25 ng/mL with line of the best fit. Error bars represent the standard deviation of three replicates.

Figure 77 shows a calibration curve obtained by plotting the SERS intensities of the TLs and the concentration of hCG. As for the RGB detection, a linear range was found between 0 and 1.25 ng/mL of hCG. An LOD for the SERS detection was calculated with the same method mentioned above and it was found to be equal to 41.8 pg/mL of hCG. This value is almost four times lower than the LOD calculated for the RGB detection method. This shows an advantage of the SERS method for this assay. A further SERS-based LFIA was performed using hCG concentrations on the picogram range. LF strips were run with various concentrations of hCG from 0 to 65 pg/mL. Images of the strips are shown in Table 21.

Table 21. Images of nitrocellulose compartment of LF strips containing hCG from 0 to 65 pg/mL. hCG solutions were prepared in borate buffer pH 7.5 that contained 90% of synthetic urine. Tests were performed in triplicate.

N° replicas:	(1)		(2)		(3)	
[hCG, pg/mL]	lines:	T C	lines:	T C	lines:	T C
0						
5						
20						
35						
50						
65						

Images of the NC compartment of LF strips on Table 21 shows that TLs were not visible with the naked-eye for the concentrations explored in this assay. However, LF strips were scanned and subsequently analysed by SERS using the same method described in Section 3.2.3. The red channel values and SERS intensity from the TLs are shown in Figure 78.

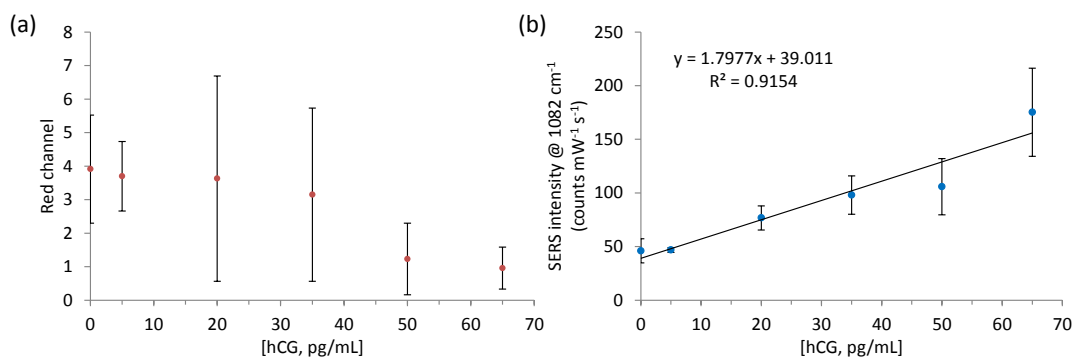


Figure 78. (a) Red channel values and (b) SERS intensity of test lines for various hCG concentration in LFIA performed in a buffer solution containing 90% synthetic urine.

Results show that the visual detection in the picogram range is impossible as the signal from the blank cannot be distinguished from positive samples. On the other hand, SERS measurements show a linear correlation with the hCG concentration and a LOD was possible to be calculated to equal to 18.72 pg/mL. These results demonstrated that the use of AuNSs in combination with SERS is a very sensitive technique that can be applied in the LFIA for the detection of various analytes.

4.3. Conclusions

Anisotropic nanostructures show many advantage over traditional spherical particles. For example, their morphology allows the formation of hot spots that increase the intensity of the SERS signals. Moreover, as it was demonstrated in this chapter, the use of AuNSs in LFIA gave an advantage in terms of sensitivity when compared to spherical AuNPs.

Various BBI AuNSs batches were analysed during this project and it was found that the stability of the batches was an issue over time as the extinction profile of the AuNSs changed. A blue-shift of the LSPR peak was noted, indicating a possible transformation of the AuNSs morphology. This phenomena was most likely due to the Ostwald ripening that caused the deterioration of AuNSs' branches and concavities. However, this did not seem to affect their performance in LFIA or SERS applications.

One AuNSs batch was identified for the development of SERS-based LFIA. After a series of optimisation studies, AuNSs were functionalised with MBA and it was demonstrated that it gave stronger enhancement than other RRM when a 785 nm laser was used. Anti-hCG antibody were successfully conjugated by passive absorption to MBA functionalised AuNSs and 1% of BSA was used to block any exposed gold surface. This conjugate was then used in LFIA for the detection of hCG which is one of the hormones correlated to pregnancy. This antigen was chosen because of the availability of antibody pairs that are needed for a sandwich immunoassay.

The assay developed in this chapter was performed either in buffer solutions or synthetic urine. Results demonstrated that AuNSs conjugates were more sensitive than commercially available anti-hCG AuNPs conjugates when a visible readout was performed. Also, AuNSs conjugates had the advantage of SERS amplification. In fact, the SERS readout gave circa 4 times lower LOD compared to the visible readout. SERS-based LFIA using AuNSs also allowed the detection of hCG in biological matrix in the picogram range, with a calculated LOD of 18.72 pg/mL. This value is 2 times lower than limit of detection claimed by a published work based on AuNPs and electroanalytical methods for the detection of hCG.²⁶² Amongst published works that claim to detect hCG in a highly-sensitive manner, it is worth noticing an immunoradiometric assay (IRMA) that can detect level of hCG of 10 pg/mL.²⁶³ However, IRMAs requires antibodies to be labelled with radioactive compounds. This could be a disadvantage compared to LFIA for health hazard and waste disposal.

Finally, the combination of AuNSs and SERS exploited during this research, demonstrated to give a very high sensitivity in the detection of analytes. Another important features for the SERS-based LFIA is the possibility of multiplexing analysis in one device as describe in previous published work by Sanchez-Purra *et al.* that were able to detect zika and dengue viruses in one test strip.²⁶⁴

CHAPTER 5: Experimental

5.1. Materials

CuSO₄ (MW 249.69), ZnCl₂ (MW 136.28), CoCl₂ (MW 237.93), NiCl₂ (MW 129.52), poly-L-histidine (MW 5000-25000), poly-L-arginine hydrochloride (MW 5000-15000), poly-L-lysine hydrochloride (MW15000-30000), poly-L-glutamic acid sodium salt (MW 15000-50000) N_αN_α-bis(carboxymethyl)-L-lysine hydrate (NTA unit), imidazole, sodium hydroxide (NaOH), hydrochloric acid (HCl), 2-(N-morpholino) ethane sulfonic acid (MES), 4-(2-hydroxyethyl)-1-piperazine ethane sulfonic acid (HEPES), bovine serum albumin (BSA), foetal bovine serum (FBS), Tween 20, 1-Ethyl-3-(3-dimethylaminopropyl) carbodiimide (EDC), Surine Negative Urine Control, 1,2-bis(4-pyridyl)ethylene (BPE), 4-mercaptobenzoic acid (MBA), 5-(pyridine-4-yl)-1,3,4-oxadiazole-2-thiol (PYOT), 4-(1H-pyrazol-4-yl)pyridine (PPY), boric acid and sodium tetraborate were all purchased from Sigma Aldrich, UK. Malachite green isothiocyanate (MGITC), sodium chloride (NaCl), sulfo-NHS and monodentate thiol polyethylene glycol (1-mercapto-3,6,9,12,15,18,21,24,27,30,33,36-dodecaoxanona triacontan-39-oic acid (CT-PEG12)) were all purchased from Thermo Fisher Scientific. C-reactive protein (CRP), citrate 40 nm gold nanoparticles (AuNPs), C-reactive protein monoclonal antibody (mAb) (capture antibody, Scripps), human chorionic gonadotropin (hCG), histidine-tagged Fab monoclonal anti-CRP antibody (his-tag Fab), anti-hCG antibody-gold conjugate and anti-CRP antibody-gold conjugate were kindly provided by BBI Solutions. Lateral flow strips were assembled and provided by BBI Solutions (more info about LF strips in Appendix I). Monoclonal antibodies anti-alpha subunit of human FSH and anti-human chorionic gonadotropin (anti-hCG) were acquired from Medix Biochemica.

5.2. Methods and instrumentation

5.2.1. Extinction spectroscopy

Extinction spectra were carried out on two instruments, depending on the availability: Agilent CARY 300 BIO and CARY 60 spectrophotometers. The instrument was left to warm up and equilibrate for at least 10 minutes. The range of wavelengths scanned was for analysis of AuNSs 400-1100 nm and for the AuNPs 400-800 nm. The molar concentration of AuNPs can be calculated according the Beer-Lambert Law (Equation 10).²⁶⁵

$$A = \epsilon l C$$

Equation 10. Beer-Lambert Law for calculating molar concentration of AuNPs.

Where:

A = absorbance measured by the extinction spectroscopy

ϵ = molar extinction coefficient ($\text{mol}^{-1} \text{L cm}^{-1}$)

C = concentration in moles per litre

l = path length (cm).

The molar extinction coefficient measures the degree of interaction between a chemical species and light. This coefficient depends on the size and composition of nanoparticles, i.e. for AuNPs 40 nm in diameter the value for ϵ is equal to $9.264 \times 10^9 \text{ mol}^{-1} \text{L cm}^{-1}$.²⁶⁶

Normalised extinction spectra of AuNPs samples are obtained by firstly subtracting the extinction value at 800 nm from each extinction value in the range 800 to 400 nm. This operation assigns an arbitrary extinction value of zero to the 800 nm wavelength. Lastly, the maximum peak of the new extinction spectra is normalised to an arbitrary value of 1 by applying the following formula:

$$\text{Normalised Extinction} = \text{Extinction}_{\lambda_i} \times \frac{1}{\text{Extinction}_{\lambda_{max}}}$$

Equation 11. Calculation for obtaining normalised extinction spectra.

Where λ_i goes from 800 to 400 nm.

5.2.2. Dynamic light scattering (DLS)

A Malvern Zetasizer Nano ZS system was used for dynamic light scattering (DLS) and zeta potential measurements. This technique can be used to determine the size distribution profile of small particles in suspension by measuring the dynamic properties of nanoparticles.

The particles suspended in a medium are constantly moving due to the random collision with the molecules of the liquid that surround them.⁴⁷ This phenomenon is called Brownian motion. An important feature of Brownian motion for DLS is that small particles move quickly and large particles move more slowly.²⁶⁷ The relationship between the size and its speed is defined in the Stokes-Einstein equation (Equation 12).²⁶⁸

$$D_h = \frac{k_B T}{3 \pi \eta D_t}$$

Equation 12. Stokes-Einstein equation.

Equation 12 connects the diffusion coefficient, D_t , measured by DLS with the hydrodynamic diameter, D_h , that is the diameter of the particles in the solution taking into account all the water molecules it carries in its hydration sphere.⁷⁷ The other parameters are known: k_B is Boltzmann's constant, T is thermodynamic temperature and η is dynamic viscosity.²⁶⁸ The hydrodynamic parameter used to describe the size of AuNPs in this thesis is the Z-Average mean, as the particles are spherical and monomodal (only one peak). On the other hand, the intensity distribution was used to describe size of AuNSs as two peaks were measured. The polydispersity index (PDI) gives an indication of the various size distribution in a sample. If PDI is higher than 0.7 the sample has a very broad size and is probably not suitable for DLS.²⁶⁷

5.2.3. Scanning electron microscopy (SEM)

Imaging was carried out using a Quanta 250 FEG-ESEM (FEI Company), a high resolution scanning electron microscope with an acceleration voltage of 10 kV and working distance 6.3 mm. SEM analysis was performed by Dr Samuel Mabbott.

5.2.4. Raman spectroscopy

SERS, SERRS or Raman spectra of solutions were collected using Snowy Range Sierra series readers equipped with 638 nm excitation wavelength with a 30 mW laser power or 785 nm excitation wavelength with a 45 mW laser power. SERS or SERRS spectra from the nitrocellulose surface of LF strips were collected using Renishaw InVia microscope equipped with a 633 nm and 785 nm excitation wavelength. The maximum power of both lasers was 80 mW and SERS measurements on the strips were performed at various power levels, depending on the experiment.

5.3. Gold nanoparticles for a universal conjugation method of histidine-tagged antibodies

5.3.1. PEGs concentration study

11 samples of commercially available citrate AuNPs (40 nm, 3 mL, O.D. 1.07) were incubated with various aliquots (0.15, 0.3, 1.5, 3, 10, 35, 70, 150, 300, 600 and 1200 μ L) of CT-PEG (1 mM) and shaken for 3 hours. Subsequently, same aliquots of MT-PEG (1 mM) was added to the AuNPs samples and shaken overnight. 1 ml of each sample was collected and analysed by DLS. The rest of the samples were centrifuged for 30 minutes at 6000 rpm. Pellets (10 μ L) were dissolved in 990 μ L of MilliQ water and analysed by extinction spectroscopy and DLS.

5.3.2. Preparation of optimised PEGylated AuNPs

Commercially available citrate AuNPs (40 nm, 20 mL, O.D. 1.06) were incubated with 735 μ L of CT-PEG (1 mM) and shaken for 3 hours. Subsequently, 735 μ L of MT-PEG (1mM) was added to the AuNPs and shaken overnight. After a centrifugation step (5500 rpm for 20 min) pellets were dispersed in MES buffer (2 mL, pH 6, 25 mM). PEGylated AuNPs were characterised by DLS (hydrodynamic diameter = 47.6 ± 1.1 nm) and extinction spectroscopy ($\lambda_{\text{max.}} = 528$ nm; 1.05 nM). Experiment was performed in triplicate.

5.3.3. Preparation of NTA functionalised AuNPs

PEGylated AuNPs (2 mL, O.D. 9.74) were incubated with a solution of EDC (58 μ L, 10 mg/mL, MES 25 mM, pH 6) and sulfo-NHS (132 μ L, 10 mg/mL, MES 25 mM pH 6) for 15 minutes. Subsequently, HEPES buffer (2 mL, 25 mM, pH 7.4) and the NTA unit solution (240 μ L, 10 mg/mL, HEPES 25 mM pH 7.4) were added to the PEGylated AuNPs and left mixing overnight. MilliQ water (5.57 mL) was added to the NTA functionalised AuNPs and these were centrifuged at 5500 rpm for 20 minutes. Pellets were collected and resuspended in MilliQ water (5 mL). Purified NTA AuNPs were characterised by DLS (hydrodynamic diameter = 58.1 ± 2 nm) and extinction spectroscopy ($\lambda_{\text{max.}} = 529$ nm; 0.42 nM). Experiment was performed in triplicate.

5.3.4. Stability of NTA AuNPs in NaCl solutions

Commercially available citrate AuNPs (40 nm, 500 μ L, O.D. 1.025) and NTA AuNPs (500 μ L, $\lambda_{\text{max.}} = 529$ nm, O.D. 1.086) were placed in two PMMA cuvettes. Aliquots of a NaCl solution

were added sequentially (1 M, 10 aliquots of 5 μL , 5 aliquots of 10 μL and 8 aliquots of 50 μL) to each of two cuvettes and extinction spectra were measured after each addition. Samples were performed in triplicate.

5.3.5. Metals incubation study

4 aliquots of NTA AuNPs (50 μL , O.D. 9.95) were incubated with the following aqueous solutions: CuSO_4 , ZnCl_2 , CoCl_2 and NiCl_2 (0.65 mM, 500 μL). After 20 minutes from incubation, metal functionalised NTA AuNPs were purified by centrifugation (6000 rpm for 15 min). Pellets were dissolved in MilliQ water and analysed by extinction spectroscopy.

5.3.6. Optimisation study of NTA AuNPs with nickel and cobalt ions

5 aliquots of NTA AuNPs (100 μL , O.D. 5.46) were incubated overnight with various solutions of NiCl_2 at the following concentrations: 2.23 (1 eqv), 11.15 (5 eqv), 22.3 (10 eqv), 111.5 (10 eqv) and 223 μM (100 eqv); (final volume = 500 μL , HEPES buffer pH 7.4, 25 mM). 5 aliquots of NTA AuNPs (100 μL , O.D. 5.46) were incubated overnight with various solutions of CoCl_2 at the following concentrations: 2.23 (1 eqv), 11.15 (5 eqv), 22.3 (10 eqv), 111.5 (10 eqv) and 223 μM ; (final volume = 500 μL , HEPES buffer pH 7.4, 25 mM).

5.3.7. His-tag Fab conjugation to metal ions functionalised NTA AuNPs

NTA-Ni AuNPs (500 μL , O.D. 1.02, HEPES 25 mM, pH 7.4) that were previously incubated with 22.3 μM of NiCl_2 and NTA-Co AuNPs (500 μL , O.D. 1.02, HEPES 25 mM, pH 7.4) that were previously incubated with 115.5 μM of CoCl_2 , were purified by centrifugation (5000 rpm for 20 min) and pellets resuspended in HEPES buffer (480 μL , 25 mM, pH 7.4). His-tag Fab antibody (0.1 mg/mL, 5 μL) was added to the samples and the mix was shaken for 1 hour. Pellets (10 μL) were obtained by centrifugation at 4000 rpm for 20 minutes and resuspended in 90 μL of buffer solution (O.D. 4.57, HEPES 25 mM, pH 7.4). LFIA tests were performed using strips that contained 4 lines of CRP at the following concentrations: 500, 250, 125 and 62.5 $\mu\text{g}/\text{mL}$. NTA-Ni and NTA-Co AuNPs antibody conjugates (10 μL) were placed in the conjugate pad. In order to allow nanoparticles to flow through the nitrocellulose, strips were placed in glass vials, which contain HEPES buffer (pH 7.4 25mM, 100 μL). Washing buffer (100 μL , HEPES 25 mM, 0.2% BSA, 0.5% Tween 20, pH 7.4) was used to wash any unreacted conjugate. When strips were dry, photographs were taken with a mobile phone camera of 13 megapixel (autofocus).

5.3.8. Role of nickel in the antibody conjugation

5.3.8.1. Nickel concentration study

3 samples containing NTA AuNPs (100 μL , O.D. 5.46) were incubated overnight with 2.23, 11.15 and 22.3 μM of NiCl_2 (total volume = 500 μL ; HEPES pH 7.4, 25 mM). Pellets were purified by centrifugation (5000 rpm for 20 min), resuspended in HEPES buffer (480 μL ; pH 7.4, 25 mM) and incubated for 1 hour with his-tag Fab (5 μL , 0.1 mg/mL). Pellets were purified by centrifugation (4000 rpm for 20 min) and resuspended in HEPES buffer (90 μL ; pH 7.4, 25 mM). LF tests were performed using strips that contained 4 various concentration of CRP from 0.0625 to 0.5 mg/mL. His-tag NTA-Ni AuNPs (10 μL , O.D. 5) were placed on to the conjugate pads. In order to allow colloids to flow through the NC, strips were placed within glass vials, which contained HEPES buffer (100 μL ; pH 7.4, 25 mM). Washing buffer (100 μL , HEPES 25 mM, 0.2% BSA, 0.5% Tween 20, pH 7.4) was used to wash the strips to remove any colloidal residues. When the strips were dry, photographs were taken with a 13 megapixel camera (autofocus). Experiment was performed in triplicate.

5.3.8.2. Nickel incubation time study

3 test samples of NTA AuNPs (200 μL , O.D. 5.46) were incubated with 22.3 μM of NiCl_2 (1 mL; HEPES 25 mM, pH 7.4) and left to shake at room temperature for 16, 20 and 44 hours respectively. 3 control samples were prepared by incubating NTA AuNPs with HEPES only (1 mL; 25 mM, pH 7.4). Control samples were incubated for the same duration of time as the test samples. 3 aliquots of 250 μL were taken from each sample after 16, 20 and 44 hours. Each aliquot was purified by centrifugation (5000 rpm for 20 min) and incubated for 1 hour with his-tag Fab (1 $\mu\text{g}/\text{mL}$; HEPES, pH 7.4, 25 mM, final volume = 250 μL). Pellets were purified by centrifugation (4000 rpm for 15 min) and resuspended in HEPES buffer (45 μL ; pH 7.4, 25 mM). LF tests were performed with the same conditions used for the concentration study

5.3.8.3. Antibody displacement study

His-tag Fab NTA-Ni AuNPs (O.D. 5), which were previously incubated for 44 hours with 22.3 μM of NiCl_2 , were used in this experiment. Conjugates (50 μL) were incubated overnight with an imidazole solution (450 μL ; 0.264 M, pH 8.6). Pellets were purified by centrifugation (4000 rpm for 15 min) and resuspended in HEPES buffer (45 μL ; pH 7.4, 25 mM). LF tests were performed with the same conditions used for the concentration and incubation time studies.

5.3.9. Antibody optimisation study

6 samples of NTA-Ni AuNPs (200 μ L, O.D. 1, $\lambda_{\text{max.}}$ = 530 nm, HEPES pH 7.4, 25mM) were incubated for 1 hour with HEPES buffer (pH 7.4, 25mM) that contained the following his-tag Fab concentrations: 0 (control), 0.5, 1, 2.5, 5 and 10 μ g/mL. Pellets (10 μ L) were collected by a centrifugation step (4000 rpm for 15 minutes) and resuspended in 15 μ L of HEPES buffer (pH 7.4, 25mM). Lateral flow tests were performed using strips that were previously prepared by placing 0.5 mg/mL of CRP solution (0.3 μ L) on the nitrocellulose and left to dry at room temperature for 1 hour. A running buffer solution (100 μ L, HEPES pH 7.4, 25 mM) was placed on to the sample pad to allow the AuNPs to flow through the strip. When strips were dry, photographs were taken with a mobile phone camera 13 megapixel (autofocus).

5.3.10. Interactions between NTA-Ni AuNPs and poly-L amino acids

NTA AuNPs (200 μ L, O.D. 4) were incubated overnight with HEPES (755 μ L, 25 mM pH 7.4) and NiCl_2 (45 μ L, 0.5 mM) with a final nickel concentration of 22.3 μ M. Pellets were collected by centrifugation (4000 rpm for 18 min) and resuspended in HEPES (100 μ L, 25 mM, pH 7.4) in order to obtain NTA-Ni AuNPs that showed O.D. 8. NTA-Ni AuNPs (12 μ L) were incubated in 10 μ g/mL solutions (HEPES, 25 mM, pH 7.4) of: poly-L-glutamic acid, poly-L-lysine, poly-L-arginine, poly-L-histidine. A control sample was prepared using only HEPES (25 mM, pH 7.4). Samples were placed in PMMA cuvettes and spectra were recorded every 10 minutes. Experiment was performed in triplicate.

5.4. SERS-based lateral flow immunoassay for the detection of C-reactive protein

5.4.1. Raman reporter molecule study

Two aliquots of his-tag Fab NTA-Ni AuNPs (10 μ L, O.D. 8.7) were incubated overnight with an aqueous solution of MGITC (0.1 μ M, HEPES buffer 20 mM pH 7.4, final volume = 100 μ L) and of MBA (0.5 mM, HEPES buffer 20 mM pH 7.4, final volume = 100 μ L). Pellets were collected by a centrifugation step (4000 for 15 minutes) and placed into the conjugate pads of two competitive format test strips containing four lines of CRP at various concentration. A running buffer (100 μ L, HEPES 20 mM pH 7.4) was placed in the sample pad to allow conjugates moved through the strip. After a washing step (100 μ L, HEPES 20 mM pH 7.4), strips were left to dry overnight. A Raman spectrometer (Witec Alpha 300 R, laser wavelength = 633 nm) with a 20x objective was used to collect spectra from the LF strips. Three spectra were taken on each line. Spectra were baselined corrected and averaged. The optimised MGITC labelled his-tag Fab NTA-Ni AuNPs were prepared as followed.

5.4.2. Preparation of MGITC labelled his-tag Fab NTA-Ni AuNPs

NTA AuNPs (200 μ L, O.D. 4) were incubated with HEPES (755 μ L; 25 mM, pH 7.4) and NiCl₂ (45 μ L, 0.5 mM) for 44 hours. Pellets (20 μ L) were collected after centrifugation (4000 rpm for 20 min) and resuspended in HEPES (840 μ L; 25 mM, pH 7.4) and his-tag Fab (50 μ L, 0.1 mg/mL). The mixture was reacted for 1 hour under shaking. MGITC solution (100 μ L, 0.5 μ M) was added to the mixture and it was shaken for 30 minutes. The mixture was centrifuged at 4000 rpm for 15 minutes and pellets were resuspended in HEPES (100 μ L; 25 mM, pH 7.4, O.D. 6). Colloids were analysed using Raman spectroscopy. Colloids (20 μ L) were suspended in HEPES buffer (480 μ L; 25 mM, pH 7.4) and placed in a glass vial for the analysis. The theoretical concentration of MGITC on the conjugate surface, after purification steps, was calculated to be 4 nM. Therefore, a 4 nM solution of MGITC in HEPES was analysed using Raman spectroscopy for comparison. A Snowy Range Raman spectrometer equipped with a 638 nm laser was used for the measurements (laser power 15, integration time 5 seconds, baselined spectra).

5.4.3. Compatibility study of MGITC labelled conjugates with LFIA

4 test strips that contained 4 lines of CRP gradient each (from 500 to 62.5 $\mu\text{g}/\text{mL}$) were used in this experiment. Table 22 describes the properties of four different colloid samples that were placed on the conjugate pads of the 4 strips. A buffer solution (HEPES 25 mM, pH 7.4, 100 μL) was then placed to the sample pads to allow colloids to flow through the strips. Once strips were dried, photographs were taken with a mobile phone camera Motorola Moto G of 13 megapixel (autofocus).

Table 22. Properties of various functionalised AuNPs that were placed on the conjugate pads of 4 lateral flow strips for the compatibility study.

Sample	AuNPs functionalisations	His-tag Fab ($\mu\text{g}/\text{mL}$)	MGITC ($\mu\text{g}/\text{mL}$)	Concentration of colloids (nM)	Vol. on conjugate pad (μL)
(a)	His-tag Fab NTA-Ni	1	0	0.98	10
(b)	MGITC his-tag Fab NTA-Ni	1	0.05	0.98	10
(c)	MGITC NTA-Ni	0	0.05	0.98	10
(d)	NTA-Ni	0	0	0.98	10

5.4.4. Conjugation methods comparison study

Three samples of NTA-Ni AuNPs (250 μL , O.D. 1.09) and three samples of citrate AuNPs (250 μL , O.D. 1.05) were incubated for 1 hour with his-tag Fab solutions (25 μL , 0.1 mg/mL). Subsequently, a solution of MGITC (50 μL , 5 μM) was added to each aliquot and left mixing for another 30 minutes (total volume = 500 μL , HEPES buffer 25 mM, pH 7.6). Pellets were collected by centrifugation (4000 rpm for 15 minutes) and resuspended in HEPES buffer (50 μL , 25 mM and pH 7.6). Extinction spectroscopy and DLS were carried out in a 33.3 times diluted solution (500 μL of MilliQ H_2O) of each sample.

5.4.5. Sandwich SERRS-based LFIA

MGITC labelled his-tag Fab NTA-Ni AuNPs (5 μL , O.D. 6.11, λ_{max} 528.5 nm, particle diameter 68.2 ± 4) were placed in the conjugate pad of lateral flow strips that contained a line of 500 $\mu\text{g}/\text{mL}$ of monoclonal CRP antibody (capture Ab) across the nitrocellulose. 7 CRP sample solutions (HEPES; 100 μL , 25 mM, pH 7.4) from 0 to 100 ng/mL, were placed in glass vials and strips were dipped into the sample solutions. 100 μL of washing buffer (HEPES 25 mM, BSA and Tween 20, pH 7.4) was subsequently added to the vials. Once strips were dried, photographs were taken with a mobile phone camera 13 megapixel (autofocus). Furthermore, strips were analysed using a Raman microscope in mapping mode. 91 spectra were taken within the area that contains the capture antibody (ON area). 40 spectra were taken on the NC away from the lines (OFF area). A 633 nm laser (~ 8 mW) was used with 5 seconds exposure time. Spectra were baseline corrected and cosmic rays removed using Renishaw WiRe software. Spectra were background adjusted by subtracting average of the spectra OFF-area from the average of the spectra ON-area using Matlab software. Three replicates were performed for each CRP concentration. Other 5 CRP samples (from 250 to 5000 ng/mL) were tested using the same procedure described above in this paragraph.

5.4.6. Competitive SERRS-based LFIA

CRP (0.5 μL , 50 $\mu\text{g}/\text{mL}$) was spotted on to the middle of NC on LF strips and strips were incubated at 37°C for 1 hour. MGITC labelled his-tag Fab NTA-Ni AuNPs (5 μL) were added to the conjugate pad of each strip. 8 CRP solutions (HEPES; 100 μL , 25 mM, pH 7.4) from 0 to 500 $\mu\text{g}/\text{mL}$, were placed in glass vials and strips were dipped into them. Each CRP concentration was tested three times using different batches of conjugate (Table 23). 100 μL of washing buffer (HEPES 25 mM, BSA and Tween 20, pH 7.4) was subsequently added to the vials. Strips were analysed using a Raman microscope in mapping mode. 81 spectra were taken in the area of CRP spot. A 633 nm laser (~ 8 mW) was used with 3 seconds exposure time. Spectra were baseline corrected and cosmic rays removed using Renishaw WiRe software. Spectra were averaged using Matlab software. Finally, photographs were taken on the nitrocellulose compartment of the strips with a mobile phone camera 13 megapixel (autofocus).

Table 23. Characteristics of three different batches of MGITC labelled his-tag Fab NTA-Ni AuNPs that were placed on the conjugate pads of competitive lateral flow test strips.

Batch n°	O.D.	λ max.	Extinction @ 650 nm	Z-Average (DLS, nm)
1	13	534	0.039	82 ± 3
2	12.8	534.5	0.038	89 ± 1
3	11.5	538	0.052	92 ± 1

5.4.7. Biological samples study

5.4.7.1. Sandwich assay

9 lateral flow strips that contained a test line of 1 mg/mL mAb anti-CRP antibody (capture antibody) were used in this experiment. MGITC labelled his-tag Fab NTA-Ni AuNPs (5 μ L, O.D. ~10) were added to the conjugate pad of each strip. Strips were divided into 3 groups and they were dipped respectively into the following solutions that contained 50% of foetal bovine serum (FBS).

- (1) CRP solution (5 μ g/mL, HEPES 25 mM, pH 7.4),
- (2) hCG solution (5 μ g/mL, HEPES 25 mM, pH 7.4),
- (3) Blank solution (HEPES 25 mM, pH 7.4).

The test area of the strips were analysed by SERRS in mapping mode. 49 spectra were taken in the test area. A Raman spectrometer equipped with a 633 nm laser (~8 mW) was used with 9 seconds exposure time. Spectra were baseline corrected, cosmic rays removed using Renishaw WiRe software and averaged using Matlab.

5.4.7.2. Competitive assay

Nitrocellulose compartment of 9 blank strips were spotted with 0.5 μ L of a CRP solution (50 μ g/mL, HEPES buffer, 25 mM, pH 7.4). Strips were then placed to dry at 37 °C for 1 hour. MGITC labelled his-tag Fab NTA-Ni AuNPs (5 μ L, O.D. ~10) were added to the conjugate pad of each strip. Strips were divided into 3 groups and they were dipped respectively into the following solutions that contained 50% of foetal bovine serum (FBS).

- (1) CRP solution (5 $\mu\text{g}/\text{mL}$, HEPES 25 mM, pH 7.4),
- (2) hCG solution (5 $\mu\text{g}/\text{mL}$, HEPES 25 mM, pH 7.4),
- (3) Blank solution (HEPES 25 mM, pH 7.4).

The test area of the strips were analysed by SERRS in mapping mode. 37 spectra were taken in the test area. A Raman spectrometer equipped with a 633 nm laser (~8 mW) was used with 9 seconds exposure time. Spectra were baseline corrected, cosmic rays removed using Renishaw WiRe software and averaged using Matlab.

5.5. The use of gold nanostars for highly-sensitive lateral flow immunoassay

5.5.1. Characterisation of BBI AuNSs

UV-vis spectroscopy of BBI AuNSs was performed upon arrival and after 30 days. 10 different batches of AuNSs were analysed in the range from 400 to 1100 nm using an Agilent Cary 60 spectrophotometer. Samples (500 μL) were analysed using MilliQ water as reference standard. DLS measurements were performed for each AuNSs batch using a Malvern Zetasizer Nano ZS instrument. Samples (500 μL) were transferred into a PMMA disposable micro-cuvette and 3 replica were taken for each sample. SEM analysis was performed for each batch of AuNSs. A 10 times diluted solution of AuNSs in MilliQ water (2 μL) was pipetted into carbon coated copper grids and left them to dry at room temperature for 20 minutes in a dust free container. The procedure was repeated for three times before the analysis.

5.5.2. Comparison between BBI AuNSs and AuNPs for SERS applications

Two different batches of AuNSs (n° 13098 and n° 17003) and one batch of commercially available 40 nm AuNPs were used during this study. Samples (500 μL , O.D. 1) were incubated with an aqueous solution of MBA (25 μL , 10 μM) for 15 min. After this time, samples were analysed by extinction and Raman spectroscopy using Sierra benchtop Raman reader (Snowy Range instruments) equipped with a 785 nm excitation. Samples were made and analysed in triplicate.

5.5.3. Comparison between BBI AuNSs and AuNPs for LFIA applications

In order to prepare antibody-conjugated AuNSs or AuNPs, each gold sample (1 mL, O.D. 1) was incubated with a solution of anti-CRP mAb (14 μL , 1 mg/mL) for 5 min. Mix colloids were then added to a HEPES buffer solution (500 μL , 10 mM and pH 7.4) that contained 0.2% of BSA and 0.5% of Tween-20. Conjugates were purified by a centrifugation step (6000 rpm for 30 min) and pellets were resuspended in HEPES buffer (100 μL , 5 mM and pH 7.5). Three replica for each conjugate were prepared and tested. LF test was performed using competitive type strips containing 4 CRP lines varying from 62.5 to 500 $\mu\text{g}/\text{mL}$. Blank strips, that were previously spotted with a solution of BNP (500 $\mu\text{g}/\text{mL}$) on the middle of NC, were also used as control samples. 3 aliquots of AuNSs conjugates (10 μL , O.D. 10) and 3 aliquots of AuNPs conjugates (10 μL , O.D. 10) were individually placed into the CP of competitive type

strips. Control experiment was performed as follows. 1 aliquot of each conjugate (10 μ L, O.D. 10) was placed into the CP of BNP strips and 1 aliquot of each gold sample (10 μ L, O.D. 10) was placed into the CP of competitive type strips with 4 lines of CRP. Strips were immersed into glass vials that contained a buffer solution (90 μ L, 5 mM HEPES at pH 7.5). Finally, photographs were taken on the nitrocellulose compartment of the strips with a mobile phone camera 13 megapixel (autofocus).

5.5.4. Functionalisation of AuNSs with anti-hCG antibody and MBA

Two different protocols were evaluated for the conjugation of anti-hCG antibodies onto MBA labelled AuNSs. In order to exchange the buffer in which AuNSs are suspended in, the first step for both methods consisted on an initial centrifugation step (6 aliquots of 1 mL, O.D. \sim 1) for 15 min at 4000 rpm. Pellets from each aliquot were collected and resuspended in buffer solution (5.13 mL, 25 mM borate at pH 7.55). In method 1, AuNSs (5.13 mL) were incubated with a solution of anti-hCG antibodies (150 μ L, 0.1 mg/mL) and left stirring overnight at room temperature. Subsequently, while stirring, an aqueous solution of MBA (300 μ L, 50 μ M) was incubated with the AuNSs@anti-hCG conjugate for 1 h. A BSA solution (300 μ L, 10% w/w at pH 9) was then added to the mix and left stirring for another 1 h. AuNSs@anti-hCG@MBA pellets were then collected by a centrifugation step (4000 rpm for 15 min) and resuspended in buffer (600 μ L, 25 mM borate at pH 7.55). AuNSs@anti-hCG@MBA was characterised by extinction spectroscopy (λ_{\max} = 662 nm). In method 2, AuNSs (5.13 mL) were firstly incubated with an aqueous solution of MBA (300 μ L, 50 μ M) for 30 min and secondly a solution of anti-hCG antibodies (150 μ L, 0.1 mg/mL) was added to the mix and left stirring for 1 h. A BSA solution (300 μ L, 10% w/w and pH 9) was added to the mix and left stirring for another 1 h. AuNSs@MBA@anti-hCG pellets were then collected by a centrifugation step (4000 rpm for 15 min) and resuspended in buffer (600 μ L, 25 mM borate at pH 7.55). AuNSs@MBA@anti-hCG was characterised by extinction spectroscopy (λ_{\max} = 660 nm). Both conjugates were analysed by Raman spectroscopy using a Sierra benchtop Raman reader (Snowy Range instruments) equipped with a 785 nm excitation laser.

5.5.5. SERS-based LFIA for the detection of hCG in buffer solutions

LFIA was performed using sandwich type strips containing anti-FSH antibodies as TL (0.25 mg/mL) and anti-mouse IgG as CL (1 mg/mL). AuNSs@MBA@anti-hCG (5 μ L, O.D. 7.48, λ_{\max} 659 nm) was placed onto the CP of 9 strips. Eight hCG sample solutions (100 μ L, 25 mM

borate at pH 7.55) varying from 0.005 to 50 ng/mL, were placed in glass vials and strips were immersed into the sample solutions. 1 strip was immersed in glass vial that contained no hCG (100 μ L, 25 mM borate at pH 7.55). Once glass vials were empty of solution, a further aliquot of buffer (100 μ L, 25 mM borate at pH 7.4) was added in order to wash any conjugate residues on NC. The same procedure was performed using commercially available anti-hCG-AuNPs conjugate (5 μ L, O.D. 10, λ_{max} 530 nm). Three replica were performed for each hCG sample. Once strips were dried, they were scanned with a resolution of 600 DPI using an HP office jet 6500A scanner. The picture of the LF strips was analysed by using Image J software. RGB values for each sample were calculated by subtracting the averaged RGB value of the nitrocellulose (out of 15 strips) to the RGB value of the TL for each sample. Furthermore, strips containing AuNSs@MBA@anti-hCG was analysed using a Raman microscope in mapping mode. 80 SERS spectra were taken on an area of 600 x 3800 μ m within the TL. A 785 nm laser (77 mW) was used at various powers and exposure times, depending on the sample analysed. Spectra were baseline corrected, cosmic rays removed and averaged using Renishaw WiRe software. In order to normalise the data, averaged intensities of the peak at 1082 cm^{-1} for each map were reported as counts x sec^{-1} x mW^{-1} , where: counts are the arbitrary unit of the intensity at 1082 cm^{-1} peak given by the instrument; sec^{-1} is the exposure time used for the measurement and mW^{-1} is the power of the laser used during the measurement.

5.5.6. Raman reporter molecule evaluation

AuNSs (3 mL, O.D. 1.06) were centrifuged at 4000 rpm for 12 min and pellets were resuspended in buffer (2.4 mL, 25 mM borate at pH 7.55). An aqueous solution of MBA (150 μ L, 50 μ M) was added to the colloids and the mix was left stirring for 30 min at room temperature. The same procedure was repeated with BPE, PPY and PYOT solutions (150 μ L, 50 μ M). 4 aliquots of anti-hCG antibodies (75 μ L, 0.1 mg/mL) were incubated respectively with each of the AuNSs@dyes for 1 h. Each of the AuNSs@dye@anti-hCG was incubated for 1 h with a BSA solution (300 μ L, 10% w/w and pH 9). Pellets from each sample were collected by a centrifugation step (4000 rpm for 15 min) and resuspended in buffer (3 mL, 25 mM borate at pH 7.55). In order to discharge any non-reacted antibodies, the AuNSs@dye@anti-hCG samples were centrifuged for a second time at 3400 rpm for 10 min and pellets were resuspended in buffer (180 μ L, 25 mM borate at pH 7.55). Extinction spectroscopy and DLS were performed for the AuNSs@dye@anti-hCG samples. SERS measurement were taken

with a Raman reader equipped with a 785 nm excitation laser. Each AuNSs@dye@anti-hCG sample (5 μL) was tested in sandwich LFIA (TLs at 0.25 mg/mL) using 4 solutions (95 μL each, 25 mM borate at pH 7.55) that contained hCG from 0 to 10 ng/mL. There replicates were performed for each solution. Once strips were dried, photographs were taken at a resolution of 72 DPI with a Samsung mobile phone camera SM-A310F. Strips were also analysed using a Raman microscope in mapping mode. 80 SERS spectra were taken on an area of 600 x 3800 μm within the TL. A 785 nm laser (77 mW) was used at various powers and exposure times, depending on the sample analysed. Spectra were baseline corrected, cosmic rays removed and averaged using Renishaw WiRe software. In order to normalise the data, averaged intensities of the peak at 1082 cm^{-1} for each map were reported as counts x sec^{-1} x mW^{-1} , where: counts are the arbitrary unit of the intensity at 1082 cm^{-1} peak given by the instrument; sec^{-1} is the exposure time used for the measurement and mW^{-1} is the power of the laser used during the measurement.

5.5.7. Optimisation of the AuNSs@MBA@anti-hCG conjugation method

8 aliquots of AuNSs (0.5 mL each, O.D. 1.06) were placed in centrifuge tubes and given the following sample identifications: 1A, 2A, 3A, 4A, 1C, 2C, 3C and 4C. Samples were centrifuged (4000 rpm for 15 min) and pellets (10 μL) were resuspended in various volumes of borate buffer (25 mM, pH 7.55). 2 pellets (1A and 1C) were resuspended in 427.5 μL of buffer. 2 pellets (2A and 2C) were resuspended in 402.5 μL of buffer. 2 pellets (3A and 3C) were resuspended in 377.5 μL of buffer. 2 pellets (4A and 4C) were resuspended in 352.5 μL of buffer. Each of the 8 samples was subsequently incubated with MBA (25 μL , 10 μM) for 30 min and anti-hCG (12.5 μL , 0.1 mg/mL) for 1 h. Samples 1, 2, 3 and 4 were incubated respectively with 25, 50, 75 and 100 μL of a BSA solution (10%) for further 1 h. Samples were centrifuged at various time and frequency of rotation. All samples were centrifuged one time for 15 min at 4000 rpm. 4 pellets (1C, 2C, 3C and 4C) were resuspended in 500 μL of borate buffer and centrifuged for a second time at 3500 rpm for 10 min. Finally, all the 8 pellets were resuspended in buffer (50 μL , 25 mM borate at pH 7.55). For LF tests, each sample (5 μL) was placed on the CPs of 5 hCG sandwich type strips (TL at 0.25 mg/mL). Strips were placed in glass vials containing 4 different hCG solutions (0.005, 0.05, 0.5 and 5 ng/mL, 95 μL in borate buffer 25mM and pH 7.55) and a blank sample that contained only the buffer. Once strips were dried, they were scanned with a resolution of 350 DPI using an Epson scanner Perfection V370. Strips were analysed using a Raman microscope in mapping mode. 80 SERS

spectra were taken on an area of 600 x 3800 μm within the TL. A 785 nm laser (77 mW) was used at various powers and exposure times, depending on the sample analysed. Spectra were baseline corrected, cosmic rays removed and averaged using Renishaw WiRe software. In order to normalise the data, averaged intensities of the peak at 1082 cm^{-1} for each map were reported as counts x sec^{-1} x mW^{-1} , where: counts are the arbitrary unit of the intensity at 1082 cm^{-1} peak given by the instrument; sec^{-1} is the exposure time used for the measurement and mW^{-1} is the power of the laser used during the measurement.

5.5.8. SERS-based LFIA for the detection of hCG in a pseudo-biological matrix

AuNSs@MBA@anti-hCG (5 μL , O.D. 6.35, λ_{max} 665 nm) was placed on the CP of 9 hCG sandwich type LF test strips (TL at 0.25 mg/mL). Strips were placed individually in 8 glass vials containing solutions of hCG varying from 0.078 to 10 ng/mL (95 μL , 25mM borate at pH 7.55) and a blank sample that contained only the buffer (95 μL). Each solution contained 90% of Surine. Once glass vials were empty of solution, a further aliquot of buffer (100 μL , 25 mM borate at pH 7.4) was added in order to wash any conjugate residues on NC Each test was performed in triplicate. Once strips were dried, they were scanned with a resolution of 350 DPI using an Epson scanner Perfection V370. LF strip images were analysed by using Image J software. RGB values for each sample were calculated by subtracting the averaged RGB value of the nitrocellulose (out of 9 strips) to the RGB value of the TL for each sample. Strips were also analysed using a Raman microscope in mapping mode. 80 SERS spectra were taken on an area of 600 x 3800 μm within the TL. A 785 nm laser (77 mW) was used at various powers and exposure times, depending on the sample analysed. Spectra were baseline corrected, cosmic rays removed and averaged using Renishaw WiRe software. In order to normalise the data, averaged intensities of the peak at 1082 cm^{-1} for each map were reported as counts x sec^{-1} x mW^{-1} , where: counts are the arbitrary unit of the intensity at 1082 cm^{-1} peak given by the instrument; sec^{-1} is the exposure time used for the measurement and mW^{-1} is the power of the laser used during the measurement. The same experiment was repeated using an additional 6 samples of hCG (0, 5, 20, 35, 50 and 65 $\mu\text{g}/\text{mL}$) that contained 90% of Surine solution (95 μL , 25mM borate at pH 7.55).

CHAPTER 6: Final Conclusion and Future Work

The understanding of the interactions at the interface between metallic NPs and biomolecules is essential to create functional, specific and sensitive nanosensors. With expanding biotechnology techniques, a wide range of antibody molecules have become available to researchers for their use as recognition tools in the development of nanosensors. In particular, antibody-conjugated NPs have been developed for biomedical applications such as therapy and diagnosis.¹⁵² The ability of conjugating Abs onto NPs mainly depends on the surface composition of NPs and the functional groups of the Abs. Many conjugation methods, that are based on the use of external reagents such as crosslinkers and blocking reagents have been developed.¹⁵⁰ In this research, the development of a universal method that can be rapid, straightforward and allow the creation of a stable conjugate to be used in many applications, was performed. In order to achieve this, an antibody conjugation, based on the interaction between metal ions complexes and the imidazole ring of a histidine unit, was investigated during this research. Recombinant antibodies can be tagged with specific amino acids sequences such as poly-L-histidine units, to allow their purification in IMAC columns.²¹³ These columns usually contain divalent ions of nickel, cobalt, copper or zinc that are immobilised to a solid matrix via a chelating group such as IDA and NTA. Several works on functionalised NPs that are able to bind, carry or recognise his-tag proteins or enzymes have been developed in the last few decades.

A linker for AuNPs that can attach the his-tag of a recombinant Fab anti-CRP antibody, while providing stability and protection against non-specific protein bindings, was created during this thesis. The AuNPs surface was initially modified with PEG molecules that are known to prevent any non-specific interactions and protect the AuNPs from aggregations.²²³ The NTA group was then covalently attached to the PEGylated AuNPs by using the zero-length crosslinkers EDC and sulfo-NHS. Amongst four metal ions that were evaluated in the formation of a coordination complex with the NTA at the surface of AuNPs, nickel performed best. The NTA-Ni AuNPs showed good stability and a stronger interaction towards the his-tag Fab antibody. It was also established that the nickel concentration and the incubation time drove the antibody uptake. The nickel/histidine conjugation method also allowed the his-tag

Fab antibody to be immobilised on the AuNPs surface in an oriented manner, as the his-tag was located on the opposite side of the antigen-binding region. The antigen binding efficiency of the NTA-Ni AuNPs his-tag Fab conjugate was compared to commercially available antibody-gold conjugates, by using the “half-dipstick” lateral flow test. Results demonstrated a high binding efficiency, suggesting that the antigen-binding site of the Ab was not blocked by steric hindrance. Moreover, it was discovered that the his-tag Fab interaction with the NTA-Ni AuNPs was reversible. By using an imidazole solution, it was possible to regenerate the NTA-Ni AuNPs that were previously attached to the his-tag Fab. This characteristic is important for those applications where carry/release nanosystems are required, such as drug delivery. The NTA-Ni AuNPs could potentially be used for the conjugation of any commercially available his-tag antibody. With further optimisation the NTA-Ni AuNPs could be also used in future work for the purification of recombinant his-tag antibodies from cell media. Current methodologies involves the use of affinity chromatography columns. These systems are usually expensive and time consuming as they require sample preparation such as buffer exchange and post-purification columns that removes specific contaminants. The NTA-Ni AuNPs developed in this work, can be used as an alternative purification method for his-tag antibodies. The colloidal solutions could be inoculated on the cell culture so the antibodies conjugated NTA-Ni AuNPs could be collected by a simple centrifugation step. The conjugate can be used in immunoassays potentially without any additional steps. Also, if only antibodies are needed, they can be unloaded from the NTA-Ni AuNPs by using imidazole solutions.

The NTA-Ni AuNPs his-tag Fab conjugate was also labelled with RRM for use in a SERS-based lateral flow immunoassay (LFIA). LFIA is a robust, rapid and cost-effective analytical technique that has made a major impact on a variety of diagnostic testing over the last twenty years.²⁶⁹ Despite these advantages, LFIA often lacks of sensitivity. Many advancements have been made in order to increase the sensitivity of the LFIA.²⁷⁰ In particular signal amplification methods that are based on colorimetric, fluorescence and SERS detection have been developed in the last few years. In this thesis, amplification based on SERS were developed for two different LFIA for the detection of CRP and hCG. Nanoparticles, RRM and different conjugation strategies were evaluated in order to achieve the optimal conditions for highly sensitive LFIA.

The detection of CRP was performed by a SERRS-based LFIA using the his-tag Fab conjugated NTA-Ni AuNPs. The conjugate was labelled with MGITC, showing strong SERRS signals when a 633 nm laser was used in the assay, due to the Resonance effect. The stability of the MGITC labelled NTA-Ni conjugate was higher than labelled conjugates that were prepared by using a passive adsorption method. A sandwich-like format of the assay was developed and a 25-folds improvement in sensitivity was achieved by using the SERRS detection compared to visual detection. Also an LOD equal to 1.84 ng/mL of CRP was calculated. This value is the same order of magnitude of LODs obtained with other signal amplified-LFIAs such as fluorescence and chemiluminescence that can detect respectively 8.5 and 1.05 ng/mL of CRP.^{237,239} A competitive format SERRS-based LFIA was also developed in order to overcome assay interferences such as the hook effect. Furthermore, both sandwich and competitive assays were evaluated with the presence of serum and a non-specific target, suggesting that the compatibility of SERRS-based LFIA for detection in biological matrices. Due to the simplicity of the antibody conjugation/labelling procedures used here, the SERRS active NTA-Ni AuNPs may be used as a universal platform for PoC analyte detection. The LF signal can be analysed by using portable Raman readers for assay sensitivity improvement.

Finally, anisotropic NPs such as AuNSs, were evaluated for use in SERS-based LFIA and their performance was compared to spherical AuNPs, showing an overall superiority. Numerous papers and reviews have been published showing many advantages of anisotropic NPs in several fields of nanotechnology, especially in bioanalytical applications.⁵²⁻⁵⁴ In particular, AuNSs are often used as substrates for SERS applications, thanks to their morphology that can allow the generation of "hot spots", resulting in stronger SERS signals.²⁵⁸

A sandwich-like SERS-based LFIA for the detection of hCG was performed in buffer solutions and in pseudo-biological matrices by using AuNSs functionalised with RRM and anti-hCG antibodies. The performance of SERS active AuNSs in buffer was compared to commercially available anti-hCG antibody conjugated to spherical AuNPs. Results showed a 10-folds sensitivity increase when AuNSs were used. Also a calibration curve was generated by using the SERS signals from the TLs of the strips. An LOD equal to 0.62 ng/mL of hCG was calculated. This value was 40 times more sensitive than LODs of commercially available pregnancy tests.²⁵⁴ Therefore, the assay can be used for early detection of pregnancy or for cancer, where high sensitivity is required.^{255,256}

After optimising the antibody conjugation process and choosing MBA molecules amongst various RRM, the MBA functionalised anti-hCG AuNSs conjugates were tested in LFAs using solution containing 90% of synthetic urine. Results showed an LOD of 18.72 pg/mL of hCG thanks to the SERS signal readout. This value is 2 times lower than an LOD claimed by a published work based on AuNPs and electroanalytical methods for the detection of hCG.²⁶²

The development of a multiplexing assay that uses SERS active AuNSs is suggested as future work. Also, as the AuNSs show intense SERS signal at 785 nm, they may be used for in-vivo diagnostics as biological fluids are transparent at that wavelength. Another feature for AuNSs is the localised heat that can be generated when they interact with a monochromatic light source. This could lead to the development of photothermal therapy techniques.

In conclusion, the results achieved during this thesis suggested that the use of SERS readout in lateral flow test is essential for the development of sensitive and quantitative immunoassays. In particular, the sensitivity can improve by choosing the right surface chemistry between gold colloid and antibodies or by using anisotropic nanostructures, such as AuNSs.

References

- (1) Feynman, R. P. There's Plenty of Room at the Bottom. *Engineering and Science* **1960**, *23*, 22-36.
- (2) Steed, J.; Turner, D.; J. Wallace, K. *Core Concepts in Supramolecular Chemistry and Nanochemistry*; John Wiley & Sons, Chichester, 2007.
- (3) Hawk's Perch Technical Writing, LLC - Nanotechnology Applications: A Variety of Uses <http://www.understandingnano.com/nanotech-applications.html> (accessed Apr 8, 2018).
- (4) Ghosh, P.; Han, G.; De, M.; Kim, C. K.; Rotello, V. M. Gold Nanoparticles in Delivery Applications. *Advanced Drug Delivery Reviews* **2008**, *60*, 1307–1315.
- (5) Cortie, M. 'Technological Applications of Gold Nanoparticles'. In *Gold Nanoparticles for Physics, Chemistry and Biology*; Imperial College Press, London, 2012, 355–377.
- (6) Villiers, C. 'Gold Nanoparticles for Sensors and Drug Delivery'. In *Gold Nanoparticles for Physics, Chemistry and Biology*; Imperial College Press, London, 2012, 299–332.
- (7) Omidfar, K.; Khorsand, F.; Darziani Azizi, M. New Analytical Applications of Gold Nanoparticles as Label in Antibody Based Sensors. *Biosensors and Bioelectronics* **2013**, *43*, 336–347.
- (8) Kocbek, P.; Obermajer, N.; Cegnar, M.; Kos, J.; Kristl, J. Targeting Cancer Cells Using PLGA Nanoparticles Surface Modified with Monoclonal Antibody. *Journal of Controlled Release* **2007**, *120*, 18–26.
- (9) Zhang, G.; Guo, J.; Wang, X. 'Immunochromatographic Lateral Flow Strip Tests'. In *Biosensors and Biodetection*; Humana Press, New York, 2009, 169–183.
- (10) Wang, Y.; Yan, B.; Chen, L. SERS Tags: Novel Optical Nanoprobes for Bioanalysis. *Chemical Reviews* **2013**, *113*, 1391–1428.
- (11) Rosi, N. L.; Mirkin, C. A. Nanostructures in Biodiagnostics. *Chemical Reviews* **2005**, *105*, 1547–1562.
- (12) Li, S.; Yu, X.; Zhang, G.; Ma, Y.; Yao, J.; Keita, B.; Louis, N.; Zhao, H. Green Chemical Decoration of Multiwalled Carbon Nanotubes with Polyoxometalate-Encapsulated Gold Nanoparticles: Visible Light Photocatalytic Activities. *Journal of Materials*

Chemistry **2011**, *21*, 2282–2287.

- (13) Tian, B.; Zheng, X.; Kempa, T. J.; Fang, Y.; Yu, N.; Yu, G.; Huang, J.; Lieber, C. M. Coaxial Silicon Nanowires as Solar Cells and Nanoelectronic Power Sources. *Nature* **2007**, *449*, 885–889.
- (14) Algar, W. R.; Tavares, A. J.; Krull, U. J. Beyond Labels: A Review of the Application of Quantum Dots as Integrated Components of Assays, Bioprobes, and Biosensors Utilizing Optical Transduction. *Analytica Chimica Acta* **2010**, *673*, 1–25.
- (15) Whitesides, G. M. Nanoscience, Nanotechnology and Chemistry. *Small* **2005**, *1*, 172–179.
- (16) Jain, P.; Huang, X.; El-Sayed, I.; El-Sayed, M. Review of Some Interesting Surface Plasmon Resonance-Enhanced Properties of Noble Metal Nanoparticles and Their Applications to Biosystems. *Plasmonics* **2007**, *2*, 107–118.
- (17) Zamborini, F. P.; Bao, L.; Dasari, R. Nanoparticles in Measurement Science. *Analytical Chemistry* **2012**, *84*, 541–576.
- (18) Louis, C.; Pluchery, O. *Gold Nanoparticles for Physics, Chemistry and Biology*; Imperial College Press, London, 2012.
- (19) Freestone, I.; Meeks, N.; Sax, M.; Higgitt, C. The Lycurgus Cup — A Roman Nanotechnology. *Gold Bulletin* **2007**, *40*, 270–277.
- (20) Trustees of the British Museum - The Lycurgus Cup http://www.britishmuseum.org/research/collection_online/collection_object_details.aspx?objectId=61219&partId=1&searchText=lycurgus+cup&page=1 (accessed Feb 18, 2018).
- (21) Hunt, L. B. The True Story of Purple of Cassius. *Gold Bulletin* **1976**, *9*, 134–139.
- (22) Moir, J. Colloidal gold and “Purple of Cassius”. *Transactions of the Royal Society of South Africa* **1910**, *2*, 203–204.
- (23) Faraday, M. The Bakerian Lecture: Experimental Relations of Gold (and Other Metals) to Light. *Philosophical Transactions of the Royal Society of London* **1857**, *147*, 145–181.
- (24) Edwards, P. ; Thomas, J. Gold in a Metallic Divided State—From Faraday to Present-

- Day Nanoscience. *Angewandte Chemie International Edition* **2007**, *46*, 5480–5486.
- (25) Tiwari, P.; Vig, K.; Dennis, V.; Singh, S. Functionalized Gold Nanoparticles and Their Biomedical Applications. *Nanomaterials* **2011**, *1*, 31–63.
- (26) Sperling, R. A.; Rivera Gil, P.; Zhang, F.; Zanella, M.; Parak, W. J. Biological Applications of Gold Nanoparticles. *Chemical Society Reviews* **2008**, *37*, 1896–1908.
- (27) Murthy, S. K. Nanoparticles in Modern Medicine: State of the Art and Future Challenges. *International Journal of Nanomedicine* **2007**, *2*, 129–141.
- (28) Thanh, N. T. K.; Maclean, N.; Mahiddine, S. Mechanisms of Nucleation and Growth of Nanoparticles in Solution. *Chemical Reviews* **2014**, *114*, 7610–7630.
- (29) Wangoo, N.; Bhasin, K. K.; Mehta, S. K.; Suri, C. R. Synthesis and Capping of Water-Dispersed Gold Nanoparticles by an Amino Acid: Bioconjugation and Binding Studies. *Journal of Colloid and Interface Science* **2008**, *323*, 247–254.
- (30) Mittal, A. K.; Chisti, Y.; Banerjee, U. C. Synthesis of Metallic Nanoparticles Using Plant Extracts. *Biotechnology Advances* **2013**, *31*, 346–356.
- (31) Turkevich, J.; Stevenson, P. C.; Hillier, J. A Study of the Nucleation and Growth Processes in the Synthesis of Colloidal Gold. *Discussion of the Faraday Society* **1951**, *11*, 55–75.
- (32) Sperling, R. A.; Parak, W. J. Surface Modification, Functionalization and Bioconjugation of Colloidal Inorganic Nanoparticles. *Philosophical Transactions of the Royal Society A: Mathematical, Physical and Engineering Sciences* **2010**, *368*, 1333–1383.
- (33) Frens, G. Controlled Nucleation for the Regulation of the Particle Size in Monodisperse Gold Suspensions. *Nature Physical Science* **1973**, *241*, 20–22.
- (34) Xia, H.; Xiahou, Y.; Zhang, P.; Ding, W.; Wang, D. Revitalizing the Frens Method To Synthesize Uniform, Quasi-Spherical Gold Nanoparticles with Deliberately Regulated Sizes from 2 to 330 nm. *Langmuir* **2016**, *32*, 5870–5880.
- (35) Schmid, G. Large Clusters and Colloids. Metals in the Embryonic State. *Chemical Reviews* **1992**, *92*, 1709–1727.
- (36) Brust, M.; Walker, M.; Bethell, D.; Schiffrin, D. J.; Whyman, R. Synthesis of Thiol-

- Derivatised Gold Nanoparticles in a Two-Phase Liquid–Liquid System. *J. Chem. Soc., Chemical Communications* **1994**, *0*, 801–802.
- (37) Lee, P. C.; Meisel, D. Adsorption and Surface-Enhanced Raman of Dyes on Silver and Gold Sols. *The Journal of Physical Chemistry* **1982**, *86*, 3391–3395.
- (38) Murphy, C. J.; Sau, T. K.; Gole, A. M.; Orendorff, C. J.; Gao, J.; Gou, L.; Hunyadi, S. E.; Li, T. Anisotropic Metal Nanoparticles: Synthesis, Assembly, and Optical Applications. *The Journal of Physical Chemistry B* **2005**, *109*, 13857–13870.
- (39) Kereselidze, Z.; Romero, V. H.; Peralta, X. G.; Santamaria, F. Gold Nanostar Synthesis with a Silver Seed Mediated Growth Method. *Journal of Visualized Experiments* **2012**, *59*, 3570-3575.
- (40) Jana, N. R.; Gearheart, L.; Murphy, C. J. Wet Chemical Synthesis of High Aspect Ratio Cylindrical Gold Nanorods. *The Journal of Physical Chemistry B* **2001**, *105*, 4065–4067.
- (41) Gole, A.; Murphy, C. J. Seed-Mediated Synthesis of Gold Nanorods: Role of the Size and Nature of the Seed. *Chemistry of Materials* **2004**, *16*, 3633–3640.
- (42) Manson, J.; Kumar, D.; Meenan, B. J.; Dixon, D. Polyethylene Glycol Functionalized Gold Nanoparticles: The Influence of Capping Density on Stability in Various Media. *Gold Bulletin* **2011**, *44*, 99–105.
- (43) Grönbeck, H.; Curioni, A.; Andreoni, W. Thiols and Disulfides on the Au(111) Surface: The Headgroup–Gold Interaction. *Journal of the American Chemical Society* **2000**, *122*, 3839–3842.
- (44) Häkkinen, H. The Gold–sulfur Interface at the Nanoscale. *Nature Chemistry* **2012**, *4*, 443–455.
- (45) Wilson, R. The Use of Gold Nanoparticles in Diagnostics and Detection. *Chemical Society Reviews* **2008**, *37*, 2028-2045.
- (46) Connor, E. E.; Mwamuka, J.; Gole, A.; Murphy, C. J.; Wyatt, M. D. Gold Nanoparticles Are Taken Up by Human Cells but Do Not Cause Acute Cytotoxicity. *Small* **2005**, *1*, 325–327.
- (47) Grzelczak, M.; Pérez-Juste, J.; Mulvaney, P.; Liz-Marzán, L. M. Shape Control in Gold Nanoparticle Synthesis. *Chemical Society Reviews* **2008**, *37*, 1783-1791.

- (48) Chen, K.; Zhang, M.; Chang, Y.-N.; Xia, L.; Gu, W.; Qin, Y.; Li, J.; Cui, S.; Xing, G. Utilizing Gold Nanoparticle Probes to Visually Detect DNA Methylation. *Nanoscale Research Letters* **2016**, *11*, 304-313.
- (49) Mie, G. Articles on the optical characteristics of turbid tubes, especially colloidal metal solutions. *Annals of Physics* **1908**, *25*, 377–445.
- (50) Kelly, K. L.; Coronado, E.; Zhao, L. L.; Schatz, G. C. The Optical Properties of Metal Nanoparticles: The Influence of Size, Shape, and Dielectric Environment. *The Journal of Physical Chemistry B* **2003**, *107*, 668–677.
- (51) Oxford English Dictionary - “Anisotropic”
<https://en.oxforddictionaries.com/definition/anisotropic> (accessed Mar 29, 2018).
- (52) Sajanlal, P. R.; Sreeprasad, T. S.; Samal, A. K.; Pradeep, T. Anisotropic Nanomaterials: Structure, Growth, Assembly, and Functions. *Nano Reviews* **2011**, *2*, 5883.
- (53) Mannelli, I.; Marco, M. P. Recent Advances in Analytical and Bioanalysis Applications of Noble Metal Nanorods. *Analytical and Bioanalytical Chemistry* **2010**, *398*, 2451–2469.
- (54) Cederquist, K. B.; Dean, S. L.; Keating, C. D. Encoded Anisotropic Particles for Multiplexed Bioanalysis. *Wiley Interdisciplinary Reviews: Nanomedicine and Nanobiotechnology* **2010**, *2*, 578–600.
- (55) Whitney, T. M.; Searson, P. C.; Jiang, J. S.; Chien, C. L. Fabrication and Magnetic Properties of Arrays of Metallic Nanowires. *Science* **1993**, *261*, 1316–1319.
- (56) Perez Juste, J.; Pastoriza Santos, I.; Liz Marzan, L.; Mulvaney, P. Gold Nanorods: Synthesis, Characterization and Applications. *Coordination Chemistry Reviews* **2005**, *249*, 1870–1901.
- (57) Niu, W.; Chua, Y. A. A.; Zhang, W.; Huang, H.; Lu, X. Highly Symmetric Gold Nanostars: Crystallographic Control and Surface-Enhanced Raman Scattering Property. *Journal of the American Chemical Society* **2015**, *137*, 10460–10463.
- (58) Wang, X.; Yang, D.-P.; Huang, P.; Li, M.; Li, C.; Chen, D.; Cui, D. Hierarchically Assembled Au Microspheres and Sea Urchin-like Architectures: Formation Mechanism and SERS Study. *Nanoscale* **2012**, *4*, 7766-7772.
- (59) Teranishi, T.; Inoue, Y.; Nakaya, M.; Oumi, Y.; Sano, T. Nanoacorns: Anisotropically

- Phase-Segregated CoPd Sulfide Nanoparticles. *Journal of the American Chemical Society* **2004**, *126*, 9914–9915.
- (60) Shende, P.; Kasture, P.; Gaud, R. S. Nanoflowers: The Future Trend of Nanotechnology for Multi-Applications. *Artificial Cells, Nanomedicine and Biotechnology* **2018**, 1–10.
- (61) Sau, T. K.; Rogach, A. L.; Jäckel, F.; Klar, T. A.; Feldmann, J. Properties and Applications of Colloidal Nonspherical Noble Metal Nanoparticles. *Advanced Materials* **2010**, *22*, 1805–1825.
- (62) Shiohara, A.; Novikov, S. M.; Solís, D. M.; Taboada, J. M.; Obelleiro, F.; Liz-Marzán, L. M. Plasmon Modes and Hot Spots in Gold Nanostar–Satellite Clusters. *The Journal of Physical Chemistry C* **2015**, *119*, 10836–10843.
- (63) Jana, N. R.; Pal, T. Anisotropic Metal Nanoparticles for Use as Surface-Enhanced Raman Substrates. *Advanced Materials* **2007**, *19*, 1761–1765.
- (64) Ming, T.; Zhao, L.; Yang, Z.; Chen, H.; Sun, L.; Wang, J.; Yan, C. Strong Polarization Dependence of Plasmon-Enhanced Fluorescence on Single Gold Nanorods. *Nano Letters* **2009**, *9*, 3896–3903.
- (65) Käll, M.; Xu, H.; Johansson, P. Field Enhancement and Molecular Response in Surface-Enhanced Raman Scattering and Fluorescence Spectroscopy. *Journal of Raman Spectroscopy* **2005**, *36*, 510–514.
- (66) Nehl, C. L.; Liao, H.; Hafner, J. H. Optical Properties of Star-Shaped Gold Nanoparticles. *Nano Letters* **2006**, *6*, 683–688.
- (67) Murphy, C. J.; Gole, A. M.; Hunyadi, S. E.; Stone, J. W.; Sisco, P. N.; Alkilany, A.; Kinard, B. E.; Hankins, P. Chemical Sensing and Imaging with Metallic Nanorods. *Chemical Communications* **2008**, 544–557.
- (68) Barbosa, S.; Agrawal, A.; Rodríguez-Lorenzo, L.; Pastoriza-Santos, I.; Alvarez-Puebla, R. A.; Kornowski, A.; Weller, H.; Liz-Marzán, L. M. Tuning Size and Sensing Properties in Colloidal Gold Nanostars. *Langmuir* **2010**, *26*, 14943–14950.
- (69) Skrabalak, S. E.; Chen, J.; Sun, Y.; Lu, X.; Au, L.; Cobley, C. M.; Xia, Y. Gold Nanocages: Synthesis, Properties, and Applications. *Accounts of Chemical Research* **2008**, *41*, 1587–1595.
- (70) Loo, C.; Lin, A.; Hirsch, L.; Lee, M.-H.; Barton, J.; Halas, N.; West, J.; Drezek, R.

Nanoshell-Enabled Photonics-Based Imaging and Therapy of Cancer. *Technology in Cancer Research & Treatment* **2004**, *3*, 33–40.

- (71) Pallavicini, P.; Chirico, G.; Collini, M.; Dacarro, G.; Donà, A.; D'Alfonso, L.; Falqui, A.; Diaz-Fernandez, Y.; Freddi, S.; Garofalo, B. Synthesis of Branched Au Nanoparticles with Tunable near-Infrared LSPR Using a Zwitterionic Surfactant. *Chemical Communications* **2011**, *47*, 1315–1317.
- (72) Yuan, H.; Fales, A. M.; Khoury, C. G.; Liu, J.; Vo-Dinh, T. Spectral Characterization and Intracellular Detection of Surface-Enhanced Raman Scattering (SERS)-Encoded Plasmonic Gold Nanostars. *Journal of Raman Spectroscopy* **2013**, *44*, 234–239.
- (73) Fales, A. M.; Yuan, H.; Vo-Dinh, T. Silica-Coated Gold Nanostars for Combined Surface-Enhanced Raman Scattering (SERS) Detection and Singlet-Oxygen Generation: A Potential NanoplatforM for Theranostics. *Langmuir* **2011**, *27*, 12186–12190.
- (74) Hirsch, L. R.; Stafford, R. J.; Bankson, J. A.; Sershen, S. R.; Rivera, B.; Price, R. E.; Hazle, J. D.; Halas, N. J.; West, J. L. Nanoshell-Mediated near-Infrared Thermal Therapy of Tumors under Magnetic Resonance Guidance. *Proceedings of the National Academy of Sciences* **2003**, *100*, 13549–13554.
- (75) The Swedish Royal Academy - The Nobel Prize in Physics: 1930 https://www.nobelprize.org/nobel_prizes/physics/laureates/1930/raman-facts.html (accessed Mar 30, 2018).
- (76) Crouch, S.; Holler, S.; Skoog, D. *Principles of Instrumental Analysis, 6th Ed.*; Thomson Brooks/Cole, Belmont, 2007.
- (77) Atkins, P.; De Paula, J. *Atkins' Physical Chemistry, 9th Ed.*; Oxford University Press, Oxford, 2010.
- (78) Ferraro, J.; Nakamoto K.; Brown C. *Introductory Raman Spectroscopy, 2nd Ed.*; Academic press, San Diego, 2003.
- (79) Kneipp, K.; Kneipp, H.; Itzkan, I.; Dasari, R. R.; Feld, M. S. Surface-Enhanced Raman Scattering and Biophysics. *Journal of Physics: Condensed Matter* **2002**, *14*, 597.
- (80) Smith, E.; Dent, G. *Modern Raman Spectroscopy: A Practical Approach*; John Wiley & Sons, Chichester, 2005.
- (81) Baker, M.; Hughes, C.; Hollywood, K. *Biophotonics: Vibrational Spectroscopic*

Diagnostics; Morgan & Claypool, Bristol, 2016.

- (82) Schlücker, S. Surface-Enhanced Raman Spectroscopy: Concepts and Chemical Applications. *Angewandte Chemie International Edition* **2014**, *53*, 4756–4795.
- (83) Fleischmann, M.; Hendra, P. J.; McQuillan, A. J. Raman Spectra of Pyridine Adsorbed at a Silver Electrode. *Chemical Physics Letters* **1974**, *26*, 163–166.
- (84) Jeanmaire, D. L.; Van Duyne, R. P. Surface Raman Spectroelectrochemistry: Part I. Heterocyclic, aromatic, and aliphatic amines adsorbed on the anodized silver electrode. *Journal of Electroanalytical Chemistry and Interfacial Electrochemistry* **1977**, *84*, 1–20.
- (85) Albrecht, M. G.; Creighton, J. A. Anomalously Intense Raman Spectra of Pyridine at a Silver Electrode. *Journal of the American Chemical Society* **1977**, *99*, 5215–5217.
- (86) Le Ru, E.; Etchegoin, P.; *Principles of Surface-Enhanced Raman Spectroscopy: and Related Plasmonic Effects, 1st Ed.*; Elsevier, Amsterdam, 2009.
- (87) Schatz, G.; Young, M.; Van Duyne, R. 'Electromagnetic Mechanism of SERS'. In *Surface-Enhanced Raman Scattering*; Springer, Berlin & Heidelberg, 2006, 19–45.
- (88) Lombardi, J. R.; Birke, R. L. A Unified View of Surface-Enhanced Raman Scattering. *Accounts of Chemical Research* **2009**, *42*, 734–742.
- (89) Rodríguez-Lorenzo, L.; Álvarez-Puebla, R. A.; Pastoriza-Santos, I.; Mazzucco, S.; Stéphan, O.; Kociak, M.; Liz-Marzán, L. M.; García de Abajo, F. J. Zeptomol Detection Through Controlled Ultrasensitive Surface-Enhanced Raman Scattering. *Journal of the American Chemical Society* **2009**, *131*, 4616–4618.
- (90) Nikoobakht, B.; Wang, J.; El-Sayed, M. A. Surface-Enhanced Raman Scattering of Molecules Adsorbed on Gold Nanorods: Off-Surface Plasmon Resonance Condition. *Chemical Physics Letters* **2002**, *366*, 17–23.
- (91) Stacy, A. A.; Van Duyne, R. P. Surface Enhanced Raman and Resonance Raman Spectroscopy in a Non-Aqueous Electrochemical Environment: Tris (2, 2' -Bipyridine) Ruthenium (II) Adsorbed on Silver from Acetonitrile. *Chemical Physics Letters* **1983**, *102*, 365–370.
- (92) McNay, G.; Eustace, D.; Smith, W. E.; Faulds, K.; Graham, D. Surface-Enhanced Raman Scattering (SERS) and Surface-Enhanced Resonance Raman Scattering (SERRS): A

- Review of Applications. *Applied Spectroscopy* **2011**, *65*, 825–837.
- (93) Zavaleta, C. L.; Smith, B. R.; Walton, I.; Doering, W.; Davis, G.; Shojaei, B.; Natan, M. J.; Gambhir, S. S. Multiplexed Imaging of Surface Enhanced Raman Scattering Nanotags in Living Mice Using Noninvasive Raman Spectroscopy. *Proceedings of the National Academy of Sciences* **2009**, *106*, 13511-13516.
- (94) Hudson, S. D.; Chumanov, G. Bioanalytical Applications of SERS (Surface-Enhanced Raman Spectroscopy). *Analytical and Bioanalytical Chemistry* **2009**, *394*, 679–686.
- (95) Han, X. X.; Zhao, B.; Ozaki, Y. Surface-Enhanced Raman Scattering for Protein Detection. *Analytical and Bioanalytical Chemistry* **2009**, *394*, 1719–1727.
- (96) David, C.; Smith, W. E. A New Approach for DNA Detection by SERRS. *Faraday Discussions* **2006**, *132*, 261–268.
- (97) Faulds, K.; Jarvis, R.; Smith, W. E.; Graham, D.; Goodacre, R. Multiplexed Detection of Six Labelled Oligonucleotides Using Surface Enhanced Resonance Raman Scattering (SERRS). *Analyst* **2008**, *133*, 1505-1512.
- (98) Willets, K. A. Surface-Enhanced Raman Scattering (SERS) for Probing Internal Cellular Structure and Dynamics. *Analytical and Bioanalytical Chemistry* **2009**, *394*, 85–94.
- (99) Xu, L.-J.; Zong, C.; Zheng, X.-S.; Hu, P.; Feng, J.-M.; Ren, B. Label-Free Detection of Native Proteins by Surface-Enhanced Raman Spectroscopy Using Iodide-Modified Nanoparticles. *Analytical Chemistry* **2014**, *86*, 2238–2245.
- (100) Choi, S.; Hwang, J.; Lee, S.; Lim, D. W.; Joo, H.; Choo, J. Quantitative Analysis of Thyroid-Stimulating Hormone (TSH) Using SERS-Based Lateral Flow Immunoassay. *Sensors and Actuators B: Chemical* **2017**, *240*, 358–364.
- (101) Fu, X.; Cheng, Z.; Yu, J.; Choo, P.; Chen, L.; Choo, J. A SERS-Based Lateral Flow Assay Biosensor for Highly Sensitive Detection of HIV-1 DNA. *Biosensors and Bioelectronics* **2016**, *78*, 530–537.
- (102) Hwang, J.; Lee, S.; Choo, J. Application of a SERS-Based Lateral Flow Immunoassay Strip for the Rapid and Sensitive Detection of Staphylococcal Enterotoxin B. *Nanoscale* **2016**, *8*, 11418–11425.
- (103) Yedomon, B.; Fessi, H.; Charcosset, C. Preparation of Bovine Serum Albumin (BSA) Nanoparticles by Desolvation Using a Membrane Contactor: A New Tool for Large

- Scale Production. *European Journal of Pharmaceutics and Biopharmaceutics* **2013**, *85*, 398–405.
- (104) Eck, W.; Craig, G.; Sigdel, A.; Ritter, G.; Old, L. J.; Tang, L.; Brennan, M. F.; Allen, P. J.; Mason, M. D. PEGylated Gold Nanoparticles Conjugated to Monoclonal F19 Antibodies as Targeted Labeling Agents for Human Pancreatic Carcinoma Tissue. *ACS Nano* **2008**, *2*, 2263–2272.
- (105) Cho, J.; Kushiro, K.; Teramura, Y.; Takai, M. Lectin-Tagged Fluorescent Polymeric Nanoparticles for Targeting of Sialic Acid on Living Cells. *Biomacromolecules* **2014**, *15*, 2012–2018.
- (106) Choi, K. Y.; Chung, H.; Min, K. H.; Yoon, H. Y.; Kim, K.; Park, J. H.; Kwon, I. C.; Jeong, S. Y. Self-Assembled Hyaluronic Acid Nanoparticles for Active Tumor Targeting. *Biomaterials* **2010**, *31*, 106–114.
- (107) Giljohann, D. A.; Seferos, D. S.; Prigodich, A. E.; Patel, P. C.; Mirkin, C. A. Gene Regulation with Polyvalent siRNA–Nanoparticle Conjugates. *Journal of the American Chemical Society* **2009**, *131*, 2072–2073.
- (108) Herr, J. K.; Smith, J. E.; Medley, C. D.; Shangguan, D.; Tan, W. Aptamer-Conjugated Nanoparticles for Selective Collection and Detection of Cancer Cells. *Analytical Chemistry* **2006**, *78*, 2918–2924.
- (109) Harlow, E.; Lane, D. *Antibodies : A Laboratory Manual*; Cold Spring Harbor Laboratory Press, New York, 1988.
- (110) Biedermann, F.; Schneider, H.-J. Experimental Binding Energies in Supramolecular Complexes. *Chemical Reviews* **2016**, *116*, 5216–5300.
- (111) Buxbaum, E. 'Immunoproteins'. In *Fundamentals of Protein Structure and Function*, 2nd Ed.; Springer International Publishing, Switzerland, 2015, 225–285.
- (112) Liddell, E. 'Antibodies'. In *The Immunoassay Handbook*, 4th Ed.; Elsevier, Oxford, 2013, 245–265.
- (113) Mak, T.; Saunders, M. 'B Cell Receptor Structure and Effector Function'. In *The Immune Response*, 1st Ed.; Elsevier, Oxford, 2006, 93–120.
- (114) Lydyard, P.; Whelan, A.; Michael, W. *Immunology*; BIOS Scientific, Oxford, 2003.

- (115) Gould, H.; Beavil, R. 'IgE'. In *Encyclopedia of Immunology*, 2nd Ed.; Elsevier, Oxford, 1998, 1202–1208.
- (116) Underdown, B. 'IgA'. In *Encyclopedia of Immunology*, 2nd Ed.; Elsevier, Oxford, 1998, 1196–1199.
- (117) Van der Burg, M.; Weemaes, C. ; Cunningham-Rundles, C. 'Isotype Defects'. In *Stiehm's Immune Deficiencies*, Elsevier, Oxford, 2014, 389–408.
- (118) Metzger, H. 'Antibody Structure and the Immune Response'. In *The Immune System*, 1st Ed.; Elsevier, Oxford, 1974, 1–6.
- (119) Freysdóttir, J. 'Production of Monoclonal Antibodies'. In *Diagnostic and Therapeutic Antibodies*; Humana Press, New Jersey, 2000, 267–279.
- (120) Gorman, S. D.; Clark, M. R. Humanisation of Monoclonal Antibodies for Therapy. *Seminars in Immunology* **1990**, *2*, 457–466.
- (121) Donzeau, M.; Knappik, A. 'Recombinant Monoclonal Antibodies'. In *Monoclonal antibodies - methods and protocols*; Humana Press, New Jersey, 2007, 15–31.
- (122) Schmitt, J.; Hess, H.; Stunnenberg, H. G. Affinity Purification of Histidine-Tagged Proteins. *Molecular Biology Reports* **1993**, *18*, 223–230.
- (123) Hermanson, G. T. 'Antibody Modification and Conjugation'. In *Bioconjugate Techniques*, 3rd Ed.; Elsevier, Boston, 2013, 867–920.
- (124) Trilling, A. K.; Beekwilder, J.; Zuilhof, H. Antibody Orientation on Biosensor Surfaces: A Minireview. *Analyst* **2013**, *138*, 1619–1627.
- (125) Bickerstaff, G. *Immobilization of Enzymes and Cells*; Humana Press, New York, 1997.
- (126) Goodfriend, T. L.; Levine, L.; Fasman, G. D. Antibodies to Bradykinin and Angiotensin: A Use of Carbodiimides in Immunology. *Science* **1964**, *144*, 1344–1346.
- (127) Hermanson, G. T. 'Heterobifunctional Crosslinkers'. In *Bioconjugate Techniques*, 3rd Ed.; Elsevier, Boston, 2013, 299–339.
- (128) Hermanson, G. T. 'Homobifunctional Crosslinkers'. In *Bioconjugate Techniques*, 3rd Ed.; Elsevier, Boston, 2013, 275–298.
- (129) Hermanson, G. T. 'Zero-Length Crosslinkers'. In *Bioconjugate Techniques*, 3rd Ed.; Elsevier, Boston, 2013, 259–273.

- (130) Pang, L.; Cui, H.; Liu, Y.; Zhong, W. Anti-VEGF Antibody Conjugated CdHgTe Quantum Dots as a Fluorescent Probe for Imaging in Living Mouse. *Journal of Luminescence* **2016**, *173*, 274–278.
- (131) Zhou, Y.; Andersson, O.; Lindberg, P.; Liedberg, B. Reversible Hydrophobic Barriers Introduced by Microcontact Printing: Application to Protein Microarrays. *Microchimica Acta* **2004**, *146*, 193–205.
- (132) Yezhelyev, M. V; Gao, X.; Xing, Y.; Al-Hajji, A.; Nie, S.; O'Regan, R. M. Emerging Use of Nanoparticles in Diagnosis and Treatment of Breast Cancer. *The Lancet Oncology* **2006**, *7*, 657–667.
- (133) Haddadi, A.; Jahan, S. T. Investigation and Optimization of Formulation Parameters on Preparation of Targeted Anti-CD205 Tailored PLGA Nanoparticles. *International Journal of Nanomedicine* **2015**, *10*, 7371-7384.
- (134) Kumar, S.; Aaron, J.; Sokolov, K. Directional Conjugation of Antibodies to Nanoparticles for Synthesis of Multiplexed Optical Contrast Agents with Both Delivery and Targeting Moieties. *Nature Protocols* **2008**, *3*, 314–320.
- (135) Akkapeddi, P.; Azizi, S.-A.; Freedy, A. M.; Cal, P. M. S. D.; Gois, P. M. P.; Bernardes, G. J. L. Construction of Homogeneous Antibody–drug Conjugates Using Site-Selective Protein Chemistry. *Chemical Science* **2016**, *7*, 2954–2963.
- (136) Loo, C.; Hirsch, L.; Lee, M.-H.; Chang, E.; West, J.; Halas, N.; Drezek, R. Gold Nanoshell Bioconjugates for Molecular Imaging in Living Cells. *Optics Letters* **2005**, *30*, 1012.
- (137) Hermanson, G. T. 'The Reactions of Bioconjugation'. In *Bioconjugate Techniques*, 3rd Ed.; Elsevier, Boston, 2013, 229–258.
- (138) Kausaite-Minkstimiene, A.; Ramanaviciene, A.; Kirlyte, J.; Ramanavicius, A. Comparative Study of Random and Oriented Antibody Immobilization Techniques on the Binding Capacity of Immunosensor. *Analytical Chemistry* **2010**, *82*, 6401–6408.
- (139) Park, M.; Jose, J.; Pyun, J.-C. SPR Biosensor by Using E. Coli Outer Membrane Layer with Autodisplayed Z-Domains. *Sensors and Actuators B: Chemical* **2011**, *154*, 82–88.
- (140) Le Brun, A. P.; Holt, S. A.; Shah, D. S. H.; Majkrzak, C. F.; Lakey, J. H. The Structural Orientation of Antibody Layers Bound to Engineered Biosensor Surfaces. *Biomaterials* **2011**, *32*, 3303–3311.

- (141) Hermanson, G. T. 'Microparticles and Nanoparticles'. In *Bioconjugate Techniques*, 3rd Ed.; Elsevier, Boston, 2013, 549–587.
- (142) Hoefsmit, E. C. M.; Korn, C.; Blijleven, N.; Ploem, J. S. Light Microscopical Detection of Single 5 and 20 nm Gold Particles Used for Immunolabelling of Plasma Membrane Antigens with Silver Enhancement and Reflection Contrast. *Journal of Microscopy* **1986**, *143*, 161–169.
- (143) Wong, J.; Chilkoti, A.; Moy, V. T. Direct Force Measurements of the Streptavidin–biotin Interaction. *Biomolecular Engineering* **1999**, *16*, 45–55.
- (144) Krager, K. J.; Sarkar, M.; Twait, E. C.; Lill, N. L.; Koland, J. G. A Novel Biotinylated Lipid Raft Reporter for Electron Microscopic Imaging of Plasma Membrane Microdomains. *The Journal of Lipid Research* **2012**, *53*, 2214–2225.
- (145) Bornhorst, J.; Falke, J. Purification of Proteins Using Polyhistidine Affinity Tags. *Methods in enzymology* **2000**, *326*, 245–254.
- (146) Porath, J.; Carlsson, J. A. N.; Olsson, I.; Belfrage, G. Metal Chelate Affinity Chromatography, a New Approach to Protein Fractionation. *Nature* **1975**, *258*, 598–599.
- (147) Yang, L.; Mao, H.; Wang, Y. A.; Cao, Z.; Peng, X.; Wang, X.; Duan, H.; Ni, C.; Yuan, Q.; Adams, G. Single Chain Epidermal Growth Factor Receptor Antibody Conjugated Nanoparticles for in Vivo Tumor Targeting and Imaging. *Small* **2008**, *5*, 235–243.
- (148) Balevicius, Z.; Ramanaviciene, A.; Baleviciute, I.; Makaraviciute, A.; Mikoliunaite, L.; Ramanavicius, A. Evaluation of Intact- and Fragmented-Antibody Based Immunosensors by Total Internal Reflection Ellipsometry. *Sensors and Actuators B: Chemical* **2011**, *160*, 555–562.
- (149) Della Ventura, B.; Schiavo, L.; Altucci, C.; Esposito, R.; Velotta, R. Light Assisted Antibody Immobilization for Bio-Sensing. *Biomedical Optics Express* **2011**, *2*, 3223–3231.
- (150) Jazayeri, M. H.; Amani, H.; Pourfatollah, A. A.; Pazoki-Toroudi, H.; Sedighimoghaddam, B. Various Methods of Gold Nanoparticles (GNPs) Conjugation to Antibodies. *Sensing and Bio-Sensing Research* **2016**, *9*, 17–22.
- (151) Zheng, M.; Davidson, F.; Huang, X. Ethylene Glycol Monolayer Protected

- Nanoparticles for Eliminating Nonspecific Binding with Biological Molecules. *Journal of the American Chemical Society* **2003**, *125*, 7790–7791.
- (152) Arruebo, M.; Valladares, M.; González-Fernández, Á. Antibody-Conjugated Nanoparticles for Biomedical Applications. *Journal of Nanomaterials* **2009**, *2009*, 1–24.
- (153) Ahmed, N.; Fessi, H.; Elaissari, A. Theranostic Applications of Nanoparticles in Cancer. *Drug Discovery Today* **2012**, *17*, 928–934.
- (154) Godin, B.; Sakamoto, J. H.; Serda, R. E.; Grattoni, A.; Bouamrani, A.; Ferrari, M. Emerging Applications of Nanomedicine for the Diagnosis and Treatment of Cardiovascular Diseases. *Trends in Pharmacological Sciences* **2010**, *31*, 199–205.
- (155) M. Cardoso, M.; N. Peca, I.; C. A. Roque, A. Antibody-Conjugated Nanoparticles for Therapeutic Applications. *Current Medicinal Chemistry* **2012**, *19*, 3103–3127.
- (156) Daraee, H.; Eatemadi, A.; Abbasi, E.; Fekri Aval, S.; Kouhi, M.; Akbarzadeh, A. Application of Gold Nanoparticles in Biomedical and Drug Delivery. *Artificial Cells, Nanomedicine and Biotechnology* **2016**, *44*, 410–422.
- (157) Tyner, K. M.; Schiffman, S. R.; Giannelis, E. P. Nanobiohybrids as Delivery Vehicles for Camptothecin. *Journal of Controlled Release* **2004**, *95*, 501–514.
- (158) Hayes, M. E.; Drummond, D. C.; Kirpotin, D. B.; Zheng, W. W.; Noble, C. O.; Park, J. W.; Marks, J. D.; Benz, C. C.; Hong, K. Genospheres: Self-Assembling Nucleic Acid-Lipid Nanoparticles Suitable for Targeted Gene Delivery. *Gene Therapy* **2006**, *13*, 646–651.
- (159) West, J. L.; Drezek, R.; Sershen, S.; Halas, N. J. Optically-Absorbing Nanoparticles for Enhanced Tissue Repair. Patent US6685730B2. February 3, 2004.
- (160) Dutz, S.; Hergt, R. Magnetic Particle Hyperthermia—a Promising Tumour Therapy? *Nanotechnology* **2014**, *25*, 452001-452029.
- (161) Ashikaga, T.; Wada, M.; Kobayashi, H.; Mori, M.; Katsumura, Y.; Fukui, H.; Kato, S.; Yamaguchi, M.; Takamatsu, T. Effect of the Photocatalytic Activity of TiO₂ on Plasmid DNA. *Mutation Research/Genetic Toxicology and Environmental Mutagenesis* **2000**, *466*, 1–7.
- (162) El-Sayed, I.; Huang, X.; El-Sayed, M. Selective Laser Photo-Thermal Therapy of Epithelial Carcinoma Using Anti-EGFR Antibody Conjugated Gold Nanoparticles.

Cancer Letters **2006**, *239*, 129–135.

- (163) Kandzia, J.; Anderson, M. J. D.; Mller-Ruchholtz, W. Cell Separation by Antibody-Coupled Magnetic Microspheres and Their Application in Conjunction with Monoclonal HLA-Antibodies. *Journal of Cancer Research and Clinical Oncology* **1981**, *101*, 165–170.
- (164) Kemmner, W.; Moldenhauer, G.; Schlag, P.; Brossmer, R. Separation of Tumor Cells from a Suspension of Dissociated Human Colorectal Carcinoma Tissue by Means of Monoclonal Antibody-Coated Magnetic Beads. *Journal of Immunological Methods* **1992**, *147*, 197–200.
- (165) Suwa, T.; Ozawa, S.; Ueda, M.; Ando, N.; Kitajima, M. Magnetic Resonance Imaging of Esophageal Squamous Cell Carcinoma Using Magnetite Particles Coated with Anti-Epidermal Growth Factor Receptor Antibody. *International Journal of Cancer* **1998**, *75*, 626–634.
- (166) Syedmoradi, L.; Daneshpour, M.; Alvandipour, M.; Gomez, F. A.; Hajghassem, H.; Omidfar, K. Point of Care Testing: The Impact of Nanotechnology. *Biosensors and Bioelectronics* **2017**, *87*, 373–387.
- (167) Justino, C.; Duarte, A.; Rocha-Santos, T. Recent Progress in Biosensors for Environmental Monitoring: A Review. *Sensors* **2017**, *17*, 2918-2932.
- (168) Yasmin, J.; Ahmed, M. R.; Cho, B.-K. Biosensors and Their Applications in Food Safety: A Review. *Journal of Biosystems Engineering* **2016**, *41*, 240–254.
- (169) Tsourkas, A.; Shinde-Patil, V. R.; Kelly, K. A.; Patel, P.; Wolley, A.; Allport, J. R.; Weissleder, R. In Vivo Imaging of Activated Endothelium Using an Anti-VCAM-1 Magneto-optical Probe. *Bioconjugate Chemistry* **2005**, *16*, 576–581.
- (170) Hirsch, L. R.; Jackson, J. B.; Lee, A.; Halas, N. J.; West, J. L. A Whole Blood Immunoassay Using Gold Nanoshells. *Analytical Chemistry* **2003**, *75*, 2377–2381.
- (171) Cui, Y.; Ren, B.; Yao, J.-L.; Gu, R.-A.; Tian, Z.-Q. Synthesis of Ag Core Au Shell Bimetallic Nanoparticles for Immunoassay Based on Surface-Enhanced Raman Spectroscopy. *The Journal of Physical Chemistry B* **2006**, *110*, 4002–4006.
- (172) Fritz, J. Cantilever Biosensors. *Analyst* **2008**, *133*, 855-863.
- (173) Pavey, K. .; Ali, Z.; Olliff, C. .; Paul, F. Application of the Quartz Crystal Microbalance to

- the Monitoring of Staphylococcus Epidermidis Antigen–antibody Agglutination. *Journal of Pharmaceutical and Biomedical Analysis* **1999**, *20*, 241–245.
- (174) Kokkinos, C.; Economou, A.; Prodromidis, M. I. Electrochemical Immunosensors: Critical Survey of Different Architectures and Transduction Strategies. *Trends in Analytical Chemistry* **2016**, *79*, 88–105.
- (175) Posthuma-Trumpie, G. A.; Korf, J.; van Amerongen, A. Lateral Flow (Immuno) Assay: Its Strengths, Weaknesses, Opportunities and Threats. A Literature Survey. *Analytical and Bioanalytical Chemistry* **2009**, *393*, 569–582.
- (176) Office of NIH History - A Timeline of Pregnancy Testing <http://history.nih.gov/exhibits/thinblueline/timeline.html> (accessed Apr 9, 2018).
- (177) Vaitukaitis, J. L.; Braunstein, G. D.; Ross, G. T. A Radioimmunoassay Which Specifically Measures Human Chorionic Gonadotropin in the Presence of Human Luteinizing Hormone. *American Journal of Obstetrics & Gynecology* **1972**, *113*, 751–758.
- (178) Sajid, M.; Kawde, A.-N.; Daud, M. Designs, Formats and Applications of Lateral Flow Assay: A Literature Review. *Journal of Saudi Chemical Society* **2015**, *19*, 689–705.
- (179) Ngom, B.; Guo, Y.; Wang, X.; Bi, D. Development and Application of Lateral Flow Test Strip Technology for Detection of Infectious Agents and Chemical Contaminants: A Review. *Analytical and Bioanalytical Chemistry* **2010**, *397*, 1113–1135.
- (180) Banerjee, R.; Jaiswal, A. Recent Advances in Nanoparticle-Based Lateral Flow Immunoassay as a Point of Care Diagnostic Tool for Infectious Agents and Diseases. *Analyst* **2018**, *143*, 1970-1996.
- (181) Yetisen, A. K.; Akram, M. S.; Lowe, C. R. Paper-Based Microfluidic Point-of-Care Diagnostic Devices. *Lab on a Chip* **2013**, *13*, 2210-2251.
- (182) Parolo, C.; Merkoçi, A. Paper-Based Nanobiosensors for Diagnostics. *Chemical Society Reviews* **2013**, *42*, 450–457.
- (183) Wong, R.; Tse, H. *Lateral Flow Immunoassay*; Humana Press, New York, 2009.
- (184) O'Farrell, B. 'Lateral Flow Immunoassay Systems'. In *The Immunoassay Handbook*, 4th Ed.; Elsevier, Oxford, 2013, 89–107.
- (185) Shin, J.; Chakravarty, S.; Choi, W.; Lee, K.; Han, D.; Hwang, H.; Choi, J.; Jung, H.-I.

- Mobile Diagnostics: Next-Generation Technologies for in Vitro Diagnostics. *Analyst* **2018**, *143*, 1515–1525.
- (186) Hu, J.; Cui, X.; Gong, Y.; Xu, X.; Gao, B.; Wen, T.; Lu, T. J.; Xu, F. Portable Microfluidic and Smartphone-Based Devices for Monitoring of Cardiovascular Diseases at the Point of Care. *Biotechnology Advances* **2016**, *34*, 305–320.
- (187) Roda, A.; Michelini, E.; Zangheri, M.; Di Fusco, M.; Calabria, D.; Simoni, P. Smartphone-Based Biosensors: A Critical Review and Perspectives. *Trends in Analytical Chemistry* **2016**, *79*, 317–325.
- (188) Xiao, W.; Huang, C.; Xu, F.; Yan, J.; Bian, H.; Fu, Q.; Xie, K.; Wang, L.; Tang, Y. A Simple and Compact Smartphone-Based Device for the Quantitative Readout of Colloidal Gold Lateral Flow Immunoassay Strips. *Sensors and Actuators B: Chemical* **2018**, *266*, 63-70.
- (189) Zangheri, M.; Cevenini, L.; Anfossi, L.; Baggiani, C.; Simoni, P.; Di Nardo, F.; Roda, A. A Simple and Compact Smartphone Accessory for Quantitative Chemiluminescence-Based Lateral Flow Immunoassay for Salivary Cortisol Detection. *Biosensors and Bioelectronics* **2015**, *64*, 63-68.
- (190) Srinivasan, B.; O'Dell, D.; Finkelstein, J. L.; Lee, S.; Erickson, D.; Mehta, S. Iron Phone: Mobile Device-Coupled Point-of-Care Diagnostics for Assessment of Iron Status by Quantification of Serum Ferritin. *Biosensors and Bioelectronics* **2018**, *99*, 115–121.
- (191) Pilavaki, E.; Demosthenous, A. Optimized Lateral Flow Immunoassay Reader for the Detection of Infectious Diseases in Developing Countries. *Sensors* **2017**, *17*, 2673-2682.
- (192) Tang, R.; Yang, H.; Gong, Y.; Liu, Z.; Li, X.; Wen, T.; Qu, Z.; Zhang, S.; Mei, Q.; Xu, F. Improved Analytical Sensitivity of Lateral Flow Assay Using Sponge for HBV Nucleic Acid Detection. *Scientific Reports* **2017**, *7*, 1360-1369.
- (193) Wang, Y.; Qin, Z.; Boulware, D. R.; Pritt, B. S.; Sloan, L. M.; González, I. J.; Bell, D.; Rees-Channer, R. R.; Chiodini, P.; Chan, W. C. W. Thermal Contrast Amplification Reader Yielding 8-Fold Analytical Improvement for Disease Detection with Lateral Flow Assays. *Analytical Chemistry* **2016**, *88*, 11774–11782.
- (194) Liu, B.; Du, D.; Hua, X.; Yu, X.-Y.; Lin, Y. Paper-Based Electrochemical Biosensors: From

- Test Strips to Paper-Based Microfluidics. *Electroanalysis* **2014**, *26*, 1214–1223.
- (195) Choi, D. H.; Lee, S. K.; Oh, Y. K.; Bae, B. W.; Lee, S. D.; Kim, S.; Shin, Y.-B.; Kim, M.-G. A Dual Gold Nanoparticle Conjugate-Based Lateral Flow Assay (LFA) Method for the Analysis of Troponin I. *Biosensors and Bioelectronics* **2010**, *25*, 1999–2002.
- (196) Tanaka, R.; Yuhi, T.; Nagatani, N.; Endo, T.; Kerman, K.; Takamura, Y.; Tamiya, E. A Novel Enhancement Assay for Immunochromatographic Test Strips Using Gold Nanoparticles. *Analytical and Bioanalytical Chemistry* **2006**, *385*, 1414–1420.
- (197) Yang, W.; Li, X.; Liu, G.; Zhang, B.; Zhang, Y.; Kong, T.; Tang, J.; Li, D.; Wang, Z. A Colloidal Gold Probe-Based Silver Enhancement Immunochromatographic Assay for the Rapid Detection of Abrin-A. *Biosensors and Bioelectronics* **2011**, *26*, 3710–3713.
- (198) Duan, D.; Fan, K.; Zhang, D.; Tan, S.; Liang, M.; Liu, Y.; Zhang, J.; Zhang, P.; Liu, W.; Qiu, X. Nanozyme-Strip for Rapid Local Diagnosis of Ebola. *Biosensors and Bioelectronics* **2015**, *74*, 134–141.
- (199) Bahadır, E. B.; Sezgintürk, M. K. Lateral Flow Assays: Principles, Designs and Labels. *Trends in Analytical Chemistry* **2016**, *82*, 286–306.
- (200) Li, Z.; Wang, Y.; Wang, J.; Tang, Z.; Pounds, J. G.; Lin, Y. Rapid and Sensitive Detection of Protein Biomarker Using a Portable Fluorescence Biosensor Based on Quantum Dots and a Lateral Flow Test Strip. *Analytical Chemistry* **2010**, *82*, 7008–7014.
- (201) Hu, J.; Zhang, Z.-L.; Wen, C.-Y.; Tang, M.; Wu, L.-L.; Liu, C.; Zhu, L.; Pang, D.-W. Sensitive and Quantitative Detection of C-Reaction Protein Based on Immunofluorescent Nanospheres Coupled with Lateral Flow Test Strip. *Analytical Chemistry* **2016**, *88*, 6577–6584.
- (202) Bruno, J. Application of DNA Aptamers and Quantum Dots to Lateral Flow Test Strips for Detection of Foodborne Pathogens with Improved Sensitivity versus Colloidal Gold. *Pathogens* **2014**, *3*, 341–355.
- (203) Hu, L.-M.; Luo, K.; Xia, J.; Xu, G.-M.; Wu, C.-H.; Han, J.-J.; Zhang, G.-G.; Liu, M.; Lai, W.-H. Advantages of Time-Resolved Fluorescent Nanobeads Compared with Fluorescent Submicrospheres, Quantum Dots, and Colloidal Gold as Label in Lateral Flow Assays for Detection of Ractopamine. *Biosensors and Bioelectronics* **2017**, *91*, 95–103.
- (204) Paterson, A. S.; Raja, B.; Garvey, G.; Kolhatkar, A.; Hagström, A. E. V.; Kourentzi, K.;

- Lee, T. R.; Willson, R. C. Persistent Luminescence Strontium Aluminate Nanoparticles as Reporters in Lateral Flow Assays. *Analytical Chemistry* **2014**, *86*, 9481–9488.
- (205) Wang, Z.; Zong, S.; Wu, L.; Zhu, D.; Cui, Y. SERS-Activated Platforms for Immunoassay: Probes, Encoding Methods, and Applications. *Chemical Reviews* **2017**, *117*, 7910–7963.
- (206) Serebrennikova, K.; Samsonova, J.; Osipov, A. Hierarchical Nanogold Labels to Improve the Sensitivity of Lateral Flow Immunoassay. *Nano-Micro Letters* **2018**, *10*, 24-32.
- (207) Maneeprakorn, W.; Bamrungsap, S.; Apiwat, C.; Wiriyaichaiorn, N. Surface-Enhanced Raman Scattering Based Lateral Flow Immunochromatographic Assay for Sensitive Influenza Detection. *RSC Advances* **2016**, *6*, 112079–112085.
- (208) Blanco-Covián, L.; Montes-García, V.; Girard, A.; Fernández-Abedul, M. T.; Perez-Juste, J.; Pastoriza-Santos, I.; Faulds, K.; Graham, D.; Blanco-López, M. C. Au@Ag SERRS Tags Coupled to a Lateral Flow Immunoassay for the Sensitive Detection of Pneumolysin. *Nanoscale* **2017**, *9*, 2051-2058.
- (209) Li, J.; Macdonald, J. Multiplexed Lateral Flow Biosensors: Technological Advances for Radically Improving Point-of-Care Diagnoses. *Biosensors and Bioelectronics* **2016**, *83*, 177–192.
- (210) Wang, X.; Choi, N.; Cheng, Z.; Ko, J.; Chen, L.; Choo, J. Simultaneous Detection of Dual Nucleic Acids Using a SERS-Based Lateral Flow Assay Biosensor. *Analytical Chemistry* **2017**, *89*, 1163–1169.
- (211) Baio, J. E.; Cheng, F.; Ratner, D. M.; Stayton, P. S.; Castner, D. G. Probing Orientation of Immobilized Humanized Anti-Lysozyme Variable Fragment by Time-of-Flight Secondary-Ion Mass Spectrometry. *Journal of Biomedical Materials Research Part A* **2011**, *97A*, 1–7.
- (212) Pearson, R. G. Hard and Soft Acids and Bases. *Journal of the American Chemical Society* **1963**, *85*, 3533–3539.
- (213) Gaberc-Porekar, V.; Menart, V. Perspectives of Immobilized-Metal Affinity Chromatography. *Journal of Biochemical and Biophysical Methods* **2001**, *49*, 335–360.
- (214) Ueda, E. K. .; Gout, P. .; Morganti, L. Current and Prospective Applications of Metal

- Ion–protein Binding. *Journal of Chromatography A* **2003**, *988*, 1–23.
- (215) Gupta, M.; Caniard, A.; Touceda-Varela, A.; Campopiano, D. J.; Mareque-Rivas, J. C. Nitrilotriacetic Acid-Derivatized Quantum Dots for Simple Purification and Site-Selective Fluorescent Labeling of Active Proteins in a Single Step. *Bioconjugate Chemistry* **2008**, *19*, 1964–1967.
- (216) Abad, J. M.; Mertens, S. F. L.; Pita, M.; Fernández, V. M.; Schiffrin, D. J. Functionalization of Thioctic Acid-Capped Gold Nanoparticles for Specific Immobilization of Histidine-Tagged Proteins. *Journal of the American Chemical Society* **2005**, *127*, 5689–5694.
- (217) Kim, C.; Galloway, J. F.; Lee, K. H.; Searson, P. C. Universal Antibody Conjugation to Nanoparticles Using the Fcγ Receptor I (FcγRI): Quantitative Profiling Of Membrane Biomarkers. *Bioconjugate Chemistry* **2014**, *25*, 1893–1901.
- (218) Hainfeld, J. F.; Liu, W.; Halsey, C. M. R.; Freimuth, P.; Powell, R. D. Ni–NTA–Gold Clusters Target His-Tagged Proteins. *Journal of Structural Biology* **1999**, *127*, 185–198.
- (219) De, M.; Rana, S.; Rotello, V. M. Nickel-Ion-Mediated Control of the Stoichiometry of His-Tagged Protein/Nanoparticle Interactions. *Macromolecular Bioscience* **2009**, *9*, 174–178.
- (220) Susumu, K.; Medintz, I. L.; Delehanty, J. B.; Boeneman, K.; Mattoussi, H. Modification of Poly(ethylene Glycol)-Capped Quantum Dots with Nickel Nitrilotriacetic Acid and Self-Assembly with Histidine-Tagged Proteins. *The Journal of Physical Chemistry C* **2010**, *114*, 13526–13531.
- (221) Zhang, L.; Zhu, X.; Jiao, D.; Sun, Y.; Sun, H. Efficient Purification of His-Tagged Protein by Superparamagnetic Fe₃O₄/Au–ANTA–Co²⁺ Nanoparticles. *Materials Science and Engineering: C* **2013**, *33*, 1989–1992.
- (222) Swartz, J. D.; Gulka, C. P.; Haselton, F. R.; Wright, D. W. Development of a Histidine-Targeted Spectrophotometric Sensor Using Ni(II)NTA-Functionalized Au and Ag Nanoparticles. *Langmuir* **2011**, *27*, 15330–15339.
- (223) Jokerst, J. V.; Lobovkina, T.; Zare, R. N.; Gambhir, S. S. Nanoparticle PEGylation for Imaging and Therapy. *Nanomedicine* **2011**, *6*, 715–728.
- (224) Thermo Fisher Scientific - Chemical structure and properties of CT(PEG)12

- <http://www.piercenet.com/product/carboxy-peg-thiol-compounds> (accessed Apr 10, 2018).
- (225) Thermo Fisher Scientific - Chemical structure and properties of MT(PEG)₄ <https://www.thermofisher.com/order/catalog/product/26132?SID=srch-srp-26132> (accessed Apr 10, 2018).
- (226) Qian, X.; Peng, X.-H.; Ansari, D. O.; Yin-Goen, Q.; Chen, G. Z.; Shin, D. M.; Yang, L.; Young, A. N.; Wang, M. D.; Nie, S. In Vivo Tumor Targeting and Spectroscopic Detection with Surface-Enhanced Raman Nanoparticle Tags. *Nature Biotechnology* **2008**, *26*, 83–90.
- (227) Wuelfing, W. P.; Gross, S. M.; Miles, D. T.; Murray, R. W. Nanometer Gold Clusters Protected by Surface-Bound Monolayers of Thiolated Poly (Ethylene Glycol) Polymer Electrolyte. *Journal of the American Chemical Society* **1998**, *120*, 12696–12697.
- (228) Hermanson, G. T. 'PEGylation and Synthetic Polymer Modification'. In *Bioconjugate Techniques*, 3rd Ed.; Elsevier, Boston, 2013, 787–838.
- (229) Bartczak, D.; Kanaras, A. G. Preparation of Peptide-Functionalized Gold Nanoparticles Using One Pot EDC/Sulfo-NHS Coupling. *Langmuir* **2011**, *27*, 10119–10123.
- (230) Staros, J. V.; Wright, R. W.; Swingle, D. M. Enhancement by N-Hydroxysulfosuccinimide of Water-Soluble Carbodiimide-Mediated Coupling Reactions. *Analytical Biochemistry* **1986**, *156*, 220–222.
- (231) Volanakis, J. Human C-Reactive Protein: Expression, Structure, and Function. *Molecular Immunology* **2001**, *38*, 189–197.
- (232) Koenig, W. C-Reactive Protein and Cardiovascular Risk: Has the Time Come for Screening the General Population? *Clinical Chemistry* **2001**, *47*, 9–10.
- (233) French, D.; Wu, A. 'Cardiac Markers'. In *The Immunoassay Handbook*, 4th Ed.; Elsevier, Oxford, 2013, 817–831.
- (234) Vashist, S. K.; Venkatesh, A. G.; Schneider, E. M.; Beaudoin, C.; Lippa, P. B.; Luong, J. H. T. Bioanalytical Advances in Assays for C-Reactive Protein. *Biotechnology Advances* **2016**, *34*, 272–290.
- (235) Oh, Y. K.; Joung, H.-A.; Han, H. S.; Suk, H.-J.; Kim, M.-G. A Three-Line Lateral Flow Assay Strip for the Measurement of C-Reactive Protein Covering a Broad Physiological

- Concentration Range in Human Sera. *Biosensors and Bioelectronics* **2014**, *61*, 285–289.
- (236) Leung, W.; Chan, C. P.; Rainer, T. H.; Ip, M.; Cautherley, G. W. H.; Renneberg, R. InfectCheck CRP Barcode-Style Lateral Flow Assay for Semi-Quantitative Detection of C-Reactive Protein in Distinguishing between Bacterial and Viral Infections. *J. Immunological Methods* **2008**, *336*, 30–36.
- (237) Oyama, Y.; Osaki, T.; Kamiya, K.; Kawano, R.; Honjoh, T.; Shibata, H.; Ide, T.; Takeuchi, S. A Glass Fiber Sheet-Based Electroosmotic Lateral Flow Immunoassay for Point-of-Care Testing. *Lab on a Chip* **2012**, *12*, 5155-5159.
- (238) Ahn, J. S.; Choi, S.; Jang, S. H.; Chang, H. J.; Kim, J. H.; Nahm, K. B.; Oh, S. W.; Choi, E. Y. Development of a Point-of-Care Assay System for High-Sensitivity C-Reactive Protein in Whole Blood. *Clinica Chimica Acta* **2003**, *332*, 51–59.
- (239) Joung, H.-A.; Oh, Y. K.; Kim, M.-G. An Automatic Enzyme Immunoassay Based on a Chemiluminescent Lateral Flow Immunosensor. *Biosensors and Bioelectronics* **2014**, *53*, 330–335.
- (240) Campbell, F. M.; Ingram, A.; Monaghan, P.; Cooper, J.; Sattar, N.; Eckersall, P. D.; Graham, D. SERRS Immunoassay for Quantitative Human CRP Analysis. *Analyst* **2008**, *133*, 1355-1357.
- (241) Sloan-Dennison, S.; Laing, S.; Shand, N. C.; Graham, D.; Faulds, K. A Novel Nanozyme Assay Utilising the Catalytic Activity of Silver Nanoparticles and SERRS. *Analyst* **2017**, *142*, 2484–2490.
- (242) Orendorff, C. J.; Gole, A.; Sau, T. K.; Murphy, C. J. Surface-Enhanced Raman Spectroscopy of Self-Assembled Monolayers: Sandwich Architecture and Nanoparticle Shape Dependence. *Analytical Chemistry* **2005**, *77*, 3261–3266.
- (243) He, L.; Kim, N.-J.; Li, H.; Hu, Z.; Lin, M. Use of a Fractal-like Gold Nanostructure in Surface-Enhanced Raman Spectroscopy for Detection of Selected Food Contaminants. *Journal of Agricultural and Food Chemistry* **2008**, *56*, 9843–9847.
- (244) Selby, C. Interference in Immunoassay. *Annals of Clinical Biochemistry* **1999**, *36*, 704–721.
- (245) Lo, K. K.-W.; Choi, A. W.-T.; Law, W. H.-T. Applications of Luminescent Inorganic and

Organometallic Transition Metal Complexes as Biomolecular and Cellular Probes. *Dalton Transactions* **2012**, *41*, 6021-6047.

- (246) Crawford, A. C.; Skuratovsky, A.; Porter, M. D. Sampling Error: Impact on the Quantitative Analysis of Nanoparticle-Based Surface-Enhanced Raman Scattering Immunoassays. *Analytical Chemistry* **2016**, *88*, 6515–6522.
- (247) Lipson, A.; Lipson, S.; Lipson, H. *Optical Physics, 4th Ed.*; Cambridge University Press, Cambridge, 2010.
- (248) Schiettecatte, J.; Anckaert, E.; Smits, J. 'Interferences in Immunoassays'. In *Advances in Immunoassay Technology*; In Tech Open, Rijeka, 2012, 45-63.
- (249) Rey, E. G.; O'Dell, D.; Mehta, S.; Erickson, D. Mitigating the Hook Effect in Lateral Flow Sandwich Immunoassays Using Real-Time Reaction Kinetics. *Analytical Chemistry* **2017**, *89*, 5095–5100.
- (250) Povoia, P.; Almeida, E.; Moreira, P.; Fernandes, A.; Mealha, R.; Aragao, A.; Sabino, H. C-Reactive Protein as an Indicator of Sepsis. *Intensive Care Medicine* **1998**, *24*, 1052–1056.
- (251) Tang, Y. et al. Silver Nanoparticle Enhanced Raman Scattering-Based Lateral Flow Immunoassays for Ultra-Sensitive Detection of the Heavy Metal Chromium. *Nanotechnology* **2014**, *25*, 495501-495509.
- (252) Park, Y. II; Im, H.; Weissleder, R.; Lee, H. Nanostar Clustering Improves the Sensitivity of Plasmonic Assays. *Bioconjugate Chemistry* **2015**, *26*, 1470–1474.
- (253) Mehn, D.; Morasso, C.; Vanna, R.; Bedoni, M.; Prospero, D.; Gramatica, F. Immobilised Gold Nanostars in a Paper-Based Test System for Surface-Enhanced Raman Spectroscopy. *Vibrational Spectroscopy* **2013**, *68*, 45–50.
- (254) Spencer, K.; Chard, T. 'Pregnancy'. In *The Immunoassay Handbook, 4th Ed.*; Elsevier, Oxford, 2013, 757–776.
- (255) Kurman, R. J.; Scardino, P. T.; Robert McIntire, K.; Waldmann, T. A.; Javadpour, N. Cellular Localization of Alpha-Fetoprotein and Human Chorionic Gonadotropin in Germ Cell Tumors of the Testis Using an Indirect Immunoperoxidase technique: A New Approach to Classification Utilizing Tumor Markers. *Cancer* **1977**, *40*, 2136–2151.
- (256) Jacobsen, G. K.; Jacobsen, M. Alpha-Fetoprotein (Afp) and human Chorionic

- Gonadotropin (hCG) In Testicular Germ Cell Tumours. *Acta pathologica et microbiologica Scandinavica. Section A, Pathology* **2009**, *91*, 165–176.
- (257) Stenman, U.-H.; Alfthan, H.; Hotakainen, K. Human Chorionic Gonadotropin in Cancer. *Clin. Biochem.* 2004, *37*, 549–561.
- (258) Khoury, C. G.; Vo-Dinh, T. Gold Nanostars For Surface-Enhanced Raman Scattering: Synthesis, Characterization and Optimization. *The Journal of Physical Chemistry C* **2008**, *112*, 18849–18859.
- (259) Bastús, N. G.; Comenge, J.; Puentes, V. Kinetically Controlled Seeded Growth Synthesis of Citrate-Stabilized Gold Nanoparticles of up to 200 nm: Size Focusing versus Ostwald Ripening. *Langmuir* **2011**, *27*, 11098–11105.
- (260) McNaught, D.; Wilkinson, A. *IUPAC Compendium of Chemical Terminology*, 2nd Ed.; Blackwell Scientific Publications, Oxford, 1997.
- (261) Kasera, S.; Herrmann, L. O.; Barrio, J. del; Baumberg, J. J.; Scherman, O. A. Quantitative Multiplexing with Nano-Self-Assemblies in SERS. *Scientific Reports* **2015**, *4*, 6785-6791.
- (262) Idegami, K.; Chikae, M.; Kerman, K.; Nagatani, N.; Yuhi, T.; Endo, T.; Tamiya, E. Gold Nanoparticle-Based Redox Signal Enhancement for Sensitive Detection of Human Chorionic Gonadotropin Hormone. *Electroanalysis* **2008**, *20*, 14–21.
- (263) Armstrong, E. G.; Ehrlich, P. H.; Birken, S.; Schlatterer, J. P.; Siris, E.; Hembree, W. C.; Canfield, R. E. Use of a Highly Sensitive and Specific Immunoradiometric Assay for Detection of Human Chorionic Gonadotropin in Urine of Normal, Nonpregnant, and Pregnant Individuals. *The Journal of Clinical Endocrinology & Metabolism* **1984**, *59*, 867–874.
- (264) Sánchez-Purrà, M.; Carré-Camps, M.; de Puig, H.; Bosch, I.; Gehrke, L.; Hamad-Schifferli, K. Surface-Enhanced Raman Spectroscopy-Based Sandwich Immunoassays for Multiplexed Detection of Zika and Dengue Viral Biomarkers. *ACS Infectious Diseases* **2017**, *3*, 767–776.
- (265) Rodger, A. 'Beer-Lambert Law Derivation'. In *Encyclopedia of Biophysics*; Springer, Berlin & Heidelberg, 2013, 184–185.
- (266) Haiss, W.; Thanh, N. T. K.; Aveyard, J.; Fernig, D. G. Determination of Size and

Concentration of Gold Nanoparticles from UV–Vis Spectra. *Analytical Chemistry* **2007**, *79*, 4215–4221.

- (267) Malvern. *Zetasizer Nano Series User Manual*, Malvern Instruments Ltd, Worcestershire, 2010.
- (268) Horiba - The Stokes Einstein relation that connects diffusion coefficient measured by dynamic light scattering to particle size. <http://www.horiba.com/uk/scientific/products/particle-characterization/technology/dynamic-light-scattering/> (accessed Apr 14, 2018).
- (269) Cytodiagnosics Inc. - Lateral Flow Immunoassays <http://www.cytodiagnosics.com/store/pc/Lateral-Flow-Immunoassays-d6.htm> (accessed Apr 16, 2018).
- (270) Mak, W. C.; Beni, V.; Turner, A. P. F. Lateral-Flow Technology: From Visual to Instrumental. *Trends in Analytical Chemistry* **2016**, *79*, 297–305.

APPENDIX A: lateral flow strip assembling and striping procedures

Lateral flow (LF) strips were assembled and provided by BBI Solutions. Information about the fabrication of the strips used during this thesis is described in this section. Figure Appx. A1 shows a photograph of the LF strip taken from above and relative components size. Strip's components are listed below:

- Sample pad (SP): model n° 1281 (Ahlstrom), width 10 mm.
- Conjugate pad (CP): model n° 7 (BBI), width 19 mm.
- Nitrocellulose (NC): model n° SS12 (MDI), pores size 15 μm , width 25 mm.
- Absorbent pad (AP): model n° 222 (Ahlstrom), width 27 mm.
- Backing card (BC): size 75 x 349.2 mm (Kenosha).

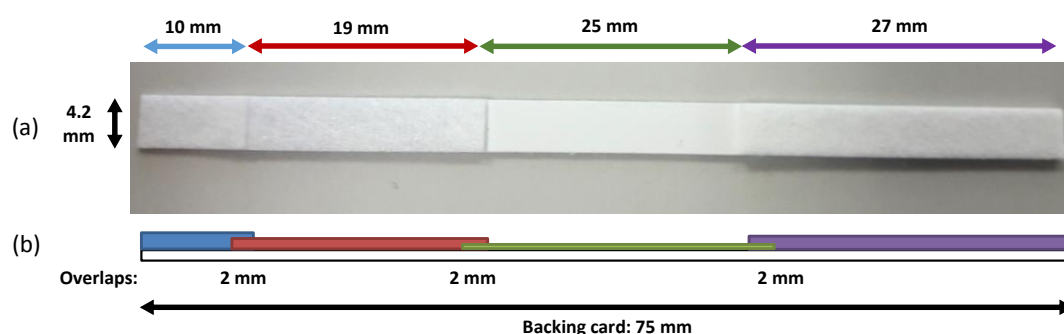


Figure Appx. A1. (a) Photograph of a lateral flow strip used in this thesis with corresponding sizes compartments: sample pad (blue), conjugate pad (red), nitrocellulose (green) and absorbent pad (purple). (b) Schematic representation of the strip section that shows the overlaps between the compartments which are bound together by a 75 mm backing card.

In order to build the strip, NC was attached onto the BC in the first place. Successively, AP was laminated to the top of backing cards, giving a 2 mm overlap with the top section of the NC. CP was laminated to give a 2 mm overlap with the bottom edge of the NC and SP was laminated to the bottom of the backing card to give a 2 mm overlap with the bottom edge of CP. Test strips were cut to 4.2 mm in width using a Kinematic cutter. Before building and cutting procedures, some NC membranes were previously striped with various line of antibody or antigen solutions, depending of the strip types. Blank strips were also built using untreated NC which did not contain any reagents. The striping of NC membranes was performed using the Imagen Technologies Isoflow dispensing system. Lines positions and concentrations for each strip type used during this thesis are summarised in Table Appx. A1.

The positions were measured from the bottom edge on the NC. After striping, NC membranes were dried at 37°C for 20 hours.

Table Appx. A1. LF strip type used during this thesis with information about test line (TL) or control line (CL) striped onto NC.

Strip type	Lines	Lines concentration (mg/mL)	Lines position (mm)
Competitive with CRP	4 x CRP (TL)	0.0625	5
		0.125	10
		0.25	15
		0.5	20
	4 x CRP (TL)	0.5	5
		0.5	10
		0.5	15
		0.5	20
Sandwich with capture Ab	1 x anti-CRP MAb (TL)	1	15
	1 x anti-CRP MAb (TL)	0.5	15
	1 x anti-CRP MAb (TL)	0.1	15
Sandwich for hCG detection	1 x anti-FSH (TL)	0.1	13
	1 x anti-mouse IgG (CL)	1	18
	1 x anti-FSH (TL)	0.25	13
	1 x anti-mouse IgG (CL)	1	18
	1 x anti-FSH (TL)	0.5	13
	1 x anti-mouse IgG (CL)	1	18

APPENDIX B: Buffers study for optimal lateral flow performance for his-tag Fab conjugated NTA-Ni AuNPs

An optimisation study was performed for his-tag Fab NTA-Ni AuNPs conjugate for the evaluation of optimum buffer conditions during a LF test. Competitive test strips with four lines, each containing 0.5 mg/mL CRP antigen, were used in this study. Four different strips were prepared by striping CRP using the following striping buffers at pH 7.6:

HEPES: 20 mM 4-(2-hydroxyethyl)-1-piperazineethanesulfonic acid (HEPES)

TBS (Tris buffer saline): 50 mM Tris (tris(hydroxymethyl)aminomethane), 150 mM NaCl

BBS1 (borate buffer saline 1): 10 mM sodium borate, 150 mM NaCl

BBS2 (borate buffer saline 2): 43 mM NaCl, 14 mM sodium borate, 170 mM boric acid.

To perform the experiment, his-tag Fab NTA-Ni AuNPs (O.D. 1.65, 30 μ L) was placed in the conjugate pad. For each of the four different striping buffers a 0.25 % Tween20 running buffer with equivalent salts was used (i.e. when CRP was striped in 0.02M HEPES striping buffer a 0.02M HEPES, 0.25% Tween20 running buffer was used). Test strips were run with 70 μ l of the relevant running buffer. The experiment was performed in duplicate. Once the conjugate had run up the test strips the strips were transferred to fresh wells containing 100 μ l running buffer. Test strips were photographed and analysed using the Camag reader 4 (Figure Appx. B1).

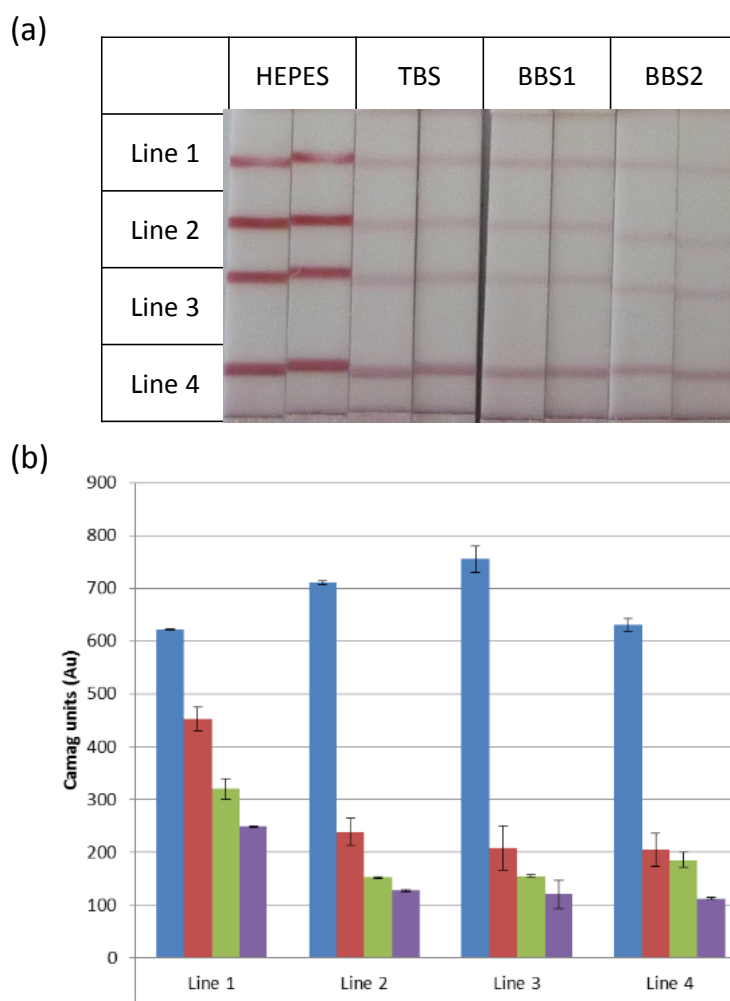


Figure Appx. B1. (a) Photographs of NC compartment of lateral flow strips used to evaluate optimum buffer conditions. Each line contains 0.5 mg/mL CRP antigen. (b) Graph representing line intensities recorded by a Camag reader: HEPES (blue), TBS (red), BBS1 (green) and BBS2 (purple). Error bars represent standard deviation of two replica.

Results showed that when the NTA-Ni test conjugates were tested against the four different striping buffers, the best signal was achieved using the 0.02 M HEPES striping and running buffers. The test strips with CRP striped in the other three buffers (TBS, BBS1 and BBS2) gave reduced signal compared to those using HEPES buffer with a reduction in signal as you move up the test strips. Therefore, HEPES buffer was used in all the lateral flow experiment that involve the use of his-tag Fab conjugated NTA-Ni AuNPs.

APPENDIX C: capture antibody line and CRP spot optimisation studies

C1. Sandwich format

In order to determine the optimum concentration of the capture antibody line for strips used in the sandwich SERRS-based lateral flow assay, an optimisation study was performed. Three sets of strips that were previously striped with a line of 0.1, 0.5 and 1 mg/mL solution of monoclonal anti-CRP antibody (capture Ab) were used in this experiment. MGITC labelled his-tag Fab NTA-Ni AuNPs (5 μ L) was used as anti-CRP conjugate and three different solutions of CRP (0, 50 and 100 ng/mL) were added on to the sample pad for each set of strips (100 μ L). Once the lateral flow test was complete, test lines were analysed by a Raman spectrometer equipped with a 633 nm laser. Tests were performed in triplicates. Figure Appx. C1 shows averaged SERRS spectra of the test lines for strips with (a) 0.1, (b) 0.5 and (c) 1 mg/mL of capture Ab.

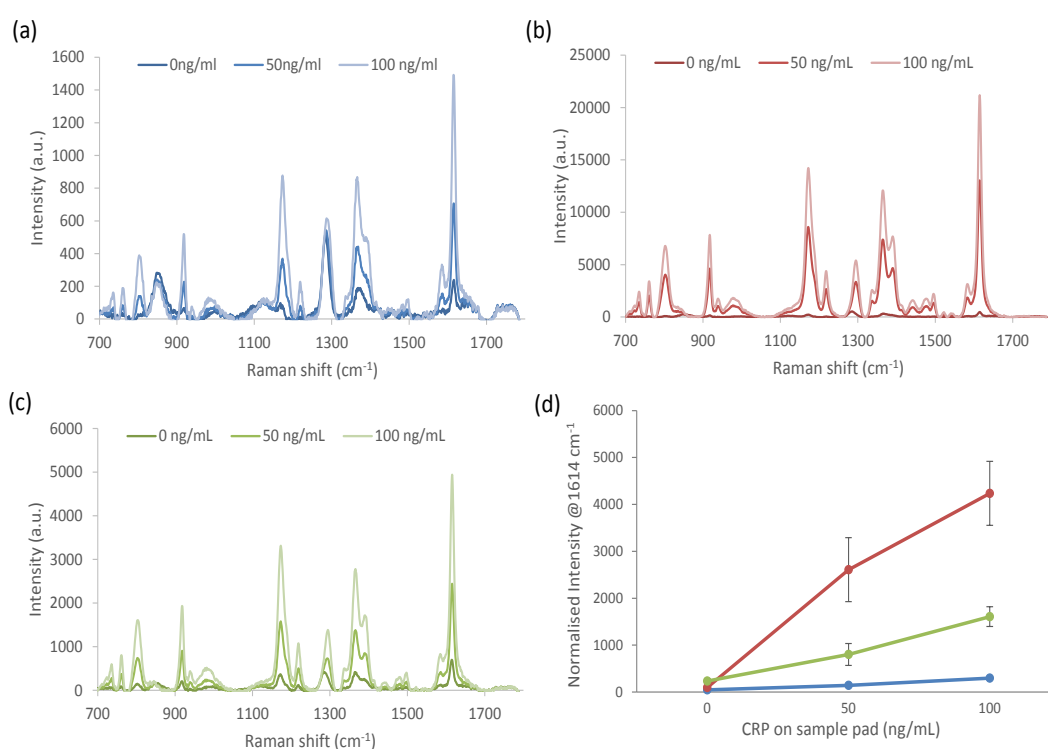


Figure Appx. C1. Averaged SERRS spectra from maps collected on the test lines of strips that contain (a) 0.1, (b) 0.5 and (c) 1 mg/mL of capture Ab. Legends on top the spectra represents the CRP concentration placed on the sample pad. (d) SERRS intensities at 1614 cm⁻¹ normalised for the exposure time of each spectra: 0.1 (blue), 0.5 (red) and 1 mg/mL (green) of capture Ab. Error bars indicates standard deviation of three replica.

Each set of strips were analysed with the following parameters:

- (a) Capture Ab 0.1 mg/mL. Rectangular map 600 x 1800 μm . 126 acquisitions (18 x 7 spectra). 5 second exposure time. 1 accumulation. Objective 5x. Power laser 100 %.
- (b) Capture Ab 0.5 mg/mL. Rectangular map 600 x 1800 μm . 91 acquisitions (13 x 7 spectra). 5 second exposure time. 1 accumulation. Objective 5x. Power laser 100 %.
- (c) Capture Ab 1 mg/mL. Rectangular map 600 x 1800 μm . 133 acquisitions (19 x 7 spectra). 3 second exposure time. 1 accumulation. Objective 5x. Power laser 100 %.

The graph in Figure Appx. C1 (d) shows that the best signal response was obtained when strips that contained 0.5 mg/mL of capture Ab were used. In general the sensitivity of an assay is higher for higher slopes. For the same amount of CRP in the sample pad, strips with 0.5 mg/mL of capture Ab provided a better SERRS signal than the other two sets of strips. Therefore, this set of strips was used.

C2. Competitive format

In order to determine what concentration of immobilised CRP is optimal for competitive SERRS-based lateral flow assays, an experiment involving three different CRP concentration was performed. The middle of nitrocellulose of blank strips were spotted with 0.5 μL of the following CRP solutions:

- (a) 50 $\mu\text{g/mL}$
- (b) 100 $\mu\text{g/mL}$
- (c) 500 $\mu\text{g/mL}$

Strips were placed to dry at 37 $^{\circ}\text{C}$ for 1 hour. SERRS-based lateral flow assay was then performed using for each set of strips the following CRP concentration on the sample pad (analyte):

- (1) 0 $\mu\text{g/mL}$ (blank)
- (2) 1 $\mu\text{g/mL}$
- (3) 100 $\mu\text{g/mL}$

After the lateral flow test was completed, test areas were scanned by a circular map mode using a 633 nm Raman microscope. Spectra collected for each strip were then averaged and the signal at 1614 cm^{-1} was used to evaluate the optimal Concentration/SERRS response.

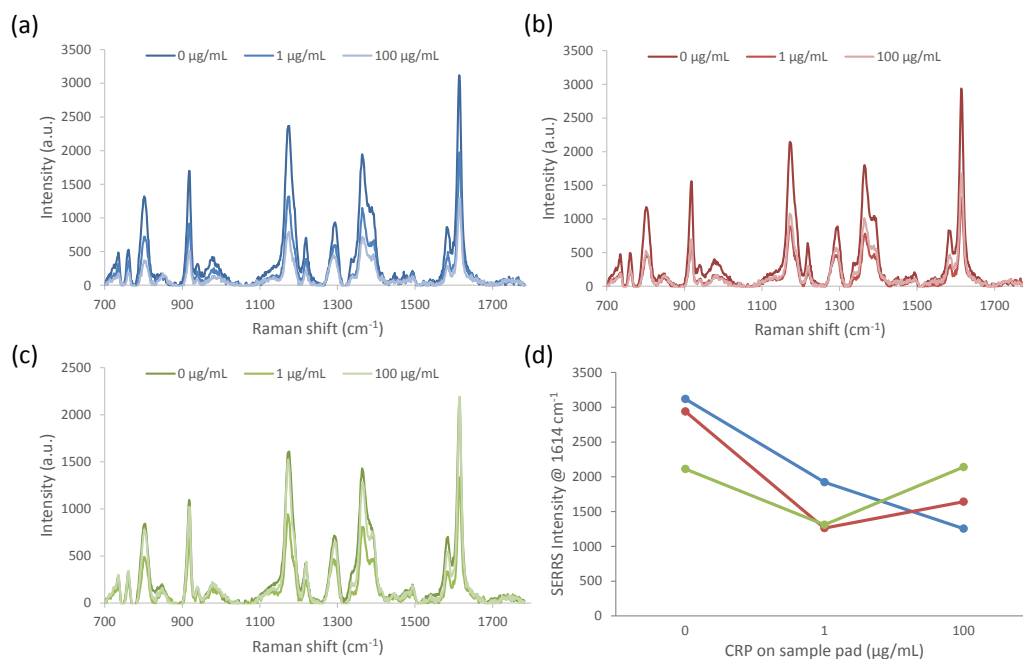


Figure Appx. C2. Averaged SERRS spectra from maps collected on the test areas of strips that contained (a) 50, (b) 100 and (c) 500 µg/mL of immobilised CRP. Legends on top the spectra represents the CRP concentration placed on the sample pad. Spectra were taken with a 633 nm laser Raman spectrometer, 3 second exposure time and 5x objective. (d) Graph representing intensity at 1614 cm⁻¹ for each set of strip: 50 (blue), 100 (red) and 500 µg/mL (green).

Figure Appx. C2 suggested that the optimal CRP concentration to be placed on the nitrocellulose was 50 µg/mL. The graph shows that there is a linear response between signal intensity and concentration. The SERRS signal decreased with the increase of the analyte concentration, as expected from a competitive assay. On the other hand, when the immobilised CRP was higher than 50 µg/mL, the decreasing was not observed.

APPENDIX D: SEM and TEM images of various AuNSs batches

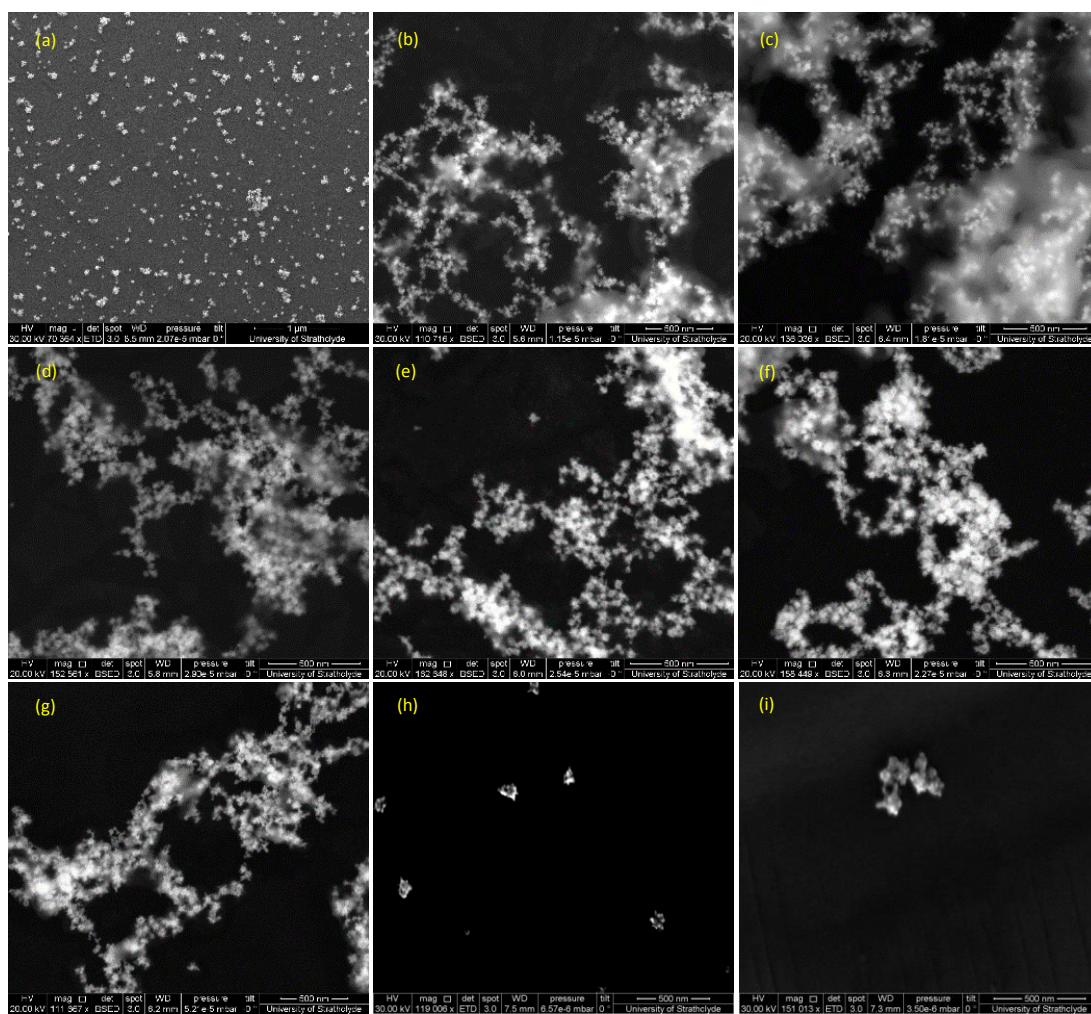


Figure Appx. D1. SEM images of various batches of citrate capped BBI Nanostars. Batch n° 16967 (a), 16975 (b), 16976 (c), 16977 (d), 16978 (e), 16979 (f), 16980 (g), 13098 (h) and 17003 (i).

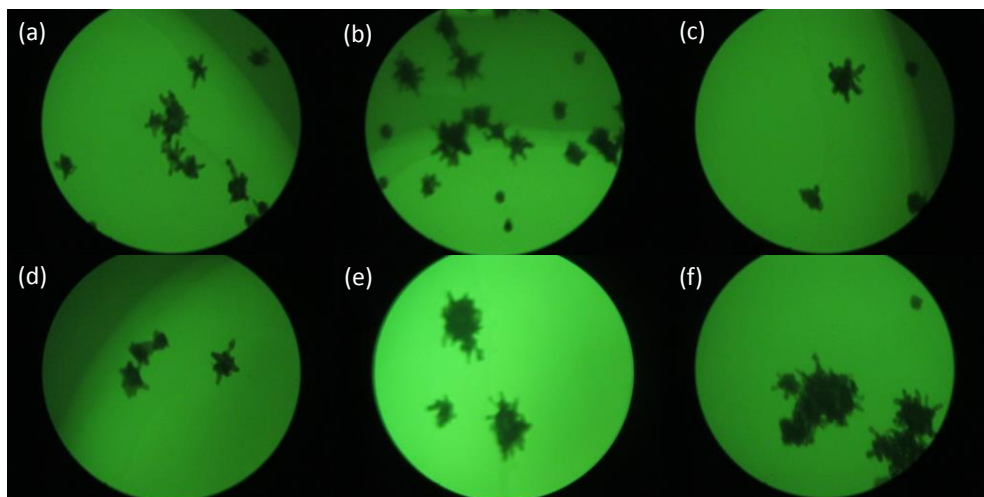


Figure Appx. D2. TEM images of various batches of citrate capped BBI Nanostars. Batch n° 16975 (a), 16976 (b), 16977 (c), 16978 (d), 16979 (e), 16980 (f). Courtesy of BBI Solutions.

APPENDIX E: test line study on lateral flow strips for detection of hCG

In order to determine the best conditions for the sandwich format SERS-based LFIA for the detection of hCG, three sets of LF strips which contained various capture Ab concentration on the test line (100, 200 and 500 $\mu\text{g}/\text{mL}$) were tested. The AuNSs@anti-hCG@MBA conjugates were deposited on to the CP of each strip. Borate buffer (pH 7.55, 25 mM) that contained Tween 20 and BSA was used as running buffer. Three hCG solutions at various concentrations (0.1, 1 and 10 ng/mL) and 1 blank solution were added to the SP of each strip set. Results are shown in Figure Appx. E1.

T line ($\mu\text{g}/\text{mL}$) \rightarrow	100			250			500		
[hCG, ng/mL]	Lines	T	C	Lines	T	C	Lines	T	C
10									
1									
0.1									
0									

Figure Appx. E1. Photographs of the NC compartment of LF strips after the test was complete. Each set of strips which contained a control line (C) of 1 mg/mL of anti-mouse IgG and test lines (T) respectively of 100, 250 and 500 $\mu\text{g}/\text{mL}$ of anti-hCG capture Ab.

Photographs shows that the test lines for the strips with 100 $\mu\text{g}/\text{mL}$ of capture antibody were not visible and only a concentration of hCG of 10 ng/mL was able to give a faint signal. On the other hand, samples that contained 250 and 500 $\mu\text{g}/\text{mL}$ showed stronger test lines for 10 ng/mL of hCG and fainter lines at 1 ng/mL. As the visual detection for strips at 0.1 ng/mL was challenging, test lines were analysed by SERS and peaks from MBA at 1082 cm^{-1} for each samples were compared with blank sample. Results are shown in Figure Appx. E2.

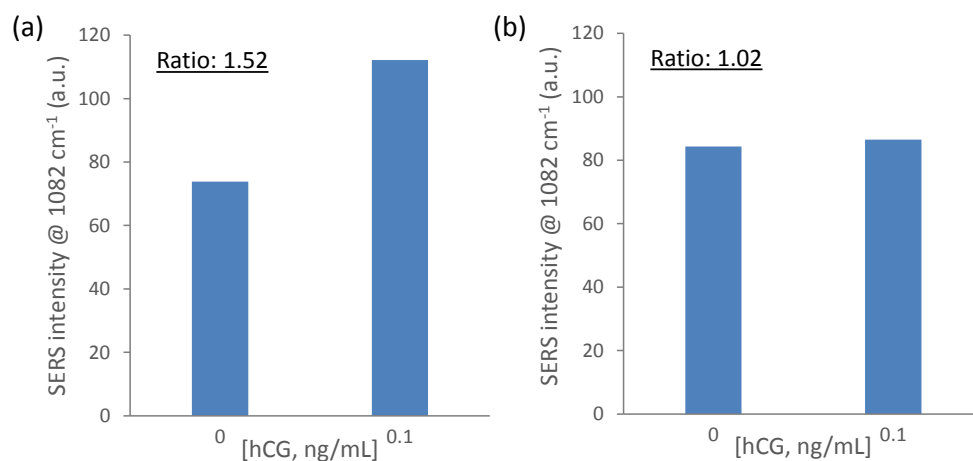


Figure Appx. E2. Bars charts representing SERS intensity of the peak at 1082 cm⁻¹ from test lines of strips containing (a) 250 and (b) 500 µg/mL of capture antibody.

Results showed that the strips containing 250 µg/mL of capture antibody gave a better signal ratio $I_{0.1}/I_{\text{blank}}$ than strips containing 500 µg/mL of Ab. These suggested that the background is higher for sample at 500 and hence less sensitive. Therefore, strips containing 250 µg/mL were chosen for the development of the SERS-based LFIA for the detection of hCG.

APPENDIX F: LF strips image for AuNSs@MBA@anti-hCG conjugates optimisation study



Figure Appx. F1. Scanned images of LFIA strips performed during the optimisation study. The AuNSs@MBA@anti-hCG conjugates are: 1A, 1C, 2A, 2C, 3A, 3C, 4A and 4C. Each conjugate was used to run 5 strips that contained a test line of 250 $\mu\text{g}/\text{mL}$ of anti-hCG and a control line of 1 mg/mL of anti-mouse IgG. Sample pads were loaded with hCG as follows: 0 (blank), 1 (0.005 ng/mL), 2 (0.05 ng/mL), 3 (0.5 ng/mL) and 4 (5 ng/mL).